Transactions of the ASME

Transactions of the ASME, Journal of Fluids Engineering (ISSN 0098-2202) is published quarterly (Mar., June, Sept., Dec.) for $110.00 per year by The American Society of Mechanical Engineers, 345 East 47th Street, New York, NY 10017. Second class postage paid at New York, NY and additional mailing offices. POSTMASTER: Send address changes to Transactions of the ASME, Journal of Fluids Engineering, c/o THE AMERICAN SOCIETY OF MECHANICAL ENGINEERS, 22 Law Drive, Box 2300, Fairfield, NJ 07007-2300.
CHANGES OF ADDRESS must be received at Society headquarters seven weeks before they are to be effective. Please send old label and new address.
PRICES: To members, $36.00, annually; to nonmembers, $110.00. Add $20.00 for postage to countries outside the United States and Canada.
STATEMENT from By-Laws. The Society shall not be responsible for statements or opinions advanced in papers or . . . printed in its publications (B7.1, Par. 3).

INDEXED by Applied Mechanics Reviews and Engineering Information, Inc.
Canadian Goods & Services Tax Registration #126148048

Journal of Fluids Engineering

Published Quarterly by The American Society of Mechanical Engineers

VOLUME 114 • NUMBER 1 • MARCH 1992

(Contents continued on page 39)

Announcements and Special Notices

Journal of Fluids Engineering

Editorial

This is a short report on the operation of this Journal, and on the effort its Editorial Board is making to reach its readers and its contributing authors. It is also an invitation for feedback from both groups. Suggestions, comments, and criticism are invited and can be provided to the Technical Editor or to any of the associate editors either by mail or by telephone. Such input will be most valuable now, because the Editorial Board is rethinking the goals of this publication and is reconsidering methods of serving better the fluids engineering community. This effort has been inspired by significant recent developments in the tools of research and design as well as a surge in the activities of our Division (see Editorial in December issue).

The March issue appears right after the ASME winter annual meeting where many committees meet and many issues are discussed. This issue also contains the authors' index and the list of reviewers for the papers published in the previous year. It, therefore, seems appropriate for a report by the Technical Editor to appear in the same issue. Starting with this issue, we will establish this practice.

Our readers should know that we are vigorously debating on how to make the material we publish more interesting and more useful. Our mission is to communicate with our audience scientific results of fundamental character which however, may find sooner or later application in design. We, therefore, always urge authors to address the broader audience of practicing engineers and not only their peer researchers.

The number of papers submitted to our Journal has doubled in the past three years. To accommodate the corresponding larger number of accepted papers, we have secured one hundred more pages this year and we hope for a similar further increase next year. To reduce our backlog, we overextended ourselves in our September and December issues. As a result, and despite the one-hundred extra pages, this and the June issue may appear a little thin, unless we can get a second emergency increase in pages approved.

We are happy to report to our authors that we have managed to reduce significantly the time from submission to publication. For papers submitted in 1991, we were able to complete the review process in nine months on the average. This includes first set of reviews, revisions, resubmission and a final decision. Unfortunately, there are annoying exceptions, but on the positive side we managed to get a few papers in print seven months after their date of submission. Authors are encouraged to contact the technical associate editors and the Technical Editor to inquire about progress on the review of their submitted papers.

Finally, we should acknowledge the invaluable contributions of five of our associate editors whose tenure has expired. They are (i) Dr. Upendra S. Rohatgi who served one extra year for a total of four and (ii) Dr. Widen Tabakoff, both in the area of fluid machinery; (iii) Dr. Christopher J. Freitas who worked in the area of fluid mechanics, (iv) Dr. David G. Lilley who was responsible for computational fluid mechanics and (v) Dr. Michael L. Billet in the area of multiphase flow. Dr. Efstathios E. Michaelides will serve for another year covering some areas in multiphase flow. New individuals have been nominated to serve three-year terms as associate editors. These and the areas they will be working on are: Dr. Oktay Baysal (Old Dominion University) computational fluid mechanics, Dr. Ronald L. Panton (University of Texas) fluid mechanics and Dr. Michael W. Reeks (Berkeley Nuclear Lab, Berkeley, Gloucestershire, UK) multiphase flow.

The Technical Editor

On the Motion of Solid Spheres Falling Through Viscous Fluids in Vertical and Inclined Tubes

Joseph A. C. Humphrey

Hiroyuki Murata[1]

Department of Mechanical Engineering,
University of California at Berkeley,
Berkeley, California 94720

Little is known about the rotational motion of spheres falling through viscous fluids in inclined tubes. Most studies have investigated translational and rotational motions in vertical tubes. These works show that in creeping flow a sphere's translational and rotational velocities are independent. Rotation is predicted and observed for eccentric spheres while concentric spheres fall without rotation. Experiments were performed by us with steel spheres of radius r falling through glycerine in a tube of variable inclination angle and of radius R such that $r/R = 0.882, 0.757, 0.442$. For the cases involving two or three spheres falling together various modes of motion were observed. Especially interesting was the finding that the rotation direction of a sphere gradually changes from positive (opposite to downhill rolling) to negative (in the sense of downhill rolling) as the tube inclination angle is increased. This is allowed by the inertia-induced lift force which maintains a sphere at a very small but finite distance from the inclined tube wall. However, by further increasing the inclination angle the lift force eventually becomes smaller than the apparent weight of the sphere which, upon finally contacting the tube wall, descends by rolling along it. Examination of our findings in the light of earlier results for vertical and inclined tubes suggests that, through its effect on sphere eccentricity, inertia indirectly affects the rotational motion of a falling sphere when $Re_p > 10^{-3}$ but it does not significantly affect the translational motion when $Re_p < 1$. None of the inclined tube studies performed to date has been completely devoid of inertia-induced lift effects.

1 The Problem of Interest and Earlier Work

We are concerned with the translational and rotational motions of spheres falling through vertical and inclined tubes of constant circular cross-section containing a viscous fluid. The problem is of fundamental and practical interest, with applications ranging from the modeling of blood flow through capillaries to falling ball viscosimetry.

1.1 Spheres in Vertical Tubes (Theory). It is well known that the presence of solid boundaries can substantially retard the rate of descent of particles falling through viscous fluids. Cox and Mason (1971) have reviewed the early literature pertinent to single spheres and particle suspensions moving through Newtonian fluids in tubes of circular cross-section. With reference to Fig. 1(*a*), for the case of a single solid sphere of radius r in creeping flow at a distance b from the axis of a vertical tube of radius R, Cox and Mason show that the sphere translates axially along the tube while maintaining a constant radial position. This finding has been verified experimentally and the conclusion is that in creeping motion along a vertical tube ($Re_p << 1$) a sphere will not cross the flow streamlines. An eccentrically located sphere will rotate as well as translate, as a result of the net torque induced upon it by fluid shear.

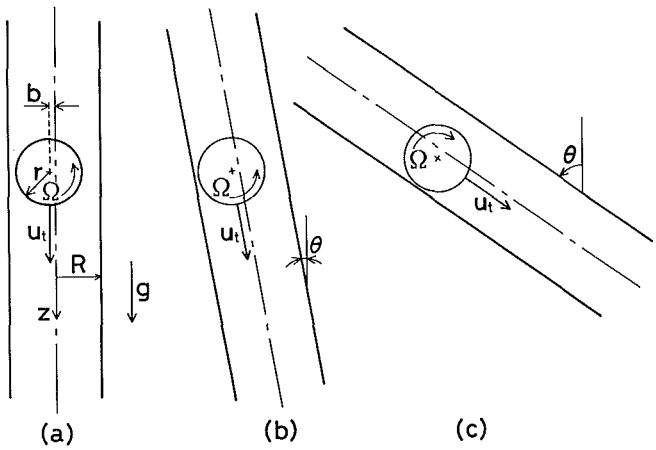

Fig. 1 Definition of system geometry and velocity directions for a sphere with $r/R = O(1)$ falling through a viscous fluid in a tube of variable inclination angle. (*a*) $\theta = 0$: $\Omega r/u_t = 0$ when $e = 0$; $\Omega r/u_t > 0$ when $0 < e < 1$; $\Omega r/u_t < 0$ as $e \to 1$. (*b*) $\theta < \theta_{crit}$ and $e \to 1$: $\Omega r/u_t > 0$ (positive rotation, opposite to contact-rolling); (*c*) $\theta > \theta_{crit}$ and $e \to 1$: $-1 < \Omega r/u_t < 0$ (negative rotation, in the direction of contact-rolling); $\Omega r/u_t = -1$ (contact-rolling) when $e = 1$.

[1]Present Address: Nuclear Technology Division, Ship Research Institute, Ministry of Transport, Tokyo 181, Japan.

Contributed by the Fluids Engineering Division for publication in the JOURNAL OF FLUIDS ENGINEERING. Manuscript received by the Fluids Engineering Division March 20, 1991.

The translational and rotational motions are independent and, generally, the direction of rotation is opposite to that which would arise from a no-slip contact-rolling condition along the tube wall to which the sphere is nearest. However, as discussed below, the latter is not the case for highly eccentric closely fitting spheres where $e \to 1$ and $r/R \to 1$ simultaneously.

Using the "method of reflections," Brenner (1966) and Greenstein and Happel (1968) have derived theoretical expressions for the force and torque due to the creeping flow past a sphere placed in a vertical tube at a distance b from the tube axis. The analysis assumes that the distance of the sphere from the tube wall is large compared to the sphere radius ($r << (R-b)$). This constraint translates to $r << R$ for a sphere on the tube axis ($b=0$), or to the condition that $r \to 0$ as $b \to R$. By means of analysis using a regular perturbation expansion procedure, Bungay and Brenner (1973a) examined the hydrodynamic particle-wall interaction experienced by an eccentrically positioned sphere in close proximity to the wall of a vertical tube ($r \leq R-b << R$).

By means of singular perturbation theory, Bungay and Brenner (1973b) also solved for the case corresponding to a closely fitting sphere in a vertical tube ($r \leq R-b \leq R$, $r=O(R)$) and this analysis interests us especially. As in their (1973a) study, all relevant particle Reynolds numbers were assumed to be sufficiently small compared to unity to justify the neglect of the inertial terms in the Navier-Stokes equations. For the case of a single sphere falling through a quiescent fluid in a vertical tube, the authors derived equations for the terminal translational (u_t) and rotational (Ω) velocities of the sphere as a function of its lateral position or eccentricity ($e=b/(R-r)$), and the clearance between the sphere and the wall ($\epsilon=(R-r)/r$). Their results, subject to the condition that $\epsilon << 1$, are as follows:

For $e<1$:

$$u_t = \frac{2\sqrt{2}F}{9\pi^2\mu r}\left(\frac{1}{\eta_0}+\frac{e^2}{2\eta_3}\right)\epsilon^{5/2}+O(\epsilon^3) \tag{1}$$

$$\Omega = \frac{\sqrt{2}eF\epsilon^{3/2}}{6\pi^2\mu r^2\eta_3}+O(\epsilon^2) \tag{2}$$

For $e \to 1$:

$$u_t \sim -\frac{F\epsilon^{1/2}}{4\pi\mu r \ln\left(\frac{32}{1-e}\right)} \tag{3}$$

$$\Omega \sim -\frac{F\epsilon^{3/2}}{12\pi\mu r^2 \ln\left(\frac{32}{1-e}\right)} \tag{4}$$

In these equations, F (see Nomenclature) is the net external gravitational force experienced by the sphere, equal and opposite to the hydrodynamic force, and μ is the dynamic viscosity of the fluid. The quantities η_0 and η_3 are theoretically determined functions, plotted in the authors' paper, that depend on the eccentricity, e. (The direction and signs of u_t and Ω, in the above equations and as used in this paper, are defined in Fig. 1.)

For the conditions analyzed, the above equations show that the sphere translational and rotational velocities are independent. The equations predict that a concentric sphere ($e=0$) settles without rotation. However, if displaced to an eccentric position it will descend more rapidly while simultaneously rotating in a direction opposite to that which would arise from a no-slip contact-rolling condition along the tube wall to which the sphere is nearest. The maximum settling velocity is achieved when $e=0.98$, approximately. At this radial location the sphere falls about 2.1 times faster than when $e=0$. At $e=1$ the sphere is in contact with the tube wall and, theoretically, cannot translate or rotate. Although the accuracy of the equations is constrained by the condition that $\epsilon << 1$, they can be used to qualitatively illustrate the variations of u_t and Ω as a function of e when $\epsilon=0.134$, one of the experimental cases of this work. The results are plotted in Fig. 4 and they will later help us interpret some of our experimental findings.

It is of special interest that the theory of Bungay and Brenner (1973b) also predicts that as $e \to 1$ the rotation direction of a sphere changes. (See the signs on Eqs. (1) and (3) and the corresponding rotation directions defined in Fig. 1.) The authors point out that the resulting motion is quite different from no-slip contact-rolling, for which one would expect $-\Omega r/u_t = 1$ when $e=1$. That this is not what the analysis predicts can be seen by combining Eqs. (3) and (4) to yield $-\Omega r/u_t = (1/3)\epsilon$ (in the limit $e \to 1$) which is a very small quantity since $\epsilon << 1$. This limiting behavior is in qualitative agreement with corresponding predictions by Goldman et al. (1967) for the case of a sphere falling parallel to a plane wall.

1.2 Spheres in Vertical Tubes (Experiments). There have been numerous experimental investigations concerning wall effects on the viscous dominated (but not necessarily inertialess) motion of spheres falling in vertical tubes. Iwaoka and Ishii (1979) tabulate various noteworthy contributions, including measurements of their own, in the form of correlations of the type

$$u_\infty/u_t = f(r/R) \tag{5}$$

obtained over various ranges of r/R. In Eq. (5) u_∞ is a reference translational velocity corresponding to the terminal velocity of the sphere in free fall, calculated assuming Stokes flow.

Figure 3 shows the $f(r/R)$ correlations derived experimentally by Francis (1933) using steel balls in glucose ($10^{-6} < \mathrm{Re}_p < 10^{-4}$, approximately) and by Iwaoka and Ishii using steel balls in aqueous solutions of millet jelly ($\mathrm{Re}_p < 0.0762$). Also shown are the analytical predictions using

Nomenclature

- b = distance between the sphere center and the tube axis
- e = $[=b/(R-r)]$ sphere lateral position or eccentricity
- F = $[=\pi d^3 g(\rho_p-\rho)/6]$ net gravitational force experienced by a sphere in a vertical tube
- g = gravitational acceleration constant (9.8 m/s^2)
- r = $[=d/2]$ sphere radius
- R = $[=D/2]$ tube radius
- Re_p = $[=du_t/\nu]$ sphere Reynolds number
- u_t = terminal translational velocity of a sphere in a tube
- u_∞ = $[=d^2(\rho_p-\rho)g/18\mu]$ terminal translational velocity of a sphere in free fall (from Stokes' law)
- ϵ = $[=(R-r)/r]$ dimensionless clearance between the sphere and the tube wall
- η_0, η_3 = theoretically determined functions that depend on the eccentricity, e
- Ω = rotational (angular) velocity of a sphere (radians/second)
- μ = fluid dynamic viscosity
- ν = $[=\mu/\rho]$ fluid kinematic viscosity
- Π_3 = $[=\pi d^3 g(\rho_p-\rho)\cos\theta/6\mu\nu]$ Grashof number for a sphere in an inclined tube
- ρ = fluid density
- ρ_p = sphere density
- θ = inclination angle of the tube with respect to the vertical

Table 1 Parameter range of inclined tube experiments

	r/R ϵ θ e	Re_p Π_3 and $\Omega r/u_t$
Block (1940): steel sphere, solutions of glyerine in methyl alcohol, glass tube, 21 and 31°C.	0.769 0.300 67° – 87° ~1	0.016 – 85 9.0 – 4.9 10^4 and $-1 \le \Omega r/u_t < 0$
Floberg (1968): steel spheres, various oils, plastic tubes, 20°C.	0.914 – 0.997 9.435 10^{-2} – 2.657 10^{-3} 3° – 11.5° ~1	0.016 – 4.117 1.50 10^3 – 1.39 10^7 and $\Omega r/u_t \sim 0$ for $\theta = 3° - 4°$ when $0.988 \le r/R \le 0.997$ $\Omega r/u_t > 0$ for $\theta = 11.5°$ when $0.914 \le r/R \le 0.977$
Zolotykh (1962): glass and metal spheres, various oils and solutions of glycerine in water or ethyl alcohol, glass tubes, temperature not stated.	0.125 – 0.992 6.974 – 8.573 10^{-3} 10° ~1	10^{-4} – 31.62 3.11 10^{-3} – 3.11 10^7 and text says rolling replaced by sliding for small r/R (meaning $r/R < 0.834$, approximately)
This work: steel spheres, pure glycerine, plexiglas tube, 24.5 – 26.5°C	0.442 – 0.882 1.263 – 0.134 0° – 80° $0 \le e < 1$ (vertical tube) ~1 (inclined tube)	0.060 – 0.210 1.4 – 61 and $-1 \le \Omega r/u_t < 1$ depending on values of θ and r/R

the theories of: Bungay and Brenner (1973a) for small spheres ($r/R << 1$); Bungay and Brenner (1973b) for large spheres ($r = O(R)$): and, Paine and Scherr (1975) for $r/R < 0.9$, based on an extension of the solution provided by Haberman and Sayre (1958) in terms of an infinite set of linear algebraic equations for the Stokes' stream function coefficients. As in the theory of Paine and Scherr, the experimental correlations of Iwaoka and Ishii and Francis do not include a dependence on the eccentricity, e. Notwithstanding, Iwaoka and Ishii observed that for values of $r/R > 0.8$ the spheres in their experiment were eccentrically located and rotated in spite of the precautions taken. In similar experiments using glycerine instead of glucose, Francis also observed that in the range $3\ 10^{-2} < Re_p < 3$, approximately, the spheres fell with "rapid rotation" and "always near one side of the tube" with the sense of rotation opposite to contact-rolling. If in the experiments of Iwaoka and Ishii and of Francis inertial effects were significant, the translational and rotational motions were coupled in a complex manner.

The experiments conducted by Francis and the subsequent theoretical analysis performed by Tanner (1963) both show that, to within an axial displacement equal to one tube radius from either end of a tube, neither the closed end at the bottom of the tube nor the open surface at its top induce detectable effects on the sphere translational velocity.

1.3 Spheres in Inclined Tubes (Experiments). In contrast to the vertical tube data, results for the motions of spheres falling through viscous fluids in tubes of arbitrary inclination angle are sparse and contradictory. Experiments have been performed by Block (1940), Zolotykh (1962), and Floberg (1968) but we are unaware of corresponding theoretical analyses. Table 1 summarizes the parameter ranges investigated experimentally, including the conditions of this study. Because of the implications to inertia effects, discussed later, the relatively large values of Re_p and Π_3 for all the cases in the table are noteworthy. Included in the table are some observations pertaining to the rotational velocities of the spheres in each study.

An extension of the dimensional analysis in Zolotykh will show that the expression for the terminal translational velocity of a sphere in creeping motion down an inclined tube is of the form

$$Re_p = f[\Pi_3, \epsilon, e] \tag{6}$$

where $\Pi_3 = F\cos\theta/\mu\nu$ is an effective Grashof number for the sphere. This parameter provides a relative measure of the buoyancy and viscous forces acting on the sphere.

In all of his experiments, Zolotykh fixed the inclination angle of the tube with respect to the vertical to a value $\theta = 10$ degrees. For each of the clearances investigated in the range $0.834 < r/R < 1$ he obtained simpler correlations based on Stokes' equation of the form $Re_p = A\Pi_3$, where A is an empirical constant. Thus, the sphere translational velocity was taken to be independent of the eccentricity for which a nominal value of $e = 1$ must have been assumed. All of the data in this range of r/R were correlated by the author in a single equation (Eq. (21) in the paper) that can be rearranged in the form

$$Re_p = A\Pi_3\epsilon^b \left(\frac{1}{1+\epsilon}\right)^b,$$

where A and b are empirical constants. For $r/R \to 1$ ($\epsilon \to 0$) this correlation reduces to $Re_p = A\Pi_3\epsilon^b$ which is of the form derived theoretically by Bungay and Brenner (1973b), see Eqs. (1) and (3). Zolotykh found $b = 2.5258$ from his data, a number in close agreement with the theoretical value of 5/2 corresponding to Eq. (1) for $0 < e < 1$.

Floberg obtained analytical expressions for u_t and Ω yielding the same exponents for F and ϵ as in the more accurate equations for these velocities, Eqs. (1) and (2), subsequently derived by Bungay and Brenner (1973b). In his experiments, the author inclined the tubes by nominal amounts, between 3 and 11.5 degrees, in order to "get a definite eccentricity of $e = 1$." When $e = 1$ one expects frictional contact between a sphere and the wall of an inclined tube. For this condition the sphere rotational and translational velocities are related according to $-\Omega r/u_t = 1$, corresponding to a down-hill rolling motion without slip; see Fig. 1(*c*). However, neither Floberg nor Zolotykh report data confirming this relation although, in the translation of Zolotykh's paper, it is mentioned that for small spheres (meaning $r/R < 0.834$, approximately) "the rolling of the ball is replaced by sliding along the wall of the tube." In contrast, as shown in Table 1, Floberg observed nonrotating falling spheres when $r/R > 0.988$. In the cases where rotation was observed its direction was always opposite to rolling, that is, positive, as illustrated in Fig. 1(*b*).

Block performed experiments for much larger tube inclination angles than Zolotykh and Floberg. Using a single value of $r/R = 0.769$, he paid special attention to determining and correlating the conditions that induce a pure contact-rolling motion of the sphere. By simultaneously measuring the trans-

lational and rotational components of motion he showed that, as the tube inclination angle was decreased, the sphere's motion evolved from pure contact-rolling to translation with rotation in the direction of contact-rolling (sliding with rolling). All Block's experiments fell in the range $-1 \le \Omega r/u_t < 0$. Conditions were never attained where the sphere translated with a positive rotational velocity.

Block suspected the presence of weak inertial effects in his translational velocity data at high Reynolds numbers and proposed the relation

$$\frac{\Pi_3}{\mathrm{Re}_p^2} = A\mathrm{Re}_p^a + C \tag{7}$$

based on Oseen's equation to correlate all the data for contact-rolling motion only. Equation (7) can be rearranged to read $\mathrm{Re}_p = (B\Pi_3 - D\mathrm{Re}_p^2)^a$. For $\mathrm{Re}_p < 1$ the second term on the right-hand side of the rearranged equation is negligible compared to the first and the simpler relation, $\mathrm{Re}_p = A\Pi_3^a$ is obtained where A and a are empirical constants different from those in Eq. (7). From Block's data it is possible to show that $a = 1.10$, in close agreement with the theoretical value of unity corresponding to Stoke's equation.

1.4 Comments on Lift Force Due to Inertia. For a sphere translating in a pure shear flow, or for a sphere simultaneously translating and rotating in a fluid at rest, with the sphere Reynolds number such that viscous and inertia effects are of the same order of magnitude, Saffman (1965) and Rubinow and Keller (1961) have, respectively, demonstrated the existence of a transverse lift force acting on the sphere, the direction of which depends on the vector product between the angular velocity of the sphere and its translational velocity relative to the fluid. Other, more inclusive, inertial analyses which take into consideration the presence of a vertical tube wall as well as the nonuniformity of shear, have been performed by, for example, Cox and Brenner (1968), Ho and Leal (1974) and Shinohara and Hashimoto (1979). However, these analyses are limited to configurations with $r/R << 1$ and, according to Bungay and Brenner (1973b), there has been no theoretical analysis concerning the lift force acting on falling spheres with $r/R \to 1$.

In this study, we denote the inertia-induced lift force as the component of force normal to the translational direction of motion of a falling sphere. It is induced by the fore and aft asymmetric distribution of the stress field around the sphere in the presence of the tube wall. When inertia induces a transverse lift force on a sphere in a tube whose wall modifies the shear caused by the falling sphere, one must rely on experimental observations of sphere migration, such as those summarized by Brenner (1966), to determine the magnitude and direction of this force. For example, Goldsmith and Mason (1962) show that spherical particles suspended in the flow along a vertical tube are not significantly affected by lift for values of the tube flow Reynolds number less than 10^{-3}. The spheres investigated by these authors had $0.123 < r/R < 0.135$, thus yielding $\mathrm{Re}_p < 10^{-4}$, approximately, as the condition on the particle Reynolds number for neglecting the effect of lift due to inertia.

Some indication of how inertia might affect the motion of spheres falling through quiescent fluids in inclined tubes can be gleaned from the study by Eichhorn and Small (1964) who studied spheres suspended in a Poiseuille flow in an inclined tube with $0.146 < r/R < 0.301$ and $80 < \mathrm{Re}_p < 247$. While their flow configuration is not identical to ours in a transformation that moves the reference frame from the tube wall (in their Poiseuille flow case) to the falling sphere (in our quiescent fluid case) their findings are very informative. These authors correlated measurements of sphere drag and lift coefficients, as well as rotational velocity, with Re_p, e, and r/R. Drag, lift, and rotation acquired their largest values at the largest inclination angles, when the spheres were closest to the tube wall. For all the conditions investigated (including the most inclined, when the spheres were observed to bump against the tube wall) the rotation direction of the spheres was always positive, in the sense shown in Fig. 1(*b*). We conclude that in these experiments the inertia-induced lift force displaced the spheres sufficiently from the wall to allow them to rotate in situ, with a rotation direction dictated by the shearing action of the flow in the larger space between the sphere surface and the tube wall.

1.5 Summary. Relative to vertical tubes, there is little work describing the simultaneous translational and rotational motions of spheres falling through viscous fluids in inclined tubes. In particular, the information available for rotational velocity is contradictory, with little known about the precise conditions which might induce a change in the rotation direction of a sphere falling down an inclined tube, or the role of inertia in this regard. The experimental data for translational velocity supports the notion that, for spheres with $\mathrm{Re}_p < 1$ falling in vertical and inclined tubes, inertial effects on drag and, therefore, on the value of the translational velocity, are negligible. In contrast, the corresponding data for rotation suggests that when $\mathrm{Re}_p > 10^{-3}$, approximately, the lift force induced by inertia can significantly alter the position of a sphere relative to the tube wall and, as a result, its rotational velocity.

We present and discuss measurements addressing these and related points. In this connection, our experiments bridge the gap in tube inclination angles existing between the studies of Block and those by Zolotykh and Floberg, and we will find that all these inclined tube experiments were performed for conditions where inertia influenced rotation in the sense described above. If the authors of these studies suspected such effects in their measurements, they were not discussed.

The studies reviewed have dealt with the motions of single spheres. Attempts to uncover studies dealing with the motions of two or three spheres falling simultaneously in a tube were unsuccessful. Some preliminary findings concerning such motions are also presented here.

2 Test Section, Uncertainties, and Experimental Procedure

The test section consisted of a straight Plexiglas tube filled with pure glycerine. The tube was 180 cm long. Its average inner and outer diameters were 12.58 mm and 15.97 mm, respectively (± 0.050 mm). (All ($\pm$) quantities in this paper represent rms values estimated from repeated measurements.) The inside and outside tube surfaces were of polished finish quality and smooth to within less than 16 microns, approximately. There were no observable systematic variations of the inside and outside diameters, or of their rms values, along the length of the tube. The tube was firmly supported by means of three clamps placed equidistantly along its length. The tube inclination angle with respect to the vertical, θ, was determined by means of a plumb line and a protractor with an rms uncertainty less than ± 0.5 degrees.

Three sizes of highly spherical carbon steel balls of density $\rho_p = 7{,}860$ kg/m^3 were used in the experiment. Their average diameters were 11.09 mm, 9.52 mm and 5.56 mm, respectively, as determined from the sample distributions. The steel spheres had a mirror-like surface finish and were highly uniform in size; in no case was the rms of a sample size distribution larger than ± 0.005 mm.

To avoid possible temperature differences among components during an experiment, the steel spheres and the glycerine were stored by the test section in the room in which the experiments were performed. The temperatures of the room and of the glycerine in the tube were continuously monitored with a mercury thermometer to within ± 0.25°C and their difference was always found to be negligible. Over an 8 hour period the

temperature of the glycerine in the room rose about two degrees, typically from about 24.5°C to 26.5°C. The results presented here are based on the temperature-adjusted physical properties of glycerine (density and viscosity), interpolated from the data tabulated in the *JSME Data Book* (1986). At 25°C these values are $\rho = 1257.8$ kg/m^3 and $\nu = 7.751 \cdot 10^{-4}$ m^2/s.

Prior to an experimental run, the tube was plugged at its bottom end and fixed to a predetermined inclination angle. It was then filled with fresh reaction-grade glycerine from Fisher Chemical Co. Special care was taken to avoid the inclusion of air bubbles in the tube. Because glycerine is hygroscopic and this affects viscosity, the tube was also plugged at its top during the course of experimentation. To check possible changes in viscosity, falling velocities were measured for the largest spheres at the beginning and (several hours later) at the end of an experimental run, for the same tube inclination angle. After adjusting for temperature-dependent viscosity differences, the falling velocities were found to be identical to within experimental error. This indicated that the viscosity of the glycerine had not varied due to the absorption of moisture in the course of experimentation. In spite of this reassuring check, the tube was replenished with fresh glycerine every 6–8 hours for work sessions exceeding this time.

Measurements were made for single spheres falling in a tube with $\theta = 0$, 5, 15, 30, 45, 60, 70, and 80 degrees. In addition, pairs and trios of equal size spheres were investigated for $\theta = 0$, 5, 15, and 30 degrees. All three sphere sizes were investigated for each inclination angle. The sphere to tube radius ratios were $r/R = 0.882$, 0.757, and 0.442 for the large, medium, and small spheres, respectively. These radius ratios correspond to values of $\epsilon = 0.134$, 0.321, and 1.263, respectively. For each r/R and θ combination, a minimum number of five runs was performed to measure the sphere translational and rotational velocities. Each run consisted in dropping one, two, or three spheres through the tube and measuring: (*a*) the time it took for the sphere(s) to translate between the "start" and "end" marks of three consecutive tube segments; and, (*b*) the number of revolutions performed by the sphere(s) while translating along the segments, by monitoring the rotation of indelible ink X-markings made on the sphere(s). The tube measurement segments were each 20 cm (± 0.05 cm) long and spaced 25 cm apart. The "start" mark of the first segment was located 30 cm from the top of the tube, while the "end" mark of the third segment was located 40 cm from the bottom. Time was measured with a stop watch with a precision of ± 0.02 s.

The three translational and three rotational velocities obtained for each run were indistinguishable to within experimental error. They were, respectively, pooled and averaged to yield the mean values for that run. The data for five (or more) runs were then averaged to yield the final values for the translational and rotational velocities corresponding to the r/R and θ pair examined.

3 Discussion of Results

Table 1 summarizes the conditions investigated in this study. The Reynolds number range of the experiments, with Reynolds based on the diameter and the translational velocity of a sphere falling singly, was $0.060 < \mathrm{Re} < 0.210$, approximately. The lowest value in this range corresponds to a large sphere falling down the tube with an inclination angle of 80 degrees, while the largest value corresponds to a small sphere with the tube in a vertical orientation. Thus, as concluded in the summary in Section 1.5, we anticipate (and will show) that, via the induced lift force, inertia strongly influenced the rotational velocity observations discussed here.

3.1 Modes of Motion. Translational and rotational velocity measurements were made for a single sphere falling down the tube, and for two or three spheres of equal diameter falling simultaneously. For the latter two cases, the spheres were introduced closely together and, in the vertical tube orientation, no attempt was made to control their initial cross-section locations. The falling patterns were observed to depend on the number and size of the spheres as well as the tube inclination angle. The two and three-sphere patterns revealed initial transients consisting of variable relative displacements between pairs, or among triads, of spheres until final steady state equilibrium spacings (of order one sphere diameter) were established. In some cases time delays were incurred between the insertions of the first (or the last) of three spheres and the other two, leading to a spacing of several sphere diameters between the sphere falling singly and the accompanying pair. This resulted in independent modes of motion for the sphere falling singly and the accompanying pair.

Vertical Tube Orientation. The photographs in Fig. 2 serve to illustrate the modes, or patterns, displayed by spheres falling in a tube with $\theta = 0$ degrees. They are briefly discussed in turn.

Mode 1: This pattern was displayed by all three sphere sizes. The eccentricity of any sphere was $0 < e < 1$ and, whether falling singly or in groups of two or three, they rotated in the direction opposite to that which would arise from contact-rolling along the tube surface to which they were nearest, as illustrated in Fig. 1(*a*). In the cases of two and three spheres, they appeared to fall with their centers closely aligned along an axis parallel to the tube axis of symmetry.

Mode 2: This pattern was only observed for pairs of small and medium size spheres. While it was not possible to discern whether the spheres fell concentrically with the tube axis ($e = 0$) or along a path parallel and very near to the axis ($e \to 0$), rotational motion was not observed for this mode.

Mode 3: This pattern was only observed for pairs of small spheres. The spheres fell together in the same z-plane so that their respective eccentricities were $e > 0.79$. The rotational motion of each sphere was opposite to contact-rolling, as in Mode 1. Mode 3 was unstable and often evolved into Mode 4, described below.

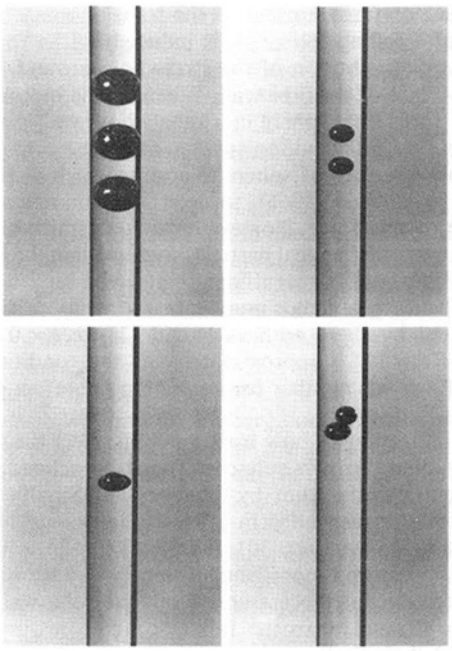

Fig. 2 Examples of modes of motion described in the text for two or three stainless steel spheres falling simultaneously through glycerine in a vertical tube. Top Left) Mode 1: 3 spheres with $r/R = 0.882$; Top Right) Mode 2: 2 spheres with $r/R = 0.442$; Bottom Left) Mode 3: 2 spheres with $r/R = 0.442$; Bottom Right) Mode 4: 2 spheres with $r/R = 0.442$.

Mode 4: As for Mode 3, this pattern was observed only for pairs of small spheres. In this mode, the pair of spheres spiralled down the tube, one closely behind the other, following an orbit centered about the tube axis of symmetry. Infrequently, the translational motion of the leading sphere was strongly decelerated by the tube wall and the second sphere would overtake the first, exchanging places with it. This exchange process sometimes repeated itself in the course of a run. The spiraling motion impaired the determination of the sphere rotational velocities and all we can say about the eccentricity is that $0<e<1$.

Mode 5: Although not pictured here, this mode of motion was observed only for single, small spheres. The sphere translated, without rotating, along a vertical trajectory that brought its surface very close to that of the tube ($e\rightarrow 1$).

We note that Modes 1 and 2 of motion for single spheres are the outcome of early theoretical analyses; see Cox and Mason (1971). Bungay and Brenner (1973b) also show that there is an eccentric position at which a freely sedimenting homogeneous sphere with $r=O(R)$ can translate without rotating. This is consistent with Mode 5 of motion observed here. To our knowledge, no theoretical analysis has been developed that describes the motion of pairs of spheres falling in tubes according to Modes 3 and 4.

Inclined Tube Orientation. Two very reproducible modes of motion were observed for the spheres in an inclined tube. This is because tube inclination works to reduce experimental variability by: (*a*) fixing the same tube cross-section location for all spheres of the same size; while, (*b*) allowing the imposition of the initial condition $e=1$ for the eccentricity of the spheres. (In practice, the initial condition that $e=1$ was guaranteed by pressing the glycerine-immersed spheres against the tube wall prior to releasing them.) In the experiments with two and three spheres it was possible to insert them closely together. However, in moving down the tube the spheres gradually separated to establish an equilibrium configuration of smaller inter-sphere spacing than in a vertical tube.

Whether descending singly or in groups of two or three, the rotation direction was the same for all spheres and was observed to depend on the tube inclination angle. For each sphere size there was a particular inclination angle below which the rotation direction was positive, as shown in Fig. 1(*b*). For inclination angles larger than this critical value the rotation direction changed sign and became negative, as shown in Fig. 1(*c*). However, except for the largest spheres at very large inclination angles, negative contact-rolling motion was not observed. It appears that for most of the conditions of this study frictional contact between the sphere surface and the tube wall was not established so that, in general, $\Omega r/u_t > -1$.

3.2 Measurements in a Vertical Tube. The vertical tube case was investigated first, to check that we could reproduce the trends and some of the especially interesting findings of earlier investigations for single spheres. The data base was extended to include results for two and three spheres falling simultaneously.

Measurements of the "wall correction factor," defined as u_∞/u_t, are plotted in Fig. 3 for the cases of 1, 2, and 3 spheres falling in a vertical tube. The figure also shows experimental correlations and theoretical predictions of some earlier studies for single spheres. Immediately obvious are the limitations of the theories of Bungay and Brenner (1973a,b) to relatively small and large spheres respectively. For spheres with $r/R<0.3$ there is better agreement between the measurements and their (1973a) theory when $e=0$ than when $e=0.98$. This is attributed to the practical difficulty of establishing a condition where $e\rightarrow 1$ in experiments with small spheres. It is especially noteworthy that theory predicts that eccentric large spheres will fall faster than concentric ones while the opposite is predicted for small spheres.

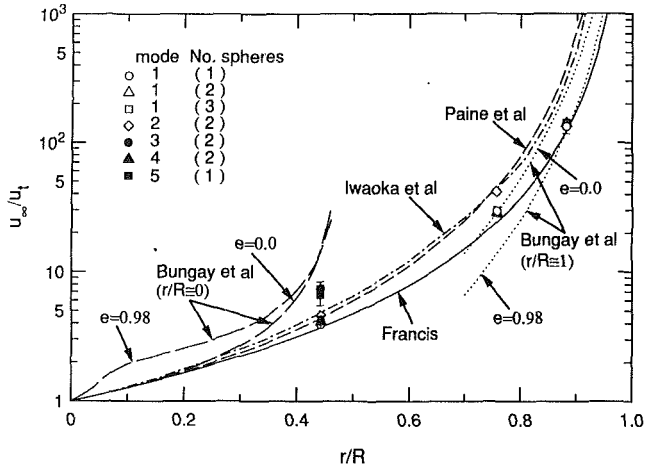

Fig. 3 Analytical predictions and best fits to existing measurements for the dimensionsless translational velocity of spheres with different r/R falling through viscous fluids in vertical tubes. Data from this work are shown as points with uncertainty bars and include 1, 2, or 3 spheres falling simultaneously.

The correlation of Iwaoka and Ishii (1979) is in close agreement with the analytical prediction of Paine and Scherr (1975) which is for concentric translational motion (nonrotating spheres). However, Iwaoka and Ishii noticed that their spheres with $r/R>0.8$ rotated, which means that they were not concentric with the tube. Therefore, according to the analysis by Bungay and Brenner (1973b) for large eccentric spheres, the large spheres observed by Iwaoka and Ishii should have been falling faster than predicted by the theory of Payne and Scherr. We believe that this explains the cross-over between the two curves at about $r/R=0.75$.

The differences between the correlations obtained by Iwaoka and Ishii and Francis (1933) provide some indication of the experimental reproducibility between laboratories. It is encouraging to observe that the bulk of our measurements are bounded by these two curves. In fact, present uncertainty estimates (shown as error bars on the data points) are smaller than the differences between the two earlier correlations.

In spite of unavoidable uncertainties associated with the initial cross-section locations of spheres inserted in the tube in its vertical orientation, we can safely state that for spheres falling according to Modes 2 and 5 of motion their eccentricities were very near to 0 and 1, respectively. For the other modes of motion we can say that $0<e<1$, but the actual eccentricities are unknown. However, using the analysis of Bungay and Brenner (1973b) for large closely fitting spheres, it is possible to argue that $e\rightarrow 1$ for our largest spheres falling according to Mode 1. Figure 4 shows analytical profiles for u_t and Ω, calculated for our experimental case with $r/R=0.882$. The corresponding experimental values of the translational and rotational velocities are also shown. Of the two possible intersections between the experimental and analytical results, only the case with $e\rightarrow 1$ is common to both velocities. Therefore, we conclude that $e\rightarrow 1$ must have been close to the true value of the eccentricity for Mode 1 of motion.

The analytical profiles in Fig. 4 also reflect the theoretical result that, for a closely fitting sphere, the maximum translational velocity is acquired when $e=0.98$. This would explain why the cluster of Mode 1 data corresponding to $r/R=0.882$ in Fig. 3 (for which we argued in the previous paragraph that $e\rightarrow 1$) is closer to the $e=0.98$ analytical result of Bungay and Brenner (1973b) than the $e=0$ result derived by them, or by Paine and Scherr.

Anticipating that the qualitative features of the profiles shown in Fig. 4 also apply to our spheres with $r/R=0.757$, we expect spheres falling concentrically according to Mode 2 to have smaller translational velocities than the same spheres

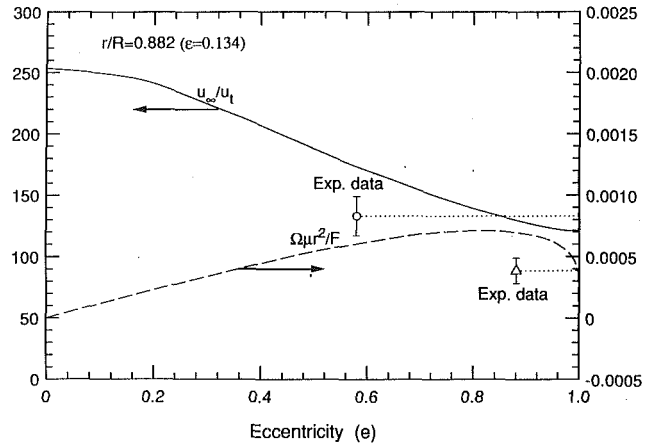

Fig. 4 Predictions, based on the analysis of Bungay and Brenner (1973b), showing the dependence on the eccentricity (e) of the translational (u_t) and rotational (Ω) velocities for spheres with $\epsilon << 1$ ($r/R = O(1)$) falling through a viscous fluid in a vertical tube. The two data points are from this work.

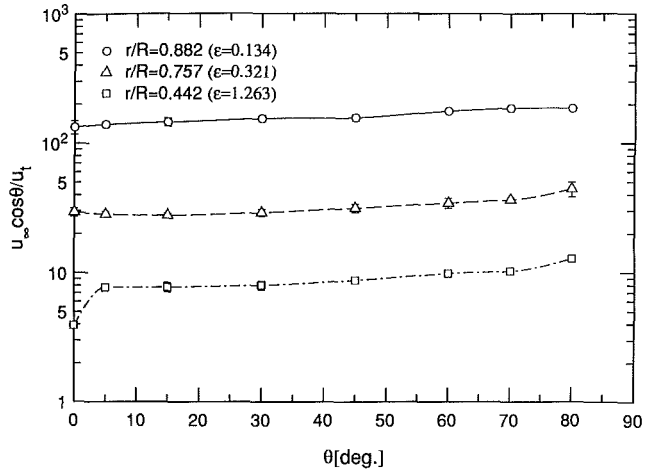

Fig. 5 Dimensionless plots of measured translational velocity versus tube inclination angle for stainless steel spheres falling through glycerine

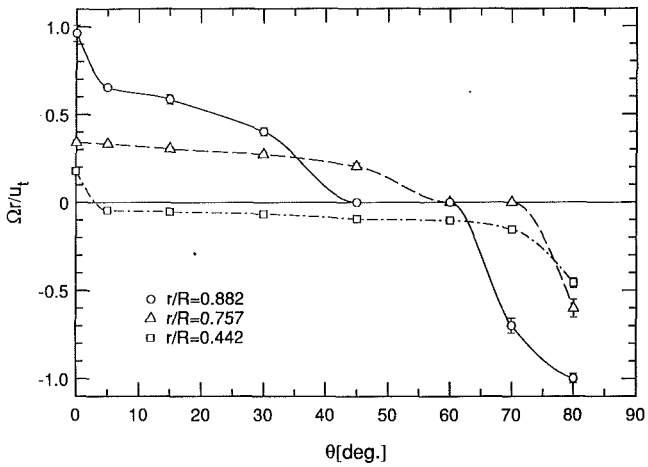

Fig. 6 Dimensionless plots of measured rotational velocity versus tube inclination angle for stainless steel spheres falling through glycerine

falling eccentrically according to Mode 1. This is, indeed, what we measured. However, we note that the coincidence of the cluster of Mode 1 data at $r/R = 0.757$ with the analytical curve for $e = 0$ is entirely fortuitous since we know that spheres in this mode rotated and, therefore, could not have been falling concentrically with the tube.

For $r/R = 0.442$, spheres falling according to Modes 3 and 5 had significantly lower translational velocities than spheres in Modes 1, 2, and 4. We know for sure that the spheres in Mode 5 had $e \to 1$, those in Mode 3 had $e > 0.79$ and those in Mode 2 had $e \to 0$. In terms of the analyses for small spheres (see Cox and Mason (1971) and Bungay and Brenner (1973a)) one would expect small spheres near the tube wall (Modes 3 and 5) to fall more slowly than spheres away from the wall (Mode 2) and the data support this trend.

In concluding this section, we note that once the equilibrium configurations had been established for spheres falling according to Modes 1, 2, or 3, the translational and rotational velocities of the spheres in a group were indistinguishable, respectively. This was not the case for Mode 4 on the occasions when one sphere overtook the other and exchanged places with it.

3.3 Measurements in an Inclined Tube. Translational and rotational velocities for single spheres falling down inclined tubes are plotted in Figs. 5 and 6. (Corresponding measurements for two or three spheres falling simultaneously did not differ significantly from these results.) Except for the marked reduction in u_t between $\theta = 0$ and 5 degrees for the small sphere case, the profiles in Fig. 5 show that the translational velocity decreases slowly with increasing tube angle. The decrease in u_t with increasing θ is attributed to the increase in eccentricity, e, with increasing θ. As e increases the sphere approaches the wall to experience a larger value of drag. For all values of $\theta > 5$ degrees, the dimensionless velocity $u_\infty \cos\theta/u_t$ in Fig. 5 maintains the approximate ratios 140:30:8, going from the largest to the smallest spheres.

More striking are the variations in sphere rotational velocity shown in Fig. 6. These should be interpreted with the help of Figs. 1(*b*) and 1(*c*). Each sphere size in Fig. 6 is characterized by an inclination angle (or an interval of this angle) about which transition takes place from positive rotation (dictated by the shearing action of the fluid on the sphere, in the large space between it and the wall) to negative rotation (dictated by the shearing action of the fluid on the sphere, in the much smaller space between it and the wall) as the inclination angle is increased. Inspection of Fig. 6 shows that this critical inclination angle does not vary monotonically with r/R since it is largest for the medium size spheres. Especially noteworthy is the fairly quick transition from positive to negative rotation for the smallest spheres which remains relatively constant and of small magnitude between $\theta = 5$ and 70 degrees, approximately. The medium size spheres show the change in rotation taking place between $\theta = 60$ and 70 degrees, while the largest spheres experience the change between $\theta = 45$ and 60 degrees.

Only in the case of the large spheres with $\theta \geq 80$ degrees was the contact-rolling condition, $\Omega r/u_t = -1$, obtained in this study. In all the other cases the surfaces of the spheres and the tube wall were in relative motion. Even when $\Omega = 0$, because $u_t > 0$, we must conclude that there was always a film of fluid, however thin, between the respective sphere and wall surfaces. Although we did not perform measurements for $\theta > 80$ degrees, Block's work shows that with increasing tube inclination angle the medium and small size spheres would have eventually acquired a contact-rolling motion also. Notwithstanding this limitation in our data, we not that present rotational velocities are not limited to the range $-1 \leq \Omega r/u_t < 0$ observed by Block.

In Section 2 we explained that the glycerine-immersed spheres were placed in contact with the inclined tube wall ($e = 1$) prior to being released. However, for all except one of our large-sphere experimental conditions, relative motion was observed between the sphere surfaces and the inclined tube wall indicating that after being released the inertia-induced lift force displaced the spheres sufficiently from the tube wall to allow this relative motion. It is pertinent, therefore, to ask how this radial displacement (or, equivalently, the eccentricity) varied

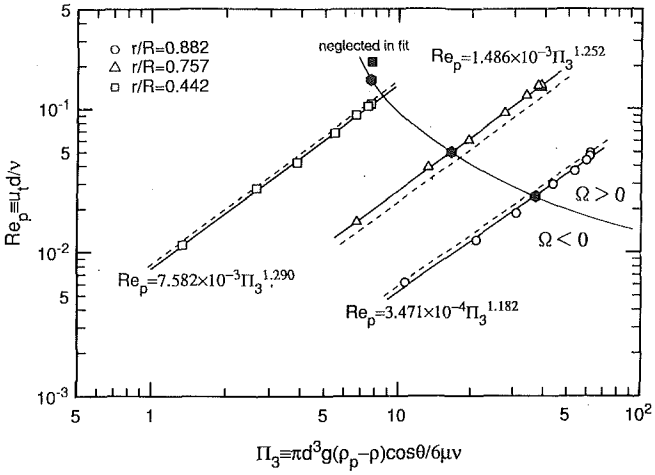

Fig. 7 Alternative representation of the experimental u_t data in Fig. 5 using Re_p and Π_3 as dimensionless parameters. Continuous lines correspond to the equations shown which are least squares fits to data with the same r/R or, equivalently, ϵ. Dotted lines correspond to Eq. (8) which is a least squares fit to all the data. In the figure, the results from Table 2 separate spheres with opposite rotation direction.

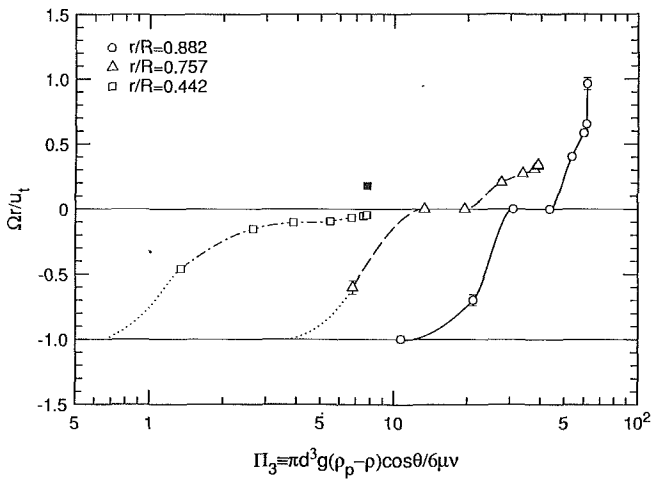

Fig. 8 Alternative representation of the Ω data in Fig. 6 using $\Omega r/u_t$ and Π_3 as dimensionless parameters

with the tube inclination angle, but a direct measurement of this minute quantity was beyond the scope of our work. However, from the analysis of Bungay and Brenner (1973b) for a large sphere falling in a vertical tube we know that for $e>0.98$ a sphere's rotational velocity decreases and that it changes sign (from positive to negative, in the sense shown in Fig. 1) in the limit $e\to1$. In our experiments the values of r/R do not satisfy the $r/R\to1$ requirement of the theory of Bungay and Brenner. Nevertheless, taking the change in sphere rotation direction as an indication that $e\to1$, the data in Fig. 6 suggest that the small spheres approached this condition first, followed by the large spheres and finally the medium spheres. We attribute to the complexity of the inertia-induced lift the non-monotonic nature of this variation, as well as the ϵ-dependence of the rotational velocity observed at $\theta=80$ degrees which is opposite to the theoretical prediction that $-\Omega r/u_t=(1/3)\epsilon$ in the limit $e\to1$ when $\epsilon<<1$. While it appears that the small spheres were the first to come very close to the tube wall at small and intermediate inclination angles, only the large spheres attained the condition $e=1$, as manifested by their contact-rolling motion at $\theta=80$ degrees.

Contrasting the weak θ-dependence of u_t in Fig. 5 (for any r/R) with the marked θ-dependence of Ω in Fig. 6 (for the same r/R) suggests that, of the two, the rotational velocity is much more sensitive to the value of the eccentricity which is determined by the inertia-induced lift force associated with every $(r/R,\ \theta)$ pair. At small Reynolds numbers we expect inertial drag and lift forces to contribute only weakly to the total drag acting on a falling sphere (see, for example, Eq. (37*a*) in Cox and Mason (1971). However, by changing the sphere's location relative to the tube wall, the lift force allows significant variations in the torque balance that determines the sphere's rotational velocity. Therefore, we conclude for the conditions of our experiments that while u_t was essentially independent of direct inertial effects, as well as those associated with Ω, the rotational velocity was strongly influenced by inertia through the positioning effect of the lift force.

Figure 7 shows the translational velocity data and corresponding linear least squares regressions plotted as Re_p versus Π_3 for the three clearances of this study. The correlation for each r/R fits the data from which it was derived very well without explicitly involving the eccentricity. However, the exponent of Π_3 is observed to decrease with decreasing ϵ, tending to unity as $\epsilon\to0$ or, equivalently, as $r/R\to1$. The trends in these correlations and the functional forms of Eqs. (1) and (3), which are supported by the experimental studies discussed, suggest that a single correlation of the form

$$Re_p=A\Pi_3^{1+f(\epsilon)}\epsilon^b \tag{8}$$

should fit all the data in Fig. 7. The extent to which this is achieved when $A=5.936\ 10^{-3}$, $b=1.361$, and $f(\epsilon)=0.3095e^{-0.0705/\epsilon}$ is shown by the dotted lines in Fig. 7. The values of the numerical parameters in this fit were also obtained by least squares regression to our experimental results.

A comparison between Eq. (8) and Eqs. (1) or (3) suggests an explanation for the term $\Pi_3^{f(\epsilon)}$. This can be interpreted as the effect of the eccentricity on the translational velocity and is justified heuristically. First, we expect the eccentricity to be determined by a balance among the gravitational, inertial and viscous forces acting on the sphere. However, for $Re_p=O(1)$ inertial and viscous forces are of the same order of magnitude and we expect $e=f(\Pi_3)$ for any ϵ or, equivalently, r/R.

Second, for fixed Π_3 in a tube of fixed R, the net (surface integrated) lift force acting on a small sphere should be larger, relative to the sphere's weight, than the corresponding lift force acting on a large sphere. This is because of the stronger flow asymmetry associated with the sphere with smaller r/R due to its surface being closer to one side of the inclined tube than the other. The result is for the small sphere to experience a slightly larger relative displacement from the tube wall which allows it to fall faster. (It is important to note that this effect is quite distinct from the geometrical one captured by the ϵ^b term in Eq. (8).)

Thus, we seek a dependence on the eccentricity in Eq. (8) of the form $f(e)=f(\Pi_3,\epsilon)$ and this has been modeled as $\Pi_3^{f(\epsilon)}$ with $f(\epsilon)$ as defined above. (It is remarkable that this proposal captures the experimentally observed variation of the total exponent, $1+f(\epsilon)$, to within less than 0.2 percent!) As modeled, the exponent varies in such a way that: (i) as $\epsilon\to0$ the theoretical result for vertical tubes is obtained, since then $1+f(\epsilon)\to1$; while, (ii) for $\epsilon>3$ $(r/R<0.25)$ the limit $1+f(\epsilon)\to1.3095$ is rapidly approached.

It is interesting to compare the experimentally determined value of the exponent for ϵ in Eq. (8) $(b=1.361)$, with the values derived theoretically for spheres with $\epsilon<<1$ in vertical tubes. Inspection of Eqs. (1) and (3) shows that $b=5/2$ when $0\le e<1$, and $b=1/2$ when $e\to1$. The present value of b is less than 3/2, supporting the notion that in our inclined tube experiments the eccentricity was indeed quite close to unity.

In contrast to u_t, the marked dependence of Ω on the tube inclination angle strongly suggests a corresponding marked dependence on the eccentricity but, because of the more complicated dependence of rotation on inertia it is not possible to determine a corresponding general correlation for Ω from the

Table 2 Experimental values of Π_3 and Re_p marking transition between spheres with positive and negative rotation

ϵ	r/R	Π_3	Re_p
1.263	0.442	7.739	$1.581\ 10^{-1}$
0.321	0.757	16.39	$4.942\ 10^{-2}$
0.134	0.882	37.1	$2.40\ 10^{-2}$

rotational velocity data. However, Fig. 8 shows that plotting $\Omega r/u_t$ versus Π_3 at least removes the non-monotonic variation of Ω with respect to r/R present in Fig. 6.

We end the discussion by drawing attention to an especially interesting feature captured by Block's experiments which, apparently, he did not notice. Block remarked that in his plots for Π_3/Re_p^2 versus Re_p, for spheres with $r/R = 0.769$, a sudden change in the slope of the curves revealed the transition from true contact-rolling motion to sliding with negative rotation (in the direction of contact-rolling but with a speed of rotation different from true contact rolling). What Block missed is that the change in slope always occurred at a value of $\Pi_3/Re_p = 568$ (± 59) and that the transition was due to the inertia-induced lift force. This empirical result yields the condition

$$\Pi_3/Re_p^2 = 568/Re_p \tag{9}$$

as the critical ratio of buoyant to inertial forces to be exceeded to achieve a true contact-rolling condition for this particular value of r/R. For the $\Pi_3 - Re_p$ parameter range explored in the present study with $r/R = 0.757$, comparable to Block's case, this critical ratio was not exceeded and true contact rolling was never observed.

The above finding suggests the use of Π_3/Re_p as a parameter to characterize the transition from positive to negative rotation in the case of spheres already displaced from the tube wall. The data in Figs. 7 and 8 yield the results in Table 2. For each ϵ the table gives estimates of the critical values of Π_3 and Re_p marking the change in the sign of rotation. Plotting and connecting these experimental values in Fig. 7 allows a distinction to be made between spheres with positive and negative rotation. A least squares fit to the data in Table 2 gives

$$\Pi_3/Re_p = 72.42\epsilon^{-1.48} \tag{10}$$

to within ± 10 percent as the critical ratio to be exceeded for transition from positive to negative rotation. Together with Eq. (8) (or the equations shown in Fig. 7) this result provides a numerical method for estimating the loci of points in Fig. 7 separating spheres with opposite rotation.

4 Conclusions

Experiments have been performed for solid metal spheres falling through a viscous fluid in a tube. The data reveal the full range of the dependence of a sphere's translational and rotational velocity on the tube inclination angle, θ, and the sphere to tube radius ratio, r/R. The measurements for spheres falling in the tube with a vertical orientation agree well with earlier results and, in the case of two or three spheres falling simultaneously, reveal various new modes of motion.

For small tube inclination angles the rotational velocity of a sphere is positive, dominated by the shearing action of the fluid in the larger of the two spaces between the sphere surface and the tube wall. At a critical value of the inclination angle (which depends on r/R) the rotational velocity changes sign due to the increased friction in the smaller of the two spaces between the sphere surface and the tube wall. In this case the sphere displays a "downhill rolling"-like motion. However, the contact-rolling condition that $\Omega r/u_t = -1$ was only obtained for the largest sphere size ($r/R = 0.882$) when $\theta \geq 80$ degrees. For all the other cases investigated the sphere and tube wall surfaces were in relative motion. For these cases we conclude that: (*a*) there was always a film of fluid, however thin, between the sphere and tube surfaces in closest proximity; (*b*) although small, the inertia-induced transverse lift force present in our experiments was responsible for the miniscule displacement of a sphere from the inclined tube wall.

The sphere translational velocity displays a small but significant sensitivity to the tube inclination angle, θ. In contrast, the rotational velocity varies markedly with this parameter and, therefore, with the eccentricity. While it has been possible to derive a single correlation of the form $Re_p = f[\Pi_3, \epsilon, e]$ for all our u_t data, because of the more complex dependence of rotation on inertia, the same is not possible for Ω. The determination of the dependence of the eccentricity on θ and r/R would be an excellent subject for research in future experiments.

We conclude this paper by offering the following question for consideration: What is the minimum displacement from the wall required of a sphere falling through a viscous fluid in an inclined tube that will allow a transition from pure contact-rolling to sliding with rotation? In the absence of direct measurements, Eq. (3) yields a crude estimate of 10^{-52} cm for our largest sphere experiments! It is clear that this subatomic dimension is incommensurate with the continuum analysis from which it is derived and that long before submicron distances are approached surface roughness becomes an important consideration for the contact forces involved. Notwithstanding, we may safely conclude from the estimate that the displacement required is, indeed, very small, and that its accurate determination as a function of θ and r/R remains a considerable challenge.

Acknowledgments

One of us, J. A. C. H., gratefully acknowledges helpful discussions held with Professors S. Morris, F. S. Sherman, and L. M. Trefethen in the course of writing the manuscript. He also thanks Professor R. Eichhorn for providing the corrections to the data in the reference to his work. Thanks go to M. A. Peters and J. Christian for their typographical assistance with the manuscript.

References

Block, R. B., 1940, "On the Resistance to the Uniform Motion of a Solid through a Viscous Liquid," *J. Appl. Phys.*, Vol. 11, pp. 635–642.

Brenner, H., 1966, "Hydrodynamic Resistance of Particles at Small Reynolds Numbers," *Advan. Chem. Eng.*, Vol. 6, Academic Press, eds. Drew, T. B., Hoopes, J. W., and Vermuelen, T., pp. 287–438.

Bungay, P. M., and Brenner, H., 1973a, "Pressure Drop due to the Motion of a Sphere near the Wall Bounding a Poiseuille Flow," *J. Fluid Mech.*, Vol. 60, Part 1, pp. 81–96.

Bungay, P. M., and Brenner, H., 1973b, "The Motion of a Closely-Fitting Sphere in a Fluid-Filled Tube," *Int. J. Multiphase Flow*, Vol. 1, pp. 25–56.

Clift, R., Grace, J. R., and Weber, M. E., 1978, *Bubbles, Drops and Particles*, Academic Press.

Cox, R. G., and Brenner, H., 1968, "The Lateral Migration of Solid Particles in Poiseuille Flow—I. Theory," *Chem. Eng. Sci.*, Vol. 23, pp. 147–173.

Cox, R. G., and Mason, S. G., 1971, "Suspended Particles in Fluid Flow through Tubes," *Annual Rev. Fluid Mech.*, Van Dyke, M., Vincenti, W. G. and Wehausen, J. V., eds. Annual Reviews Inc., Palo Alto, CA.

Eichhorn, R., and Small, S., 1964, "Experiments on the Lift and Drag of Spheres Suspended in a Poiseuille Flow," *J. Fluid Mech.*, Vol. 20, pp. 513–527.

Floberg, L., 1968, "On the Ball Flowmeter and the Ball Viscosimeter," *Acta Polytech. Scand., Mech. Eng.*, Ser. No. 36, 28 pp.

Francis, A. W., 1933, "Wall Effect in Falling Ball Method for Viscosity," *Physics*, Vol. 4, pp. 403–406.

Goldman, A. J., Cox, R. G., and Brenner, H., 1967, "Slow Viscous Motion of a Sphere Parallel to a Plane Wall—I. Motion Through a Quiescent Fluid," *Chem. Eng. Sci.*, Vol. 22, pp. 637–651.

Goldsmith, H. L., and Mason, S. G., 1962, "The Flow of Suspensions Through Tubes—I. Single Spheres, Rods and Discs," *J. Coll. Sci.*, Vol. 17, pp. 448–476.

Greenstein, T., and Happel, J., 1968, "Theoretical Study of the Slow Motion of a Sphere and a Fluid in a Cylindrical Tube," *J. Fluid Mech.*, Vol. 34, Part 4, pp. 705–710.

Haberman, W. L., and Sayre, R. M., 1958, "Motion of Rigid and Fluid Spheres in Stationary and Moving Liquids Inside Cylindrical Tubes," David Taylor Model Basin, Report No. 1143, U.S. Navy, Washington, D.C.

Happel, J., and Brenner, H., 1965, *Low Reynolds Number Hydrodynamics*, Prentice-Hall, Englewood Cliffs, N. J.

Ho, B. P., and Leal, L. G., 1974, "Inertial Migration of Rigid Spheres in Two-Dimensional Flows," *J. Fluid Mech.*, Vol. 65, pp. 365–400.

Iwaoka, M., and Ishii, T., 1979, "Experimental Wall Correction Factors of Single Solid Spheres in Circular Cylinders," *J. Chem. Eng.*, Japan, Vol. 12, No. 3, pp. 239–242.

JSME Data Book: Heat Transfer, 1986, 4th Edition, p. 325, Japan Society of Mechanical Engineers, Tokyo.

Paine, P. L., and Scherr, P., 1975, "Drag Coefficients for the Movement of Rigid Spheres Through Liquid-Filled Cylindrical Pores," *Biophysical J.*, Vol. 15, pp. 1087–1091.

Rubinow, S. I., and Keller, J. B., 1961, "The Transverse Force on a Spinning Sphere Moving in a Viscous Fluid," *J. Fluid Mech.*, Vol. 11, pp. 447–459.

Shinohara, M., and Hashimoto, H., 1979, "The Lateral Force on a Small Sphere Sedimerting in a Viscous Fluid Bounded by a Cylindrical Wall," *J. Phys. Soc. Japan.*, Vol. 46, pp. 320–327.

Tanner, R. I., 1963, "End Effects in Falling-Ball Viscometry," *J. Fluid Mech.*, Vol. 17, pp. 161–170.

Zolotykh, E. V., 1962, "Deriving Basic Formulas for Viscometers with an Inclined Tube," Translated from *Izmeritel'naya Tekhnika*, No. 4, pp. 44–48.

On Stability Analysis of a Flexible Cylinder in an Array of Rigid Cylinders

J. Marn

I. Catton

Mechanical Aerospace and Nuclear Engineering Dept.,
University of California, Los Angeles,
Los Angeles, CA 90024

The concept of an unsteady control volume is used to predict the onset of instability for a simple array of cylinders. The array consists of a flexible cylinder placed amidst rigid cylinders. The fluid is assumed to be incompressible with a "slip" boundary condition used on the solid/liquid interface. The equations derived for the model from first principles are solved in the complex plane. The results are compared to experimental data. The paper is concluded with a discussion of the advantages and disadvantages of the model and an assessment of the accuracy of the predictions.

Introduction

Flow-induced vibrations are important phenomena for many engineering applications, especially those connected with flow through and across tube bundles. The designer of such systems needs to understand the phenomena so as to predict and avoid dangerous flow conditions. Flow induced vibrations of cylindrical structures are thought to be induced by three different mechanisms (Price, 1988): 1) amplification when the response frequencies of the cylinders coincide with the natural frequencies of the structures, 2) forced response of the cylinders because of buffeting, and 3) self-excited fluidelastic instability.

Our review of past research led to the conclusion that most theoretical investigations of flow-induced vibrations can be grouped into two categories: first, investigations where the emphasis is on the response of the structure (solid mechanics dominant), and second where the fluid mechanics is the focus of the problem. We believe that a more balanced approach dealing with both the fluid and the structural response is needed. In this paper, a critique of the main ideas behind each of these categories is presented and supplemented by our understanding and solutions to the problem.

Mechanisms of Vibrations

Paidoussis (1988) divides vibrations into two types:

(*a*) Strouhal type periodicity in the interstitial flow which leads to resonance and subsequent vibration of the cylinder. This type of mechanism is often associated with expressions such as "jet switch," "wake swing," and "jet instabilities."

(*b*) Fluidelastic instability which occurs when the flow velocity exceeds a threshold value.

The first type of vibration can be explained by considering the periodic behavior of the vortices created by flow passing through a bundle of cylinders. When the frequency of the vortex shedding approaches the natural frequency of the cylinders in the bundle, the motion is amplified and is observed as a resonance.

The second type of vibration is known as flutter and is connected to the dynamic response of the cylinder and fluid-solid interactions. This effect is diminished by damping of the system.

Chen (1987) distinguishes between static and dynamic type of vibrations. He claims that the structure responds to the flow-induced force in different ways; i.e., the structure may deflect statically in the flow, resonate with periodic excitation of the flow, respond to random fluid excitation or be subjected to dynamic instability by flutter. He further suggests that the types of response can be classified according to excitation mechanisms.

Static displacements are caused by steady drag and lift forces and with oscillatory forces that have frequencies much lower than the structural resonant frequencies of the cylinders (tubes). Static instability is caused by a fluid stiffness. Buckling of an elastic tube while transporting steady flow is an example of divergence.

Dynamic response is the structural response to various excitation mechanisms such as vortex shedding or turbulence. Once the excitation is known, structural response can be calculated in straightforward manner. Dynamic instability is typically caused by high velocity flow. Examples are flutter and the whirling instability of a cantilevered pipe conveying fluid. These modes of instability could be classified as a single mode and a coupled mode flutter. Words single and coupled indicate the influence of adjacent tubes: in single mode flutter the effect of vibrations diminish before the adjacent tube is influenced by them, in coupled mode the neighboring tubes develop a relationship such as lock-in phenomena or vibrations in phase.

Both of the above descriptions rely on the assumption that the fluid force is something foreign to the system or is being controlled by an outside source (such as vortex shedding or turbulent buffeting). Most of the flows are driven by a pressure gradient yet the local behavior is dependent only on local geometry and flow conditions. It is our opinion that the structure affects the local fluid motion as much as the fluid flow affects the structural response. Further, the equations for fluid motion are valid and uniquely describe the stresses acting within the bundle. Since the fluid forces result mainly from the pressure field, the equations of fluid motion can easily be coupled

Contributed by the Fluids Engineering Department for publication in the JOURNAL OF FLUIDS ENGINEERING. Manuscript received by the Fluids Engineering Division November 6, 1990.

with the equations of solid motion. Treating the fluid forces as strictly a function of Reynolds number, which is in effect what most of investigations of structural response address, is both incomplete and unnecessary. Flow induced vibrations are described by coupled fluid and solid equations of motion and should be modeled accordingly, using necessary assumptions and simplifications.

An interesting model was introduced by Lever and Weaver (1984) and further developed by Yetisir and Weaver (1988). The essence of the model is the idea of a non-steady control volume. The conservation equations forming the basis of such a model are the continuity equation,

$$\frac{\partial}{\partial t}[\rho V(t)] + \nabla \cdot [\rho V(t)\mathbf{u}] = 0 \tag{1}$$

and the momentum equation,

$$\rho \frac{\partial}{\partial t}[\mathbf{u}V(t)] + \rho \nabla [|\mathbf{u}|\mathbf{u}V(t)] = \Sigma \mathbf{f} \tag{2}$$

The derivation of both equations can be found in Appendix A.

Lever and Weaver's idea of a flexible control volume is adopted here, since it can be adjusted easily to fit modern numerical techniques. The derivation of the final forms of equations will be shown later in this text. Both of the above mentioned papers have assumed one-dimensional unsteady incompressible flow. There is only one flexible cylinder surrounded by rigid cylinders. Since the model is one dimensional, viscosity effects cannot be accounted for other than in the form of some kind of friction factor, as employed in both papers. The important conclusion, drawn from the papers is that there is a single complex transcendental equation, whose roots yield, in different combinations, different thresholds to different forms of the amplified vibrations, depending on flow Reynolds number.

One-Dimensional Unsteady Model

In this section the one-dimensional unsteady integral model, based on the idea of a nonsteady control volume, is derived. The derivation is followed by the results for dynamic and static thresholds and compared to available experimental results from Weaver and Fitzpatrick (1988) and Paidoussis et al. (1988) for a rotated square array. The geometry is represented by a flexible streamtube within the cylindrical bundle, as shown in Fig. 1. One of the cylinders in the bundle is flexible and the others are held fixed. Although cylindrical bundles will probably not sustain substantial damages due to vibration of the single cylinder, there are two important reasons for conducting this type of investigation: 1) readily available experimental data for comparison, and 2) in certain types of applications (such as steam generators), the first cylinder which becomes unstable may serve as an indicator. There is of course no guarantee that the first cylinder showing growing response will be located within the bundle rather than on the perimeter but fluidelastic instabilities are unlikely to occur in the first row due to turbulent buffeting.

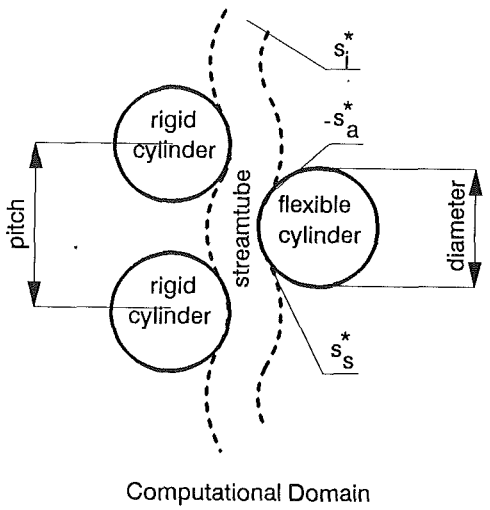

Fig. 1 Flexible streamtube within the bundle

Derivation of One-Dimensional Unsteady Integral Model

The continuity equation valid in unsteady control volume (see Appendix A for derivation) is

$$\frac{\partial}{\partial t}[\rho V(t)] + \nabla \cdot [\rho V(t)\mathbf{u}] = 0 \tag{3}$$

Nomenclature

A = area [m^2]
$\tilde{A}^*$ = dimensionless area
A^*, a^* = dimensionless mean, perturbed area
C = terms in equation of tube motion, associated with fluid damping
c = damping [kg/s]
d = diameter of the tube [m]
f = body forces vector [N]
f^* = dimensionless decay function
$F_{T,L}$ = force in transverse, longitudinal direction, also lift, drag [N/m]
$F^*_{T,L}$ = dimensionless force in transverse, longitudinal direction, also lift, drag
K = terms in equation of tube motion, associated with fluid stiffness
k = stiffness [kg/s^2]
l_0 = characteristic decay length, usually 2 d [m]
M = terms in equation of tube motion, associated with acceleration
p = pressure [Pa]
p^* = dimensionless pressure
p_0^*, = dimensionless mean, disturbed pressure
s^* = dimensionless coordinate along streamline
$s^*_{a,s}$ = dimensionless position of the attachment, separation point
$s^*_{e,i}$ = dimensionless position of exit, inlet from control volume calculational domain
t = time [s]
t^* = dimensionless time
U_r = dimensionless "reduced velocity," used as a mean velocity
u = velocity vector [m/s]
u, u^* = velocity, dimensionless component along the streamline [m/s]
V = volume [m^3]
x = coordinate along streamline [m]
α = angle between attachment point on the tube and midplane [rad]
δ = logarithmic decrement of tube damping
$\eta^* \xi^*$ = dummy variables in integral involving s^*
λm = tube mass [kg]
ρ = density [kg/m^3]
ω = frequency of the tube [Hz]
ω_n = natural frequency of the tube [Hz]

The scaling parameters are

$$A=\tilde{A}^* d;\ u=\tilde{u}^* U_r \omega_n l_0;\ t=\frac{t^*}{\omega}$$

$$x=s^* d;\ p=\tilde{p}^* \rho d l_0 \omega_n^2 U_r;\ U_r=\frac{U}{d\omega_n} \tag{4}$$

where the units for pressure are Pa/m (unit depth).

This yields the dimensionless form of the continuity equation,

$$\frac{1}{U_r}\frac{\omega}{\omega_n}\frac{\partial \tilde{A}^*}{\partial t^*}+\frac{l_0}{d}\frac{\partial}{\partial s^*}(\tilde{u}^*\tilde{A}^*) \tag{5}$$

The area, pressure, and velocity are decomposed into mean and perturbed (due to cylinder's feedback) quantities

$$\tilde{u}^*=U_r+u^*;\ \tilde{A}^*=A_0^*+a^*;\ \tilde{p}^*=p_0^*+p^* \tag{6}$$

These expressions are substituted into the dimensionless continuity Eq. (5) with the following simplifying assumptions:

(*a*) neglect nonlinear perturbed terms. This is a standard perturbation analysis assumption and limits the solutions to small amplitude motion at the onset of instability.

(*b*) assume A_0^* and U_0^* are constant along a streamtube. This assumption is based on the fact that the mean flow parameters cannot affect the perturbations. The constant velocity and area in effect describe the rotated square array if the wake area of the cylinder is excluded from the perturbation velocity field.

(*c*) assume the velocity has a uniform profile in the direction perpendicular to the flow direction s^* (which effectively means using a 1-D approximation). This assumption will be relaxed in the future.

The basis for the above assumptions is that fluctuating components of the flow are of small amplitude (discard high order terms) and obey the continuity equation in the mean flow (moderate Re number and constant mean flow velocity and streamtube crossection area), and that there is negligible cross flow (1-D approximation). With the above assumptions, the continuity equation becomes

$$\frac{1}{U_r}\frac{\omega}{\omega_n}\frac{\partial a^*}{\partial t^*}+\frac{l_0}{d}U_r\frac{\partial a^*}{\partial s^*}+\frac{l_0}{d}A_0^*\frac{\partial u^*}{\partial s^*}=0 \tag{7}$$

Integrating it along the control volume length from some arbitrary inlet position s_i^* to some arbitrary exit position s_e^* yields

$$\frac{1}{U_r}\frac{\omega}{\omega_n}\int_{s_i^*}^{s_e^*}\frac{\partial a^*}{\partial t^*}ds^*=\frac{l_0}{d}\{U_r[a^*(s_i^*)-a^*(s_e^*)]+A_0^*[u^*(s_i^*)-u^*(s_e^*)]\} \tag{8}$$

The velocity can be calculated anywhere along the streamline with respect to some starting boundary conditions and an assumed form of area perturbation term a^*. The latter assumption can be defended by noting that the motion of the cylinder does not become random unless we are dealing with turbulent flows. The final form of the continuity equation used in this model is

$$u^*(s^*)=u^*(s_i^*)+\frac{U_r}{A_0^*}[a^*(s_i^*)-a^*(s^*)]-\frac{d}{A_0^* U_r l_0}\frac{\omega}{\omega_n}\int_{s_i^*}^{s^*}\frac{\partial a^*(\xi^*)}{\partial t^*}d\xi^* \tag{9}$$

The pressure field is evaluated using the momentum equation (see Appendix A),

$$\rho\frac{\partial}{\partial t}[\mathbf{u}V(t)]+\rho\nabla[|\mathbf{u}|\mathbf{u}V(t)]=\Sigma\mathbf{f} \tag{10}$$

Using the assumptions listed above, Eq. (10) becomes:

$$\rho\frac{\partial}{\partial t}[Au]=-\frac{\partial}{\partial x}[\rho|u|uA]-\frac{\partial}{\partial x}[pA] \tag{11}$$

which after scaling is:

$$\frac{1}{U_r}\frac{\omega}{\omega_n}\frac{\partial}{\partial t^*}[\tilde{u}^*\tilde{A}^*]=-\frac{l_0}{d}\frac{\partial}{\partial s^*}[|\tilde{u}^*|\tilde{u}^*\tilde{A}^*]-\frac{1}{U_r}\frac{\partial}{\partial s^*}[\tilde{p}^*\tilde{A}^*] \tag{12}$$

Decomposing the flow field as before, neglecting non linear perturbation terms and noting that

$$\frac{\partial}{\partial t^*}(A_0^* U_r)=\frac{\partial}{\partial s^*}(A_0^* U_r|U_r|)=\frac{\partial}{\partial s^*}(A_0^* p_0^*)=0 \tag{13}$$

yields

$$\frac{1}{U_r}\frac{\omega}{\omega_n}\frac{\partial}{\partial t^*}[A_0^* u^*+a^* U_r]=-\frac{l_0}{d}\frac{\partial}{\partial s^*}[A_0^*|U_r|U_r+a^*|U_r|U_r+A_0^* U_r|u^*|]-\frac{1}{U_r}\frac{\partial}{\partial s^*}[A_0^* p^*+a^* p_0^*] \tag{14}$$

Integrating the momentum equation along the length of the control volume from some arbitrary inlet point s_i^* to some arbitrary exit point s_e^* yields

$$\frac{1}{U_r}\frac{\omega}{\omega_n}\int_{s_i^*}^{s_e^*}A_0^*\frac{\partial u^*}{\partial t^*}ds^*+\frac{1}{U_r}\frac{\omega}{\omega_n}\int_{s_i^*}^{s_e^*}U_r\frac{\partial a^*}{\partial t^*}ds^*$$

$$=\frac{l_0}{d}\{2|U_r|A_0^*[u^*(s_i^*)-u^*(s_e^*)]+U_r|U_r|[a^*(s_i^*)-a^*(s_e^*)]\}$$

$$+\frac{1}{U_r}\{A_0^*[p^*(s_i^*)-p^*(s_e^*)+p_h^*]+p_0^*[a^*(s_i^*)-a^*(s_e^*)]\} \tag{15}$$

where p_{h*} is a surrogate to account for the hydraulic pressure loss neglected by the inviscid flow assumption. Also, the mean flow and perturbed flow velocities are assumed to have the same character with respect to time. Up to this point our approach is essentially the same as that of Yetisir and Weaver. In Eq. (15) the partial derivative of the perturbation velocity with respect to time is an unknown function which can be related to the assumed perturbed area through the continuity equation,

$$\frac{\partial u^*(s^*)}{\partial t^*}=\frac{\partial u^*(s_i^*)}{\partial t^*}+\frac{U_r}{A_0^*}\left[\frac{\partial a^*(s_i^*)}{\partial t^*}-\frac{\partial a^*(s^*)}{\partial t^*}\right]-\frac{d}{A_0^* U_r l_0}\frac{\omega}{\omega_n}\int_{s_e^*}^{s^*}\frac{\partial^2 a^*(\xi^*)}{\partial t^{*2}}d\xi^* \tag{16}$$

The pressure at some arbitrary location s^* along the streamtube is then found from

$$p^*(s^*)=p^*(s_i^*)-\frac{\omega}{\omega_n}\int_{s_i^*}^{s^*}\left[\frac{\partial u^*(s_i^*)}{\partial t^*}+\frac{U_r}{A_0^*}\frac{\partial a^*(s_i^*)}{\partial t^*}\right]d\xi^*$$

$$-\frac{d}{A_0^* U_r l_0}\left(\frac{\omega}{\omega_n}\right)^2\int_{s_i^*}^{s^*}\int_{s_i^*}^{\xi^*}\frac{\partial^2 a^*(\eta^*)}{\partial t^{*2}}d\eta^* d\xi^*$$

$$+\frac{2}{A_0^*}\frac{\omega}{\omega_n}|U_r|\int_{s_i^*}^{s^*}\frac{\partial a^*(\xi^*)}{\partial t^*}d\xi^*$$

$$+\left(\frac{U_r l_0}{d}|U_r|U_r-p_0^*\right)\frac{a^*(s^*)-a^*(s_i^*)}{A_0^*}+p_h^* \tag{17}$$

Forces on the Cylinder

The lift and drag are found by integrating the pressure around

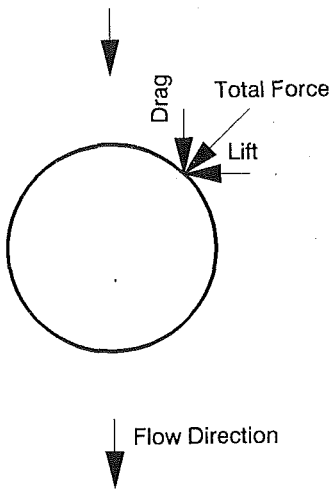

Fig. 2 Forces on cylinder

the cylinder as a function of time. As shown in Fig. 2, the resultant force, caused by the pressure on the cylinder can be separated into two components, one in the x and the other in the y direction. The first one is sometimes called the drag force, whereas the second is denoted as lift. Some researchers would call these the longitudinal and transverse components for the x and y directions, respectively. We will use subscripts L for streamwise flow and T for crossflow directions (to be consistent with other authors).

The transverse force on an infinitesimal area of the cylinder is:

$$dF_T = dF\cos\beta = dF\cos\left(\frac{2s}{P}\right) = dF\cos\left(\frac{2s^*}{P/d}\right) \tag{18}$$

so the net transverse force is:

$$F_T = \int_{-s_a^*}^{s_s^*} dF_T = \int_{-s_a^*}^{s_s^*} p\cos\left(\frac{2s^*}{P/d}\right) ds^*$$

$$= \int_{-s_a^*}^{s_s^*} \rho d^2 l_0 \omega_n^2 U_r p^* \cos\left(\frac{2s^*}{P/d}\right) ds^* \tag{19}$$

which yields a "natural" scaling for the force in the transverse direction,

$$F_T = F_T^* \rho l_0 d^2 \omega_n^2 U_r \tag{20}$$

where it should be noted that the units of force have to be N/m as the problem is described in units per unit length.

The final form of the dimensionless transverse component of the fluid force on the cylinder is

$$F_T^* = \int_{-s_a^*}^{s_s^*} p^*(s^*,t^*)\cos\left(\frac{2s^*}{P/d}\right) ds^* \tag{21}$$

and similarly the streamwise component of the fluid force is

$$F_L^* = \int_{-s_a^*}^{s_s^*} p^*(s^*,t^*)\sin\left(\frac{2s^*}{P/d}\right) ds^* \tag{22}$$

The closed-form solution for the transverse force is:

$$F_T^* = \int_{-s_a^*}^{s_s^*} \left\{ p^*(s_i^*) - \frac{\omega}{\omega_n}\int_{s_i^*}^{s^*}\left[\frac{\partial u^*(s_i^*)}{\partial t^*} + \frac{U_r}{A_0^*}\frac{\partial a^*(s_i^*)}{\partial t^*}\right] d\xi^* \right.$$

$$- \frac{d}{A_0^* U_r l_0}\left(\frac{\omega}{\omega_n}\right)^2 \int_{s_i^*}^{s^*}\int_{s_i^*}^{\xi^*} \frac{\partial^2 a^*(\eta^*)}{\partial t^{*2}}\, d\eta^* d\xi^*$$

$$+ \frac{2}{A_0^*}\frac{\omega}{\omega_n}|U_r| \int_{s_i^*}^{s^*} \frac{\partial a^*(\xi^*)}{\partial t^*}\, d\xi^*$$

$$\left. + \left(\frac{U_r l_0}{d}|U_r|U_r - p_0^*\right)\frac{a^*(s^*) - a^*(s_i^*)}{A_0^*} + p_h^* \right\} \cos\left(\frac{2s^*}{P/d}\right) ds^* \tag{23}$$

The remaining task is to determine the numerical value or a function of the variables inside the integral. Lever and Weaver (1984) and Yetisir and Weaver (1988) have determined that the effect of a flexible cylinder in an array of the rigid cylinders dies out within 2 diameter lengths upstream and downstream. This, in effect, means that all perturbation variables, such as pressure p^*, velocity v^*, and area a^* as well as their derivatives with respect to both space and time are approximately zero more than two diameters away from their source. This simplifies Eq. (23) to

$$F_T^* = \int_{-s_a^*}^{s_s^*} \left\{ -\frac{d}{A_0^* U_r l_0}\left(\frac{\omega}{\omega_n}\right)^2 \int_{s_i^*}^{s^*}\int_{s_i^*}^{\xi^*} \frac{\partial^2 a^*(\eta^*)}{\partial t^{*2}}\, d\eta^* d\xi^* \right.$$

$$+ \frac{2}{A_0^*}\frac{\omega}{\omega_n}|U_r| \int_{s_i^*}^{s^*} \frac{\partial a^*(\xi^*)}{\partial t^*}\, d\xi^*$$

$$\left. + \left(\frac{U_r l_0}{d}|U_r|U_r - p_0^*\right)\frac{a^*(s^*)}{A_0^*} + p_h^* \right) \cos\left(\frac{2s^*}{P/d}\right) ds^* \tag{24}$$

and similarly for the streamwise direction

$$F_L^* = \int_{-s_a^*}^{s_s^*} \left\{ -\frac{d}{A_0^* U_r l_0}\left(\frac{\omega}{\omega_n}\right)^2 \int_{s_i^*}^{s^*}\int_{s_i^*}^{\xi^*} \frac{\partial^2 a^*(\eta^*)}{\partial t^{*2}}\, d\eta^* d\xi^* \right.$$

$$+ \frac{2}{A_0^*}\frac{\omega}{\omega_n}|U_r| \int_{s_i^*}^{s^*} \frac{\partial a^*(\xi^*)}{\partial t^*}\, d\xi^*$$

$$\left. + \left(\frac{U_r l_0}{d}|U_r|U_r - p_0^*\right)\frac{a^*(s^*)}{A_0^*} + p_h^* \right\} \sin\left(\frac{2s^*}{P/d}\right) ds^* \tag{25}$$

The number of unknowns (a^*, p^*, ω) exceeds the number of equations (Eqs. (17) and (24)) by one. Thus (similar to earlier authors) we must assume a harmonic functional dependance of a^* on t^* and s^*.

The harmonic dependance on s^* is given by:

$$a^*(s^*,t^*) = a^*(s_m^*,t^*) f(s^*) e^{i\Phi^*(s^*)} \tag{26}$$

where $a^*(s_m^*, t^*)$ is the minimum perturbation area function (see Eq. (28)), f^* is the decay function for the perturbation and Φ^* is a phase function along the streamtube. f^* and Φ^* are given by

$$f^*(s^*) = \frac{1}{1 + b(s_a^* + s^*)^a} \qquad s \le -s_a^*$$

$$= 1 \qquad -s_a^* \le s^* \le s_s^*$$

$$\Phi^*(s^*) = \frac{1}{U_r}\frac{s^* + s_a^*}{s_i^* - s_a^*} \tag{27}$$

where a and b are constants chosen to fit the boundary conditions far up and downstream. From the geometry of the problem it can be deduced that the minimum perturbation area function will have the following form

$$a^*(s_m^*,t^*) = x_0^* e^{it^*}\sin\alpha + y_0^* e^{it^* + \Psi}\cos\alpha \tag{28}$$

where Ψ stands for phase lag and x_0^* and y_0^* are amplitudes in the flow and crossflow directions, respectively. This formulation of the area function allows us to calculate derivatives of the area function with respect to time as

$$\frac{\partial a^*}{\partial t^*} = ia^*; \quad \frac{\partial^2 a^*}{\partial t^{*2}} = -a^* \tag{29}$$

Stability Analysis

The equations of motion for the cylinder are customarily (Yetisir and Weaver, 1988) written

$$\lambda m\ddot{x}+c\dot{x}+kx=\Sigma a_x F_x$$

$$\lambda m\ddot{y}+c\dot{y}+ky=\Sigma a_y F_y \tag{30}$$

where λm, c, and k stand for mass of the cylinder, the damping coefficient and the stiffness, x and y are displacement of the cylinder in the flow and crossflow directions, respectively. The RHS term in Eqs. (30) contains the effects of two 1-D streamtubes touching the cylinder from the left and right sides. In order to complete the problem the displacement of the cylinder and the gap perturbations need to be connected as

$$a_1^*(s^*,t^*)=x^*(t^*)\sin\left(\frac{2s^*}{P/d}\right)+y^*(t^*)\cos\left(\frac{2s^*}{P/d}\right)$$

$$a_2^*(s^*,t^*)=x^*(t^*)\sin\left(\frac{2s^*}{P/d}\right)-y^*(t^*)\cos\left(\frac{2s^*}{P/d}\right) \tag{31}$$

By using Eq. (31) in Eq. (30) and noting that movement in the flow direction affects only drag and the movement in crossflow direction enhances lift only, one may conclude that cylinder movement in the flow and crossflow direction do not affect each other and the equations of motion are decoupled. This is not true only for one cylinder vibrating in the array of rigid cylinder, but Squire's Theorem (Squire, 1933, described in Drazin and Reid, 1981) shows that the most dangerous perturbation motion direction coincides with the direction parallel and perpendicular to the main flow direction. By decoupling the equations, the model can be used to predict instability of the tube in one direction while remaining stable in another. Thus, the phase lag function Ψ can be neglected, at least at this order of approximation. To obtain a solution to the equations of cylinder motion, the damping parameter c and the stiffness k will be taken as

$$c=i\lambda m\delta\frac{\omega_n}{\pi}$$

$$k=\lambda m\omega_n^2 \tag{32}$$

Introducing Eq. (32) into Eq. (30), and scaling yields the characteristic equations,

$$-\frac{m}{\rho d^2}\left(\frac{\omega}{\omega_n}\right)^2+\frac{i}{\pi}\frac{m\delta}{\rho d^2}\left(\frac{\omega}{\omega_n}\right)+\frac{m}{\rho d^2}=2F_L^* l_0 U_r\sin\alpha$$

$$-\frac{m}{\rho d^2}\left(\frac{\omega}{\omega_n}\right)^2+\frac{i}{\pi}\frac{m\delta}{\rho d^2}\left(\frac{\omega}{\omega_n}\right)+\frac{m}{\rho d^2}=2F_T^* l_0 U_r\cos\alpha \tag{33}$$

where δ represents the logarithmic decrement of tube damping. These equations will yield the ratio ω/ω_n and δ for any given flow conditions. Since the ratio ω/ω_n is needed to evaluate the fluid forces, an iterative scheme must be employed. The fluid forces as a function of time are the result as well as stability thresholds, associated with real and complex roots of the ratio ω/ω_n.

The stability thresholds need to be divided into two categories. One is connected to a damping matrix, and another one to the fluid stiffness. These modes are called dynamic and static (divergence) thresholds, respectively. Terms on the LHS of Eq. (33) are not the complete fluid stiffness and damping parameter terms. They have to be associated with terms of the same order (in ω/ω_n) from expressions for streamwise (drag) forces. Denoting the terms associated with acceleration (order ω/ω_n^2) as M, those associated with fluid damping as C, and those associated with fluid stiffness with K, we arrive at

$$M_L=-\left[\frac{m}{\rho d^2}+\frac{2\sin\alpha}{A_0^* U_r l_0^*}\int_{s_a^*}^{s_s^*}\sin\left(\frac{2s^*}{P/d}\right)\int_{s_i^*}^{s^*}\int_{s_i^*}^{\xi}a^*(\eta)\,d\eta\,d\xi\,ds^*\right]$$

$$C_L=i\left[\frac{\delta}{\pi}\frac{m}{\rho d^2}-4\sin\alpha\frac{U_r}{A_0^*}\int_{s_a^*}^{s_s^*}\sin\left(\frac{2s^*}{P/d}\right)\int_{s_i^*}^{s^*}a^*(\xi)\,d\xi\,ds^*\right]$$

$$K_L=\frac{m}{\rho d^2}-2\sin\alpha\frac{l_0^*}{A_0^*}U_r^3\int_{s_a^*}^{s_s^*}\sin\left(\frac{2s^*}{P/d}\right)a^*(s^*)\,ds^* \tag{34}$$

for the streamwise direction, and similarly

$$M_T=-\left[\frac{m}{\rho d^2}+\frac{2\cos\alpha}{A_0^* U_r l_0^*}\int_{s_a^*}^{s_s^*}\cos\left(\frac{2s^*}{P/d}\right)\int_{s_i^*}^{s^*}\int_{s_i^*}^{\xi}a^*(\eta)\,d\eta\,d\xi\,ds^*\right]$$

$$C_T=i\left[\frac{\delta}{\pi}\frac{m}{\rho d^2}-4\cos\alpha\frac{U_r}{A_0^*}\int_{s_a^*}^{s_s^*}\cos\left(\frac{2s}{P/d}\right)\int_{s_i^*}^{s^*}a^*(\xi)\,d\xi\,ds^*\right]$$

$$K_T=\frac{m}{\rho d^2}-2\cos\alpha\frac{l_0^*}{A_0^*}U_r^3\int_{s_a^*}^{s_s^*}\cos\left(\frac{2s^*}{P/d}\right)a^*(s^*)\,ds^* \tag{35}$$

for the normal direction. The instabilities occur when

- the coefficients C_L and C_T become positive. The system will react to applied pressure so forcefully that it will actually overshoot the stable position on the other side. This kind of behavior is called overstability or dynamic instability. The threshold of dynamic instability occurs when the value of the coefficients are equal to zero.
- the coefficients K_L and K_T become negative. The system becomes statically unstable (divergence) and the threshold occurs when the coefficients are equal to zero.

It is evident that the model enables the solid-liquid system to become unstable in one direction, while retaining a stable mode in the other direction as discussed above.

Results

A complex arithmetic eigenvalue solver was used to solve the above equations. The nature of the problem is time dependent yet this facet is dismissed in all available experimental data. One of the implications of the lack of data is relative unimportance of temporal terms but this has not yet been proven. The first task is therefore to determine the dependence of the frequencies ratio on time and nondimensional velocity. Results are given in Fig. 3 for the transverse component. The conclusion from this figure is that smaller Re results in a stronger dependence on time. As we approach high Re this dependence vanishes. Results in Figs. 3 and 4 can be used to justify the relative insignificance of the temporal dependence of the area function. Moreover, it is impossible (for an experimentalist) to determine the true position of the cylinder at the onset of instability. Any theoretical result will therefore have to be averaged over the cycle period to compare with available data. Figure 3 proves that one may use a quasi stationary approach to eliminate a temporal dependence (e.g., in the form $e^{i\omega t}$).

The time and velocity are by no means the only parameters. Another parameter is the logarithmic decrement. Figure 4 examines the influence of logarithmic decrement on relationship between reduced velocity and frequency ratio. The figure shows that logarithmic decrement plays virtually no role in determining the frequency ratio.

The threshold of instabilities as a function of reduced velocity versus mass damping parameter are presented in Figs. 5 and 6. Solutions in Fig. 5 for divergence and dynamic instabilities, respectively, show trends similar to those predicted by Yetisir and Weaver (1988), although their numerical scheme (employing curvilinear coordinates while calculating solutions to integral equations) differs significantly from our simple algorithm for evaluating eigenvalues in the complex plane. The

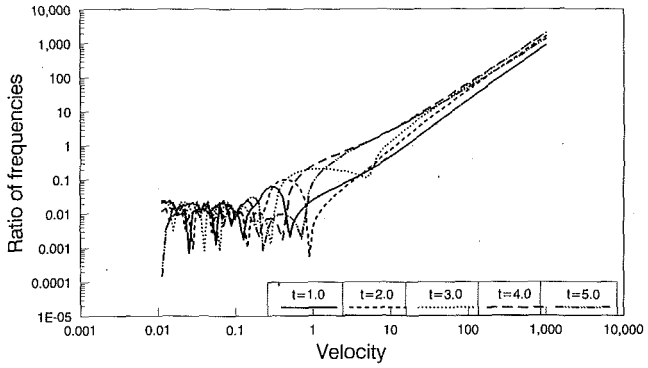

Fig. 3 Ratio of frequencies as function of velocity and time

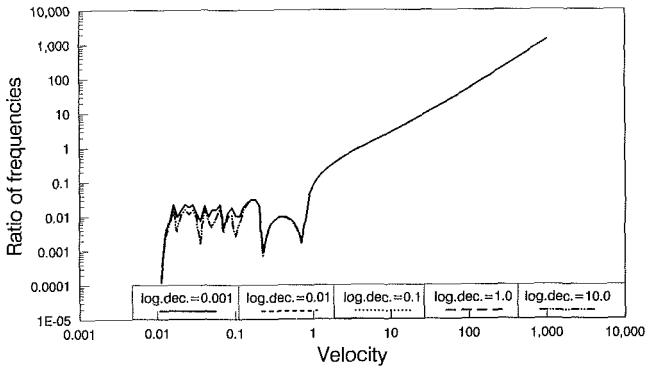

Fig. 4 Ratio of frequencies as function of velocity and log decrement

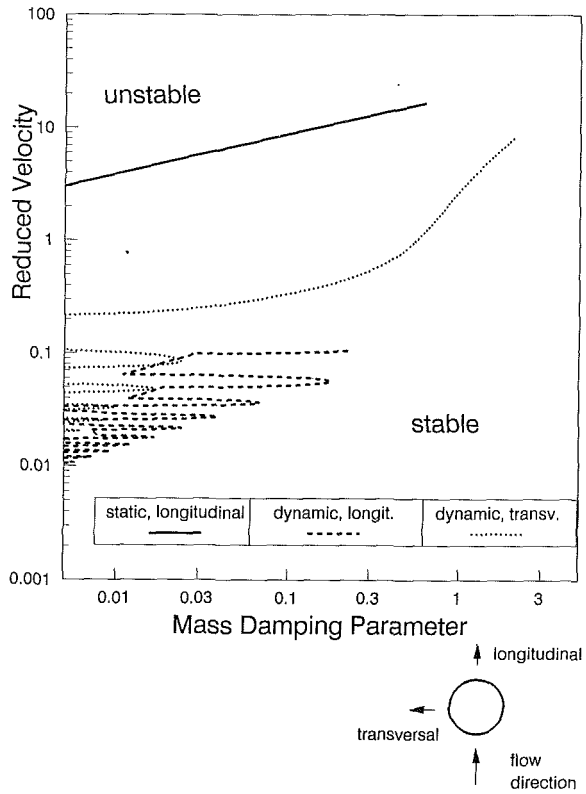

Fig. 5 The onset of instability—triangular array

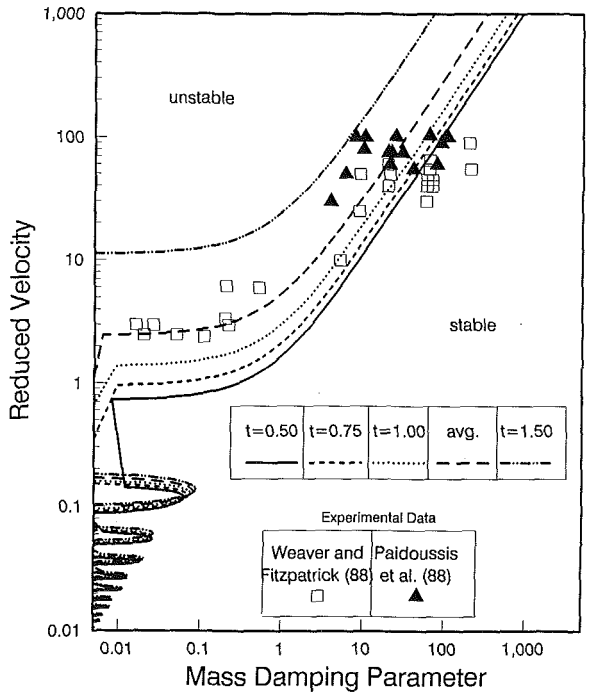

Fig. 6 The onset of instability—rotated square array

predictions in the present work are closer to experimental measurements for the low reduced velocity region than those of Yetisir and Weaver, 1988 (this model is mostly analytical with exception of integration while their uses curvilinear algorithms thus introducing possible errors). Again, there is a peculiar behavior at the onset of the instability especially with respect to time. Figure 6 depicts the values of the transverse dynamic thresholds calculated at different times and compared to experimental results. A rotated square array with pitch to diameter ratio 1.5 was assumed. It is important to recognize that when the flexible cylinder moves, the flow conditions change and thus the conditions for the onset of instability are shifted. There are some points where the system is always stable.

In the cases where a threshold is calculated, the values vary with time. Because of that we tried to determine whether an upper and lower limit existed. These results are also presented in Fig. 6. (We did not employ an optimization routine, since the calculations are rather costly, however most of the experimental results were in between the limits). One needs to note that the experimental data themselves were scattered. This could mean that the model needs to be averaged with respect to time and then the thresholds sought or that the one dimensional character of the solution contributes to inaccuracies. It should be noted also that the solutions for mass damping parameters larger than 5 agree with experimental predictions in a sense that the reduced velocity is proportional to the power of approximately 0.65 of mass damping parameter, in rough agreement with the experimental finding that the reduced velocity is proportional to the half power of damping.

The stable/unstable portions in lower left corner of the Fig. 6 are due to the nature of the solution and should be neglected for practical purposes.

Conclusion

This paper presents a new approach to the idea introduced by Lever and Weaver (1984) and expanded by Yetisir and Weaver (1988). The equations are solved using analytical techniques (with exception of integration which is performed numerically). This decreases the error introduced by the curvilinear

approach used by Yetisir and Weaver and at the same time circumvents the restrictions employed by Lever and Weaver due to entirely analytical solution. The governing equations are derived and a clear derivation of the model is presented.

The notion of an unsteady control volume is not often used in a single phase flow. In this particular case it has proven to be very useful. We assumed that the area perturbation behaved as a harmonic function, and by using the notion of an unsteady volume, we could easily conserve mass without affecting the one-dimensional character of the model. By solving the equations in a complex plane we simplified the procedure for determining the conditions under which the threshold occurs considerably.

The results presented in Figs. 4 and 5 show a definite periodic behavior of the cylinder motion. The results could be associated with Strouhal number for any particular flow conditions if a second dimension along z-axis were to be used. This clearly shows the need for a more complex analysis than is presented here. The results also show that at higher values of the non-dimensional velocity, the temporal character of the frequency ratio vanishes. One of the most important conclusions of this work not previously recognized is the justification for the use of quasi stationary models due to the relatively unimportant temporal character of the problem at higher ω/ω_n ratios. This also assures compatibility with experimental work which is by its very nature subject to averaging since it is impossible to detect in which position the tube has become unstable.

There is a discrepancy between the available experimental data and our results. The probable reasons are that a one dimensional model is not accurate enough although it can be used to bracket the data. One should expect significant effects of vortex shedding and additional instabilities due to fluid fluxes normal to the streamtube direction. The use of an integral form of the equations might not be beneficial since the perturbations, which are filtered by integration, might not be due only to the numerical scheme. This can be dealt with by using higher order integral procedures. The assumption of a fixed "attachment" point reduces the effect of pressure fluctuations on movement in the streamwise direction.

Acknowledgments

Authors would like to thank Department of Energy, which has sponsored this work as a part of grant No. DE-FG07-89ER12902.

References

Chen, S. S., 1987, *Flow Induced Vibration of Circular Cylindrical Structures*, Springer-Verlag, Berlin.

Drazin, P. G., and Reid, W. H., 1981, *Hydrodynamic Stability*, Cambridge University Press, New York.

Kim, C. M., and Conlisk, A. T., 1988, "Flow Induced Vibration and Noise by a Pair of Tandem Cylinders Due to Buffeting," *1988 Int. Symp. on Flow Induced Vibrations and Noise*, Vol. 2, ASME.

Lever, J. H., and Weaver, D. S., 1984, "On the Stability Behaviour of Heat Exchanger Tube Bundles," Parts I and II, *1984 Symp. on Flow Induced Vibrations*, Vol. 2, ASME.

Paidoussis, M. P., Price, S. J., Nakamura, T., Mark, B., and Njuki, W., 1988, "Flow-Induced Vibrations and Instabilities in a Rotated-Square Cylinder Array in Cross-Flow," *1988 Int. Symp. on Flow Induced Vibrations and Noise*, Vol. 3, ASME.

Price, S. J., Paidoussis, M. P., and Giannias, N., 1988, "A Generalized Constrained Mode Analysis For Cylinder Arrays in Cross Flows," *1988 Int. Symp. on Flow Induced Vibrations and Noise*, Vol. 3, ASME.

Rajaona, D. R., and Sulmont, P., 1988, "A Model of Forces Acting on a Circular Cylinder Moving along a Sinusoidal Trajectory in Calm Water at Subcritical Reynolds Numbers," *1988 Int. Symp. on Flow Induced Vibrations and Noise*, Vol. 1, ASME.

Weaver, D. S., and Fitzpatrick, J. A., 1988, "A Review of Cross-Flow Induced Vibrations in Heat Exchanger Tube Arrays," *Journal of Fluids and Structures*, Vol. 2, pp. 73-93.

Yetisir, M., and Weaver, D. S., 1988, "On an Unsteady Theory for Fluidelastic Instability of Heat Exchanger Tube Arrays," *1988 Int. Symp. on Flow Induced Vibrations and Noise*, Vol. 3, ASME.

APPENDIX A

Derivation of Governing Equation for Nonsteady Control Volume

A control volume is usually fixed in space and time. If one expects the unit volume to change its shape periodically, it may be beneficial to develop the governing equations based on that kind of property. For example, if one has a pulsating tube, one can reduce the dimensions of the system from 2 to 1 by assuming the tube motion, and defining the borders of the control volume as borders of the system. Derivations of the conservation equations are carried out for a time varying control volume.

Continuity

Denote the rate at which mass is being accumulated in the control volume by RA, then

$$\mathrm{RA} = \lim_{\Delta t \to 0} \frac{-m|_t + m|_{t+\Delta T}}{\Delta t} \tag{36}$$

If the mass of the control volume can be assumed to be a continuous function of time (which is certainly true for our purposes), it can be approximated with a Taylor series,

$$m|_{t+\Delta t} = m|_t + \frac{\partial m}{\partial t}\Delta t + \frac{1}{2}\frac{\partial^2 m}{\partial t^2}(\Delta t)^2 + \ldots \tag{37}$$

Next, assume the fluid to be incompressible, and the rate of mass accumulation is found to be

$$\mathrm{RA} = \lim_{\Delta t \to 0}\left(\rho\frac{\partial V}{\partial t}\right) = \rho\frac{\partial V}{\partial t} = \rho\Delta x\frac{\partial A}{\partial t} \tag{38}$$

Conservation of mass requires that

Rate of Mass Accumulation	=	Rate of Inflow	−	Rate of Outflow

Denoting the rate of inflow to be RI and the rate of outflow to be RO yields

$$\mathrm{RI} = \rho u A|_x$$

$$\mathrm{RO} = \rho u A|_{x+\Delta x} = \rho\mu A|_x + \frac{\partial}{\partial x}(\rho u A|_x)\Delta x + \ldots \tag{39}$$

Combining the equations above yields the nonsteady form of the continuity equation

$$\frac{\partial A}{\partial t} + \frac{\partial}{\partial x}(\rho u A) = 0 \tag{40}$$

Momentum

Following the same procedure as used when developing the continuity equation, denote the rate of change of momentum as RM, the inflow of momentum as IM, the outflow of momentum as OM, and the forces, acting on the fluid as FF. The momentum conservation equation can then be expressed as

Rate of Change of Momentum	=	Inflow of Momentum	+	Outflow of Momentum	+	Forces Acting on Fluid

The specific terms for one dimensional, inviscid, incompressible flow are

$$\mathrm{RM} = \frac{\partial}{\partial t}(um) = \rho\frac{\partial}{\partial t}(uV) = \rho\Delta x\frac{\partial}{\partial t}(uA)$$

$$\mathrm{IM} = \rho u|u|A|_x$$

$$\mathrm{OM} = \rho u|u|A|_{x+\Delta x} = \rho u|u|A|_x + \frac{\partial}{\partial x}(\rho u|u|A|_x)\Delta x + \ldots$$

$$FF = -pA|_x + pA|_{x+\Delta x} = -pA|_x + pA|_x + \frac{\partial}{\partial x}(pA|_x)\Delta x + \ldots \tag{41}$$

If the volume is a continuous function of space and time then the final form of momentum is

$$\rho \frac{\partial}{\partial t}(uA) + \frac{\partial}{\partial x}(\rho u|u|A) = -\frac{\partial}{\partial x}(pA) \tag{42}$$

To summarize, the conservation equation in vector form are

Continuity

$$\frac{\partial V}{\partial t} + \nabla \cdot (\mathbf{u}V) = 0 \tag{43}$$

Momentum

$$\frac{\partial}{\partial t}(uV) + \nabla(\rho \mathbf{u}|\mathbf{u}|V) = -\frac{1}{\rho}\nabla(pV) \tag{44}$$

On Laminar Wakes Behind a Circular Cylinder in Stratified Fluids

Robert R. Hwang

S. H. Lin

Department of Naval Architecture,
Taiwan University and Institute of Physics,
Academia Sinica, Taipei, Taiwan, R.O.C.

Finite-difference techniques based on boundary-fitted coordinates have been developed to study the flow of a stably stratified viscous fluid past a circular cylinder. A time-dependent approach is used and an implicit solution is applied in the implementation of vorticity-stream function formulation. All field equations are approximated using central differences and solved simultaneously at each time step by the SOR iteration. Results show that the stratification tends to retard the vortex shedding from the two sides of the cylinder and to narrow down the wake behind the cylinder. With increasing stratification, the drag exerted by the fluid on the cylinder at first decreases and then increases. These solutions also indicate that the periodic configurations of the oscillatory character of the wake flow decrease with the increase of stratification.

1 Introduction

The uniform flow of homogeneous fluids past a circular cylinder is a classic problem in fluid mechanics. At low Reynolds numbers (Re $<$ 40, Re $= 2aU/\nu$, where a is the radius of the cylinder, U is the free-stream velocity, and ν is the coefficient of kinematic viscosity of the fluid), a steady symmetrical flow exists. As the Reynolds number increases to a certain value (say Re $>$ 50), the flow in the wake of the obstacle becomes unsteady and periodic, and performs an alternative vortex shedding. As a result, the forces that are imposed by the fluid upon the cylinder become oscillatory in nature. Studies on the problem of wake development and vortex shedding behind the cylinder for a uniform flow of homogeneous fluid have been reported by many researchers (see, e.g., Jorden and Fromm, 1972; Deffenbaugh and Marshall, 1976; Patel, 1978, 1980; Gresho et al., 1980; Loc, 1980; Lecointe and Piquet, 1984; Hwang et al., 1986). The effect of the stratification of ambient fluid on the configuration of flow pattern such as the formulation of wake, the shedding mechanism of vortex, etc., on the other hand, has not yet been investigated.

Most studies of the density-stratified fluid flow over an obstacle have dealt with the ambient fluid in a strong density stratification. It can be found in recent studies by Pao (1986), Wei et al. (1975), Haussling (1977), and Hwang and Jang (1982). In such stratified fluid flows, one of the striking phenomena obtained is the strong upstream influence (the upstream wake) of an obstacle when the gravity effect is equivalent to, or greater than the inertial effect. The other characteristics are the lee waves formation downstream the obstacle. The study of Pao (1968) concluded that the upstream influence and the reverse wake of lee waves decreased with the decrease in the ambient density stratification. The effects of the weak stratification on the oscillatory wake development and vortex shedding behind the cylinder have not yet been investigated.

This study is then concerned with the laminar flow past a circular cylinder with uniform upstream velocity and weak density gradient. Separation and vortex shedding, that depend on viscous effects in the interaction with the mean density stratification, are considered in the problem. In solving the unsteady flow problem, the full unsteady Navier-Stokes equations for incompressible fluids utilizing the vorticity-stream function formulation are solved. With the use of boundary-fitted coordinates, all field equations are discretized into finite-difference approximations and solved simultaneously at each time step on the transformed domain. Numerical computations for flows of Re $=$ 100, 200, and 500 are carried out with the variations of density gradients.

2 Formulation of Flow Problems

We consider an incompressible viscous flow of linearly stratified fluid past a circular cylinder of diameter D with constant uniform speed U. Figure 1 shows the geometry and coordinates of the flow problem. Far upstream, in the frame of reference of the cylinder, the following conditions are assumed to exist:

$$\tilde{\rho} = \rho_0(1 - \beta\tilde{z})$$
$$\tilde{u} \to U$$
$$\tilde{w} \to 0 \tag{1}$$

in which ρ_0 is the density of fluid very far upstream at the level of the cylinder and

$$\beta = \lim_{\tilde{x} \to -\infty} |d\rho/d\tilde{z}|/\rho_0$$

is the stratification parameter. U is the constant velocity in the undisturbed stream.

Contributed by the Fluids Engineering Division for publication in the JOURNAL OF FLUIDS ENGINEERING. Manuscript received by the Fluids Engineering Division December 15, 1988.

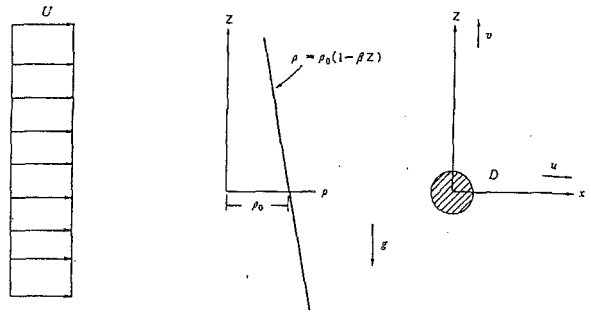

Fig. 1 The geometry of the flow problem

With the assumptions of that the flow is incompressible and laminar, the fluid has uniform transport properties, and that β is so small that the Boussinesq approximation is valid, the governing equations in vorticity-stream function formulation and the diffusion equation in density are

$$\frac{\partial\tilde{\zeta}}{\partial\tilde{t}}+\tilde{u}\frac{\partial\tilde{\zeta}}{\partial\tilde{x}}+\tilde{w}\frac{\partial\tilde{\zeta}}{\partial\tilde{z}}=-\frac{1}{\rho_0}\frac{\partial\tilde{\rho}}{\partial\tilde{x}}g+\nu\tilde{\nabla}^2\tilde{\zeta} \tag{2}$$

$$\tilde{\nabla}^2\tilde{\psi}=-\tilde{\zeta} \tag{3}$$

$$\frac{d\tilde{\rho}}{\partial\tilde{t}}+\tilde{u}\frac{\partial\tilde{\rho}}{\partial\tilde{x}}+\tilde{w}\frac{\partial\tilde{\rho}}{\partial\tilde{z}}=D_m\tilde{\nabla}^2\tilde{\rho} \tag{4}$$

$$\text{and } \tilde{u}=\partial\tilde{\psi}/\partial\tilde{z},\ \tilde{w}=-\partial\tilde{\psi}/\partial\tilde{x} \tag{5}$$

where $\tilde{u}$ and $\tilde{w}$ are the velocity components in $(\tilde{x}, \tilde{z})$ directions $\tilde{\rho}$ is the density, $\tilde{t}$ is the time, $\tilde{\nabla}^2=\partial^2/\partial\tilde{x}^2+\partial^2/\partial\tilde{z}$ and ν and D_m are the kinematic viscosity and the molecular diffusivity of fluid, respectively. $\tilde{\zeta}$ is the vorticity defined by

$$\tilde{\zeta}=\partial\tilde{w}/\partial\tilde{x}-\partial\tilde{u}/\partial\tilde{z} \tag{6}$$

For convenience, Eqs. (2) through (5) can be normalized to give a set of nondimensional equations by defining a length D, the diameter of the cylinder and the velocity U, as characteristics parameters. The dimensionless quantities are specified as follows:

$$x=\tilde{x}/D,\ z=\tilde{z}/D,\ u=\tilde{u}/U,\ w=\tilde{w}/U$$

$$t=\tilde{t}/\frac{D}{U},\ \psi=\tilde{\psi}/UD,\ \zeta=\tilde{\zeta}/\frac{U}{D},\ \rho=\frac{\rho-\rho_0}{\Delta\tilde{\rho}}$$

$$\text{Re}=UD/\nu,\ \text{S}_c=\nu/Dm \text{ and}$$

$$\text{F}=U/\sqrt{(\Delta\rho/\rho_0)gD} \tag{7}$$

where $\Delta\tilde{\rho}$ is the density difference between the levels of the upper and the lower surfaces of the cylinder infinitely far upstream. Re, S_c, and F are Reynolds number, Schmidt number and densimetric Froude number, respectively. The dimensionless governing equations now become

$$\frac{\partial\zeta}{\partial t}+\frac{\partial\psi}{\partial z}\frac{\partial\zeta}{\partial x}-\frac{\partial\psi}{\partial x}\frac{\partial\zeta}{\partial z}=\frac{1}{\text{Re}}\nabla^2\zeta-\frac{1}{\text{F}^2}\frac{\partial\rho}{\partial x} \tag{8}$$

$$\nabla^2\psi=-\zeta \tag{9}$$

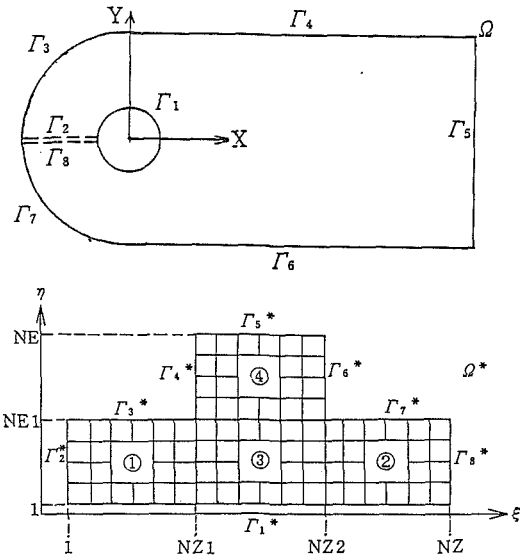

Fig. 2 Transformation of coordinate system

$$\frac{\partial\rho}{\partial t}+\frac{\partial\psi}{\partial z}\frac{\partial\rho}{\partial x}-\frac{\partial\psi}{\partial x}\frac{\partial\rho}{\partial z}=\frac{1}{\text{Re Sc}}\nabla^2\rho \tag{10}$$

$$\text{and } u=\partial\psi/\partial y,\ w=-\partial\psi/\partial x \tag{11}$$

The governing Eqs. (8) through (11) subject to the appropriate initial and boundary conditions are to be solved in studying the uniform flow with weakly density-stratified fluid past a cylinder. The initial and boundary conditions on and far from the cylinder are summarized as

(1) $\Psi=\Psi_P,\ \zeta=0,\ \rho=-\Psi_P$ for $t=0$

and $\Psi_P=-(z+z/\sqrt{x^2+z^2})$

(2) $\Psi=0,\ \zeta=\zeta_b,\ \rho=0$ on cylinder (12)

(3) $\Psi=\Psi_P,\ \zeta=0,\ \rho=-\Psi_P$ far from cylinder

The boundary conditions imposed upon the cylinder are the usual impermeability and nonslip conditions. The initial condition is obtained from the statement that the impulse start of the development of flow over the cylinder can be treated as a potential flow.

3 The Transformation

In order to simplify the numerical computation in solving the flow problem, a numerical grid generation is performed. The physical region as shown in Fig. 2, cut off suitably upstream, is transformed to a simple region which is composed of rectangles. The cylinder is mapped onto the line Γ_1^*, the downstream boundary onto Γ_5^*, the upper and lower far boundaries onto Γ_4^* and Γ_6^*, respectively, and the upstream boundary

Nomenclature

C_D = drag coefficient
C_L = lift coefficient
C_T = torque coefficient
D = diameter of circular cylinder
Dm = the molecular diffusivity
F = the densimetric Froude number
g = acceleration of gravity
p = pressure
R_e = Reynolds number
S = Strouhal number
S_c = Schmidt number
(x, z) = Cartesian coordinates
(u, w) = velocity components of (x, z) direction
t = time
ρ = density
β = stratification parameter
ψ = stream function
ζ = vorticity
ν = kinematic viscosity
(ξ, η) = transform coordinates

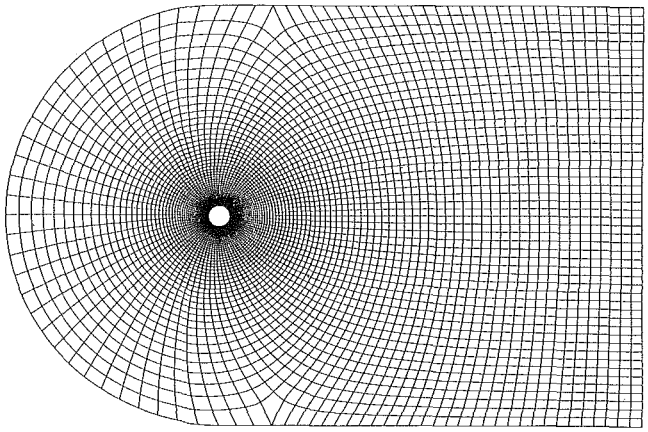

Fig. 3 Coordinates in physical plane

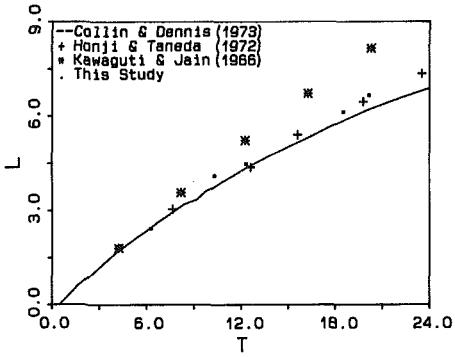

Fig. 4(*a*) Re = 100

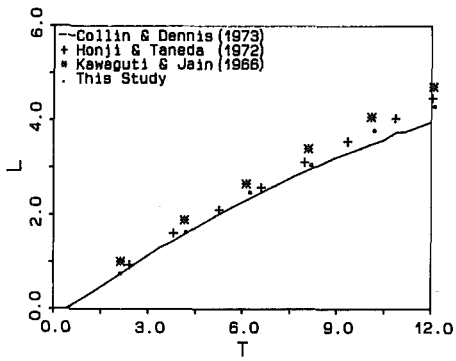

Fig. 4(*b*) Re = 200

Fig. 4 Comparison of computational and experimental results for evolution with time of the wake length of homogeneous fluid

splitting onto Γ_3^* and Γ_7^*, the boundaries Γ_2^* and Γ_8^* represent cut within the fluid.

Following the work of Thompson et al. (1976) and Thames et al. (1977), the curvilinear coordinates (ξ, η) are generated by solving an elliptic system of the form

$$\xi_{xx}+\xi_{zz}=P(\xi,\eta,t) \tag{13}$$

$$\eta_{xx}+\eta_{zz}=Q(\xi,\eta,t) \tag{14}$$

with Dirichlet boundary conditions. The ξ coordinate is specified as constant on one boundary and equals to another constant on the opposite boundary with the η coordinate varying monotonically over the same range on both the boundaries. Subscripts indicate differentiation and will be used in the following sections. The source functions P and Q are specified in a way that it allows coordinate lines to be attracted to specified lines and/or points in the domain or on the boundaries in making the numerical scheme to be efficient. Figure 3 displays the grid in the physical plane.

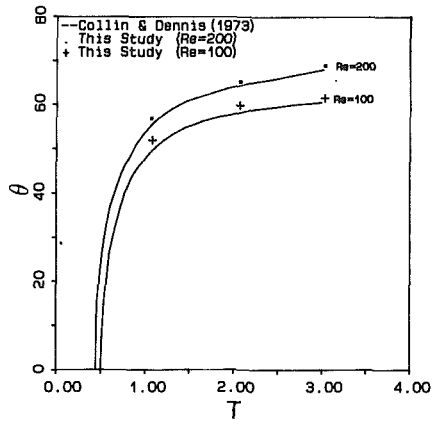

Fig. 5 Comparison between the computed values of evolution with time of the separation angle

Table 1 Comparison between computed values of mean drag, lift, and Strouhal number

Re	C_D	C_L	S	Author(s)
	1.29	±0.38	0.164	Present
	1.28	±0.54	0.16	Jordan and Fomn (1972)
100	1.29	±0.50	0.133	Patel (1978)
	1.43	±0.50	0.166	Smith and Brebbia (1977)
	1.27	±0.6	0.161	Gresho et al. (1980)
	1.28	±0.6	0.182	Present
	1.17		0.18	Lin et al. (1976)
200	1.27	±0.7	0.154	Patel (1978)
	1.17		0.15	Thoman and Szewczyk (1969)
	1.46	±0.7	0.194	Lecointe and Piquet (1984)

Since we desire to perform all computations in the transformed plane, where the mesh system consists of simple rectangles, the governing equations and boundary conditions must be described in terms of ξ and η as the independent variables. Using the fully conservative form of the differential operators given by

$$f_x=\frac{1}{J}\left[(fz_\eta)_\xi-(fz_\xi)_\eta\right]$$

$$f_z=\frac{1}{J}\left[-(fx_\eta)_\xi-(fx_\xi)_\eta\right] \tag{15}$$

where f denotes some arbitrary function and J is the Jacobian defined in Eq. (17), the governing Eqs. (8) through (11) become

$$\zeta_t+(\psi_\eta\zeta_\xi-\psi_\xi\zeta_\eta)J$$

$$=\frac{1}{Re}\left[\frac{1}{J^2}(\alpha\zeta_{\xi\xi}-2\beta\zeta_{\xi\eta}+\gamma\zeta_{\eta\eta})+(Q\zeta_\eta+P\zeta_\xi)\right] \tag{16}$$

$$(\alpha\psi_{\xi\xi}-2\beta\psi_{\xi\eta}+\gamma\psi_{\eta\eta})/J^2+Q\psi_\eta+P\psi_\xi=-\zeta \tag{17}$$

$$\rho_t+(\psi_\eta\rho_\xi-\psi_\xi\rho_\eta)/J$$

$$=\frac{1}{Re\,Sc}\left[(\alpha\rho_{\xi\xi}-2\beta\rho_{\xi\eta}+\gamma\rho_{\eta\eta})/J^2+(P\rho_\xi+Q\rho_\eta)\right] \tag{18}$$

$$u=(\chi_\xi\psi_\eta-\chi_\eta\psi_\xi)/J,\ v=(y_\xi\psi_\eta-y_\eta\psi_\xi)/J. \tag{19}$$

The boundary conditions under the transformation can be specified in the computational plane as follows

(1) On the boundary Γ_1^*

$$\Psi(\xi,1,t)=0,\ \zeta(\zeta,1,t)=-\gamma\Psi_{\eta\eta}/J^2,\ \rho(\zeta,1,t)=0. \tag{20a}$$

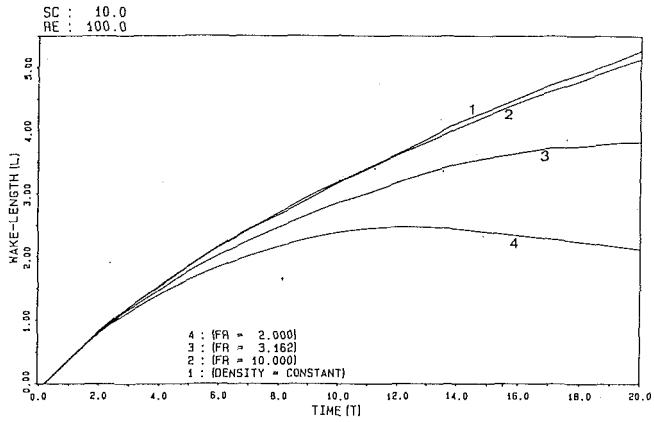

Fig. 6 Evolution of wake-length varied with the densimetric Froud number, F, for Re = 100

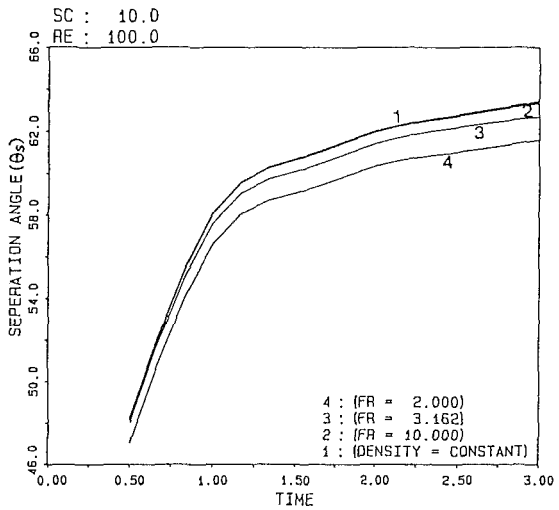

Fig. 7 Evolution of separation angle varied with F for Re = 100

(2) On boundaries Γ_3^*, Γ_4^*, Γ_6^*, and Γ_7^*,

$$\Psi(\xi,1,t)=\Psi_P,\ \zeta(\xi,1,t)=0,\ \rho(\xi,1,t)=-\Psi_P \qquad (20b)$$

(3) On the boundary Γ_5^*,

$$\Psi_\eta=0,\ \zeta_\eta=0,\ \rho_\eta=0. \qquad (20c)$$

4 Computational Procedures

Given the description of the mesh system, the governing Eqs. (16), (17), (18), and (19) with boundary conditions of Eq. (20) were solved numerically with the fully implicit, backward-time, central-space formulation. A two-point, first-order backward difference was used to approximate the time derivative, while second-order central differences were employed for the spatial derivatives. The alternating direction implicit method of splitting the time step to obtain a multidimensional system equation was applied to solve Eqs. (16) and (19), while the point SOR iteration was employed to converge the elliptic space variation of Eq. (17). The basic steps of calculating algorithm involved in advancing the configuration through the cycle from time t to time t + Δt are as follows:

(1) At the beginning of the cycle, all required quantities are available either as initial data or as results from the previous cycle.

(2) Applying the ADI method, new values of ζ and ρ are obtained by solving Eqs. (16) and (18) numerically subject to the appropriate boundary conditions in advancing a time step.

(3) With the new value for the vorticity field, a new value for the stream function Ψ is found from solving a finite-difference approximation of Eq. (17) by the SOR iteration.

(4) From the finite-difference approximations of Eq. (19), u and w are found for the new components of velocity.

(5) Find the vorticity on the cylinder surface from Eq. (20*a*).

(6) For selected cycles, a summary information is computed and this, together with various configurations, is recorded for studying the time development of the flow field.

5 Presentation and Discussion of Results

The impulsively started unsteady viscous flows of the stably

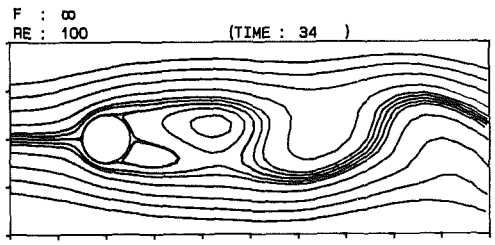

Fig. 8(*a*) τ = 34

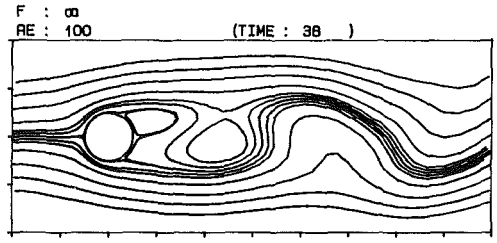

Fig. 8(*c*) τ = 38

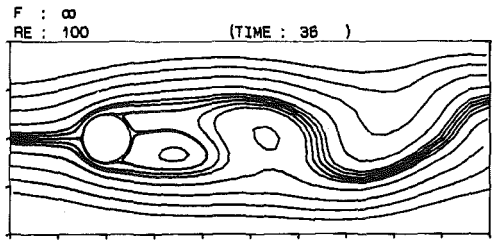

Fig. 8(*b*) τ = 36

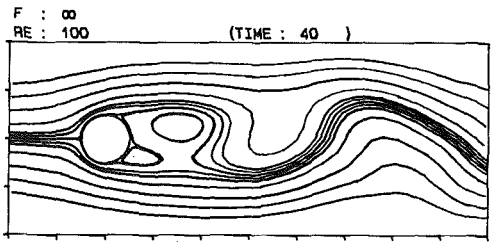

Fig. 8(*d*) τ = 40

Fig. 8 Development with time of the instantaneous streamlines for Re = 100, F = ∞. The values of the dimensionless stream function corresponding to the streamlines are Ψ = − ±0.001, 0.05, 0.1, 0.25, 0.5, 0.75, 1.0.

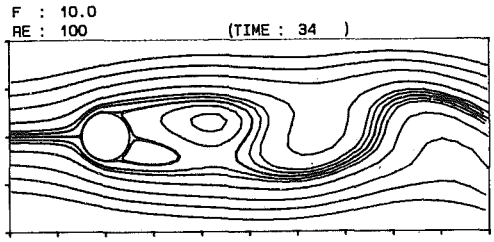

Fig. 9(*a*) $\tau = 34$

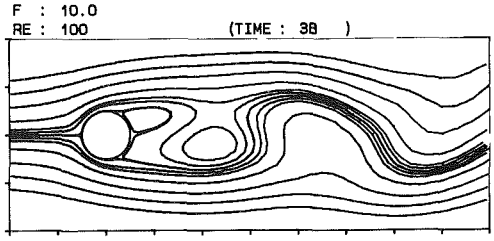

Fig. 9(*c*) $\tau = 38$

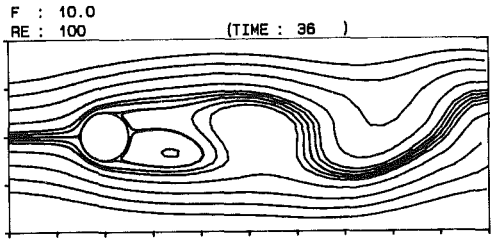

Fig. 9(*b*) $\tau = 36$

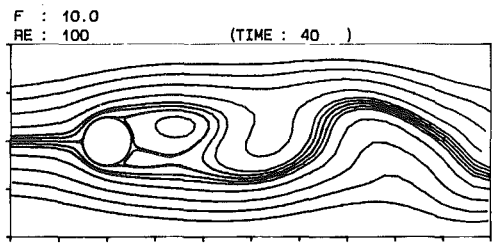

Fig. 9(*d*) $\tau = 40$

Fig. 9 Development with time of the instantaneous streamlines for Re = 100, F = 10

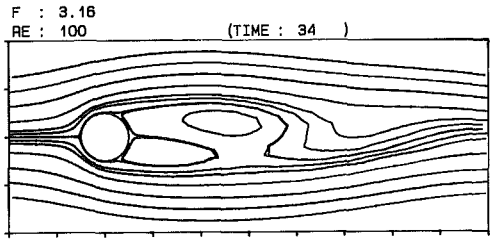

Fig. 10(*a*) $\tau = 34$

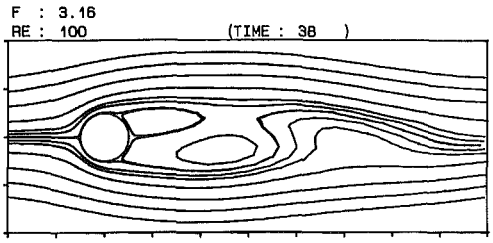

Fig. 10(*c*) $\tau = 38$

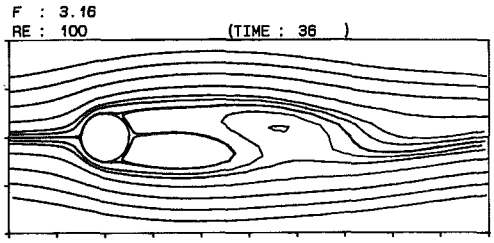

Fig. 10(*b*) $\tau = 36$

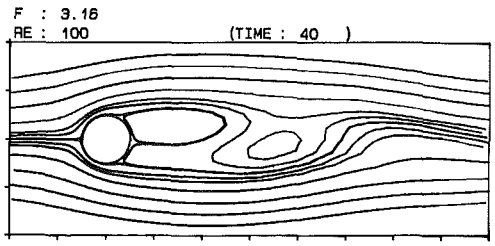

Fig. 10(*d*) $\tau = 40$

Fig. 10 Development with time of the instantaneous streamlines for Re = 100, F = 3.16

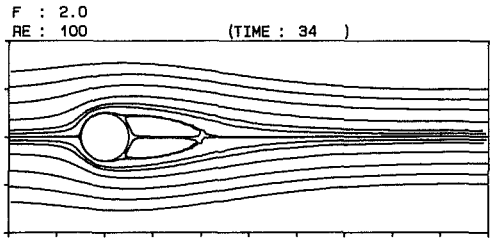

Fig. 11(*a*) $\tau = 34$

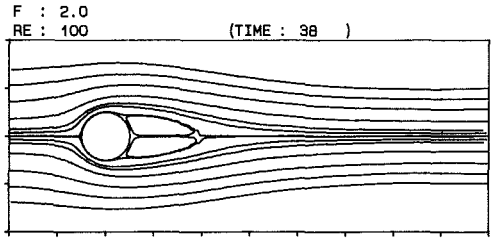

Fig. 11(*c*) $\tau = 38$

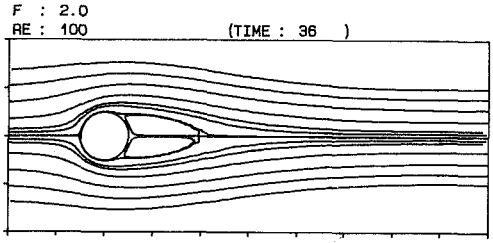

Fig. 11(*b*) $\tau = 36$

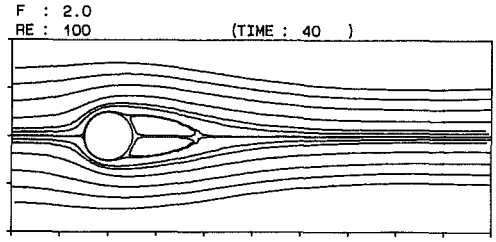

Fig. 11(*d*) $\tau = 40$

Fig. 11 Development with time of the streamlines for Re = 100, F = 2.0

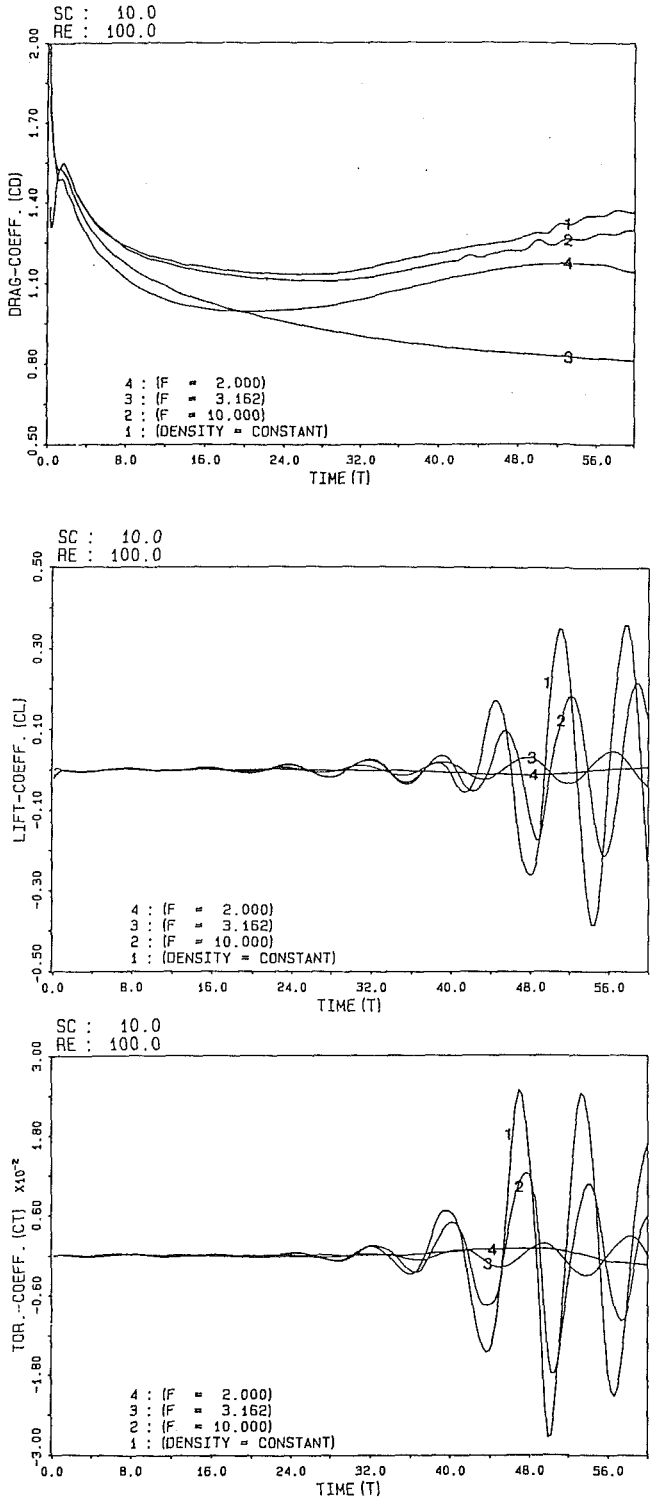

Fig. 12 Variation of the drag, lift and torque coefficients with time for Re = 100

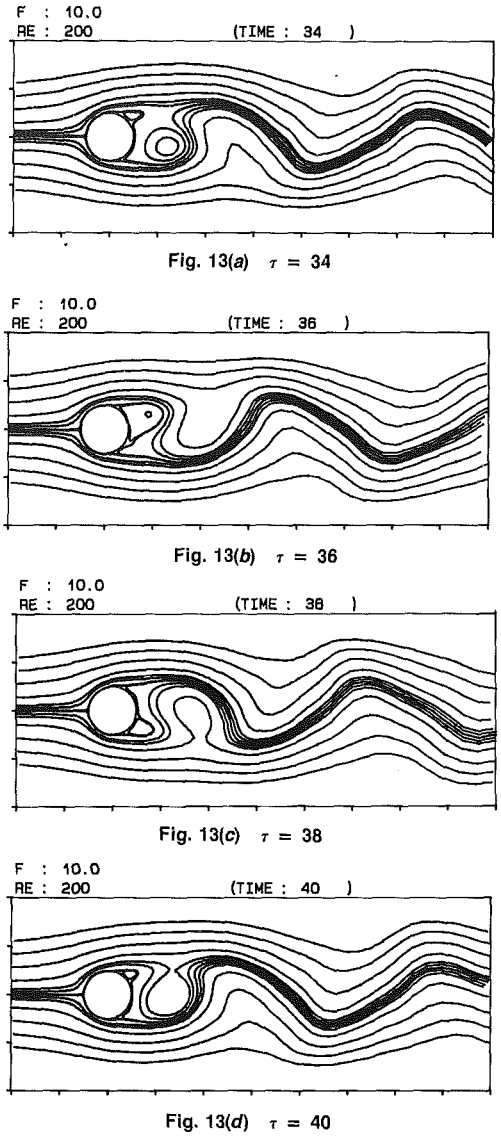

Fig. 13(*a*) τ = 34

Fig. 13(*b*) τ = 36

Fig. 13(*c*) τ = 38

Fig. 13(*d*) τ = 40

Fig. 13 Streamlines during vortex shedding for Re = 200, F = 100. The values of the dimensionless stream function corresponding to the streamlines are the same as in Fig. 8.

stratified fluid past a circular cylinder for both of various Reynolds numbers and densimetric Froude numbers were calculated in using the numerical procedures outlined above. In the implementation of the numerical scheme, small time steps (Δt = 0.002) were utilized in the initial phase to resolve the fluid motion under the effects of impulsive start. Time step were then subsequently increased to values of the order of 2/Re without significant increase in the number of iterations required to converge at each step. The spatial grid resolution in the computational domain as shown in Fig. 2, was set as $\Delta\xi = \Delta\eta = 1$, and NZ = 90 NE = 80, NZ_1 = 20, NZ_2 = 70, and NE_1 = 50.

In order to test the accuracy of the numerical computation of the present study, some results for the limiting case of homogeneous fluid flow (F = ∞) past a circular cylinder were obtained for Re = 100 and 200. Results were compared with the existing numerical results and experimental data of previous studies (Collin and Dennis, 1973). Figures 4(*a*) and 4(*b*) give the comparisons of the evolution of the wake length between the present study and other investigations for Re = 100 and 200, respectively. The length of the recirculation zone behind the cylinder indicated by L/a, evolves almost linearly with time and appears to be correct in comparison with the results of other studies. Figure 5 shows the comparison of the time evolution of the flow separation on the cylinder surface for Re = 100 and 200. They appear to have good agreements. When the time is getting longer, the vortices of the flow pattern shed alternately from two sides of the cylinder and evolve toward a periodic configuration. It indicates the successful numerical simulation of the delicate vortex shedding phenomenon in the

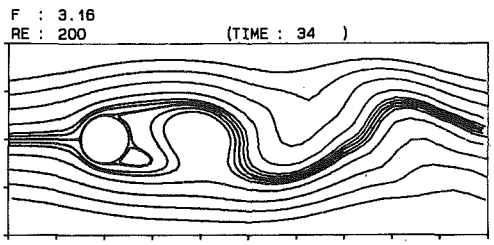

Fig. 14(*a*) $\tau = 34$

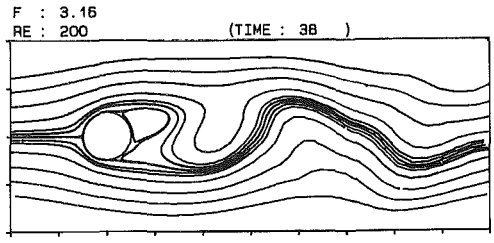

Fig. 14(*c*) $\tau = 38$

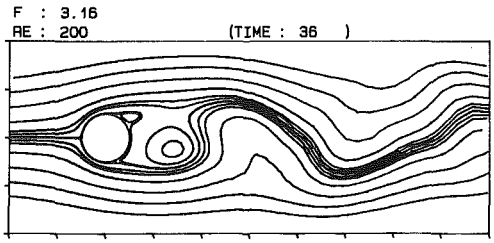

Fig. 14(*b*) $\tau = 36$

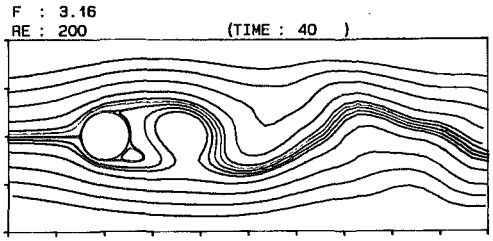

Fig. 14(*d*) $\tau = 40$

Fig. 14 Streamlines during vortex shedding for Re = 200, F = 3.16

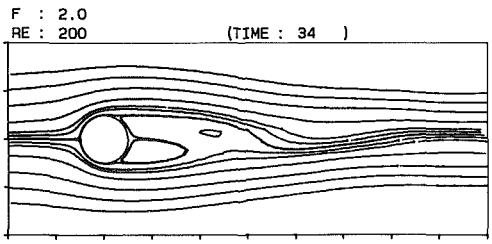

Fig. 15(*a*) $\tau = 34$

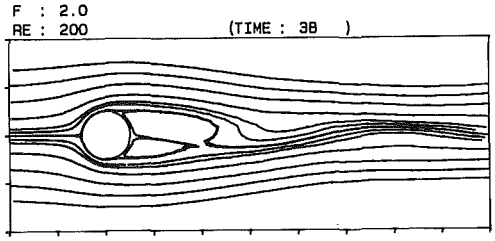

Fig. 15(*c*) $\tau = 38$

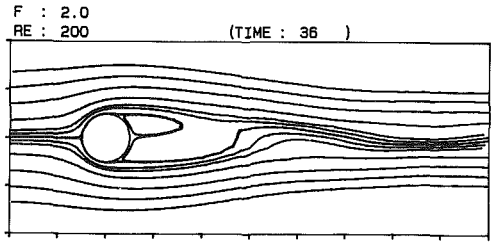

Fig. 15(*b*) $\tau = 36$

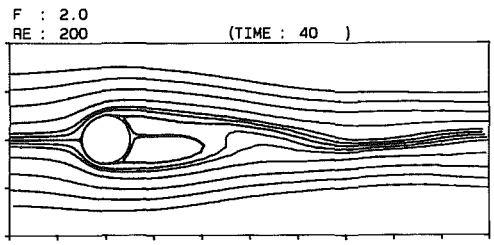

Fig. 15(*d*) $\tau = 40$

Fig. 15 Streamlines during vortex shedding for Re = 200, F = 2.0.

near wake of a circular cylinder. As shown in Table 1, computed values of averaged drag, lift and Strouhal number are found to be in good agreement with the earlier results.

Effects of density stratification on the wake development behind cylinder are investigated by varying values of densimetric Froude number. Some results are presented in the following. Figures 6 and 7 display the time evolution of the wake length and separation angle at the early times of flow development for various values of F. They indicate that the density stratification will inhibit the flow development of the wake. With the time increase, the wake of the cylinder becomes unsteady and periodic. Figures 8, 9, 10, and 11 show the streamlines of flow pattern during vortex shedding at Re = 100 for F = ∞ (homogeneous fluid), 10, 3.16, and 2, respectively. The frequency of the vortex shedding decreases with the increase of the density gradient. The frequency of vortex shedding, f, can be measured by means of the Strouchal number $S = fD/U$. The frequency of vortex shedding decreases with the ambient stratification but increases with Reynolds numbers at which vortex shedding takes place. Increasing the stratified gradient slightly, say F = 2, the wake behind the cylinder becomes symetric with respect to $\theta = 0$ and remains stationary in time.

The forces exerted by the fluid on the cylinder are influenced by variations of the density stratification. In terms of nondimensional local surface pressure and tangential shear force, the drag, lift and torque coefficients over the surface of the cylinder, represented by C_D, C_L, and C_T respectively, are defined by

$$C_D = -\int_0^{2\pi} p\cos\theta\, d\theta - \frac{1}{\mathrm{Re}}\int_0^{2\pi} \zeta \sin\theta\, d\theta$$

$$C_L = -\int_0^{2\pi} p\sin\theta\, d\theta + \frac{1}{\mathrm{Re}}\int^{\pi} \zeta\cos\theta\, d\theta$$

$$\text{and } C_T = \frac{1}{\mathrm{Re}}\int_0^{2\pi} \zeta\, d\theta. \tag{21}$$

Figure 12 shows the periodic variations of the drag, lift and

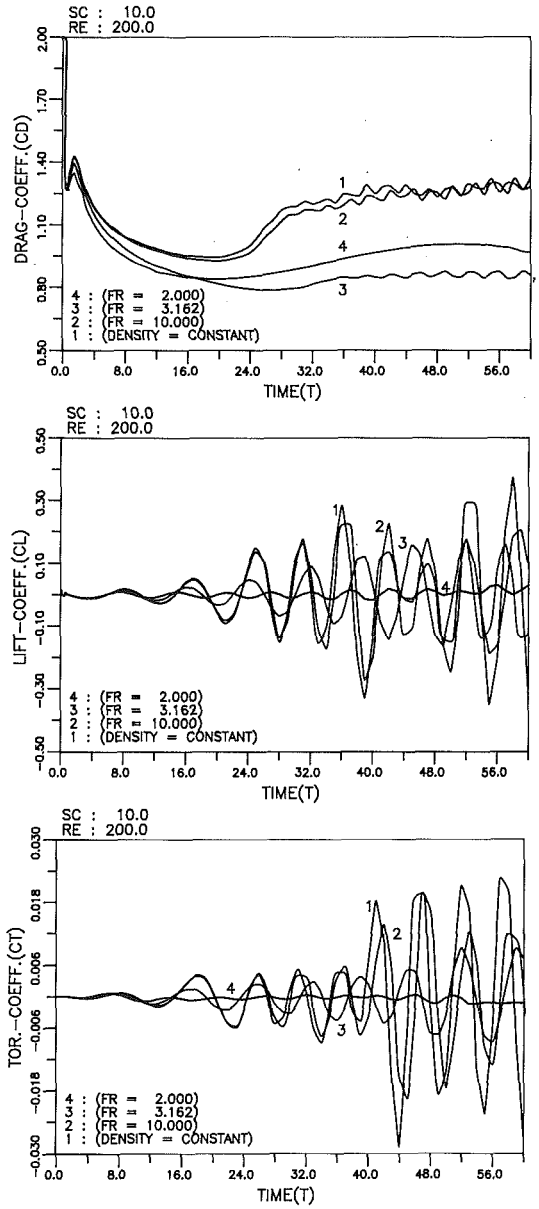

Fig. 16 Variation of the drag, lift, and torque coefficients with time for Re = 200

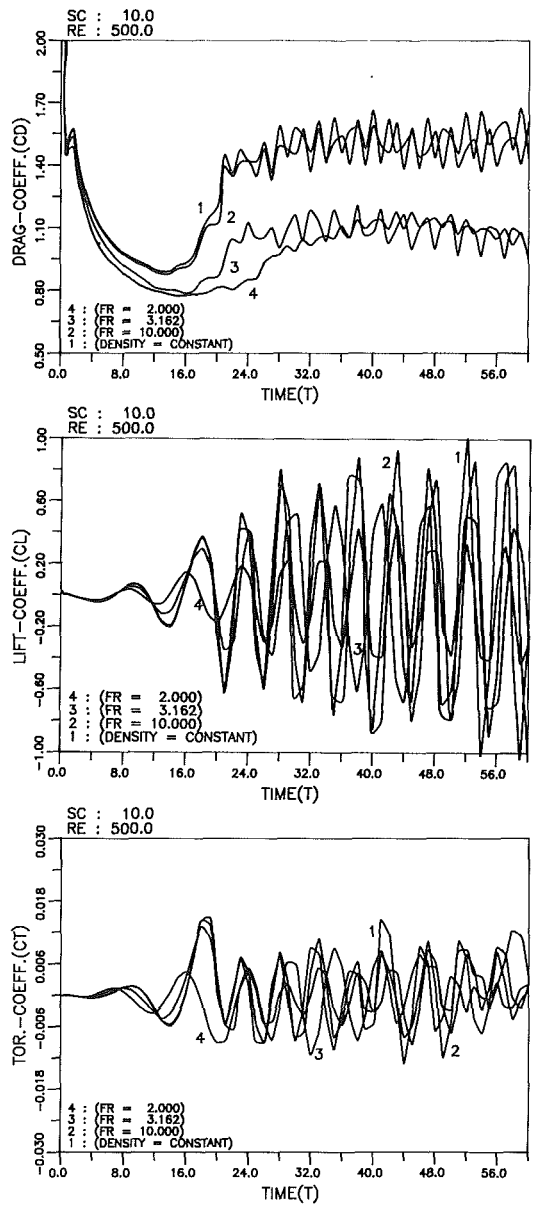

Fig. 17 Variation of the drag, lift, and torque coefficients with time for Re = 500

torque coefficients for different F at Re = 100. It shows that the oscillatory character of the drag, lift and torque is reduced with the increase of the density stratification.

Effects of Re on the flow pattern of vortex shedding are also investigated with the variation of ambient density stratification. In Figures 13–15 we show the flow pattern of vortex shedding in the case of Re = 200 for F = 10, 3.16, and 2 during a shedding cycle. An increase in the Reynolds number will have the effect of increasing the importance of the convection terms in relation to the viscous terms. It is observed that the downstream recirculatory flow region is getting smaller than that found with the case of Re = 100 and has a faster shedding frequency than that of Re = 100. This phenomenon is also found for the case of Re = 500 (not shown). Thus we can conclude that the higher the flow Reynolds number will have the smaller wake region but the faster votex shedding frequency.

The periodic variations of C_D, C_L, and C_T associated with the flow at Re = 200 and 500 for different values of F are shown in Figs. 16 and Fig. 17, respectively. The computed drag at first decreases and then increases with increasing stratification. Such a phenomenon has been observed by Davis (1969) in the case of flow about a thin obstacle towed through a stratified fluid and by Haussling (1977) in viscous flows of stably stratified fluids over barriers. The frequency of vortex shedding is also at first decreased and then increases with increasing the Strouchal number. Some results for the effect of density stratification on the shedding frequency, the averaged drag and the amplitude of the lift oscillatory for Re = 100, 200 and 500 are summarized in Table 2.

6 Conclusions

With the use of boundary-fitted coordinates the study of laminar viscous flow with density stratification past a circular cylinder was performed. In series of numerical computations for several density stratifications, some conclusions can be made:

(1) The density stratification tends to retard the vortex

Table 2 Effect of density stratification on mean drag, lift, and Strouhal number

Re = 100	F	C_D	C_L	S
	∞	1.29	±0.38	0.164
	10	1.24	±0.22	0.15
	3.16	1.0	±0.05	0.118
	2.0	1.15	0	Stationary
Re = 200	F	C_D	C_L	S
	∞	1.28	±0.6	0.182
	10	1.25	±0.75	0.178
	3.16	0.95	±0.5	0.158
	2.0	1.05	±0.05	0.17
Re = 500	F	C_D	C_L	S
	∞	1.25	±0.9	0.21
	10	1.22	±0.8	0.20
	3.16	1.10	±0.58	0.18
	2.0	1.15	±0.28	0.20

shedding from the two sides of the cylinder and to narrow down the wake development behind the cylinder.

(2) With increasing stratification the drag on the cylinder at first decreases and then increases.

(3) The amplitude of the periodic variation of the lift with time decreases with increasing the stratification while it increases with the increase of Reynolds number.

References

Collin, W. M., and Dennis, S. C. R., 1973, "Flow Past an Impulsively Circular Cylinder," *J. Fluid Mech.*, Vol. 60, pp. 105–126.

Davis, R. E., 1969, "The Two-Dimensional Flow of a Stratified Fluid Over an Obstacle," *J. Fluid Mech.*, Vol. 36, pp. 127–143.

Deffenbaugh, F. D., and Marshall, F. J., 1976, "Time Development of the Flow About an Impulsively Started Cylinder," *AIAA J.*, Vol. 14, No. 7, pp. 908–913.

Gresho, P. M., Lee, R. L., and Sani, R. L., 1980, "On the Time-Dependent Solution of the Incompressible Navier-Stokes Equations," *Recent Advances in Numerical Methods in Fluids*, ed. by C. Taylor, Pineridge Press, Swansea, U. K., pp. 27–80.

Haussling, H. J., 1977, "Viscous Flows of Stably Stratified Fluids over Barriers," *J. the Atmosphere Sc.*, Vol. 34, pp. 582–602.

Hwang, R. R., and Jang, S. W., 1982, "Viscous Flows of Stably Stratified Fluids over Semi-Circular Obstacles," *Proc. the National Science Council*, Vol. 6, No. 1, pp. 1–8.

Hwang, R. R., Chiang, T. P., and Chiao, M. T., 1986, "Time Dependent Incompressible Viscous Flow Past a Circular Cylinder," *J. the Chinese Institute of Engineers*, Vol. 9, No. 6, pp. 617–631.

Jordan, S. K., and Fromm, J. E., 1972, "Oscillatory Drag, Lift and Torque on a Circular Cylinder in a Uniform Flow," *Phys. Fluids*, Vol. 15, No. 3, pp. 371–376.

Lecointe, Y., and Piquet, J., 1984, "On the Use of Several Compat Methods for the Study of Unsteady Incompressible Viscous Flow Around a Circular Cylinder," *Conput. Fluids*, Vol. 12, pp. 255–280.

Lin, C. D., Pepper, D. W., and Lee, S. C., 1976, "Numerical Methods for Separated Flow Solutions Around a Circular Cylinder," *AIAA J.*, Vol. 14, pp. 900–907.

Loc, T. P., 1980, "Numerical Analysis of Unsteady Secondary Vortices Generated by an Impulsively Started Circular Cylinder," *J. Fluid Mech.*, Vol. 100, pp. 111–132.

Pao, Y. H., 1968, "Laminar Flow of a Stably Stratified Fluid Past a Flate," *J. Fluid Mech.*, Vol. 34, Part 4, pp. 795–808.

Patel, V. A., 1978, "Karman Vortex Street Behind a Circular Cylinder by the Series Truncation Method," *J. Comput. Phys.*, Vol. 28, pp. 14–42.

Patel, V. A., 1981, "Flow Around the Impulsively Started Elliptic Cylinder at Various Angles of Attack," *Comput. Fluid*, Vol. 9, pp. 435–446.

Smith, J. C., and Brebbia, C. A., 1977, "Improved Stability Techniques for the Solution of Navier-Stokes Equations," *Appl. Math. Modelling*, Vol. 1, pp. 227–234.

Thames, F. C., Thompson, J. F., and Mastin, C. W., 1977, "Numerical Solution for Viscous and Potential Flow About Arbitrary Two Dimensional Bodies Using Body-Fitted Coordinate System," *J. Comput. Physics*, Vol. 24, pp. 245–273.

Thoman, D., and Szewczyk, A., 1969, "Time Dependent Viscous Flow over a Circular Cylinder," *Phys. Fluid Suppl.*, Vol. II, pp. 78–86.

Thompson, J. F., Thames, F. C., and Mastin, C. W., 1976, "Solutions of the Navier-Stokes Equations in Various Flow Regimes Using Boundary-fitted Coordinate System," *Lecture Notes in Physics*, Vol. 59, pp. 421–450.

Wei, S. N., Kao, T. W., and Pao, H. P., 1975, "Experimental Study of Upstream Influence in the Two-dimensional Flow of a Stratified Fluid over an Obstacle," *Geogphysical Fluid Dynamics*, Vol. 6, pp. 315–336.

ERRATA

The paper entitled "The Structure of a Three-Dimensional Tip Vortex at High Reynolds Numbers" by D. R. Stinebring, K. J. Farrell, and M. L. Billet, ASME *Journal of Fluids Engineering*, September 1991, Vol. 113, pp. 496–503 contains a misprint. To be consistent with the text, the data in Figure 11 should be presented with Figure No. and caption 12 and vice versa.

Bounded Energy States in Homogeneous Turbulent Shear Flow—An Alternative View

P. S. Bernard
Department of Mechanical Engineering,
University of Maryland,
College Park, MD 20742

C. G. Speziale
Institute for Computer Applications in
Science and Engineering,
NASA Langley Research Center,
Hampton, VA 23665

The equilibrium structure of homogeneous turbulent shear flow is investigated from a theoretical standpoint. Existing turbulence models, in apparent agreement with physical and numerical experiments, predict an unbounded exponential time growth of the turbulent kinetic energy and dissipation rate; only the anisotropy tensor and turbulent time scale reach a structural equilibrium. It is shown that if a residual vortex stretching term is maintained in the dissipation rate transport equation, then there can exist equilibrium solutions, with bounded energy states, where the turbulence production is balanced by its dissipation. Illustrative calculations are presented for a $k-\epsilon$ model modified to account for net vortex stretching. The calculations indicate an initial exponential time growth of the turbulent kinetic energy and dissipation rate for elapsed times that are as large as those considered in any of the previously conducted physical or numerical experiments on homogeneous shear flow. However, vortex stretching eventually takes over and forces a production-equals-dissipation equilibrium with bounded energy states. The plausibility of this result is further supported by independent calculations of isotropic turbulence which show that when this vortex stretching effect is accounted for, a much more complete physical description of isotropic decay is obtained. It is thus argued that the inclusion of vortex stretching as an identifiable process may have greater significance in turbulence modeling than has previously been thought and that the generally accepted structural equilibrium for homogeneous shear flow, with unbounded energy growth, could be in need of re-examination.

1 Introduction

Homogeneous turbulent shear flow has been the subject of a variety of experimental, computational, and theoretical studies during the past four decades. The popularity of this flow lies in the fact that it accounts for an important physical effect—the alteration of the turbulence structure by shear—in a simplified setting unencumbered by such complications as rigid boundaries and mean turbulent diffusion. Von Karman (1937) first proposed the problem of homogeneous shear flow which gave rise to some mathematical studies during the 1950's (c.f. Townsend, 1956 and Hinze, 1975 for a review). It is a difficult flow to simulate experimentally and the first tangible suggestion for its generation was put forth by Corrsin (1963). The first successful experimental realization of homogeneous shear flow in the laboratory was achieved by Rose (1966) and was then followed by a series of landmark experiments by Champagne et al. (1970), Harris et al. (1977) and Tavoularis and Corrsin (1981). More recently, Tavoularis and Karnik (1989) and Rohr et al. (1988) performed more exhaustive measurements of homogeneous shear flow shedding new light on its basic structure.

With the dramatic increase in computer capacity achieved by the late 1970's, direct numerical simulations of homogeneous turbulent flows became possible. Rogallo (1981) was the first to conduct a direct simulation of homogeneous shear flow; the results that he obtained were well within the range of the experiments of Tavoularis and Corrsin (1981). Subsequently, Bardina et al. (1983) performed a coarse-grid large-eddy simulation of homogeneous shear flow and Rogers et al. (1986) conducted fine-grid $128 \times 128 \times 128$ direct simulations which further clarified its structure.

The early experiments of Rose (1966) and Champagne et al. (1970), which were conducted for relatively weak shear rates and small elapsed times, seemed to indicate that the Reynolds stresses—and, hence, the turbulent kinetic energy—asymptoted to equilibrium values. This asymptotic state is consistent with the production-equals-dissipation equilibrium that had been hypothesized by Townsend (1956) several years earlier. However, the integral length scales were still growing monotonically at the end of the Rose (1966) and Champagne et al. (1970) experiments suggesting the strong possibility that, an asymptotic state had not yet been reached. Subsequent physical experiments (Tavoularis and Corrsin, 1981; Tavoularis and Karnik, 1989; and Rohr et al., 1988) and direct numerical simulations (Rogallo, 1981; Bardina et al., 1983; and Rogers et al., 1986), conducted for stronger shear rates and larger elapsed times, confirmed this. These physical and numerical

Contributed by the Fluids Engineering Division for publication in the JOURNAL OF FLUIDS ENGINEERING. Manuscript received by the Fluids Engineering Division May 6, 1991.

experiments, along with alternative theoretical analyses (see Rogallo, 1981 and Tavoularis, 1985), have led to the following widely accepted physical picture of homogeneous shear flow:

(1) the turbulent kinetic energy k and dissipation rate ϵ grow exponentially in time at the same rate,

(2) the anisotropy tensor b_{ij} and the dimensionless turbulent time scale Sk/ϵ reach equilibrium values that are relatively independent of the initial conditions and the shear rate S.

It should be noted that Speziale and MacGiolla Mhuiris (1989) have recently shown that virtually all of the commonly used two-equation turbulence models and second-order closures are consistent with this hypothetical picture of homogeneous shear flow.

An alternative physical picture of homogeneous shear flow is presented in this paper which is consistent with the previously conducted physical and numerical experiments, yet at the same time excludes the occurrence of unbounded energy growth. In particular, it will be shown that when the effect of vortex stretching is maintained in the dissipation rate transport equation, a production-equals-dissipation equilibrium results in which the turbulent kinetic energy and dissipation rate eventually asymptote to bounded values. Illustrative calculations are presented for a $k-\epsilon$ model suitably modified to account for vortex stretching. Consistent with physical and numerical experiments, these calculations indicate an exponential time growth of the turbulent kinetic energy and dissipation rate for $St < 30$. This is the largest elapsed time considered in any of these previous experimental studies. However, for $St > 30$, vortex stretching eventually takes over causing the system to saturate and attain an equilibrium structure with bounded kinetic energy and dissipation. In the sections to follow, a detailed case is made to establish that this alternative equilibrium structure of homogeneous shear flow is a serious possibility that could have important implications for turbulence modeling at high Reynolds numbers.

2 Theoretical Background

We will consider the incompressible and isothermal turbulent flow of a viscous fluid. The governing field equations are the Navier-Stokes and continuity equations given by

$$\frac{\partial v_i}{\partial t}+v_j\frac{\partial v_i}{\partial x_j}=-\frac{\partial P}{\partial x_i}+\nu\nabla^2 v_i \tag{1}$$

$$\frac{\partial v_i}{\partial x_i}=0 \tag{2}$$

where v_i is the velocity vector, P is the modified pressure and ν is the kinematic viscosity of the fluid. As in the usual treatments of turbulence, the velocity and pressure will be decomposed into ensemble mean and fluctuating parts, respectively:

$$v_i=\overline{v_i}+u_i,\ P=\overline{P}+p. \tag{3}$$

For homogeneous shear flow, the mean velocity-gradient tensor takes the form

$$\frac{\partial \overline{v_i}}{\partial x_j}=\begin{pmatrix}0 & S & 0\\ 0 & 0 & 0\\ 0 & 0 & 0\end{pmatrix}. \tag{4}$$

In direct numerical simulations of homogeneous shear flow, an initially isotropic turbulence is subjected to the constant shear rate S and its time evolution is then computed. In laboratory experiments, an initially decaying isotropic turbulence, created downstream of a grid, is subjected to a uniform shear rate as it evolves spatially. The two problems are related, in an *approximate* sense, by the Galilean transformation

$$x=x_0+U_c t \tag{5}$$

where U_c is a characteristic mean velocity that is typically taken to be the centerline mean velocity of the uniform shear [hence, dimensionless time $St \equiv S(x-x_0)/U_c$]. For the remainder of this paper, we will only consider the temporally evolving version of homogeneous shear flow, since it is the only version of this problem that is *exactly* homogeneous.

In any homogeneous turbulent flow, the exact transport equations for the turbulence kinetic energy $k \equiv \frac{1}{2}\overline{u_i u_i}$ and dissipation rate $\epsilon \equiv \nu\overline{\frac{\partial u_i}{\partial x_j}\frac{\partial u_i}{\partial x_j}}$ take the form (Tennekes and Lumley, 1972)

$$\dot{k}=\mathcal{P}-\epsilon \tag{6}$$

$$\dot{\epsilon}=\mathcal{P}_{\epsilon_S}+\mathcal{P}_{\epsilon_V}-\Phi_\epsilon \tag{7}$$

where

$$\mathcal{P}=-\tau_{ij}\frac{\partial \overline{v_i}}{\partial x_j},\ \mathcal{P}_{\epsilon_S}=2\nu\,\overline{\omega_i\omega_j}\frac{\partial \overline{v_i}}{\partial x_j}, \tag{8}$$

$$\mathcal{P}_{\epsilon_V}=2\,\overline{\omega_i\omega_j\frac{\partial u_i}{\partial x_j}},\ \Phi_\epsilon=2\nu^2\,\overline{\frac{\partial\omega_i}{\partial x_j}\frac{\partial\omega_i}{\partial x_j}}, \tag{9}$$

are, respectively, the production of turbulent kinetic energy, the production of dissipation by mean strains, the production of dissipation by vortex stretching, and the destruction of dissipation. In (8)-(9), $\tau_{ij} \equiv \overline{u_i u_j}$ is the Reynolds stress tensor and $\omega \equiv \nabla \times \mathbf{u}$ is the fluctuating vorticity vector. At this stage, we introduce the anisotropy tensor b_{ij} defined as

$$b_{ij}=\frac{\left(\tau_{ij}-\frac{2}{3}k\delta_{ij}\right)}{2k} \tag{10}$$

which will be useful in the analysis to follow.

If we non-dimensionalize the turbulent kinetic energy, dissipation rate, and time as follows:

$$k^*\equiv\frac{k}{k_0},\ \epsilon^*\equiv\frac{\epsilon}{\epsilon_0},\ t^*\equiv St,$$

where k_0 and ϵ_0 denote initial values, then the exact transport Eq. (6) for k can be rewritten in the dimensionless form

$$\dot{k}^*=2\left(\frac{\epsilon}{\mathcal{P}}-1\right)b_{12}k^* \tag{11}$$

since $\mathcal{P}=-\tau_{12}S$ in homogeneous shear flow. It should be noted that the ratio of production to dissipation $\mathcal{P}/\epsilon$ can be related to b_{12} through the identity

$$\frac{\mathcal{P}}{\epsilon}=-2b_{12}\frac{Sk}{\epsilon}. \tag{12}$$

Consequently, if any two of the quantities $\mathcal{P}/\epsilon$, b_{12} and Sk/ϵ are known, the remaining one can be computed using (12). Furthermore, since for homogeneous shear flow $\mathcal{P}/\epsilon > 0$ and $Sk/\epsilon > 0$, it follows from (12) that $b_{12} < 0$. Physical and numerical experiments have tended to indicate that b_{12} and Sk/ϵ reach equilibrium values that are relatively independent of the initial conditions. More specifically, these experiments suggest the results

$$\left(\frac{Sk}{\epsilon}\right)_\infty\approx 6.0,\ (b_{12})_\infty\approx -0.15,\ \left(\frac{\mathcal{P}}{\epsilon}\right)_\infty\approx 1.8 \tag{13}$$

where $(\cdot)_\infty$ is the equilibrium value obtained in the limit as $t\to\infty$. From (11) and (13) it follows that for $t^* \gg 1$,

$$k^*\sim\exp(\lambda t^*) \tag{14}$$

where the growth rate λ is given by

$$\lambda=2\left[\left(\frac{\epsilon}{\mathcal{P}}\right)_\infty-1\right](b_{12})_\infty\approx 0.13. \tag{15}$$

Equations (13) and (14) then imply that for $t^* \gg 1$

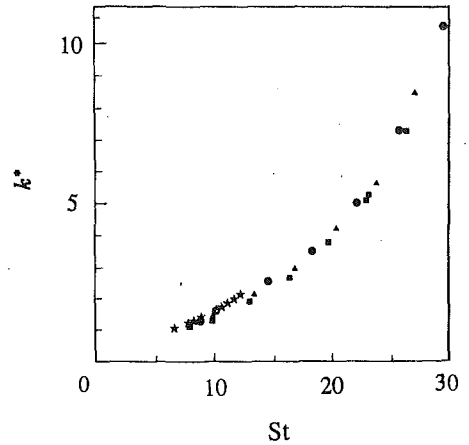

Fig. 1 Experimental data on homogeneous shear flow measured by Tavoularis and Corrsin (1981) and Tavoularis and Karnik (1989) (as compiled by Rohr et al. (1988)).

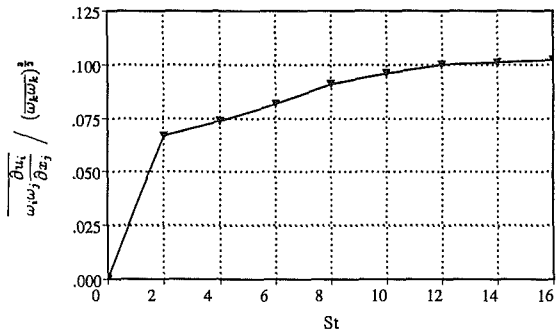

Fig. 2 Time evolution of the normalized vortex stretching in homogeneous shear flow obtained from the direct numerical simulation (case C128U) of Rogers (1990).

$$\epsilon^* \sim \exp(\lambda t^*) \tag{16}$$

since, if k grows exponentially and Sk/ϵ equilibrates, then ϵ must grow exponentially at the same rate. This constitutes an alternate derivation of the Tavoularis (1985) asymptotic law of exponential growth in shear flow. The wealth of experimental data on homogeneous shear flow collected over the past two decades appears to be in agreement with this hypothetical physical picture. This is evidenced by Fig. 1 containing several sets of measured k data versus nondimensional time that was recently compiled by Rohr et al. (1988).

The occurrence of this structural equilibrium at large times—with an unbounded exponential time growth of k and ϵ—has a number of implications for the higher-order correlations in the dissipation rate transport Eq. (7) which will now be examined. When non-dimensionalized, (7) takes the form

$$\dot{\epsilon}^* = \left(\frac{2\overline{\omega_1\omega_2}}{\overline{\omega_k\omega_k}} + \frac{\overline{2\omega_i\omega_j \frac{\partial u_i}{\partial x_j}}}{(\overline{\omega_k\omega_k})^{3/2}} \frac{\epsilon}{Sk} \sqrt{R_t} - \frac{2\nu}{S} \frac{\overline{\frac{\partial\omega_i}{\partial x_j}\frac{\partial\omega_i}{\partial x_j}}}{\overline{\omega_k\omega_k}} \right) \epsilon^* \tag{17}$$

where $R_t \equiv k^2/\nu\epsilon$ is the turbulence Reynolds number. In deriving (17), use has been made of the fact that $\epsilon \equiv \nu\overline{\omega_i\omega_i}$ since the turbulence is homogeneous. According to the Schwarz inequality, the first of the three correlations

$$\frac{\overline{\omega_1\omega_2}}{\overline{\omega_k\omega_k}}, \quad \frac{\overline{\omega_i\omega_j \frac{\partial u_i}{\partial x_j}}}{(\overline{\omega_k\omega_k})^{3/2}}, \quad \frac{2\nu \overline{\frac{\partial\omega_i}{\partial x_j}\frac{\partial\omega_i}{\partial x_j}}}{S\,\overline{\omega_k\omega_k}}$$

appearing in (17) will be bounded for all time. In addition, direct numerical simulations of Rogers (1990) for homogeneous shear flow, as shown in Fig. 2, indicate that the second of these correlations (which is proportional to the velocity derivative skewness S_K in an isotropic turbulence) asymptotes fairly quickly to an apparent equilibrium value of 0.1. Hence, assuming the equilibration of ϵ/Sk, it follows that in order to recover the exponential growth law (16) for $t^* \gg 1$, we must have the third of these correlations behave as

$$\frac{\nu}{S} \frac{\overline{\frac{\partial\omega_i}{\partial x_j}\frac{\partial\omega_i}{\partial x_j}}}{\overline{\omega_k\omega_k}} = C_\omega \sqrt{R_t} + O(1), \tag{18}$$

where the coefficient C_ω must assume the precise value

$$C_\omega = \left(\frac{\omega_i\omega_j \frac{\partial u_i}{\partial x_j}}{(\omega_k\omega_k)^{3/2}} \right)_\infty \left(\frac{\epsilon}{Sk} \right)_\infty . \tag{19}$$

The general R_t dependence indicated by (18) is consistent with traditionally accepted Kolmogorov scaling laws for the case of homogeneous turbulence. However, the validity of (19) in homogeneous shear flow is debatable. Direct numerical simulations of homogeneous shear flow by Rogers (1990) are not conclusive concerning the validity of (18) or (19). Furthermore, it may be argued that it is unlikely that the effect of vortex stretching would be *exactly* counterbalanced by the leading order part of a viscous term in an unstable high Reynolds number turbulent flow with an exponentially growing turbulent kinetic energy; one might expect vortex stretching to play an independent role in such a shear instability. The ultimate equilibrium state that a homogeneous turbulent flow achieves is determined by how the fundamental imbalance between vortex stretching and the mean production and viscous destruction terms is resolved (this imbalance arises since only the vortex stretching term depends *explicitly* on R_t). Consequently, to externally impose a balance, such as that implied by (18) and (19)–rather than to allow the balance to arise naturally from the equations of motion - runs the risk of yielding spurious equilibrium states. For the case of isotropic turbulence discussed later, it will be shown that at high turbulence Reynolds numbers an imbalance between vortex stretching and viscous dissipation drives the flow toward a $k \sim t^{-1}$ power law decay. If vortex stretching is neglected, however, this physical feature is lost and the exponent of the power law decay becomes completely arbitrary.

An examination of (17) suggests that there are two alternative equilibrium states for homogeneous shear flow apart from (13)–(14). These are:

(1) an alternative structural equilibrium where $(\epsilon/Sk)_\infty = 0$, or

(2) a production-equals-dissipation equilibrium with bounded energy states (i.e., with $k_\infty < \infty$ and $\epsilon_\infty < \infty$).

The first of these cases has been shown by Speziale and MacGiolla Mhuiris (1989) to be primarily associated with solutions for k and ϵ that undergo an algebraic growth with time (i.e., for $St \gg 1$, $k \sim t^\alpha$, $\epsilon \sim t^\beta$ where $\alpha > \beta$). Such solutions, however, are largely unstable within the context of Reynolds stress transport models (Speziale and MacGiolla Mhuiris, 1989). Furthermore, at the end of all of the previously conducted physical and numerical experiments on homogeneous shear flow, ϵ/Sk either appeared to equilibrate to a non-zero value or continued to grow - results that are not suggestive of an equilibrium state where $(\epsilon/Sk)_\infty = 0$. Hence, we conclude that this alternative equilibrium structure is not a strong possibility.

The second possibility—namely, the production-equals-dis-

sipation equilibrium— superficially appears to contradict the physical and numerical experiments indicating that the turbulent kinetic energy and dissipation rate are still growing exponentially at the end of the experiments (i.e., for elapsed times St as large as 28). However, a production-equals-dissipation equilibrium wherein

$$\mathcal{P}_{\infty} = \epsilon_{\infty} \tag{20}$$

$$\Phi_{\epsilon_{\infty}} = \mathcal{P}_{\epsilon_{S\infty}} + \mathcal{P}_{\epsilon_{V\infty}} \tag{21}$$

(with bounded values for k_{∞}, ϵ_{∞}, and $R_{t\infty}$) is not inconsistent with either the ensemble averaged or mean spectral form of the Navier-Stokes equations (Hinze, 1975). In the following sections, it will be shown that the inclusion of vortex stretching effects in the dissipation rate transport equation leads to the occurrence of this production-equals-dissipation equilibrium (with an early exponential time growth of k and ϵ for $St <$ 30). Furthermore, when such effects are included in the description of isotropic turbulence, a more complete physical description results.

3 The Dissipation Rate Transport Equation With Vortex Stretching

Batchelor and Townsend (1947) have shown that the transient behavior of the enstrophy $\omega^2 \equiv \overline{\omega_i \omega_i}$ in isotropic turbulence is governed by the equation

$$\frac{d\omega^2}{dt} = \frac{7}{3\sqrt{15}}\,\omega^3\,S_K - \frac{14}{3\sqrt{15}}\,\omega^3\,\frac{G}{R_\lambda} \tag{22}$$

where

$$S_K = -\frac{\overline{\left(\frac{\partial u}{\partial x}\right)^3}}{\left[\overline{\left(\frac{\partial u}{\partial x}\right)^2}\right]^{\frac{3}{2}}} \tag{23}$$

is the skewness of the probability density function of $\dfrac{\partial u}{\partial x}$ defined with a negative sign to make it a positive quantity. In (22), $R_\lambda \equiv u_{\rm rms}\,\lambda/\nu$ is the turbulence Reynolds number based on the Taylor microscale and G is a function defined by

$$G \equiv \lambda^4 f_o^{iv}. \tag{24}$$

Here, $u_{\rm rms}$ is the root-mean-square of a velocity fluctuation component u, λ is the Taylor microscale derived from the two point longitudinal velocity correlation function $f(r)$, and f_o^{iv} is the fourth derivative of $f(r)$ evaluated at $r = 0$. The first term on the right-hand side of (22) accounts for the effect of vortex stretching and is positive definite while the second term is always negative and leads to the destruction of enstrophy.

Equation (22) may be converted into a transport equation for ϵ through use of the identity

$$\epsilon = \nu\omega^2, \tag{25}$$

which is valid for any homogeneous turbulence. Since the defining equation for the microscale may be conveniently written as

$$\omega^2 = \frac{10k}{\lambda^2}, \tag{26}$$

it follows that (22) can be converted to the equation

$$\dot{\epsilon} = \frac{7}{3\sqrt{15}}\,\frac{S_K}{\sqrt{\nu}}\,\epsilon^{3/2} - \frac{7}{15}\,G\,\frac{\epsilon^2}{k}. \tag{27}$$

Once values are obtained for S_K and G, (27) may be solved together with the kinetic energy equation

$$k = -\epsilon \tag{28}$$

yielding a solution for isotropic decay.

Batchelor and Townsend (1947) showed that if G has the form

$$G = \frac{30}{7} + \frac{1}{2}\,R_\lambda S_K, \tag{29}$$

then the solution of (27)–(28) is compatible with their experimental data indicating a power law decay of the kinetic energy, with an exponent of approximately one, for the case of moderately large values of R_λ. More precisely, the substitution of (29) into (27) yields the equation

$$\dot{\epsilon} = -2\frac{\epsilon^2}{k}, \tag{30}$$

which, when combined with (28), gives rise to the exact solution

$$k = k_0\left(1 + \frac{\epsilon_0 t}{k_0}\right)^{-1}$$

for isotropic decay (i.e., a power law decay where $k \sim t^{-1}$). Apart from the specific value of the numerical coefficient on the right-hand side of (30), which is more commonly set to a value ranging from 1.83-1.92 to reflect more recent decay data (Comte-Bellot and Corrsin, 1971) suggesting that $k \sim t^{-1.1}$ or $k \sim t^{-1.2}$, the form of (30) has served as a cornerstone for the standard modeled ϵ transport equation that is widely used in turbulence models.

In view of the identity $R_\lambda = \sqrt{20/3}\,R_t^{1/2}$, it is easily established that (29) is formally equivalent to the relation (18) introduced earlier in the case of homogeneous shear flow. As before, the choice of G given by (29) forces the vortex stretching term in (27) to be exactly subsumed by the action of the destruction of enstrophy term. While this step, as has been noted above, guarantees compatibility with isotropic decay data, it is also tantamount to imposing an equilbrium state on the flow rather than letting the equations of motion dictate the nature of the equilibrium. In this regard, it may be noted than (29) effectively excludes from consideration a family of exact self-similar solutions for isotropic decay depending explicitly on the distinction between vortex stretching and dissipation (see Sedov, 1944 and Bernard, 1985).

Another example of the breakdown of Eq. (29) arises in the limit of zero viscosity where the destruction of enstrophy term vanishes while the vortex stretching term does not. In fact, the survival of the vortex stretching term in the limit of zero viscosity is crucial for the prediction of enstrophy blow-up—a widely accepted property of solutions of the Euler equation (see Lesieur, 1990). This can be seen by setting ν equal to zero in (22) which yields the equation

$$\frac{d\omega^2}{dt} = \frac{7}{3\sqrt{15}}\,\omega^3\,S_K^{(0)} \tag{31}$$

where $S_K^{(0)}$ is the zero-viscosity skewness. For constant $S_K^{(0)} > 0$, (31) predicts that the enstrophy blows up at the critical time.

$$t_c = \frac{6\sqrt{15}}{7\omega_0}\,\frac{1}{S_K^{(0)}}$$

where ω_0^2 is the initial enstrophy. Although the Eddy-Damped Quasi-Normal Markovian (EDQNM) model supports this result, a finite-time enstrophy blow-up has not been seen in direct numerical simulations of the Euler equation (see Lesieur, 1990 and Pumir and Siggia, 1990). This means that either $S_K^{(0)}$ is a very small constant or a monotonically decreasing function of time (in the former case the enstrophy would blow-up at $t_c \gg \omega_0^{-1}$ whereas in the latter case it would just grow monotonically without bound as $t \to \infty$). While this issue has not been fully resolved, one thing is clear: $S_K^{(0)}$ is *not* identically zero. If $S_K^{(0)} = 0$, then (31) yields the erroneous prediction

$$\omega^2 = \text{constant}$$

which is not supported by direct numerical simulations or theoretical analyses of the Euler equation (these indicate that the enstrophy grows dramatically due to vortex stretching). The standard modeled dissipation rate Eq. (30) reduces to

$$\frac{d\omega^2}{dt} = 0$$

in the limit of zero viscosity and, hence, incorrectly predicts (in agreement with the $S_K^{(0)} = 0$ case) that the enstrophy is conserved.

We will now present an alternative model for the destruction of enstrophy term which maintains the effect of vortex stretching. The consequence of this model for both isotropic decay and homogeneous shear flow will be considered in turn. Consistent with the classical Kolmogorov scaling laws embodied in (18), we will set

$$\tau_0 \frac{2\nu \overline{\frac{\partial \omega_i}{\partial x_j}\frac{\partial \omega_i}{\partial x_j}}}{\overline{\omega_k \omega_k}} = C_{\omega_1}\sqrt{R_l} + C_{\omega_2} \tag{32}$$

where $\tau_0 \equiv k/\epsilon$ is the turbulent time scale and C_{ω_1} and C_{ω_2} are dimensionless constants. Since,

$$\frac{2\nu \overline{\frac{\partial \omega_i}{\partial x_j}\frac{\partial \omega_i}{\partial x_j}}}{\overline{\omega_k \omega_k}} = \frac{7}{15} G \frac{\epsilon}{k} \tag{33}$$

it follows that (32) is equivalent to the Batchelor and Townsend result (29) if $C_{\omega_1} = 7\, S_K/3\sqrt{15}$ and $C_{\omega_2} = 2$. The choice of $C_{\omega_1} = 7\, S_K/3\sqrt{15}$ represents the external imposition of an equilibrium structure on the turbulence where there is no net vortex stretching. In contrast to this approach, we will allow for small departures from equilibrium for which

$$C_{\omega_1} = \frac{7}{3\sqrt{15}} S_K - \eta_1 \tag{34}$$

where η_1 is a small parameter. In addition, we will consider small departures from the $O(1)$ term in the Batchelor and Townsend (1947) Eq. (29) by taking

$$C_{\omega_2} = 2 - \eta_2 \tag{35}$$

where η_2 is also a small parameter. Equation (29) is recovered in the limit as η_1 and η_2 go to zero. A direct substitution of (32) - (35) into (27) yields the modeled transport equation

$$\dot{\epsilon} = \frac{7}{3\sqrt{15}} \frac{C_{\epsilon_3}}{\sqrt{\nu}} \epsilon^{3/2} - C_{\epsilon_2} \frac{\epsilon^2}{k} \tag{36}$$

where $C_{\epsilon_3} = 3\sqrt{15}\eta_1/7$ and $C_{\epsilon_2} = 2 - \eta_2$. The coefficient C_{ϵ_3} is related to the zero viscosity skewness by

$$\lim_{\nu \to 0} C_{\epsilon_3} = S_K^{(0)} \tag{37}$$

and therefore (36), unlike the Batchelor and Townsend formula (30), can accommodate the limit of zero viscosity. Equation (36) is of the same general mathematical form as the ϵ-transport equation for self-preserving isotropic turbulence (see Speziale and Bernard, 1991). Thus there is a direct relation between the vortex stretching models proposed herein and the theory of self-preservation.

It will now be demonstrated that (36) gives a much more complete picture of isotropic turbulence than does the more commonly used ϵ-transport equation obtained in the limit as $C_{\epsilon_3} \to 0$. We will consider a small imbalance in the vortex stretching of the order of 1 percent, i.e., we will set $C_{\epsilon_3} =$ 0.01. Consistent with the commonly used modeled ϵ-transport equation we set $C_{\epsilon_2} = 1.90$. For initial turbulence Reynolds numbers that are not extremely large, (36) has solutions that are almost identical to the standard model. This is illustrated in Figs. 3(*a*)-(*b*) showing the time evolution of the turbulent kinetic energy $k^* = k/k_0$ and turbulent dissipation rate $\epsilon^* = \epsilon/\epsilon_0$ for an initial turbulence Reynolds number $R_{t_0} = 300$. The differences between the new model and the standard model are negligible; both indicate a power law decay where $k \sim t^{-1.1}$.

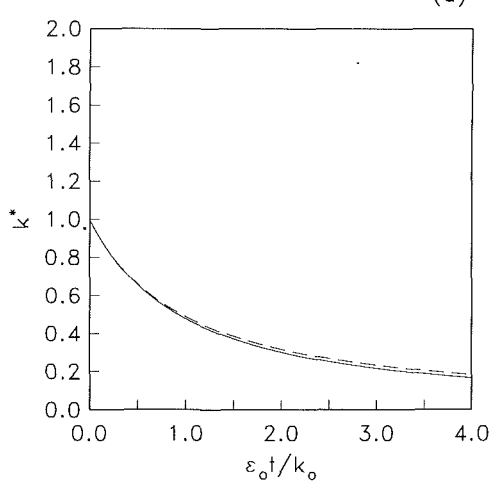

Fig. 3(*a*)

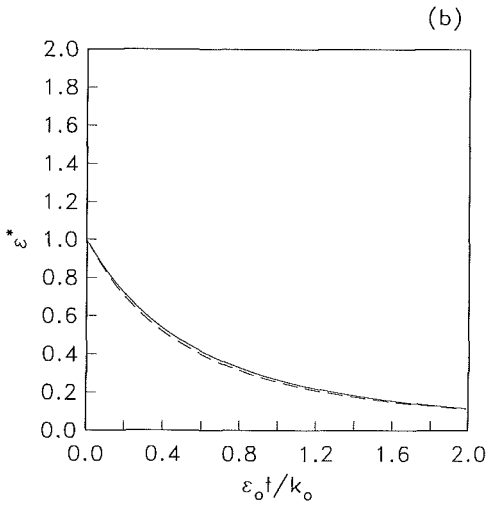

Fig. 3(*b*)

Fig. 3 Comparison of solutions for isotropic decay: ——— $k-\epsilon$ model with vortex stretching; --- standard $k-\epsilon$ model. (*a*) Time evolution of the turbulent kinetic energy for $R_{t_0} = 300$, and (*b*) time evolution of the turbulent dissipation rate for $R_{t_0} = 300$.

The importance of including the vortex stretching term becomes evident in the case of extremely large values of R_{t_0} where there is a substantial difference between the two models. In Figs. 4(*a*)-(*b*) the early time evolution of the turbulent kinetic energy and dissipation rate are shown for an initial turbulence Reynolds number $R_{t_0} = 10^6$. Unlike the standard model, the new model (36) with vortex stretching predicts a dramatic rise in the dissipation rate (and hence the enstrophy) and a precipitous drop in the turbulent kinetic energy that is highly reminiscent of the prelude to enstrophy blow-up predicted by the EDQNM model. This point is made particularly clear by Fig. 4(*c*) showing the time evolution of the enstrophy for a range of increasing values of R_{t_0}. This result bears a strong resemblance to Fig. V1-4 given by Lesieur (1990).

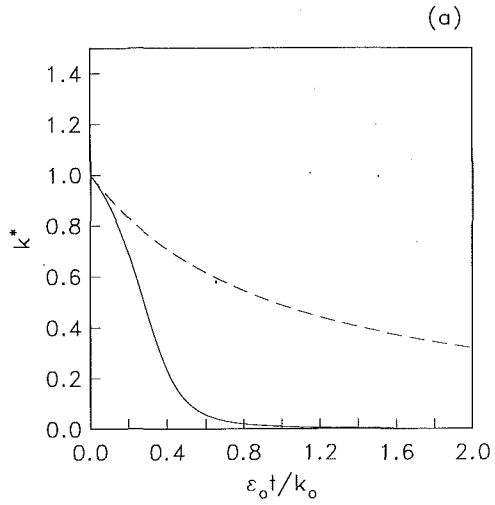

Fig. 4(*a*)

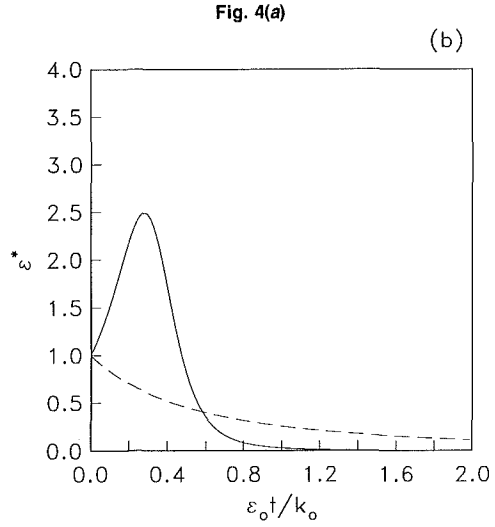

Fig. 4(*b*)

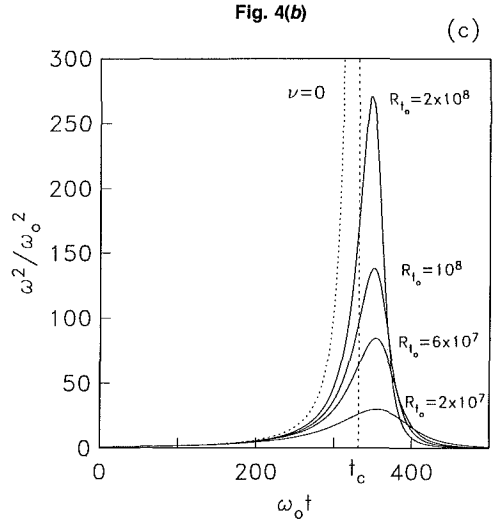

Fig. 4(*c*)

Fig. 4 Comparison of solutions for isotropic decay: ——— $k-\epsilon$ model with vortex stretching; --- standard $k-\epsilon$ model. (*a*) Time evolution of the turbulent kinetic energy for $R_{t_o} = 10^6$, (*b*) time evolution of the turbulent dissipation rate for $R_{t_o} = 10^6$, and (*c*) time evolution of the enstrophy for a variety of R_{t_o}.

The long time behavior of the solution for $R_{t_0} = 10^6$ is shown in Fig. 5. It is seen that after sufficiently large elapsed times (approximately 5–10 eddy turnover times), the turbulence begins to approach a power law decay where $k \sim t^{-1.1}$. The duration of the early time transient, for a given initial turbulence Reynolds number $R_{t_0} \gg 1$, can be shown to become smaller with increasing values of C_{ϵ_2}. For $C_{\epsilon_2} > 2$, it is a simple matter to show that equation (36) has the simple fixed point

$$R_{t\infty} = \left(\frac{C_{\epsilon_2} - 2}{\frac{7}{3\sqrt{15}} C_{\epsilon_3}} \right)^2 . \tag{38}$$

This solution can be shown to correspond to a t^{-1} power law decay for the turbulent kinetic energy. Calculations are shown in Fig. 6 pertaining to three different values of $C_{\epsilon_2} > 2$ ($C_{\epsilon_2} = 3$, 5 and 7) for an initial turbulence Reynolds number $R_{t_0} = 10^7$. It is clear that after an initial transient, the flow rapidly approaches an asymptotic solution where $k \sim t^{-1}$. This means that, in fact, the equilibrium exponent of the decay law can never be less than one, since for $C_{\epsilon_2} < 2$, the asymptotic solution is of the form $k \sim t^{-1/(C_{\epsilon_2}-1)}$. Furthermore, these results establish that for an isotropic turbulence to be close to equilibrium when R_{t_0} is extremely large, we must have $C_{\epsilon_2} > 2$, otherwise the initial transient will be of a duration longer than an eddy turnover time (i.e., the flow will be significantly far from equilibrium).

For small R_t it is well known that the turbulent kinetic energy undergoes a power law decay with an exponent substantially

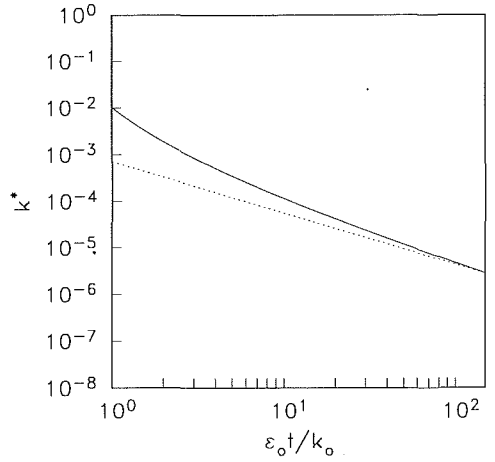

Fig. 5 Long time evolution of the turbulent kinetic energy in isotropic turbulence for $R_{t_o} = 10^6$. ——— $k-\epsilon$ model with vortex stretching ($C_{\epsilon_2} = 1.90$, $C_{\epsilon_3} = 0.01$); --- $k \sim t^{-1.1}$.

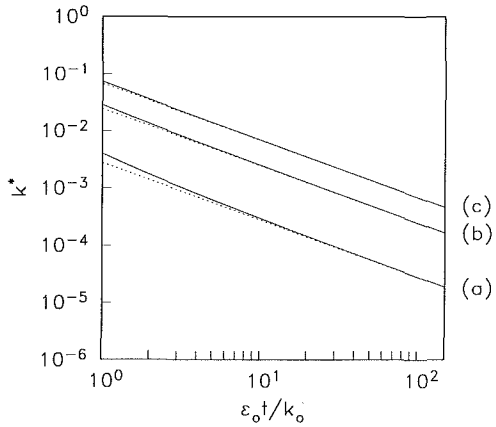

Fig. 6 Long time evolution of the turbulent kinetic energy in isotropic turbulence predicted by the $k-\epsilon$ model with vortex stretching for $R_{t_0} = 10^7$. (*a*) $C_{\epsilon_2} = 3$, (*b*) $C_{\epsilon_2} = 5$, and (*c*) $C_{\epsilon_2} = 7$. (——— model; --- $k \sim t^{-1}$).

greater than 1 – a condition that can be achieved by choosing $C_{\epsilon_2} < 2$. The implication is that C_{ϵ_2} is, in general, a function of the turbulence Reynolds number – a fact which has long been known to be the case. In summary, it may be stated that the ϵ-transport Eq. (36) with vortex stretching predicts the following physical picture of isotropic turbulence (see Speziale and Bernard, 1991):

(*a*) A power law decay where $k \sim t^{-\beta}$ (with $\beta \equiv 1/(C_{\epsilon_2} - 1) > 1$) for intermediate to low turbulence Reynolds numbers,

(*b*) for extremely high turbulence Reynolds numbers, an initial transient where there is a tendency toward enstrophy blow-up followed by a $k \sim t^{-1}$ power law decay, and

(*c*) a finite-time enstrophy blow-up in the limit of zero viscosity.

This is a much more complete physical description of isotropic turbulence than that obtained from the commonly used ϵ-transport model without vortex stetching which, for all initial conditions, predicts a power law decay where $k \sim t^{-1/(C_{\epsilon_2}-1)}$.

As far as anisotropic homogeneous turbulent flows are concerned, (36) can be generalized to the form

$$\dot{\epsilon} = \mathcal{P}_{\epsilon_S} + \frac{7}{3\sqrt{15}} \frac{C_{\epsilon_3}}{\sqrt{\nu}} \epsilon^{\frac{3}{2}} - C_{\epsilon_2} \frac{\epsilon^2}{k}, \tag{39}$$

where $\mathcal{P}_{\epsilon_S}$ is the production of dissipation by mean strains given by (8). In order to achieve closure, a model for $\mathcal{P}_{\epsilon_S}$ is needed. For simple homogeneously strained turbulent flows, it can be assumed that

$$\mathcal{P}_{\epsilon_S} \propto \mathcal{P} \tag{40}$$

which, after invoking elementary dimensional analysis, yields the model

$$\dot{\epsilon} = C_{\epsilon_1} \frac{\epsilon}{k} \mathcal{P} + \frac{7}{3\sqrt{15}} \frac{C_{\epsilon_3}}{\sqrt{\nu}} \epsilon^{3/2} - C_{\epsilon_2} \frac{\epsilon^2}{k}, \tag{41}$$

where C_{ϵ_1} is a dimensionless constant. The model for $\mathcal{P}_{\epsilon_S}$ in (40) has been used in the $k-\epsilon$ model of turbulence as well as in more complex second-order closures. Its success is largely tied to the fact that it constitutes a good approximation for plane shear flows (see Rogers et al., 1986 and Speziale and MacGiolla Mhuiris, 1989) – the type of flow being considered in this study. For practical calculations, C_{ϵ_1} can be taken to be 1.45 (a value obtained from equilibrium shear flows). In the next section, we will apply this model to homogeneous shear flow with $C_{\epsilon_1} = 1.45$, $C_{\epsilon_2} = 1.90$ and $C_{\epsilon_3} = 0.01$.

4 Illustrative Calculations for Homogeneous Shear Flow

In order to illustrate the effect of vortex stretching on homogeneous shear flow, we will present the results of calculations with a $k-\epsilon$ model for which the Reynolds stress tensor is modeled by

$$\tau_{ij} = \frac{2}{3} k \, \delta_{ij} - C_\mu \frac{k^2}{\epsilon} \left(\frac{\partial \overline{v}_i}{\partial x_j} + \frac{\partial \overline{v}_j}{\partial x_i} \right), \tag{42}$$

where $C_\mu = 0.09$ is a dimensionless constant. While the $k-\epsilon$ model is somewhat simplistic since it is based on an eddy viscosity, it was recently shown by Speziale and MacGiolla Mhuiris (1989) that this model is topologically equivalent to the more complex second-order closure models for homogeneous shear flow (the deficiencies in the $k-\epsilon$ model only become pronounced when there are combinations of shear and rotation or multi-dimensional strains). Hence, (42) will suffice to illustrate the qualitative changes induced when the effect of vortex stretching on the dissipation rate is accounted for. Equation (42) will be solved in conjunction with Eqs. (6) and (41). The standard $k-\epsilon$ model is recovered in the limit as $C_{\epsilon_3} \to 0$.

For homogeneous shear flow, the $k-\epsilon$ model with vortex stretching yields the transport equations

$$\dot{k} = C_\mu \frac{k^2}{\epsilon} S^2 - \epsilon \tag{43}$$

and

$$\dot{\epsilon} = C_{\epsilon_1} C_\mu k S^2 + \frac{7}{3\sqrt{15}} \frac{C_{\epsilon_3}}{\sqrt{\nu}} \epsilon^{\frac{3}{2}} - C_{\epsilon_2} \frac{\epsilon^2}{k} \tag{44}$$

which are obtained by substituting (4) into (6), (41) and (42).

For all nonzero values of C_{ϵ_3} it is a simple matter to show that the solution to (43) and (44) converges to an equilibrium state, with bounded energies. The equilibrium values may be found by setting the right-hand sides of (43)–(44) to zero, yielding the results

$$\frac{k_\infty}{k_0} = \frac{135}{49} \frac{\sqrt{C_\mu} (C_{\epsilon_2} - C_{\epsilon_1})^2}{C_{\epsilon_3}^2 R_{t_0}} \frac{S k_0}{\epsilon_0} \tag{45}$$

and

$$\frac{\epsilon_\infty}{\epsilon_0} = \frac{135}{49} \frac{C_\mu (C_{\epsilon_2} - C_{\epsilon_1})^2}{C_{\epsilon_3}^2 R_{t_0}} \left(\frac{S k_0}{\epsilon_0} \right)^2. \tag{46}$$

These relations clearly indicate that k_∞/k_0 and $\epsilon_\infty/\epsilon_0$ have a $C_{\epsilon_3}^{-2}$ dependence so that the standard $k-\epsilon$ model prediction of an unbounded growth of k and ϵ is easily recovered in the limit as $C_{\epsilon_3} \to 0$.

Using (45) and (46) the following additional equilibrium values are also obtained for this $k-\epsilon$ model with vortex stretching:

$$\left(\frac{Sk}{\epsilon} \right)_\infty = \frac{1}{\sqrt{C_\mu}}, \tag{47}$$

$$\left(\frac{-\overline{uv}}{k} \right)_\infty = \sqrt{C_\mu} \tag{48}$$

and

$$R_{t_\infty} = \frac{135}{49} \frac{(C_{\epsilon_2} - C_{\epsilon_1})^2}{C_{\epsilon 3}^2}. \tag{49}$$

These results differ from the values of $(Sk/\epsilon)_\infty = \sqrt{\alpha/C_\mu}$, $(-\overline{uv}/k)_\infty = \sqrt{\alpha C_\mu}$, and $R_{t_\infty} = \infty$ obtained from the standard $k-\epsilon$ model where $\alpha \equiv (C_{\epsilon_2} - 1)/(C_{\epsilon_1} - 1) \approx 2$. Consistent with the conventional view of homogeneous shear flow, Sk/ϵ and $-\overline{uv}/k$ achieve equilibrium values that are independent of the initial conditions. The mechanism by which the presence of the vortex stretching term has the effect of creating bounded long time solutions lies in its enhancement of the growth rate of ϵ. Evidently, this increase in the growth rate of ϵ is accompanied by a simultaneous reduction in the production of k, thus forcing a production-equals-dissipation equilibrium. In alternative terms, vortex stretching—which becomes more pronounced at high turbulence Reynolds numbers since it scales as $\sqrt{R_t}$—eventually causes homogeneous shear flow to undergo a saturation to an equilibrium state with bounded component energies (the values of which are set by the shear rate, the viscosity and the initial conditions).

We will now show that the $k-\epsilon$ model with vortex stretching yields temporal evolutions of the turbulence fields for $St < 30$ that are in good qualitative agreement with previously conducted physical and numerical experiments. When nondimensionalized, (43)–(44) take the form

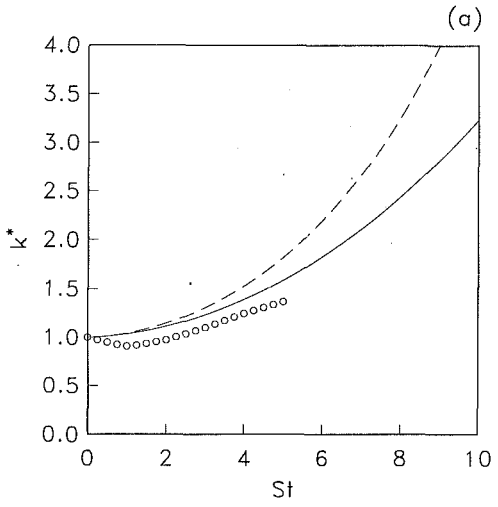

Fig. 7(*a*)

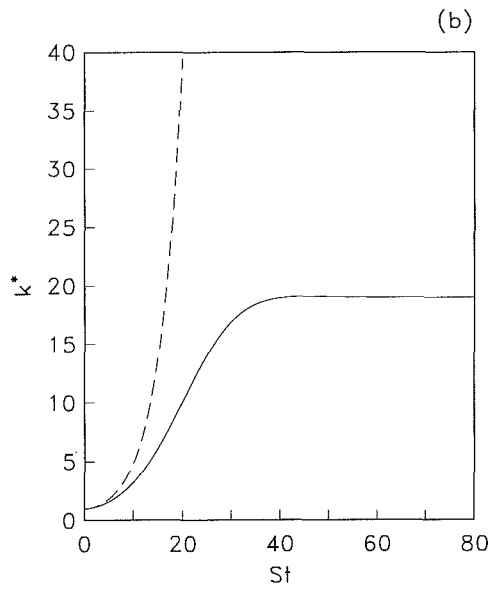

Fig. 7(*b*)

Fig. 7 Comparison of the model predictions with the large-eddy simulations of Bardina, et al. (1983) for homogeneous shear flow: o k^* from large eddy simulation; ——— k^* obtained from $k-\epsilon$ model with vortex stretching; --- k^* obtained from the standard $k-\epsilon$ model. (*a*) Short time solution, and (*b*) long time solution.

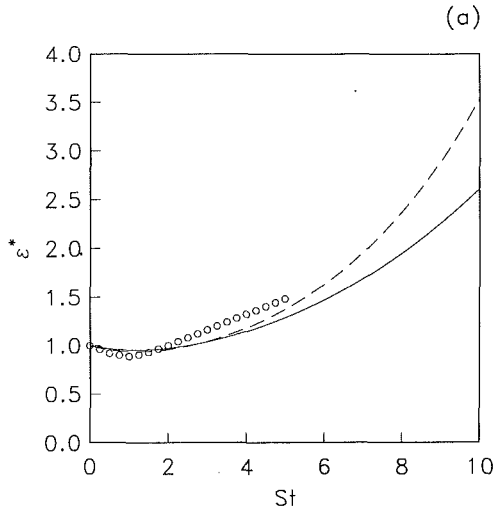

Fig. 8(*a*)

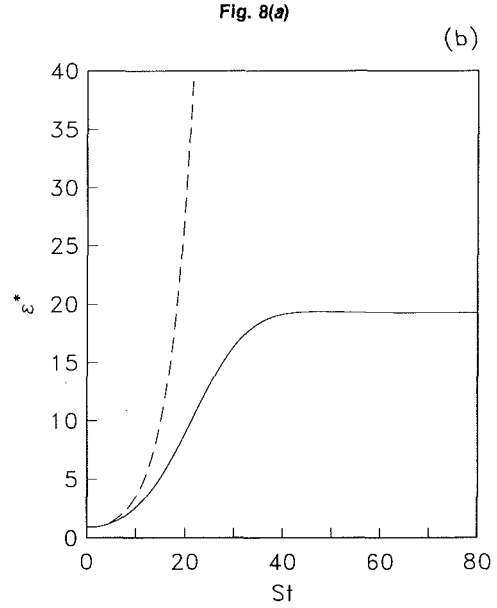

Fig. 8(*b*)

Fig. 8 Comparison of the model predictions with the large-eddy simulations of Bardina, et al. (1983) for homogeneous shear flow: o ϵ^* from large eddy simulation; ——— ϵ^* obtained from $k-\epsilon$ model with vortex stretching; --- ϵ^* obtained from the standard $k-\epsilon$ model. (*a*) Short time solution, and (*b*) long time solution.

$$\dot{k}^* = C_\mu \frac{Sk_o}{\epsilon_0}\frac{k^{*2}}{\epsilon^*} - \frac{\epsilon_0}{Sk_0}\epsilon^* \tag{50}$$

$$\dot{\epsilon}^* = C_{\epsilon_1} C_\mu \frac{Sk_0}{\epsilon_0} k^* + \frac{7}{3\sqrt{15}} C_{\epsilon_3} \frac{\epsilon_0}{Sk_0}\sqrt{R_{t_0}}\,\epsilon^{*\frac{3}{2}} - C_{\epsilon_2}\frac{\epsilon_0}{Sk_0}\frac{\epsilon^{*2}}{k^*} \tag{51}$$

where again we have $C_\mu = 0.09$, $C_{\epsilon_1} = 1.45$, $C_{\epsilon_2} = 1.90$ and $C_{\epsilon_3} = 0.01$ (the standard $k-\epsilon$ model is obtained by setting $C_{\epsilon_3} = 0$). The initial conditions, which correspond to an isotropic turbulence, are taken to be $\epsilon_0/Sk_0 = 0.296$ and $R_{t_0} = 300$. These are the approximate initial conditions of the large-eddy simulations of Bardina et al. (1983) which will allow us to make some direct comparisons between the model and the simulations.

Figures 7(*a*) and 8(*a*) display the short time solutions for k^* and ϵ^* compared to the large eddy simulation data. The solutions with vortex stretching are seen to display short term exponential growth in a manner very similar to that in the standard $k-\epsilon$ closure. The effect of the vortex stretching term is to reduce the growth rate of k^* and ϵ^*, though initially there is a slight increase in the magnitude of ϵ^*. A view of these solutions over a much longer time interval, as displayed in Figs. 7(*b*) and 8(*b*), reveals the dramatic effect that the vortex stretching term ultimately has on the long term growth of k^* and ϵ^*. It is seen that with the vortex stretching effect included, the initial exponential growth rates are eventually suppressed, so that by $St \approx 40$, k^* and ϵ^* asymptote to bounded equilibrium values.

Figures 9 and 10 show the short and long time behavior of the dimensionless ratios Sk/ϵ and $-\overline{uv}/k$ for the solutions obtained both with and without vortex stretching. The curves in Figs. 9(*a*) and 10(*a*) give the impression that an equilibrium state for these quantities may have been achieved by the time $St \approx 10$. However, the long time solutions in Figs. 9(*b*) and 10(*b*) reveal that, in the case where vortex stretching effects are included, only a local maximum is reached – further developments must occur before a true equilibrium is achieved.

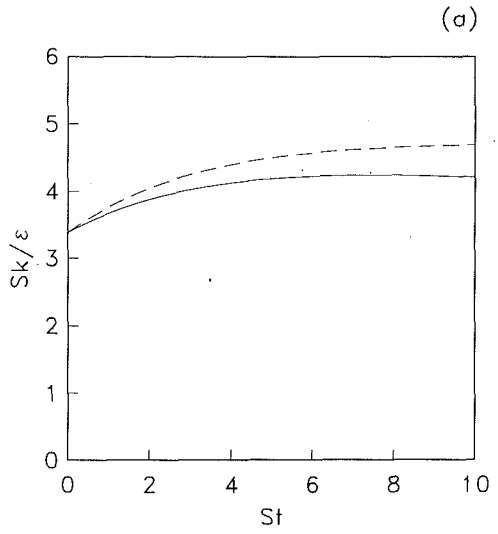

Fig. 9(*a*)

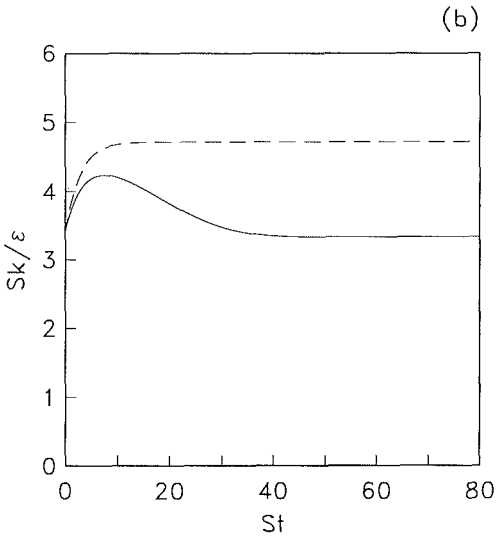

Fig. 9(*b*)

Fig. 9 Comparison of the model predictions for Sk/ϵ: ——— $k-\epsilon$ model with vortex stretching; --- standard $k-\epsilon$ model. (*a*) Short time solution, and (*b*) long time solution.

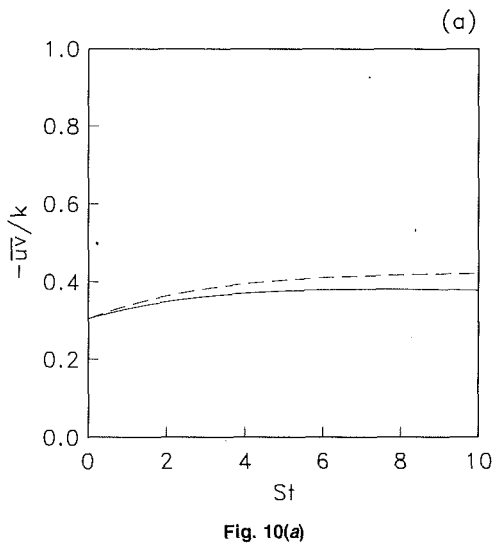

Fig. 10(*a*)

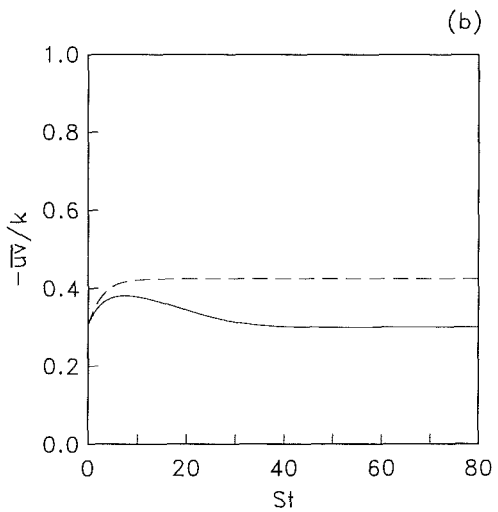

Fig. 10(*b*)

Fig. 10 Comparison of the model predictions for $-\overline{uv}/k$: ——— $k-\epsilon$ model with vortex stretching; --- standard $k-\epsilon$ model. (*a*) Short time solution, and (*b*) long time solution.

This suggests that the apparent convergence of quantities such as Sk/ϵ seen in numerical and experimental studies, may not signify that a final equilibrium state has resulted (i.e., it may only be a local maximum). The behavior of Sk/ϵ shown in Fig. 9(*b*) with vortex stretching present is remarkably consistent from a qualitative standpoint with the direct simulations of Rogers et al. (1986) shown in Fig. 11 (i.e., the tails in Sk/ϵ as time increases in the computations of Rogers et al., 1986 could indicate that an equilibrium state has not been reached).

Figure 12 provides a plot of the long time behavior of the computed turbulence Reynolds number. It achieves an equilibrium value of approximately 5600, which is more than eighteen times its initial value. The most significant effect of the vortex stretching term on k^* and ϵ^*, as seen in Figs. 7(*b*) and 8(*b*), occurs for $R_t > 4000$. This confirms the belief that vortex stretching is mostly a phenomenon associated with high turbulence Reynolds numbers. Some indication of the sensitivity of the computed solutions to the imbalance in the vortex stretching as characterized by C_{ϵ_3} is shown in Fig. 13. This contains the time evolution of k^* for a range of values of C_{ϵ_3}; as expected, k^*_∞ increases with decreasing values of C_{ϵ_3}. Figure 14 shows the effect on k^* of a change in the initial values of ϵ/Sk. As would be expected on physical grounds, an increase in the dimensionless shear rate leads to a higher equilibrium value for the turbulent kinetic energy.

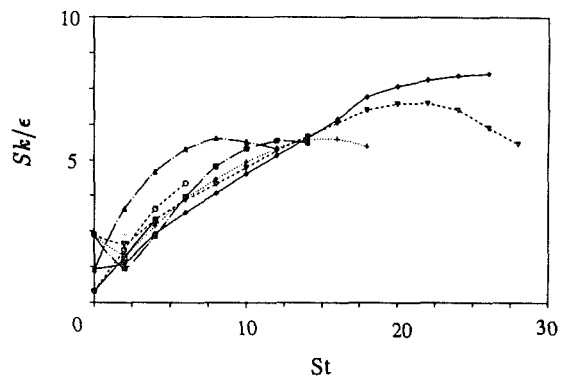

Fig. 11 Time evolution of Sk/ϵ taken from the direct numerical simulations of Rogers et al. (1986) on homogeneous shear flow.

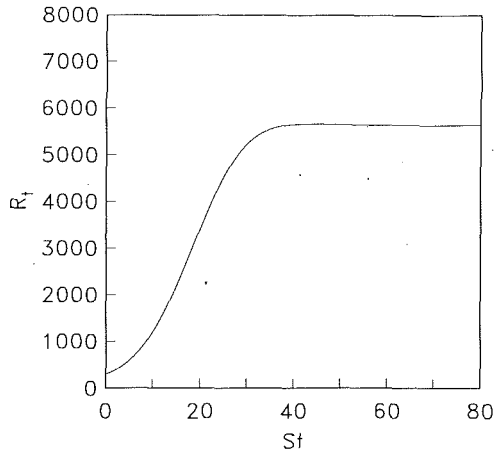

Fig. 12 Time evolution of the turbulence Reynolds number R_t predicted by the $k-\epsilon$ model with vortex stretching.

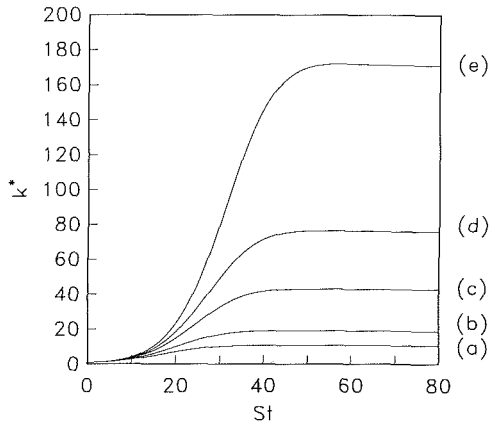

Fig. 13 Sensitivity of the model predictions for the turbulent kinetic energy to C_{ϵ_3}: (*a*) $C_{\epsilon_3} = 0.0133$, (*b*) $C_{\epsilon_3} = 0.01$; (*c*) $C_{\epsilon_3} = 0.0066$; (*d*) $C_{\epsilon_3} = 0.005$, and (*e*) $C_{\epsilon_3} = 0.0033$.

5 Conclusions

An alternative view concerning the equilibrium structure of homogeneous turbulent shear flow has been presented based on maintaining the effect of vortex stretching. It was shown that the presence of just a small net vortex stretching term in the dissipation rate equation can ultimately drive the flow to a production-equals-dissipation equilibrium with bounded energy states. For elapsed times $St < 30$—which includes the largest values of St considered in any of the previously conducted physical or numerical experiments—the introduction of this small unbalanced vortex stretching term into the standard modeled dissipation rate transport equation still yields an exponentially growing turbulent kinetic energy and dissipation. However, since this vortex stretching term scales as $\sqrt{R_t}$, it eventually becomes dominant, causing a saturation of the system to a production-equals-dissipation equilibrium with bounded turbulent kinetic energy and dissipation. Although this alternative physical picture of homogeneous shear flow is contrary to the commonly accepted asymptotic laws—for which an unbounded exponential time growth of k and ϵ is postulated—it is a real possibility that should be seriously considered in the future. The plausibility of these results were supported by independent calculations of isotropic turbulence which demonstrated that the inclusion of this vortex stretching effect yields a much more complete physical description. In fact, the calculations suggested that a $k \sim t^{-1}$ power law decay is the equilibrium state toward which a high-Reynolds-number isotropic turbulence is driven in order to resolve the $O(R_l^{1/2})$ imbalance between vortex stretching and viscous diffusion. As alluded to earlier, the results obtained in this study—for isotropic decay as well as for homogeneous shear flow—are qualitatively the same as those obtained from the theory of self-preservation (see Speziale and Bernard, 1991).

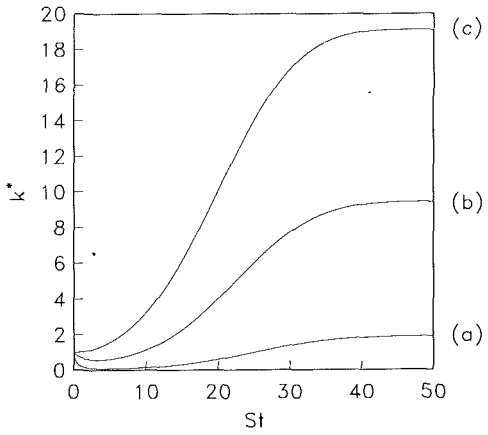

Fig. 14 Sensitivity of the model predictions for the turbulent kinetic energy to ϵ_0/Sk_0: (*a*) $\epsilon_0/Sk_0 = 3.0$; (*b*) $\epsilon_0/Sk_0 = 0.6$, and (*c*) $\epsilon_0/Sk_0 = 0.296$.

New physical and numerical experiments on homogeneous shear flow, for larger elapsed times St, could shed more light on the issue. The recent experiments of Tavoularis and Karnik (1989), which were conducted up to $St = 28$, did show some tendency of the integral length scales to level off—a feature which, if more solidly established, would be supportive of the existence of a production-equals-dissipation equilibrium. However, even if the integral length scales do grow without bound—and this is a distinct possibility since the flow field is infinite—it is still possible for the kinetic energy and dissipation rate to equilibrate to bounded values (it should be remembered that the integral length scales grow without bound in isotropic decay).

Finally, some comments should be made concerning the implications of the results of this paper for turbulence modeling. Since all of the commonly used two-equation models and second-order closures based on the turbulent dissipation rate equation neglect this vortex stretching effect, they predict an unbounded exponential time growth of k and ϵ in homogeneous shear flow. This type of behavior has been shown to cause problems in the calculation of certain inhomogeneous turbulent flows. The singularity in plane stagnation point turbulent flow represents a prime example (Speziale, 1989). Hence, the alteration of turbulence models to yield a production-equals-dissipation equilibrium in homogeneous shear flow via vortex stretching could make their behavior more robust in other turbulent flows without compromising their ability to predict results consistent with physical and numerical experiments on homogeneous turbulence. Whether or not homogeneous shear flow actually saturates to a production-equals-dissipation equilibrium remains an open question that will probably only be resolved by a rigorous mathematical proof based on an appropriate energy norm. For the meantime, however, the results of this study appear to establish the need to re-examine this issue.

Acknowledgments

The authors are indebted to Dr. M. M. Rogers (NASA Ames) for his helpful comments and for allowing us to use unpublished results from his direct simulations on homogeneous shear flow. Funding provided to P. S. Bernard through an ASEE/Navy Summer Faculty Research Fellowship at the Naval Research Laboratory, Washington, DC is greatly appreciated.

C.G. Speziale acknowledges the support of the National Aeronautics and Space Administration under NASA Contract No. NAS1-18605 while in residence at ICASE.

References

Bardina, J., Ferziger, J. H., and Reynolds, W. C., 1983, "Improved Turbulence Models Based on Large-Eddy Simulation of Homogeneous, Incompressible Turbulent Flows," *Stanford Univ. Report TF - 19.*

Batchelor, G. K., and Townsend, A. A., 1947, "Decay of Isotropic Turbulence in Initial Period," *Proc. R. Soc. London*, Series A, Vol. 193, pp. 539–558.

Bernard, P. S. 1985, "Energy and Vorticity Dynamics in Decaying Isotropic Turbulence," *Int'l J. Engrg. Sci.*, Vol. 23, pp. 1037–1057.

Champagne, F. H., Harris, V. G. and Corrsin, S., 1970, "Experiments on Nearly Homogeneous Turbulent Shear Flow," *J. Fluid Mech.*, Vol. 41, pp. 81–139.

Comte-Bellot, G., and Corrsin, S., 1971, "Simple Eulerian Time Correlation of Full- and Narrow-Band Velocity Signals in Grid-Generated, Isotropic Turbulence," *J. Fluid Mech.*, Vol. 48, pp. 273–337.

Corrsin, S., 1963, *Handbuch der Physik VIII/2*, ed. S. Flugge and C. Truesdell, Springer, New York, p. 524.

Harris, V. G., Graham, J. A., and Corrsin, S., 1977, "Further Experiments in Nearly Homogeneous Turbulent Shear Flow," *J. Fluid Mech.*, Vol. 81, pp. 657–687.

Hinze, J. O., 1975, *Turbulence*, (McGraw-Hill, NY)

Lesieur, M., 1990, *Turbulence in Fluids*, 2nd Edition, (Martinus Nijhoff, Boston).

Pumir, A., and Siggia, E., 1990, "Collapsing Solutions to the 3D Euler Equations," *Phys. Fluids A*, Vol. 2, pp. 220–241.

Rogallo, R. S., 1981, "Numerical Experiments in Homogeneous Turbulence," NASA Technical Memorandum 81315.

Rogers, M. M., 1990, *Private Communication.*

Rogers, M. M., Moin, P. and Reynolds, W. C., 1986, "The Structure and Modeling of the Hydrodynamic and Passive Scalar Fields in Homogeneous Turbulent Shear Flow," *Stanford Univ. Report TF - 25.*

Rohr, J. J., Itsweire, E. C., Helland, K. N. and Van Atta, C. W., 1988, "An Investigation of the Growth of Turbulence in a Uniform Mean Shear Flow," *J. Fluid Mech.*, Vol. 187, pp. 1–33.

Rose, W. G., 1966, "Results of an Attempt to Generate a Homogeneous Turbulent Shear Flow," *J. Fluid Mech.*, Vol. 25, pp. 97–120.

Sedov, L. I., 1944, "Decay of Isotropic Turbulent Motions of an Incompressible Fluid," *Doklady Akademie Nauk, SSSR*, Vol. 42, pp. 116–119.

Speziale, C. G., 1989, "On the Free Stream Matching Condition for Stagnation Point Turbulent Flows," *Forum on Turbulent Flows*, ed. W. W. Bower and M. J. Morris, ASME, New York, FED - Vol. 76, pp. 19–24.

Speziale, C. G., and Bernard, P. S. 1991, "The Energy Decay in Self-Preserving Isotropic Turbulence Revisited," *ICASE Report No. 91-58*, NASA Langley Research Center. (To appear in J. Fluid Mech.).

Speziale, C. G., and MacGiolla Mhuiris, N., 1989, "On the Prediction of Equilibrium States in Homogeneous Turbulence," *J. Fluid Mech.*, Vol. 209, pp. 591–615.

Tavoularis, S., 1985, "Asymptotic Laws for Transversely Homogeneous Turbulent Shear Flows," *Phys. Fluids*, Vol. 28, pp. 999–1004.

Tavoularis, S., and Corrsin, S., 1981, "Experiments in Nearly Homogeneous Turbulent Shear Flows With a Uniform Mean Temperature Gradient, Part 1," *J. Fluid Mech.*, Vol. 104, pp. 311–347.

Tavoularis, S., and Karnik, U., 1989, "Further Experiments on the Evolution of Turbulent Stresses and Scales in Uniformly Sheared Turbulence," *J. Fluid Mech.*, Vol. 204, pp. 457–478.

Tennekes, H., and Lumley, J. L, 1972, *A First Course in Turbulence*, M.I.T. Press, Cambridge, MA.

Townsend, A. A., 1956, *The Structure of Turbulent Shear Flow*, Cambridge University Press, New York.

Von Karman, T., 1937, "The Fundamentals of the Statistical Theory of Turbulence," *J. Aero Sci.*, Vol. 4, pp. 131–138.

Turbulence Modeling and Simulation of Atmospheric Boundary Layers

T. W. Abou-Arab[1]
Mechanical Engineering Department,
Faculty of Engineering,
Jordan University of Science & Technology,
Irbid, Jordan

M. A. Serag-Eldin
Mechanical Power Department,
Faculty of Engineering,
Cairo University,
Giza, Egypt

The essence and shortcoming of turbulence modeling and simulation of atmospheric boundary/surface layers are discussed. The present approach rests on the extensively tested and widely used two-equation k-ϵ model to predict such flows. All features and constants of the standard version of the k-ϵ model as it is used for shear flows are retained here. This eliminates the requirement of rigorous experimental validation. However, the model with its set of boundary conditions features compatibility and realizability with the commonly reported stable, unstable and neutral atmospheric boundary/surface layer data. The paper presents also a comparison with experimental data and other models and the need for future research in this direction.

Introduction

The essence of environmental fluid mechanics problems lies first, in heavy gas, dust and pollutant dispersion into environment. Waste heat and substance discharged from power stations, industrial plants, marine vessels carrying LPG/LNG upon damage and households are all few sources. Since these substances are discharged into the atmosphere, the understanding of their interaction with the atmospheric boundary/surface layer seem to be necessary if their concentration contours are to be predicted. Second, wind induced flow fields around surface obstructions, such as, earth's terrain, buildings, bridges, and other man-made structures have long been of interest in structural design. Moreover, operating low-speed aircraft between buildings in regions of sharp velocity gradients, large fluctuation through velocity fields is very hazardous. From the above mentioned overview, it seems that wind loading of buildings structure and obstacles located in urban environment and pollutant dispersion problems require both theoretical and experimental simulation of atmospheric flows (Serag-Eldin, 1982). Many simulation methods have been proposed (Wyngaard, 1976 and Hossain and Rodi, 1982), each differing in the accuracy of the flow field parameters representation and in the closure assumptions required to achieve the desired conditions. Experimental simulation of the atmospheric boundary/surface layers (ABL, thereafter), are also carried out by many investigators (Britter and Hunt, 1979). However, this work is mainly concerned with the turbulence modeling and simulation of such boundary layers.

The continuously reported success and achievements in predicting such flows (Wyngaard, 1976 and Hossain and Rodi, 1982) have encouraged many researchers for further progress of the existing turbulence closures. This progress is mainly based on the assumption that a closure in which the empirical inputs are chosen by reference to simple shear flows may be extrapolated to predict general shear flows (such as, atmospheric flow) and any prediction shortcomings are mainly due to inadequate modeling of flow rather than the extrapolation principle itself (Gibson and Launder, 1978).

The present article illustrates the restrictions and the precautions which must be realized before employing and developing any mathematical model. Some examples are given here to demonstrate that some of the published mathematical models are incompatible and/or unrealizable. Compatibility here implies that the boundary and initial conditions specified for all variables should be compatible with the turbulence model. In other words, these conditions must satisfy the set of the flow governing equations. However, realizability means that the employed turbulence model must guarantee realizable (physically correct) solutions for a wide variety of boundary conditions.

For better ABL-simulation, the present authors have presented the k-ϵ two-equation turbulence model with a compatible set of boundary conditions. A simple functional variation of these compatible conditions with the stability is also derived and the results obtained are plotted. Comparisons with other models are also given.

Illustration of Compatible Conditions

It is noticed that some authors, e.g., Frost et al. (1980) did not recognize that the boundary and initial conditions specified for all variables should be compatible with the turbulence model. To explain this condition the works of Frost et al. (1980) will be compared next with that of Serag-Eldin (1982). Both had applied two-equation turbulence models for the prediction of neutrally stable atmospheric flows over 2-D-obstacles. By investigating the boundary and inlet conditions for each approach, it was found that these conditions were com-

[1]On leave from Cairo University, Giza, Egypt. Presently at King Fahd University of Petroleum & Minerals, Dhahran 31261, Saudi Arabia.

Contributed by the Fluids Engineering Division and presented at the Winter Annual Meeting, Boston, Mass. December 13–18, 1987 of THE AMERICAN SOCIETY OF MECHANICAL ENGINEERS. Manuscript received by the Fluids Engineering Division February 11, 1988.

patible for the model of Serag-Eldin (1982), whereas, they were not so for that of Frost et al. (1980). This may be illustrated here as follows:

Above the molecular boundary layer and below about 150 m above the ground surface (Panofsky, 1974), the atmospheric boundary layer is considered as constant stress layer where the vertical variation of stress and other fluxes can be neglected. This layer is known as the surface layer which is the region of interest in the present analysis. For parallel atmospheric flow, the u-momentum equation yields:

$$\mu_t \frac{du}{dz} = \text{const} \tag{1}$$

and the differential equations for k and ϵ reduce to:

$$\frac{d}{dz}\left(\frac{\mu_t}{\sigma_k}\frac{dk}{dz}\right) + G_k - \rho\epsilon = 0 \tag{2}$$

$$\frac{d}{dz}\left(\frac{\mu_t}{\sigma_\epsilon}\frac{d\epsilon}{dz}\right) + C_{\epsilon 1}\frac{\epsilon}{k}G_k - C_{\epsilon 2}\frac{\epsilon^2}{k} = 0 \tag{3}$$

for compatibility the boundary conditions for u, k, and ϵ must satisfy the above set of equations. For the flow considered by Serag-Eldin (1982) the obstacle lies wholly within a constant stress surface layer, and the specified boundary conditions are:

$$\frac{u}{u_*} = \frac{1}{K}\ln\left(\frac{z}{z_0}\right)$$

$$k = \frac{u_*^2}{\sqrt{c_\mu}} \tag{4}$$

$$\epsilon = \frac{u_*^3}{Kz}$$

$$\mu_t = \rho C_\mu k^2/\epsilon = \rho u_* Kz$$

where $u_* = \sqrt{\tau_w/\rho}$ and z_0 = surface roughness.

Substitution of these boundary values in the L.H.S. of Eqs. (1)–(3), and employing the standard k-ϵ model constants reveals that the R.H.S. of Eqs. (1)–(3) is indeed satisfied.

In the case of Frost et al. (1980), the inlet conditions for 2-D flow over a backward facing step were:

$$\frac{u}{u_*} = \frac{1}{K}\ln(1 + z/z_0)$$

$$k = \frac{u_*^2}{\sqrt{C_\mu}}\left[1 - \frac{\alpha(z+z_0)}{u_*}\right]^2$$

$$l = K(z + z_0) \tag{5}$$

where

$$\mu_t = C_\mu \rho k^{1/2} \quad l = \frac{f(z)}{K(z+z_0)} \text{ and } \tau_w = \rho u_*^2\left[1 - \frac{\alpha(z+z_0)}{u_*}\right] \tag{6}$$

The expressions for u and μ_t reveal that $\mu_t\, du/dz \neq$ constant and hence Eq. (1) are not compatible with the specified boundary conditions.

Moreover, on substitution of the expressions for μ_t, k and u in the L.H.S. of Eq. (2) yields:

$$(z+z_0)^2\left[\frac{C_D}{K^2 C_\mu} - 6\right]\frac{\alpha^2 K^2}{C_\mu^2} + \left[1 - \frac{C_D}{C_\mu K^2}\right]\frac{2\alpha K^2 u_*}{C_\mu^2}(z+z_0) + C_D\frac{u_*}{C_\mu^3} \tag{7}$$

For this side to equal the R.H.S., i.e., zero:

(i) the coefficients of $(z + z_0)$ and $(z + z_0)^2$ should be zero and this is impossible since $(C_D/K^2 C_\mu - 6)$ and $(C_D/C_\mu K^2 - 1)$ cannot both be zero.

(ii) $C_D u_*^2/C_\mu^3 = 0$, i.e., $C_D = 0$ which is implausible. Similarly it could be shown that the general expression for μ_t employed by Panofsky (1974) and Jensen (1985) namely:

$$\mu_t = \frac{\mu_t}{\rho} = Ku_*^2 z/\phi_a(z/L) = u_*^2\frac{du}{dz} \tag{8}$$

does not satisfy Eq. (1). It should be mentioned here that some of the two-equation turbulence models are incompatible with the ABL profiles commonly adopted by meteorologists, except in the case of the neutrally stable ABL (Hossain and Rodi, 1982).

Nomenclature

C, C, C, C, C, C_1, C_2 = turbulence model constants
C_p = specific heat
g = gravitational acceleration
H = sensible heat flux
k = turbulence kinetic energy ($= 1/2\ \overline{u_i'^2}$)
P = pressure
$\rho u_i' u_i'$ = turbulent shear stress tensor
u_i, u, v, w = velocity components
u_* = friction velocity
q = heat flux
Ri = gradient Richardson number $\left[= \frac{g}{T}\left(\frac{dT}{dz} + \frac{g}{C_p}\right)\Big/\left(\frac{du}{dz}\right)^2\right]$
T = temperature
x, z = coordinates in horizontal and vertical-directions, respectively
α = Coriolis acceleration
ρ = density
μ_t = turbulent viscosity
ϵ = dissipation rate
$\sigma_k, \sigma_\epsilon, \sigma_B$ = Prandtl/Schmidt number of k, ϵ, and T
L = Monin-Obukhov length scale $\left[= \frac{u_*^3 C_p \rho T}{KgH}\right]$
l = length scale
l_w = wall shear stress
K = Von Kármán constant
θ = dimensionless temperature
$\beta_u, \beta_k, \beta_\epsilon, \beta_\mu$ = linear extension coefficients for u, k, ϵ, and μ_t boundary conditions
$\bar{}$ = mean
$'$ = fluctuation

Subscripts

n = neutral
in = inlet
w = wall
c-l = centerline
m = mean

Abbreviations

ABL = atmospheric boundary/surface layer
1-D = one-dimensional
2-D = two-dimensional
L.H.S. = left-hand side
R.H.S. = right-hand side

Examples of Unrealizable Turbulence Models

Schumann (1977) showed that certain existing, second order turbulence models in terms of differential equations for the Reynolds stresses $-\overline{u_i' u_j'}$ do not guarantee realizable solutions. The conditions of realizability are:

(1) Non-negative energies, i.e., $\overline{u_i' u_j'} > 0$ for $i = j$.

(2) The cross-correlation between the velocity components u_i' and u_j' is bounded by the magnitude of autocorrelations, i.e., $(\overline{u_i' u_j'})^2 \leq \overline{u_i'^2 u_j'^2}$ for $i \neq j$.

(3) A stronger requirement is that the matrix $\overline{u_i' u_j'}$ be positive semidefinite, i.e., $\det(\overline{u_i' u_j'}) \geq 0$.

This means that the cross-correlations cannot take any arbitrary values.

Thus it seems of paramount importance that any turbulence model must satisfy the above conditions in order to guarantee realizable solutions for any set of boundary conditions. Several researchers borrowed from literature models for certain correlations, e.g., Wyngaard (1976) accepted Lumely's approach (Landsberg and Mieghem, 1974) for modeling the pressure covariance and proposed that:

$$\overbrace{\overline{p'(u_{i,j}'+u_{j,i}')} = C\frac{\epsilon}{k}\left(\overline{u_i' u_j'} - \frac{2}{3}k\,\delta_{ij}\right)}^{\text{(i)}} + \overbrace{C_1 k\left(\frac{\partial u_j}{\partial x_i}+\frac{\partial u_j}{\partial x_i}\right)}^{\text{(ii)}}$$

$$+ \overbrace{C_2\left(\overline{u_i' u_k'}\frac{\partial u_j}{\partial x_k}+\overline{u_j' u_k'}\frac{\partial u_i}{\partial x_k}-\frac{2}{3}\delta_{ij}\,\overline{u_m' u_k'}\frac{\partial u_k}{\partial x_m}\right)}^{\text{(iii)}}$$

$$+ \overbrace{C_3\left(\frac{g_i}{T}\overline{\theta' u_j'}+\frac{g_j}{T}\overline{\theta' u_i'}-\frac{2}{3}\frac{g_k}{T}\overline{\theta' u_k'}\,\delta_{ij}\right)}^{\text{(iv)}} \tag{9}$$

None of the above terms (i) to (iv) can satisfy the realizability conditions for any arbitrary boundary conditions, e.g., for term (i) to give realizable solutions the value of the constant C should be bounded and should be a function of Reynolds number and the $\det(\overline{u_i' u_j'})$ is not a constant. However, these constraints are unsuitable for anisotropic turbulence, e.g., for certain atmospheric flow problems. Term (iii) also does not guarantee realizability if any normal stress component is zero. Similarly term (ii) violates realizability if any of the normal stress components is zero unless its corresponding mean velocity gradient is very large. Although models such as that of Launder et al. (1975) incorporate the influence of stratification, they violate (Schumann, 1977), however, the realizability condition for certain values of the mean velocity gradients. In addition to the increased number of Reynolds stress model equations, the number of the empirical constants to be adjusted (Wyngaard and Cote, 1974) for this closure is greater than those of the two-equation k-ϵ model or any similar models.

The previous discussion and the given examples reveal that in addition to modification of the turbulence model constants in order to match experimental data with predictions there is also need to satisfy realizability conditions and to ensure compatibility. Thus, if the flow stability changes gradually from one class to another class or if we have within the flow field any heat/mass source/sink, a good model should be able to predict these flows without violating the realizability and compatibility conditions.

Present Approach

In the present work the standard version of the k-ϵ model with boundary conditions are employed for the ABL predictions,

$$\begin{aligned}
\frac{u}{u_*} &= \beta_u \frac{u_n}{u_*} = \frac{\beta_u}{K}\ln\frac{z}{z_0},\\
\epsilon &= \beta_\epsilon \epsilon_n = \beta_\epsilon \frac{u_*^3}{Kz},\\
k &= \beta_k k_n = \beta_k \frac{u_*^2}{\sqrt{C_\mu}},\\
C_\mu &= \beta_\mu C_{\mu n},
\end{aligned} \tag{10}$$

where the subscript "n" stands for neutral conditions.

From the above set of boundary conditions it can be easily proved that

$$k = \frac{\beta_k'}{\beta_\mu}\frac{u_*^2}{\sqrt{C_{\mu_n}}}, \text{ and}$$

$$\mu_t = (\beta_k'/\beta_\epsilon)\mathrm{K}u_* z \tag{11}$$

where from Eqs. (10) and (11)

$$\beta_k' = \beta_k \beta_\mu^{1/2} \tag{12}$$

This set of boundary conditions is a linear extension to the neutrally stable ABL boundary conditions which must also satisfy the compatibility conditions. In order to make this set of boundary conditions compatible with the flow governing equations and the adopted turbulence closure, their coefficients (β's) must be interconnected through the following relations which are the outcome of the direct substitution of these conditions in the flow governing equations.

$$\beta_\epsilon = \beta_k' \beta_u \text{ or } \beta_\epsilon = \sqrt{\beta_\mu}\beta_k \beta_u, \text{ and} \tag{13}$$

$$\beta_k' = \beta_u^2 \beta_\mu^{1/2}(C_{\epsilon 2} - C_{\epsilon 1})\frac{\sigma_\epsilon}{K^2} \tag{14}$$

After the substitution of the numerical values of the constants $C_{\mu n}$, $C_{\epsilon 2}$, $C_{\epsilon 1}$, σ_ϵ and K[0.09, 1.92, 1.43, 1.3, 0.41] in the last equation, i.e., Eq. (14), it reads

$$\beta_k' = \beta_u^2 \beta_\mu^{1/2} \text{ or } \beta_k = \beta_u^2 \tag{15}$$

Derivation of Expressions for β's

Now we have derived two equations for the four unknowns, namely, β_u, β_k, β_ϵ, and β_μ, and thus two more additional relationships must be provided. To achieve better results, with minimum limitations, these additional relations should be based on realistically and physically correct assumptions or drawn from experimental data. In the present work these relationships are obtained according to the following principles:

(*a*) conservation of mass, i.e., mass in-flow in the domain should be constant irrespective of the given inlet velocity distribution law, and

(*b*) the values of turbulent shear stress defined as $\mu_t\, du/dt$ at any height are also the same irrespective of the formula used for the substitution of the velocity distribution and eddy viscosity in such an expression.

Employing "*a*" yields the following expression for $_u$,

$$\beta_u = \int_0^{z_T}\left(\ln\frac{z}{z_0} - \psi_a\right)dz \Big/ \int_0^{z_T}\ln\left(\frac{z}{z_0}\right)dz \tag{16}$$

In the above expression, the mass flow is evaluated using the following equation (Panofsky, 1974) for the velocity distribution:

$$\frac{u}{u_*} = \frac{1}{K}\left[\ln\frac{z}{z_0} - \psi_a\right] \tag{17}$$

and then equated to that obtained using the presently proposed velocity distribution:

$$\frac{u}{u_*} = \frac{\beta_u}{K}\ln\frac{z}{z_0}$$

where

$\psi_a = 1.1(-\mathrm{Ri})^{1/2}$; $\mathrm{Ri} \leq 0.0$

$= -5\ \mathrm{Ri}$; $\mathrm{Ri} \geq 0.0$, and (18)

z = height of atmospheric boundary layer to be considered; and

Ri = ambient Richardson number.

Richardson number can be replaced for slightly stable and slightly unstable ABL by other stability parameter such as z/L, where L is the Monin-Obukhov length scale.

Similarly, employing "b" yields:

$$\beta_k = \frac{1}{\phi_{a,m}}\left[1 - z\frac{d\psi_a}{dz}\right] \tag{19}$$

where the following expression [Eq. (8)] is adopted (Panofsky, 1974 and Jensen, 1985) for μ_t in the above relation

$$\mu_t = \frac{\rho}{\phi_{a,m}} K u_* z, \tag{20}$$

and

$$\phi_a^{-1} = \begin{cases} [1 - 16\ \mathrm{Ri}]^{1/4}, & \mathrm{Ri} < 0 \\ [1 + 5\ \mathrm{Ri}]^{-1}, & \mathrm{Ri} > 0 \end{cases} \tag{21}$$

For small Ri values, an expansion of Eq. (21) gives

$$\phi_a^1 = \begin{cases} [1 - 4\ \mathrm{Ri}], & \mathrm{Ri} < 0 \\ [1 - 5\ \mathrm{Ri}], & \mathrm{Ri} > 0 \end{cases} \tag{22}$$

and

$$\phi_{a,m} - 1 = 1 - 4.5\ \mathrm{Ri}_{,m} \tag{23}$$

where $\mathrm{Ri}_{,m} = (z/L)_m$ = mean Richardson number.

From the previous relations, the following relation for β_ϵ, β_k, and β_μ can be obtained:

$$\beta_\epsilon = \frac{\beta_u}{\phi_{a,m}}\left[1 - z\frac{d\psi_a}{dz}\right] \tag{24}$$

$\beta_k = \beta_u^2$, and

$$\beta_\mu = \frac{1}{\beta_u^4}\left\{\frac{1}{\phi_{a,m}}\left[1 - z\frac{d\psi_a}{dz}\right]\right\}^2 \tag{25}$$

These are only global averaged relationship for β's, i.e., they are independent of Ri and employing mean maximal values of (z/L).

Thus, finally we have obtained the following functional relationship for β's as

$$\beta_u = \int_0^{zT} \ln\left(\frac{z}{z_0} - \psi_a\right) dz \Big/ \int_0^{zT} \ln\left(\frac{z}{z_0}\right) dz$$

$$B_k = \frac{1}{\phi_{a,m}}\left[1 - z\frac{d\psi_a}{dz}\right] \text{ or } \beta_k = \beta_u^2,$$

$$\beta_\epsilon = \frac{\beta_\mu}{\phi_{a,m}}\left[1 - z\frac{d\psi_a}{dz}\right] \text{ and} \tag{26}$$

$$\beta_\mu = \frac{1}{\beta_u^4}\left\{\frac{1}{\phi_{a,m}}\left[1 - z\frac{d\psi_a}{dz}\right]\right\}^2$$

Estimation of β's

Since the main interest for some problems lies in the region close to the ground then (z/L) is, in general, small except for extremely unstable or stable flows. Thus one might think of the proposed model as a perturbation about $z/L = 0$, i.e., neutral conditions. In the present work the β estimation will be obtained for the surface layer (i.e., $z_T \cong 80$ m) and for the ranges of stability between Ri = −0.5 and Ri = 0.5 which covers many important situations. Figures 1 to 3 depict the values of the different β's at different values of Ri ranging between 0.5 to −0.5. At Richardson number of zero all β's reveal the value one. Extrapolation of these curves for higher values of Ri is not by any means recommended, since this violates the assumption under which these β's are derived.

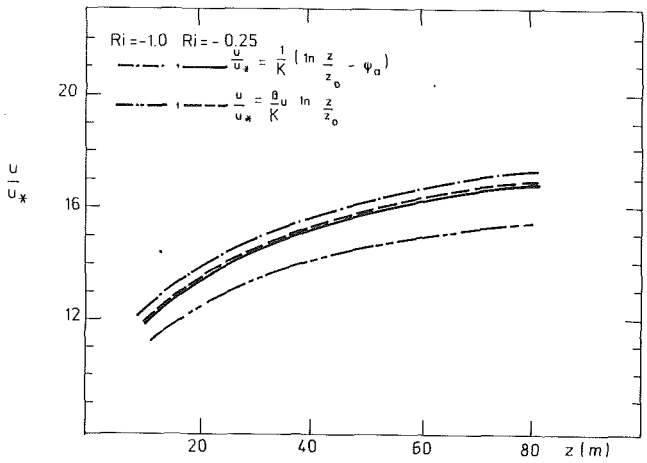

Fig. 1 Vertical distribution of axial flow velocity versus height

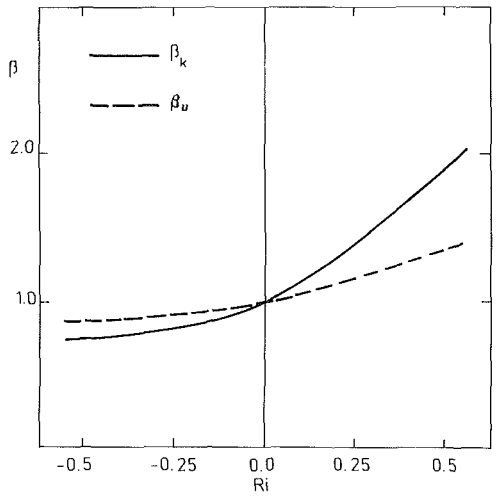

Fig. 2 β's [β_u and β_k] variations versus Ri

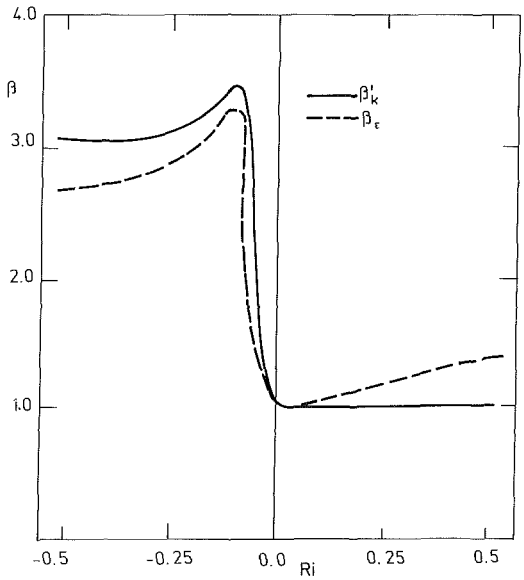

Fig. 3 β's [$\beta_{k'}$ and β_ϵ] variations versus Ri

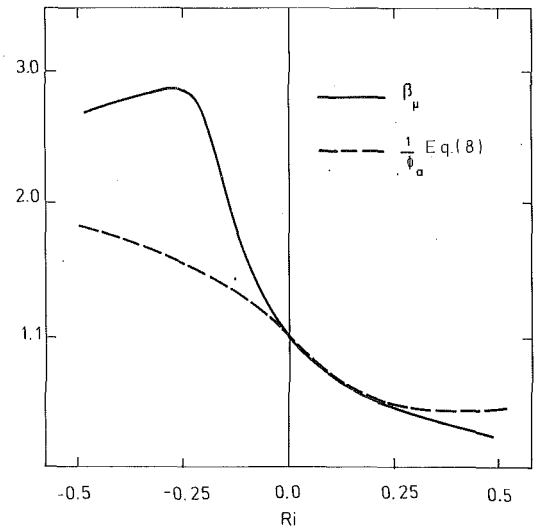

Fig. 4 β_μ variation versus Ri

Figure 1 displays the velocity versus the height above the ground level for Ri = -1.0 and -0.25 and using Eqs. (17) and (18). From this figure it is easy to notice that the approximate linear extension of the log-law velocity distribution as given by Eq. (18) satisfies the mass conservation principle only under the conditions at which β_u is estimated. This is also a further check on the value of β_u. However, the figure displays the velocity distribution for Ri < 0, the same conclusion could be drawn for Ri > 0. Figure 2 depicts β_u variation versus Ri. It gives also the variation of β_k versus Ri. Figure 3 depicts the β's distribution for different values of Ri in the range between -0.5 to 0.5. In Fig. 4, β_μ as estimated here is checked by the comparison of its value with its equivalent experimentally obtained counterpart, namely, $1/\phi_a$ [Eq. (8)]. Both display the same trend for high Ri. However, β_μ and $1/\phi_a$ curves overlapped for low |Ri| values. Finally, these figures demonstrate the dependency of β's on the stability and that β's are equal to unity for neutrally stable atmospheric boundary/surface layer.

However, it is well known that the standard set of constants for k-ϵ model is not working well for ABL predictions, these are retained here because of their reported universality. It should be mentioned here that the present approach can simply extend any set of constants, whether standard and/or modified, without any considerable difficulties and with the compatibility conditions satisfied. Also, the flow governing equations are given here in their simplest forms, however, their extension to other flow cases is a straightforward task.

In the present work, the k-ϵ model is modified by allowing the parameter C_μ to vary with the level of stability. Other turbulence closures, e.g., Hossain and Rodi 1982), Detering and Etling (1985), proposed similar modifications to the k-ϵ model for atmospheric and stratified boundary layers. In these works two constants, namely, C_μ and $C_{\epsilon 1}$ of the standard version of the k-ϵ model, have been changed. These models work quite well for the predictions of atmospheric and stratified flows. However, the conditions under which the compatibility of a turbulence model with its set of boundary conditions are not considered and/or discussed in these works. Also, the present work gives the realizability conditions, which must be satisfied by the model itself in order to guarantee realizable solution for any realizable boundary conditions. More details about the realizability of turbulence models and how to change these existing nonrealizable models into realizable ones are given in details in the work of Schumann (1977).

Conclusions

It can be concluded that much of the borrowed turbulence closure for the prediction of ABL suffers either incompatibility and/or unrealizability with boundary conditions. A new set of compatible boundary conditions is proposed here for ABL of different stability conditions. This set can be used in conjunction with the k-ϵ model for ABL prediction. Some results of the set of compatible boundary conditions of the presently developed model are presented and comparison of these results with experimental data are encouraging for further work in this direction.

Acknowledgment

The first author (T.W. Abou-Arab) wishes to acknowledge the services of Mr. Syed Ishrat Jameel of King Fahd University of Petroleum & Minerals, for his professional typing of this manuscript.

References

Britter, R. E., and Hunt, J. C. R., 1979, "Velocity Measurements and Order of Magnitude Estimate of the Flow Between Two Buildings in a Simulated Atmospheric Boundary Layer," *Journal of International Aerodynamics*, pp. 165–182.

Detering, H. W., and Etling, D., 1985, "Application of the E-ϵ Turbulence Model to the Atmospheric Boundary Layer," *Boundary Layer Metrology*, Vol. 33, pp. 113–133.

Frost, W., Bitter, J., and Shieh, C. F., 1980, "Analysis of Neutrally Stable Atmospheric Flow Over a Two-Dimensional Forward-Facing Step," *AIAA Journal*, Vol. 18, No. 4, pp. 32–38.

Gibson, M. M., and Launder, B. E., 1978, "Ground Effects on Pressure Fluctuations in the Atmospheric Boundary Layer," *Journal of Fluid Mechanics*, Vol. 86, No. 3, pp. 491–511.

Hossain, M. S., and Rodi, W., 1982, "A Turbulence Model for Bouyant Flows and Its Application to Vertical Buoyant Jets," *Turbulent Buoyant Jets, and Plumes*, Ed. Rodi, Pergamon Press.

Jensen, N. O., 1985, "Atmospheric Boundary Layer Modeling," Von Kármán Institute Lecture Series.

Landsberg, H. E,. and Mieghem, J., eds., 1974, *Advances in Geophysics*, Academic Press, New York, pp. 169–192.

Launder, B. E., Reece, G. J., and Rodi, W., 1975, "Progress in the Development of a Reynolds Stress Turbulence Closure," *Journal of Fluid Mechanics*, Vol. 68, pp. 537–566.

Panofsky, H. A., 1974, "The Atmospheric Boundary Layer Below 150 Meters," *Annual Review of Fluid Mechanics*, Vol. 6, pp. 147–244.

Schumann, U., 1977, "Realizability of Reynolds-Stress Turbulence Models," *Phys. Fluids*, Vol. 20, No. 5.

Serag-Eldin, M. A., 1982, "Computation of the Flow Field Over Long Two-Dimensional Obstacles in the Atmosphere," IBM-Cairo Scientific Center, Tech. Rep. No. 002.

Wyngaard, J. C., 1976, "The Atmospheric Boundary Layer Modeling and Measurements," *Turbulence*, ed. Bradshaw, Springer-Verlag, pp. 352–365.

Wyngaard, J. C., and Cote, O. R., 1974, "The Evolution of a Convective Planetary Boundary Layer—A Higher-Order-Closure Model Study," *Boundary Layer Metrology*, Vol. 7, pp. 289–308.

A Frequency-Domain Filtering Technique for Triple Decomposition of Unsteady Turbulent Flow

G. J. Brereton
Assistant Professor.

A. Kodal
Graduate Student.

Department of Mechanical Engineering
& Applied Mechanics,
The University of Michigan,
Ann Arbor, Mich 48109

A new technique is presented for decomposing unsteady turbulent flow variables into their organized unsteady and turbulent components, which appears to offer some significant advantages over existing ones. The technique uses power-spectral estimates of data to deduce the optimal frequency-domain filter for determining the organized and turbulent components of a time series of data. When contrasted with the phase-averaging technique, this method can be thought of as replacing the assumption that the organized motion is identically reproduced in successive cycles of known periodicity by a more general condition: the cross-correlation of the organized and turbulent components is minimized for a time series of measurement data, given the expected shape of the turbulence power spectrum. The method is significantly more general than the phase average in its applicability and makes more efficient use of available data. Performance evaluations for time series of unsteady turbulent velocity measurements attest to the accuracy of the technique and illustrate the improved performance of this method over the phase-averaging technique when cycle-to-cycle variations in organized motion are present.

1 Introduction

In the analysis of organized unsteady turbulent flow, it is useful to decompose flow variables with respect to their characteristic time dependence. In such flows, the time-dependent, turbulent behavior of the general dependent variable, $f(x, t)$, may be expressed as the summed contribution of three parts:

$$f(\mathbf{x}, t) = \bar{f}(\mathbf{x}) + \tilde{f}(\mathbf{x}, t) + f'(\mathbf{x}, t). \quad (1)$$

These components are the mean or time-averaged one, the oscillatory or periodic one, and the turbulent component, respectively. Using this kind of decomposition, equations of fluid motion may be devised for each of the mean, periodic and turbulent fields of flow. Experimental measurements may then be decomposed in the same fashion and turbulent flow oscillating about some mean condition may be examined according to the behavior of each of three components in its respective field.

2 Background

A number of methods have been proposed for deducing the turbulent and organized-unsteady component contributions to particular kinds of unsteady turbulent flow. Possibly the most widely used is the triple decomposition of Hussain and Reynolds (1970), which is appropriate for flows in which the organized unsteady motion may be treated as identical from cycle to cycle, and the turbulent motions in successive cycles may be considered as independent events. In this decomposition, the components $\bar{f}(\mathbf{x})$, $\tilde{f}(\mathbf{x}, t)$, and $f'(\mathbf{x}, t)$ are deduced by employing:

(*i*) the phase average or ensemble average:

$$\langle f(\mathbf{x}, t)\rangle = \lim_{N\to\infty} \frac{1}{N} \sum_{n=0}^{N-1} f(\mathbf{x}, t + n\tau), \quad (2)$$

where τ is the period of the cycle, and (ii) the time average:

$$\bar{f}(\mathbf{x}) = \lim_{N\to\infty} \frac{1}{N} \sum_{n=0}^{N-1} f(\mathbf{x}, t_0 + n\Delta t) \text{ where } N\Delta t \gg \tau. \quad (3)$$

Since the phase-averaged and turbulent components are uncorrelated in time, it follows that: $\langle f(\mathbf{x}, t)\rangle = \bar{f}(\mathbf{x}) + \tilde{f}(\mathbf{x}, t)$, $f'(\mathbf{x}, t) = f(\mathbf{x}, t) - \langle f(\mathbf{x}, t)\rangle$, and $\tilde{f}(\mathbf{x}, t) = \langle f(\mathbf{x}, t)\rangle - \overline{\langle f(\mathbf{x}, t)\rangle}$. By computing the phase and time averages of a time series of data and using these identities, the mean, oscillatory and turbulent components of the time series may be evaluated.

The efficacy of this technique depends on the accuracy with which the cycle period τ is known, and the repeatability of the organized motion. If τ cannot be specified with sufficient accuracy, organized motions will be interpreted as turbulence. Likewise, subharmonic motions and organized motions which vary from cycle to cycle will also be misrepresented as turbulence. In practical applications of this technique, effects of cycle-to-cycle variations may be reduced by ensemble-averaging data at the same time delay relative to a conditional event in each cycle, rather than at the same absolute phase (Witze

Contributed by the Fluids Engineering Division for publication in the JOURNAL OF FLUIDS ENGINEERING. Manuscript received by the Fluids Engineering Division May 20, 1991.

et al., 1984), thereby reducing the susceptibility of phase averages to "frequency jitter."

Decompositions which recognize the existence of cycle-to-cycle variation in periodic unsteady flow include the frequency domain filtering approaches taken by Liou and Santavicca (1985) and by Walburn et al. (1983) and Tiederman et al. (1988). In these decompositions, a low-pass digital filter is applied to a time series of measured data to recover the organized unsteady component so that the turbulent contribution may be deduced as the difference between the unfiltered and filtered series. In the internal combustion engine studies of Liou and Santavicca, the cut-off frequency of the low-pass filter was taken as the largest appreciable frequency in the power spectrum of the organized unsteady component, as estimated by ensemble averaging. Tiederman et al. selected a cut-off frequency based on the magnitude of peaks in the power spectrum of the measured time series. The clear shortcoming of these low-pass filtering technique is that, since turbulence is by its very nature a broadband phenomenon, the characteristic turbulent time/frequency scales typically overlap with those of co-existing organized unsteady motions. For the model cardiovascular flows to which Tiederman et al. applied this technique, the use of a low-pass filter decomposition was lent greater justification because order-of-magnitude estimates of the lowest frequencies of turbulence were of the order of their cut-off frequency. In addition to these decompositions, there are also related methods (time-averaging over short intervals within a cycle, and time-series curve fitting) which have the qualitative effect of low-pass filtering data (Rask, 1981), but the lack of guidance as to the kind of curve fits which should be employed, or to the interval necessary for a meaningful local time average makes these methods quite sensitive to the choice of smoothing parameters for a given application. Other methods which represent such time series as the sum of deterministic and stochastic parts have been proposed (Pandit and Wu, 1983). However, as Enotiadis et al. (1990) concluded in their comparative study of phase averaging, filtering and time-series curve fitting of velocity measurements in motored engine flows, cyclic variations cannot always be identified as deterministic processes.

3 The Filtering Technique

The decomposition technique proposed in this paper is for general classes of unsteady turbulent motion and does not rely on a precise knowledge of the period of organized motions which are identical from one cycle to another—a condition necessary for successful use of the phase-averaging technique. Instead, when the periodicity of the organized motion is imprecisely known, or might vary from cycle to cycle, periodicity information must be replaced by sufficient information of other kinds to determine the appropriate decomposition. The information used is a *model* of the shape of the power spectrum of the turbulent component. The motivation for introducing modeling information for the turbulent component, rather than the oscillatory one, is that: (i) in almost every study of turbulent flow with periodic unsteadiness that has been carried out to date, the mean turbulence field appears the same as the turbulence field found in a steady flow which matches the mean condition of the unsteady flow (Brereton et al., 1990) and may be modeled without regard for the unsteadiness[1]; and (ii) since there is no generality in the form of organized unsteadiness in fluid flow, attempts to prescribe the determinism of the oscillatory component invariably have the undesirable quality of smoothing/low-pass filtering the information. In the proposed decomposition, the model of the turbulence power spectrum is used as an initial estimate from which a refined decomposition may found by requiring that the cross-correlation between the organized and turbulent components is minimized. The model is deduced from estimates of the power spectrum of the measured time series and is then used to construct a filter for decomposition of the Fourier transform of the time series. This filter is closely related to the Wiener filter, which is optimal in the sense that it minimizes the mean square deviation between the true value of the decomposed variable and the estimate made by the filter. Its development is outlined in the following paragraphs.

When the mean value has been subtracted from a time series of measurements by averaging over all measurements, the resultant time series may be represented as the sum of oscillatory and turbulent contributions, i.e.,

$u(t) = \tilde{u}(t) + u'(t)$ or, in the frequency domain,

$$U(f) = \tilde{U}(f) + U'(f) \quad (4)$$

where $\sim$ denotes the organized oscillatory component and $'$ the turbulent contribution. A linear, time-invariant filter $\Phi(f)$ is to be constructed such that the turbulent component may be estimated as:

$$U'_{\text{est}}(f) = \Phi(f)U(f), \quad (5)$$

where Φ may, in general, be a complex function. If the estimate of $u'(t)$ is to satisfy the condition that the mean square error between the real and estimated values of $u'(t)$ is minimized, then for the idealized case of an infinite time series,

$$\int_{-\infty}^{\infty} (u'(t) - u'_{\text{est}}(t))^2 dt = \text{minimum}. \quad (6)$$

If wide-sense stationary in u' is assumed, the filter function which minimizes this integral can be shown to be purely real (see, for example, Peebles (1980) for a standard derivation of the Wiener filter). If, in addition, u' and $\tilde{u}$ are uncorrelated

[1]One exception is the high-frequency forced unsteadiness experiment of Ramaprian and Tu (1983). In this study, measurements of mean turbulence quantities differed slightly, though perceptibly, from their steady flow and low-frequency unsteady flow counterparts when oscillation was forced at a frequency close to the mean flow burst frequency. However, the evidence that there is *modification of mean turbulence measures by high-frequency forced oscillation* is inconclusive—comparable experiments of Hwang and Brereton (1991) at frequencies as high as six times the mean flow burst frequency did not reveal any frequency dependence.

Nomenclature

$f(\ )$ = general time-dependent variable of turbulent fluid flow
f = frequency
f_s = sampling frequency
R = autocorrelation function
S = power-spectral density function
t = time
$\mathbf{x}$ = position vector
U_∞ = mean free-stream velocity
U = local mean velocity
U = Fourier transform of streamwise velocity
u = streamwise velocity in the time domain
δ = boundary-layer thickness
τ = period of an organized, unsteady event
Φ = frequency-domain filter function
Ψ = frequency-domain filter function
$\overline{\ }$ = average over time
$\langle\ \rangle$ = average performed at the same phase in each of a series of periodic events
$\sim$ = periodic component of an unsteady quantity
$'$ = turbulent component

in time—a condition enforced when a phase-averaging procedure is employed—then the optimal filter $\Phi(f)$ takes the form:

$\Phi(f) = \dfrac{S_{u'u'}(f)}{S_{uu}(f)}$ with mean-square error:

$$\int_{-\infty}^{\infty} \frac{S_{\tilde{u}\tilde{u}}(f) S_{u'u'}(f)}{S_{uu}(f)}\, df, \quad (7)$$

where $S_{uu}(f)$, $S_{\tilde{u}\tilde{u}}(f)$ and $S_{u'u'}(f)$ are the power spectra of $u(t)$, $\tilde{u}(t)$, and u', respectively. Since $U'_{\text{est}}(f) = \Phi(f)U(f)$, this Wiener filter recovers the turbulent component by scaling the Fourier transform of the time series by the proportion of the turbulence power spectrum to the total power spectrum, which at any frequency varies between 0 and 1. The power spectrum S_{uu} may be estimated from a time series of data of $u(t)$ by a number of methods (Fourier, autoregressive, ARMA, etc.). Given an input model of the turbulence spectrum $S_{u'u'}$, the Wiener filter $\Phi(f)$ could be constructed to recover the optimal estimate (in a mean square error sense) of $U'(f)$ and so $u'(t)$ and ultimately $\tilde{u}(t)$ from (4). The accuracy of the resulting decomposition would be limited by the quality of the model of the turbulence spectrum $S_{u'u'}$ as well as the mean square error limitations of a filter which carries no phase information. While it would be desirable to refine the model of the turbulence spectrum by an iterative procedure which incorporates additional information—i.e., information equivalent to prescribing the period of the organized component in a phase-averaging decomposition—the Weiner filter is unsuitable for iterative refinement and would converge rapidly to one of the degenerate solutions: $S_{u'u'}(f) = 0$ or $S_{u'u'}(f) = S_{uu}(f)$, corresponding to no turbulent component and no organized unsteady component, respectively.

In order to deduce a filter which is suitable for iteration on a model turbulence spectrum, we consider the more general filter

$$\Psi(f) = \left(\frac{S_{u'u'}(f)}{S_{uu}(f)}\right)^n \quad (9)$$

which reduces to the Wiener filter for $n = 1$.

$$\text{Since } \Psi(f) = \left(\frac{S_{u'u'}(f)}{S_{uu}(f)}\right)^n,$$

$$U'_{\text{est}}(f) = U(f)\left(\frac{S_{u'u'}(f)}{S_{uu}(f)}\right)^n, \text{ and } \Psi(f) \text{ is real,}$$

then

$$|U'_{\text{est}}(f)| = \Psi(f)|U(f)|,\ |U'_{\text{est}}(f)|^2 = \Psi^2(f)|U(f)|^2,$$

$$S_{u'_{\text{est}}u'_{\text{est}}} = \Psi^2(f) S_{uu}(f),$$

$$\text{and so } S_{u'_{\text{est}}u'_{\text{est}}}(f) S_{uu}^{2n-1}(f) - S_{u'u'}^{2n}(f) = 0. \quad (10)$$

In this case an input model turbulence spectrum $S_{u'u'}(f)$ will match the filter estimate $S_{u'_{\text{est}}u'_{\text{est}}}(f)$ when $n = 1/2$, which corresponds to the square root of the Weiner filter:

$$\Psi(f) = \left(\frac{S_{u'u'}(f)}{S_{uu}(f)}\right)^{1/2} = \frac{|U'(f)|}{|U(f)|} \quad (11)$$

with mean square error:

$$\int_{-\infty}^{\infty} \frac{S_{\tilde{u}\tilde{u}}(f) S_{u'u'}(f)}{S_{uu}(f)} + S_{uu}(f)\,(\Psi(f) - \Psi^2(f))^2 df. \quad (12)$$

For many organized unsteady flows which are characterized by a broadband turbulent power spectrum and a narrow band-limited power spectrum of the organized component, the increase in error relative to that of the Weiner filter is negligible. It would only be significant in study of organized unsteady flows in which the power spectrum of their organized component were broadband and of comparable magnitude to the turbulence power spectrum. Therefore, given a time series of data, an estimate of the power spectrum of the data $S_{uu}(f)$ may be combined with a model of the turbulence power spectrum $S_{u'u'}(f)$ to form the filter $\Psi(f)$ which may then be used to decompose the time series into organized unsteady and turbulent components. By iterating on the model of the turbulence power spectrum $S_{u'u'}(f)$, one may choose the resultant decomposition which best satisfies a criterion such as minimal cross-correlation between the two components, consistent with the assumption used in development of the filter that they are uncorrelated.

It is worth pointing out that since this filter is deduced from considerations of minimization of the square of the error between the estimate and the true value of a component of the time series, the accuracy of estimates by this filtering technique is of second order with respect to the accuracy with which the filter is determined. Thus inaccurate estimates of $S_{uu}(f)$ and $S_{u'u'}(f)$, from real data which may not satisfy conditions of wide-sense stationarity, may still yield satisfactory decomposition results.

4 Implementation of the Technique

A time series of data is selected which typically represents about ten cycles of organized unsteady motion. After removal of the mean, an estimate of the power spectrum $S_{uu}(f)$ of these data is made. The estimate we employ is a standard autoregressive technique of sufficient order to assure that first-harmonic peaks of organized motion in $S_{uu}(f)$ will be resolved. The initial model of the turbulence power spectrum $S_{u'u'}(f)$ is, for convenience, selected as the first-order autoregressive model which would pass through the highest and lowest frequencies of the $S_{uu}(f)$ power-spectral density estimate. It therefore takes the shape described analytically by:

$$S_{u'u'}(f) = \frac{2(1 - R_{uu}^2(1))}{1 + R_{uu}^2(1) - 2R_{uu}(1)\cos(2\pi f/fs)} \quad (13)$$

where $R_{uu}(1)$ is the autocorrelation function for $u(t)$ delayed by one sampling interval and f_s is the sampling frequency of the time series (Box and Jenkins, 1976). Although this power spectral estimate also describes a Markov random process, it is used here purely as an initial model for $S_{u'u'}(f)$, given an estimate of $S_{uu}(f)$, which has a convenient analytical form. The autoregressive estimate of $S_{uu}(f)$ and the corresponding first-order autoregressive model for $S_{u'u'}(f)$ are shown in Fig. 1, for the case of a time series of measurements of streamwise velocity in a turbulent boundary layer with superposed sinusoidal oscillation. From this figure, it may be seen that the model of $S_{u'u'}(f)$ has the desired broadband features one would expect of a turbulence power spectrum, and that the decay at high frequencies is adequately represented. It also matches the general form of power spectra of stationary turbulent flows quite well. As such it constitutes a good initial model of $S_{u'u'}(f)$ upon which to iterate towards the optimal decomposition of $u(t)$ into $\tilde{u}(t)$ and $u'(t)$.

The rationale for choosing a time series comprising about ten cycles of data is that the somewhat flat low-frequency range of $S_{uu}(f)$ may then be resolved one decade below the expected frequency of the dominant harmonic peak. Since subharmonics of one tenth the fundamental frequency of organized motions are not expected to be significant in unsteady turbulent flows, the level of $S_{uu}(f)$ at its lowest frequency represents the contribution of $S_{u'u'}(f)$. Thus the model of the turbulence power spectrum $S_{u'u'}(f)$ may be chosen to take the value of $S_{uu}(f)$ at its lowest resolved frequency. For cases of forced oscillation at frequencies in the energy-containing or inertial sub-ranges of the power spectrum, time series of considerably more than ten cycles may be necessary to resolve the flat low-frequency range of the power spectrum. The sampling frequency f_s is chosen to resolve the highest frequencies at which there is still

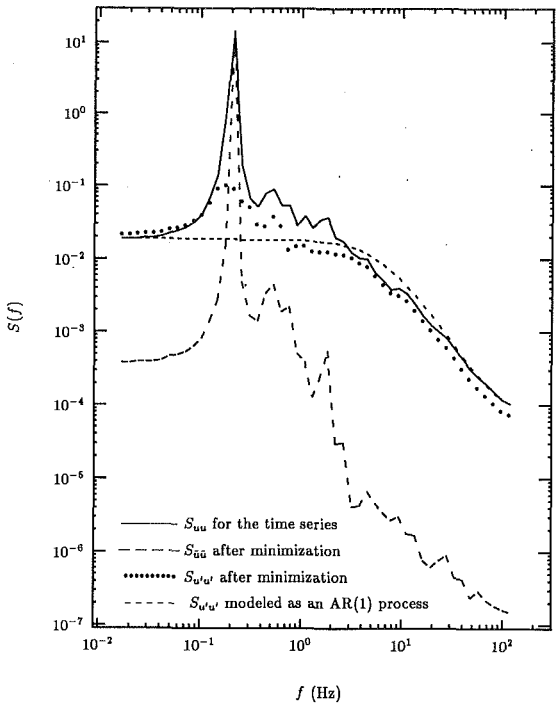

Fig. 1 Power spectral density estimates for $u(t)$, $\tilde{u}(t)$, and $u'(t)$, and the model estimate of the power spectrum of $u'(t)$

significant energy content is $S_{uu}(f)$ and, as a guideline, may be taken as the frequency at which $S_{uu}(f)$ has diminished to 1 percent of its low-frequency level.

The minimization is carried out by discretizing the model turbulence power spectrum $S_{u'u'}(f)$ as, for example, 100 elements, the centers of which are at equal intervals in logarithmic frequency space. Given the initial model as a starting condition, a constrained quasi-Newton method is then employed as the multi-dimensional minimization procedure to find the estimates of $\tilde{u}(t)$ and $u'(t)$ with minimal cross correlation. In typical unsteady turbulent flow applications, the cross-correlation coefficient $\overline{\tilde{u}u'}/(\overline{u'u'}\ \overline{\tilde{u}\tilde{u}})^{1/2}$ is usually of order 10^{-1} to 10^{-2} *before* refinement of the decomposition by minimization. It takes this low an initial value because the first-order autoregressive model constitutes a good initial estimate of $S_{u'u'}(f)$. If a rough estimate (of order of about 10 percent accuracy in $\overline{u'u'}$) of the decomposition is adequate, further refinement by minimization may be unnecessary, in which case the Weiner filter may be applied directly from $S_{uu}(f)$ and the model for $S_{u'u'}(f)$.

When refined estimates of the decomposition are required, a multi-dimensional minimization computation of the cross-correlation coefficient between $\tilde{u}(t)$ and $u'(t)$ is carried out to ascertain optimal estimates of these components of the time series. In the same sense that the phase-averaging technique enforces the requirement of no correlation between $\tilde{u}(t)$ and $u'(t)$, for *any* choice (correct or otherwise) of period of the organized unsteady motion, a minimization of correlations of filtered values of discrete data can produce multiple local minima, depending on the starting values and the prescribed convergence tolerance of the minimization scheme. However, by making a judicious choice of starting values (the model turbulence power spectrum), with a robust minimization technique and specification of an appropriate tolerance, this method should converge towards a single local minimum which yields a correct decomposition of $u(t)$ into $\tilde{u}(t)$ and $u'(t)$, avoiding the minima corresponding to the degenerate decompositions: $u(t) = \tilde{u}(t)$ and $u(t) = u'(t)$. For samples of 16,384 data and a power spectrum discretized into 100 elements, this minimization computation typically achieved a cross-correlation coefficient $\overline{\tilde{u}u'}/(\overline{u'u'}\ \overline{\tilde{u}\tilde{u}})^{1/2}$ of about 10^{-11} in about 6 minutes on a modern computer workstation.

5 Evaluation of the Technique

To assess the adequacy of the technique, it is applied to time series of measurements of streamwise velocity in steady turbulent boundary layers and unsteady ones for which sinusoidal oscillation is superposed upon an otherwise undisturbed mean flow. These measurements are taken from the water-tunnel experiments of Brereton et al. (1990), in which the sinusoidal motion was induced by controlled drainage of free-stream fluid through a gate valve, driven at constant rotational speed by a DC motor. The period of the unsteady motion never varied by more than 0.2 percent and so the repeatability of this deterministic forcing was thought to be extremely high, and representative of many controlled laboratory experiments on unsteady turbulent flow. In these experiments, the relative uncertainty (at a 95 percent confidence level) was estimated as ± 1 percent in $\tilde{u}$ and ± 6 percent in $\langle u'u' \rangle$. These measurements are also known to have minimal subharmonic content (Brereton and Reynolds, 1991) so the phase-averaged decomposition should give a very good representation of the true organized and turbulent components of velocity. Thus these data provide a good basis for evaluating the adequacy of the filtering decomposition technique.

As a preliminary test, the decomposition technique was applied to a time series of $u'(t)$ measurements from a *steady* turbulent boundary layer ($\mathrm{Re}_\theta = 3400$, $y/\delta = 0.4$). The filter decomposition detected only extremely low values of oscillatory motion (around 3 percent of $\overline{u'u'}$, shown in Tables 1 and 2) in this nominally steady turbulent data set, and estimates of turbulence intensity were in good agreement with conventional ensemble (time) averages (within 3 percent). The technique was then applied to a time series of $u'(t)$ measurements from an unsteady turbulent boundary layer ($\mathrm{Re}_\theta = 3400$, $y/\delta = 0.4$) in which the local amplitude of organized unsteady motion was 20 percent of the local mean velocity. Estimates of the power spectra of the time series $u(t)$, the initial model for $S_{u'u'}$, and the resulting power spectra for $S_{\tilde{u}\tilde{u}}$ and $S_{u'u'}$ (from which the filter $\Psi(f)$ is determined) are shown in Fig. 1 for decomposition of these data.

The decomposition of $u(t)$ into $\tilde{u}(t)$ (with $u'(t)$ as the difference between them) are shown in Figs. 2 and 3 for a single cycle of a time series of about 16 cycles of data, for the phase-average and frequency-filter techniques, respectively. The period of these data corresponded to around 20 characteristic turbulence timescales (as estimated from δ/U_∞). A comparison of the values of $\tilde{u}(t)$ deduced by these decompositions shown in Fig. 4 and it is clear that the oscillatory motions detected by the two decompositions are very similar. The relative differences in $\overline{u'u'}$ and $\overline{\tilde{u}\tilde{u}}$ evaluated by each technique over 16 cycles of data are 5 percent and 2 percent, respectively. Since the phase average requires a precise knowledge of the period of organized motion and the frequency filter requires only an estimate (to employ an autoregressive model to appropriate order), the close agreement in $\overline{\tilde{u}\tilde{u}}$ (which is about six times larger than $\overline{u'u'}$ for these data) is surprisingly good. That a frequency filtering technique which carries no phase information can provide as good a decomposition as a phase average implies that, at any phase in the cycle, the relative magnitudes of the organized and turbulent contributions to the power spectrum may be represented adequately by time-averaged power-spectral information. Phase-dependent refinement of the shape of the power-spectral description of turbulence is therefore unnecessary for decomposition of these data. An additional point of importance which may be observed from these figures is that the smoothness of the variation of the organized component with time is comparable for each

Table 1 Comparisons of phase-average and filter decompositions of turbulent motion

Test Case	$\overline{u'u'}/U^2$ (phase ave.)	$\overline{u'u'}/U^2$ (filter)	% Var.
Steady flow	0.00270	0.00262	3%
Unsteady flow, $\tilde{u}/U = 0.2$	0.00267	0.00254	5%
Cycle-to-cycle variation*	0.00537	0.00493	9%
Cycle-to-cycle variation†	0.00245	0.00211	16%
Ideal organized motion‡	0.00265	0.00264	2%

Table 2 Comparisons of phase-average and filter decompositions of oscillatory motion

Test Case	$\overline{\tilde{u}\tilde{u}}/U^2$ (phase ave.)	$\overline{\tilde{u}\tilde{u}}/U^2$ (filter)	% Var.
Steady flow		0.0001	
Unsteady flow, $\tilde{u}/U = 0.2$	0.0170	0.0173	2%
Cycle-to-cycle variation*	0.0173	0.0223	31%
Cycle-to-cycle variation†	0.0167	0.0135	24%
Ideal organized motion‡	0.0224	0.0234	4%

* A time series of 16 cycles for which $\tilde{u}/U = 0.2$ for 15 cycles and $\tilde{u}/U = 0.24$ for one.

† A time series of 16 cycles for which $\tilde{u}/U = 0.2$ for 15 cycles and $\tilde{u}/U = 0.16$ for one.

‡ A time series of 16 cycles for which a turbulent signal is superposed upon an oscillatory one which is perfectly repeated in each cycle.

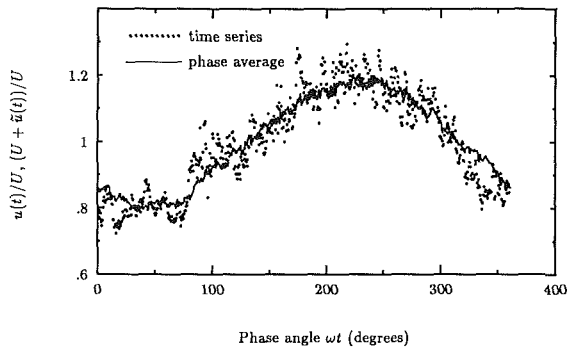

Fig. 2 Phase-average decomposition of a time series of streamwise velocity data. The data describe a cycle of forced sinusoidal unsteadiness imposed on a turbulent boundary layer flow at $Re_\theta = 3400$, measured at $y/\delta = 0.4$. The amplitude of the induced oscillatory motion is 20 percent of the local mean velocity.

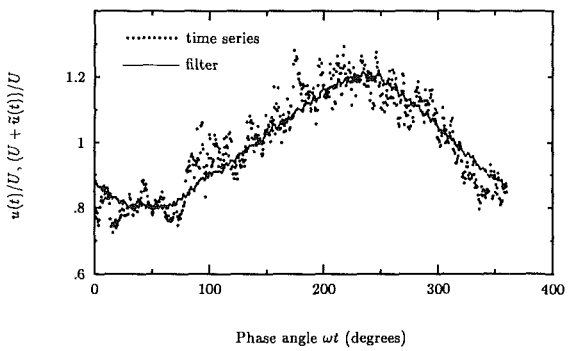

Fig. 3 Filter decomposition of the time series of Fig. 2

decomposition—the noisiness of the filter decomposition is equivalent to the variance at each phase in the ensemble average over the same data. While continued averaging over greater numbers of ensembles removes more of the noise in the phase average and would smooth the power spectral estimation of these data, the cycle averages of $\overline{\tilde{u}\tilde{u}}$ and $\overline{u'u'}$ scarcely change—after 16 cycles of data the noise in the oscillatory component is already far smaller than the turbulent component of these data.

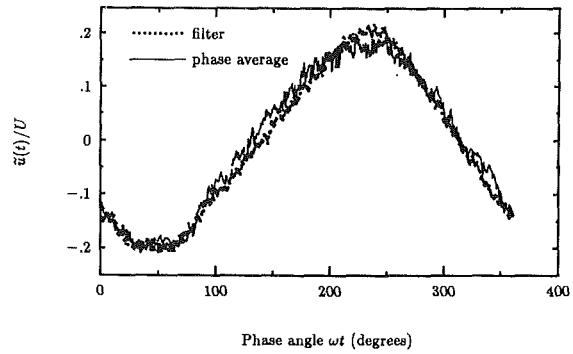

Fig. 4 Oscillatory components of the velocity time series of Fig. 2, deduced by phase averaging and filtering

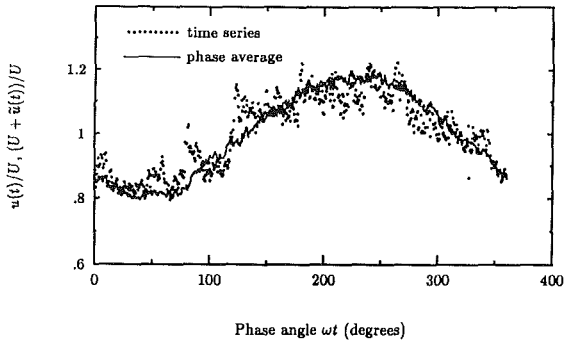

Fig. 5 Phase-average decomposition of a time series of streamwise velocity data. The data describe a cycle of forced sinusoidal unsteadiness which is lower in amplitude (16 percent of the mean velocity) than the previous 15 cycles of the time series (20 percent of the mean velocity)

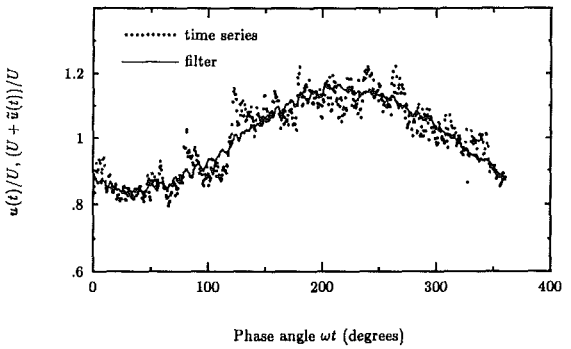

Fig. 6 Filter decomposition of the time series of Fig. 5

Unsteady turbulent velocity data from the same experiment, which include imposed cycle-to-cycle variation, are shown in Figs. 5 and 6. The particular cycle in these figures is one in which the organized motion over the cycle has a lower amplitude (16 percent of U) than the previous fifteen cycles (at an amplitude of 20 percent of U) which contribute to the phase average. In this case, the phase averaging technique produces the unrealistic result that the deviation of the turbulent component from the phase average is continuously positive for periods as long as a quarter of a cycle (0 to 90 deg in Fig. 5). When the same data is decomposed by frequency domain filtering (Fig. 6), the deviation of the turbulent component from the organized motion follows a much more realistic form with positive and negative excursions of approximately equal probability. The oscillatory motions deduced by the two decomposition procedures are shown in Fig. 7. In this figure, the failure of the phase average to adapt to the lower amplitude of this particular cycle may be seen clearly. The relative reductions in $\overline{u'u'}$ and $\overline{\tilde{u}\tilde{u}}$ when deduced by the filter technique

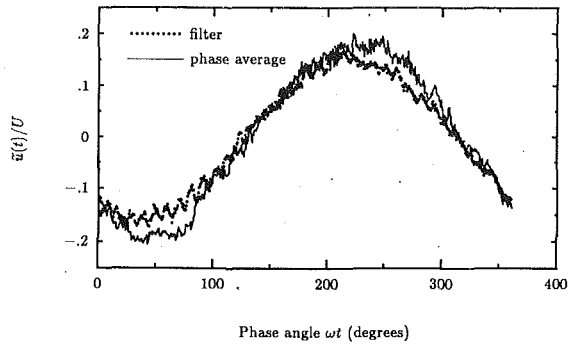

Fig. 7 Oscillatory components of the velocity time series of Fig. 5, deduced by phase averaging and filtering

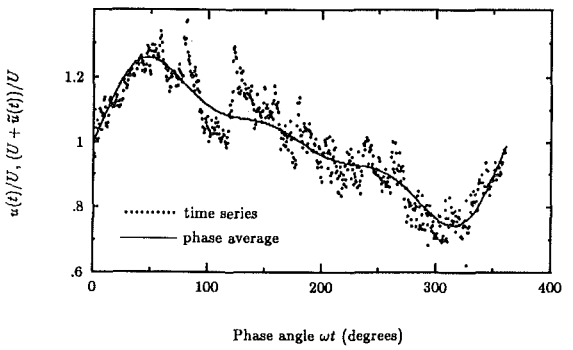

Fig. 8 Phase-average decomposition of a synthesized pulsatile motion upon which a time series of turbulence data has been superposed. The organized motion is identical in all cycles which comprise the time series.

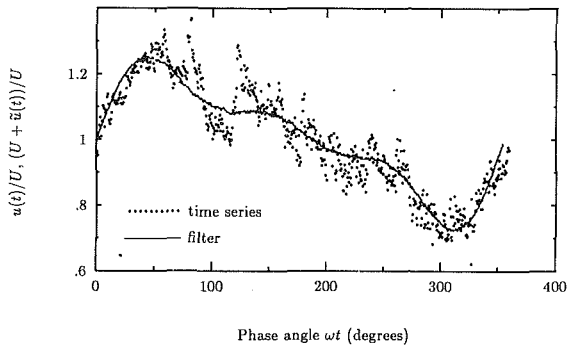

Fig. 9 Filter decomposition of the time series of Fig. 8

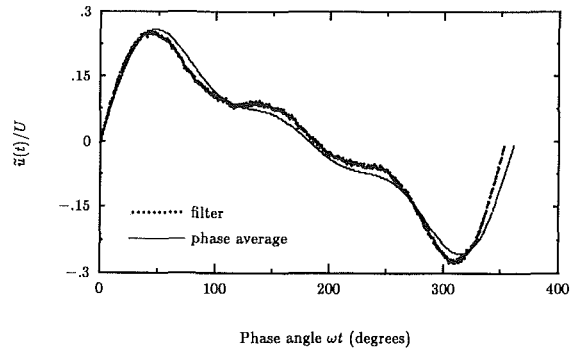

Fig. 10 Oscillatory components of the velocity time series of Fig. 8, deduced by phase averaging and filtering

are 16 percent and 24 percent, respectively. For the complementary case of a cycle in which the oscillatory motion took a higher amplitude (24 percent of U) than the fifteen previous cycles (20 percent of U) which contribute to the phase average, the same qualitative problems with the phase-average technique were observed. In this case, the relative improvement of the filter decomposition corresponded to a 31 percent increase in the estimate of $\overline{\tilde{u}\tilde{u}}$ with a commensurate 9 percent decrease in the estimate of $\overline{u'u'}$ (shown in Tables 1 and 2).

The quality of the frequency filter which makes it less sensitive to cycle-to-cycle variation is its proportional nature. While the filter is built from information pertaining to the entire time series, it uses this information only to deduce the proportions of the local signal $u(t)$ which contribute to $\tilde{u}(t)$ and to $u'(t)$. In contrast, the phase average fixes the absolute value of $\tilde{u}(t)$ based on information from multiple cycles and $u'(t)$ must take the local difference between $u(t)$ and $\tilde{u}(t)$. Thus when $|\tilde{u}(t)|$ is significantly greater than $|u'(t)|$, a small proportional error in the phase-averaged estimate of $\tilde{u}(t)$ corresponds to a large one in $u'(t)$ rather than the distribution of error by the frequency filter in proportion to the size of each component.

A fifth test case for the frequency-filtering decomposition is that of a synthesized pulsatile motion upon which a time series of measured turbulence data has been superposed. The synthesized waveform was chosen as the summation of several sine waves of different frequencies and amplitudes in a rough attempt to imitate some of the qualities of turbulent cardiovascular flows. Because the organized motion is analytical in form, it is reproduced perfectly by phase averaging and so follows the smooth curve shown in Fig. 8. The frequency filter decomposition, which *a priori* has no knowledge of the period of these motions, is shown in Fig 9 and bears a very close resemblance to the (correct) phase-average decomposition. Good agreement between the organized motions deduced by the two decompositions may be observed in Fig. 10. The relative discrepancies in $\overline{\tilde{u}\tilde{u}}$ and $\overline{u'u'}$ are about 4 percent and 2 percent, respectively, for decomposition of this time series. These close agreements attest further to the accuracy of the frequency-filter technique and to its ability to resolve more complex organized waveforms than single sine waves.

A number of other test cases of this kind have also been performed. With the exception of square waves and other steep waveforms, which are always problematic when using Fourier methods, all test cases yielded results comparable to those reported in Tables 1 and 2. Effects of small changes in the initial model for $S_{u'u'}(f)$ were also tested, by varying the level of $S_{u'u'}(f)$ by $\pm$ 10 percent both at individual frequencies and across the entire spectrum. Convergence was always to minima with comparable cross-correlation coefficients (for the same convergence tolerance), regardless of the initial model of $S_{u'u'}(f)$ chosen. However, while these minima were very close to one another, they were not unique. They corresponded to estimates of $S_{\tilde{u}\tilde{u}}(f)$ and $S_{u'u'}(f)$ the levels of which varied by up to 5 percent at any frequency, depending on the initial condition chosen. However, because the accuracy of estimates of $\tilde{u}(t)$ and $u'(t)$ are of second order with respect to the accuracy with which $S_{\tilde{u}\tilde{u}}(f)$ and $S_{u'u'}(f)$ are determined, the effect of choosing different initial models for $S_{u'u'}(f)$ was imperceptible in either $\tilde{u}(t)$, $u'(t)$, $\overline{\tilde{u}\tilde{u}}$, or $\overline{u'u'}$. Based on these tests, the frequency-domain filtering technique appears to be a reliable method for decomposition of time series of turbulent data, with proportional qualities which give it significant advantages over the phase-averaging technique when data exhibit cycle-to-cycle variation.

6 Discussion

A new technique for triple decomposition of unsteady turbulent flow has been developed which can surpass the phase-averaging technique in performance in practical circumstances when organized unsteady motions vary from cycle to cycle.

The success of the method is attributed to: (i) the novel approach of modeling information about the turbulent motion, rather than making *a priori* assumptions about the oscillatory component, and (ii) the recognition that an estimate of the proportion of the local velocity $u(t)$ which contributes to each of $\tilde{u}(t)$ and $u'(t)$ is much less sensitive to cycle-to-cycle variation than an estimate of a phase-dependent quantity as an average over successive cycles which have to be assumed identical in their organized motion. This technique should find application in numerous engineering flows in which it is important to distinguish between turbulence and organized yet imperfectly repetitive unsteady motions. It also offers advantages in processing laboratory data for which the phase-averaging technique would require averaging over a greater number of ensembles to achieve statistical convergence in cycle-to-cycle variations, as a prerequisite to deducing information on turbulent motion.

While this method is well suited to flows in which the shape of the turbulence energy spectrum is reasonably static throughout a cycle, application may prove troublesome in flows in which the shapes of the energy-spectral densities vary dramatically with time, or in regions of flows within which turbulent motion is intermittent or of very low intensity (comparable to the noise in the estimate of the organized motion); in addition the method is clearly unsuited to transitional or relaminarizing flows. For the case of flows with rapidly changing energy-spectra, an adaptive implementation of the method may be used to analyze a moving window of a densely sampled time series of data, to try to achieve local quasi-stationarity and satisfy better the assumptions on which this technique is based. The potential for application of the technique to non-stationary flows of this kind appears promising and presents a challenge for the future.

Acknowledgments

The first author is grateful to his colleague, Prof. Spilios Fassois, of the University of Michigan, for several illuminating discussions of modern time series analysis.

References

Box, G. E. P., and Jenkins, G. M., 1976, *Time Series Analysis: Forecasting and Control*, Holden-Day, Oakland, CA.

Brereton, G. J., Reynolds, W. C., and Jayaraman, R., 1990, "Response of a Turbulent Boundary Layer to Sinusoidal Free-Stream Unsteadiness," *J. Fluid Mech.*, Vol. 221, pp. 131–159.

Brereton, G. J., and Reynolds, W. C., 1991, "Dynamic Response of Boundary-Layer Turbulence to Oscillatory Shear," *Phys. Fluids A*, Vol. 3, No. 1, pp. 178–187.

Enotiadis, A. C., Vafidis, C., and Whitelaw, J. H., 1990, "Interpolation of Cycle Flow Variations in Motored Internal Combustion Engines," *Expt. Fluids.*, Vol. 10, pp. 77–86.

Hussain, A. K. M. F., and Reynolds, W. C., 1970, "The Mechanics of an Organized Wave in Turbulent Shear Flow," *J. Fluid Mech.*, Vol. 41, pp. 241–258.

Hwang, J.-L., and Brereton, G. J., 1991, "Turbulence in High Frequency Periodic Fully-Developed Pipe Flow," *Eighth Symp. Turbulent Shear Flows*, Technical University of Munich, 11-3-1.

Liou, T.-M., and Santavicca, D. A., 1985, "Cycle Resolved LDV Measurements in a Motored IC Engine," ASME *Journal of Fluids Engineering*, Vol. 107, pp. 232–240.

Pandit, S. M., and Wu, S. M., 1983, *Time Series and System Analysis with Applications*, Wiley, New York.

Peebles, P. Z., 1980, *Probability, Random Variables and Random Signal Principles*, McGraw-Hill, New York.

Ramaprian, B. R., and Tu, S. W., 1983, "Fully Developed Periodic Turbulent Pipe Flow. Part 2. The Detailed Structure of the Flow," *J. Fluid Mech.*, Vol. 137, pp. 59–81.

Rask, R. B., 1981, "Comparison of Window, Smoothed-Ensemble, and Cycle-to-Cycle Data Reduction Techniques for Laser Doppler Anemometer Measurements of in-Cylinder Velocity," *Fluid Mechanics of Combustion Systems*, ed., Morel, T., Lohmann, R. P., and Rackley, J. M., 11-20, ASME.

Tiederman, W. G., Privette, R. M., and Phillips, W. M., 1988, "Cycle-to-Cycle Variation Effects on Turbulent Shear Stress Measurements in Pulsatile Flows," *Expt. Fluids.*, Vol. 6, pp. 265–272.

Walburn, F. J., Sabbah, H. N., and Stein, P. D., 1983, "An Experimental Evaluation of the Use of an Ensemble Average for the Calculation of Turbulence in Pulsatile Flow," *Ann. Biomed. Eng.*, Vol. 11, pp. 385–399.

Witze, P. O., Martin, J. K., and Borgnakke, C., 1984, "Conditionally-Sampled Velocity and Turbulence Measurements in a Spark Ignition Engine," *Combust. Sci. Technol.*, Vol. 36, pp. 301–317.

On Turbulent Flows Dominated by Curvature Effects

G. C. Cheng
Research Scientist,
SECA, Inc.,
Huntsville, Ala

S. Farokhi
Associate Professor of Aerospace Engineering and Director of the Flight Research Laboratory,
The University of Kansas,
Lawrence, Kansas 66045

A technique for improving the numerical predictions of turbulent flows with the effect of streamline curvature is developed. Separated flows and the flow in a curved duct are examples of flow fields where streamline curvature plays a dominant role. New algebraic formulations for the eddy viscosity μ_t incorporating the $k-\epsilon$ turbulence model are proposed to account for various effects of streamline curvature. The loci of flow reversal (where axial velocities change signs) of the separated flows over various backward-facing steps are employed to test the capability of the proposed turbulence model in capturing the effect of local curvature. The inclusion of the effect of longitudinal curvature in the proposed turbulence model is validated by predicting the distributions of the longitudinal velocity and the static pressure in an S-bend duct and in 180 deg turn-around ducts. The numerical predictions of different curvature effects by the proposed turbulence models are also reported.

Introduction

The tremendous improvement of computer capabilities in the last decade, in memory and speed, has enabled accurate numerical predictions of turbulent flows. Due to the closure problem of the governing equations for turbulent flows, numerous turbulence models have been proposed. The eddy-viscosity type of turbulence closure modeling has demonstrated a variety of good numerical predictions both qualitatively and quantitatively. Among them, the $k-\epsilon$ model is the most widely employed isotropic two-equation model. It has been extensively applied to different turbulent flow problems. However, the standard $k-\epsilon$ model appears to be insufficient in predicting the complex turbulent shear layers, such as flows subjected to curvature and rotation.

Flows with streamline curvature are particularly of interest in engineering due to their frequent presence in real life applications. There are several types of streamline curvature problems that may occur in the flow field. The separated flows would be considered to involve local curvature; flows in curved ducts can be classified as a longitudinal curvature problem. The occurrence of streamline curvature could change the structure of turbulent flow fields drastically. A comprehensive literature review on the effect of streamline curvature was conducted (Cheng, 1990) and several conclusions were reached: 1) streamline curvature in the plane of the mean shear produces considerably large changes in higher-order quantities of the turbulent structure of shear layers, such as Reynolds stresses and turbulent kinetic energy, 2) turbulent mixing is inhibited by the presence of convex curvature; hence, the stabilizing effect will attenuate the Reynolds stresses and turbulent kinetic energy, 3) concave curvature has a destabilizing effect which will not only enhance the turbulence intensity and enlarge the length scale, but also induce the Görtler-type vortex structure in which the extra rate of strain becomes significant, and 4) the algebraic eddy-viscosity and the standard two-equation models are not adequate for the prediction of this type of complex shear layer.

Numerous models have been proposed in the last two decades (Cheng, 1990) to account for the effects of streamline curvature. Some of them (Launder et al., 1977; Pourahmadi and Humphrey, 1983; and Galmes and Lakshminarayana, 1984) either empirically introduce new terms into the transport equations of turbulence or artificially change modeling constants in turbulence models. Neither approaches are general enough to cover different streamline curvature effects and often lack physical justification. Some researchers (Hah and Lakshminarayana, 1980; Gibson and Rodi, 1981; Naot and Rodi, 1982; and Warfield and Lakshminarayana, 1987) suggested solving the Reynolds stress model or modifying the eddy viscosity to be a tensor such that the anisotropic effect caused by streamline curvature will be included. Clearly, more computing time and difficulties would arise in application of the proposed techniques.

In order to combine the simplicity (i.e., easily adopted into other programs or models), generality (suitable for different geometries), physical rationale, and efficiency (less computing time), the present study elaborates on algebraic formulation for the eddy viscosity μ_t. By extracting the extra strain rate and the main rate for the flow fields with different streamline curvature environments, new algebraic expressions for the eddy viscosity are derived from the algebraic Reynolds-stress model. In the proposed eddy-viscosity formulations, the flux Richardson number R_f plays an important role as it dictates the effects of various streamline curvature on the turbulence structure through the amplification or diminution of the eddy viscosity. Different coordinate systems are employed for various effects of streamline curvature in accordance with geometrical flow characteristics. In addition, the $k-\epsilon$ model will be adopted incorporating the proposed formulation for the eddy viscosity.

Contributed by the Fluids Engineering Division for publication in the JOURNAL OF FLUIDS ENGINEERING. Manuscript received by the Fluids Division January 23, 1991.

The numerical computations are performed on the Cray X-MP supercomputer at NASA-Lewis Research Center.

Governing Equations

The system of governing equations for the time-averaged, steady, incompressible, adiabatic turbulent flow field is expressed in tensor notation and shown as follows.

The continuity equation (conservation of mass)

$$\frac{\partial U_i}{\partial X_i}=0 \tag{1}$$

The momentum equations (conservation of momentum)

$$\rho U_j \frac{\partial U_i}{\partial X_j}=-\frac{\partial P}{\partial X_i}+\frac{\partial}{\partial X_j}\left[\mu\left(\frac{\partial U_i}{\partial X_j}+\frac{\partial U_j}{\partial X_i}\right)-\rho\overline{u_i u_j}\right] \tag{2}$$

where U_i and u_i represent the time-mean and fluctuating velocity components, respectively; P is the time-mean static pressure; and ρ is the density. The term $-\rho\overline{u_i u_j}$ is regarded as Reynolds stress or turbulent stress. Since the Reynolds-stress term appears in Eq. (2), additional equations are needed to solve the system of equations. Turbulence closure modeling is therefore required to balance the numbers of unknowns and the governing equations. The $k-\epsilon$ model, proposed by Launder and Spalding (1972), is the widest applied two-equation eddy-viscosity model and is employed in the present study.

In the $k-\epsilon$ model, the Boussinesq's eddy-viscosity concept is used, in which the Reynolds stress is defined as

$$-\rho\overline{u_i u_j}=\mu_t\left(\frac{\partial U_i}{\partial X_j}+\frac{\partial U_j}{\partial X_i}\right)-\frac{2}{3}\delta_{ij}\rho k \tag{3}$$

where μ_t is eddy or turbulent viscosity. The formulation for the eddy viscosity μ_t, used in the standard $k-\epsilon$ model, is obtained, based on Jones-Launder length-scale model and Prandtl-Kolmogorov formula, as

$$\mu_t=\rho C_\mu \frac{k^2}{\epsilon} \tag{4}$$

where C_μ is an empirical constant with a value of 0.09, k is the turbulent kinetic energy, and ϵ is the turbulence dissipation rate. Also, there are two transport equations for k and ϵ, and they are given as

$$C_k=P_r+D_k-\epsilon \tag{5}$$

where

$$C_k=U_k\frac{\partial k}{\partial X_k} \tag{6}$$

$$P_r=\frac{\mu_t}{\rho}\left(\frac{\partial U_i}{\partial X_k}+\frac{\partial U_k}{\partial X_i}\right)\frac{\partial U_i}{\partial X_k} \tag{7}$$

$$D_k=\frac{1}{\rho}\frac{\partial}{\partial X_k}\left(\frac{\mu_t}{\sigma_k}\frac{\partial k}{\partial X_k}\right) \tag{8}$$

and

$$U_k\frac{\partial \epsilon}{\partial X_k}=\frac{1}{\rho}\frac{\partial}{\partial X_k}\left(\frac{\mu_t}{\sigma_\epsilon}\frac{\partial \epsilon}{\partial X_k}\right)$$

$$+C_{\epsilon 1}\frac{\epsilon}{k}\frac{\mu_t}{\rho}\left(\frac{\partial U_i}{\partial X_k}+\frac{\partial U_k}{\partial X_i}\right)\frac{\partial U_i}{\partial X_k}-C_{\epsilon 2}\frac{\epsilon^2}{k} \tag{9}$$

In these equations, σ_k, $C_{\epsilon 1}$, $C_{\epsilon 2}$, and σ_ϵ are empirical constants and have the values of 1.0, 1.44, 1.92, and 1.3, respectively. The modeling constant C_μ in the eddy viscosity formulation, as shown in Eq. (4), is empirically tuned for the simple shear layers. There is no mechanism in the model which can either amplify the turbulent intensity or eddy viscosity in the presence of concave curvature, or inhibit turbulence mixing with the application of convex curvature. Therefore, the expression for the eddy viscosity in the standard $k-\epsilon$ model is considered to be inadequate in accounting for the streamline curvature effect.

Turbulence Modeling

An algebraic Reynolds stress model, proposed by Rodi (1976), is chosen to simplify the Reynolds-stress model, proposed by Launder et al. (1975). The assumption in Rodi's model is that net transport of Reynolds stresses $\overline{u_i u_j}$ is proportional to the net transport of turbulent kinetic energy, k, i.e.,

$$C_{ij}-D_{ij}=\frac{\overline{u_i u_j}}{k}(C_k-D_k) \tag{10}$$

where C_{ij} and D_{ij} are the convection and diffusion terms of the Reynolds stress. By combining Eq. (5), Eq. (10), and the Reynolds-stress model $\overline{u_i u_j}$ of Launder et al. (1975), an algebraic expression for $\overline{u_i u_j}$ can be obtained as

$$\frac{\overline{u_i u_j}}{k}=\frac{\phi}{\epsilon}\left[P_{ij}-\frac{2}{3}\delta_{ij}P_r\right]+\frac{2}{3}\delta_{ij} \tag{11}$$

where

$$\phi=\frac{1-C_2}{C_1-1+\dfrac{P_r}{\epsilon}} \tag{12}$$

and P_{ij} is the production rate of the Reynolds stress $\overline{u_i u_j}$; δ_{ij} is the Kronecker delta function; P_r and ϵ are the production and dissipation rates of the turbulent kinetic energy, respectively; and C_1 and C_2 are the inertial and forced return-to-isotropy constants, respectively. This approximation is only invalid when $\overline{u_i u_j}/k$ terms change rapidly which often occur in the nearwall region. This deficiency can be avoided, however, by using the wall function.

For the further simplification of Eq. (11), some analysis of the various streamline curvature flow fields need to be conducted. First, for the flows with local curvature, such as the flow over an airfoil and the separated flows in a backward-facing step geometry, the streamwise direction at the downstream does not change appreciably from that at the upstream. In this case, the Cartesian (x,y) coordinate system is selected, and the extra rate of strain is considered to be $\partial V/\partial x$ (Bradshaw, 1973) besides the main rate of strain $\partial U/\partial y$. By keeping terms associated with these two strain rates, and through some manipulations (Cheng, 1990), the main Reynolds stress term $-\overline{uv}$ is obtained as

$$-\overline{uv}=\frac{k^2}{\epsilon}\frac{\partial U}{\partial y}\frac{2}{3}\phi\left[1-\mathrm{R_f}-\phi\frac{P_r}{\epsilon}\frac{\mathrm{R_f^2}+4\mathrm{R_f}+1}{1-\mathrm{R_f}}\right] \tag{13}$$

where the flux Richardson number $\mathrm{R_f}$ is defined as

$$\mathrm{R_f}=-\frac{\partial V/\partial x}{\partial U/\partial y} \tag{14}$$

and U and u are the mean and fluctuating velocity components in the streamwise direction, V and v are the mean and fluctuating velocity components in the transverse direction, respectively. In conjunction with the Boussinesq's eddy-viscosity concept, an algebraic expression for the eddy viscosity μ_t can be derived as

$$\mu_t=\rho\frac{k^2}{\epsilon}\frac{2\phi}{3}\left[1-\mathrm{R_f}-\phi\frac{P_r}{\epsilon}\frac{\mathrm{R_f^2}+4\mathrm{R_f}+1}{1-\mathrm{R_f}}\right] \tag{15}$$

In the second category of flows with curvature, the streamwise direction may change significantly, for example the flow in an S-bend duct or any longitudinally curved ducts. Therefore, the approximation procedure will be performed based on the natural (s,n) coordinate system to be in accordance with the flow characteristics. The s-coordinate is in the streamwise

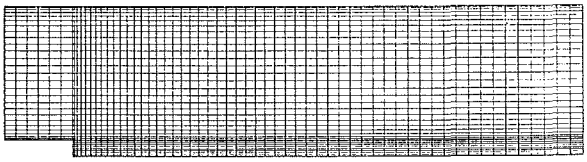

Fig. 1 Grid system for a two-dimensional backward-facing step geometry

direction with the mean and fluctuating velocity components U and u, and n-coordinate represents the direction normal to s-coordinate with the mean and fluctuating velocity components V and v. In these cases, the term "U/R" is known to represent the extra rate of strain in addition to the main rate of strain $\partial U/\partial n$. By retaining the terms associated with these two strain rates and following a similar procedure described in Cheng (1990), an identical expression for the eddy viscosity μ_t is obtained, whereas the flux Richardson number R_f is now given by

$$R_f = \frac{2U/R}{\left(1+\frac{n}{R}\right)\frac{\partial U}{\partial n}+\frac{U}{R}} \tag{16}$$

where R is the radius of surface curvature and n is the normal distance from the wall. The above formulation represents a very feasible and practical approach to turbulence modeling which requires no change for different coordinate systems for engineering applications.

With the flux Richardson number embedded in the eddy-viscosity formulation, streamline curvature can influence the eddy viscosity and so the Reynolds stress directly. It is evident that the flux Richardson number R_f is positive for convex curvature (stabilizing effect), and hence the eddy viscosity is diminished. On the other hand, concave curvature (destabilizing effect) gives a negative value for R_f which enhances the eddy viscosity. This modification is therefore consistent with both the physics of the problem and the conclusions reached in experimental research. The effect of streamline curvature on the eddy viscosity vanishes as $R_f \to 0$, and the correlation for the eddy viscosity becomes

$$\mu_t = \rho \frac{k^2}{\epsilon}\frac{2}{3}\phi\left[1-\phi\frac{P_r}{\epsilon}\right] \tag{17}$$

To determine the two return-to-isotropy modeling constants, C_1 and C_2, in Eq. (12), the above equation is matched with the correlation for the eddy viscosity in the standard $k-\epsilon$ model at the free stream conditions, which are zero curvature and local equilibrium. With these conditions, we obtain

$$C_\mu = \frac{2}{3}\phi_0(1-\phi_0) \tag{18}$$

where

$$\phi_0 = \frac{1-C_2}{C_1} \tag{19}$$

and C_μ is an empirical constant in the standard $k-\epsilon$ model with a value of 0.09. The values of C_1 and C_2 have been proposed differently by several researchers (Launder et al., 1975; Gibson and Launder, 1976 and 1978; Gibson and Younis, 1986) and were expected not to affect the results substantially. This is verified in Cheng (1990). In the present investigation, therefore, C_1 is selected to be 1.5 as suggested in Launder et al. (1975), which in turn yields $C_2 = 0.76$ from Eqs. (18) and (19).

A two-dimensional Navier-Stokes flow solver (FDNS-2D), developed by Y. S. Chen (1988a, 1988b) and embedded with the standard $k-\epsilon$ model, is employed to validate the proposed turbulence model in the present study. The numerical algorithm for the flow solver is that of a second-order finite differencing scheme which is used for temporal and spatial discretizations,

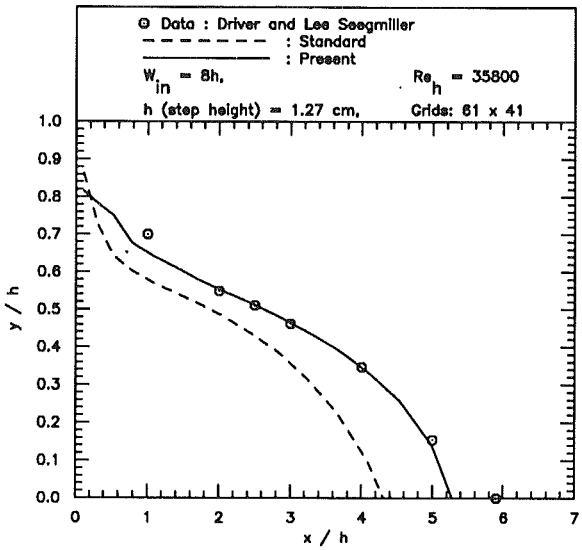

Fig. 2 Locus of flow reversal in a backward-facing step flow

incorporating a quasi-damping scheme, deduced from second-order upwind differencing scheme for the convection terms. The modified predictor-corrector solution procedure is applied in the flow solver with an explicit forth-order pressure smoothing term added to the velocity-pressure coupled discrete equation to inhibit the instability in the pressure solution.

Results and Discussions

The flow over a backward-facing step, investigated by Driver and Seegmiller (1985), is used to test the proposed model for the flow with local curvature effect. Orthogonal grids are generated for this geometry and are shown in Fig. 1. The comparison is made between the present model and the standard $k-\epsilon$ with 61 × 41 grids. The flow prediction improvement by the present model is observed from the locus of flow reversal illustrated in Fig. 2. The result indicates that the present model predicts later flow reattachment than does the standard $K-\epsilon$ model. It appears that the present model can account for the reduction of the eddy viscosity in the main flow domain. This is caused by the effect of convex curvature on the primary flow as the flow separates from the step. The flow separation will also generate the effect of concave curvature on the secondary flow in the recirculation zone. However, the mass flux and momentum flux in this region are small. The effect of the eddy-viscosity increase in the recirculation zone, thus, is much smaller than the effect of the eddy-viscosity reduction in the primary flow. Moreover, since there is no mechanism in the standard $k-\epsilon$ model to simulate the curvature effect, the predicted convex shear layer exhibits a higher viscosity and an earlier reattachment in the standard $k-\epsilon$. The streamwise velocity profiles shown in Fig. 3. demonstrate better predictions by the present model as well.

The turbulent kinetic energy profiles illustrated in Fig. 4, reveal the reductions of the turbulent kinetic energy by the convex curvature in the present model. However, both models underpredict the turbulent kinetic energy when the flow is near the reattachment location. This is possibly attributed to the effects of flow unsteadiness and turbulence anisotropy near the reattachment point. The low-frequency fluctuation induced by the flow separation will contribute to the turbulent kinetic energy in experiment, but will be omitted during the time-averaging process (where only the high-frequency fluctuation will remain) used in the turbulence modeling. The anisotropy effect, which is dominant at the near-wall region, is also left out in the isotropic $k-\epsilon$ model. The relatively successful prediction on the Reynolds shear stress $-\overline{uv}$, as shown in Fig. 5, suggests the validity of the curvature-corrected eddy viscosity

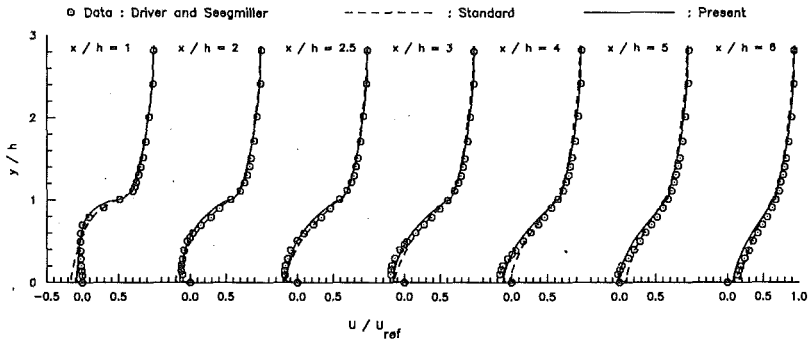

Fig. 3 Streamwise velocity profiles in a backward-facing step flow

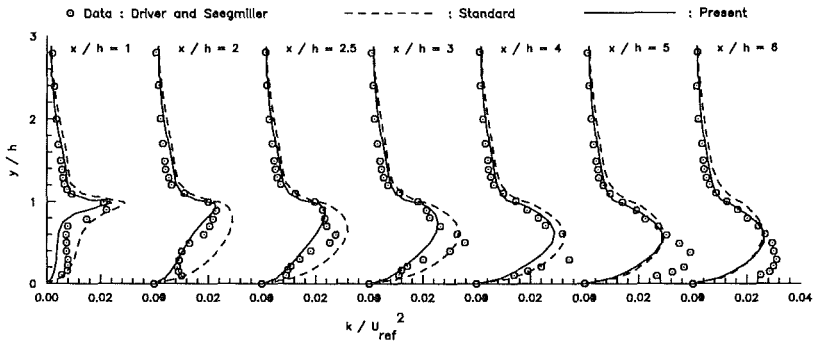

Fig. 4 Turbulent kinetic energy profiles in a backward-facing step flow

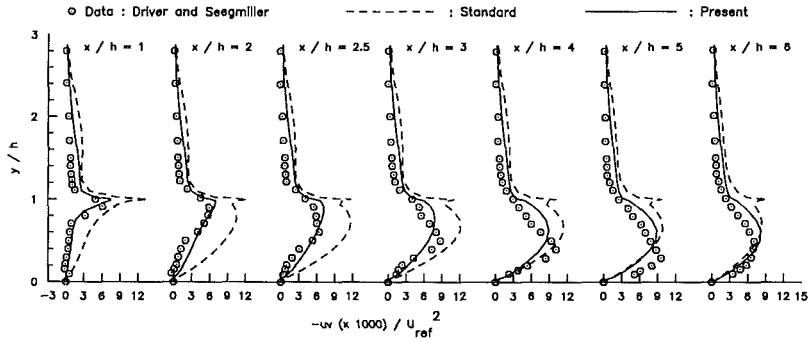

Fig. 5 Reynolds shear stress $-\overline{uv}$ profiles in a backward-facing step flow

formulation. Meanwhile, it is worth noting that with all the improvements of the numerical predictions by the present model, only minor increase of CPU time are introduced (Cheng, 1990). This indicates the practicality and feasibility of the current approach.

A good test case to evaluate a turbulence model with the effect of longitudinal curvature is a 2-D S-bend duct, since the second bend creates an opposite effect as that of the first and establishes a rather complicated flow field. An 88 × 51 orthogonal grid system is constructed for the 30 – 45 deg S-bend duct (Butz, 1979) with the radius of curvature along the centerline of the duct equal to five inlet widths, as illustrated in Fig. 6. The result of static pressure coefficients in Fig. 7 demonstrates a better agreement of the present model with the measured data on the concave side of the second bend than the standard $k-\epsilon$ model. However, both models fail to predict the static pressure on the upper surface in the first bend (concave side). The discrepancy on the upper surface in the first bend is suspected to be caused by the Görtler-type secondary flows. This occurs at the onset of the concave curvature, where the normal velocity is numerically set equal to zero at the entrance plane. The error of predicted static pressure on the upper surface in the first bend (concave side) is considered to be the primary source of deviation of the numerical calculation

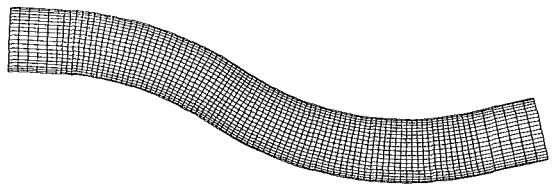

Fig. 6 Mesh system for a two-dimensional S-bend duct geometry

from the experimental results on the same surface in the second bend (convex side). It appears that both models predict the mean longitudinal velocity at the exit very well, as indicated in Fig. 8. In this case, the improvement by the present model is not significant because the surface curvature is relatively small. A 2-D curved duct with large curvature, therefore, is necessary to evaluate the performance of the present model in predicting the development of turbulence structures subjected to strong streamwise curvature effect.

A 180 deg turn-around water tunnel, with a 10 cm centerline radius of curvature and a 10-by-100 cm cross section, investigated by Sandborn and Shin (1989), is employed as the next test case. A 141 × 41 orthogonal grid mesh is constructed for this geometry, as shown in Fig. 9. The longitudinal velocity profiles in Fig. 10 display the similarity between the predictions

of the present model and those of the standard $k-\epsilon$ model upstream of the flow separation. However, the results demonstrate the success of the present model and the collapse of the standard $k-\epsilon$ model in capturing the separation bubble on the inner surface (convex curvature) near the exit of 180 deg turn. The larger eddy viscosity along the inner surface predicted by the standard $k-\epsilon$ model prevents the occurrence of flow separation; whereas, smaller eddy viscosity computed by the present model, benefiting from curvature correction, enables the natural onset of flow separation. The results indicate that the proposed implementation to the standard $k-\epsilon$ model is necessary and proper. The separation bubble in the turn-around duct can be clearly observed from Fig. 11, where particle traces are plotted.

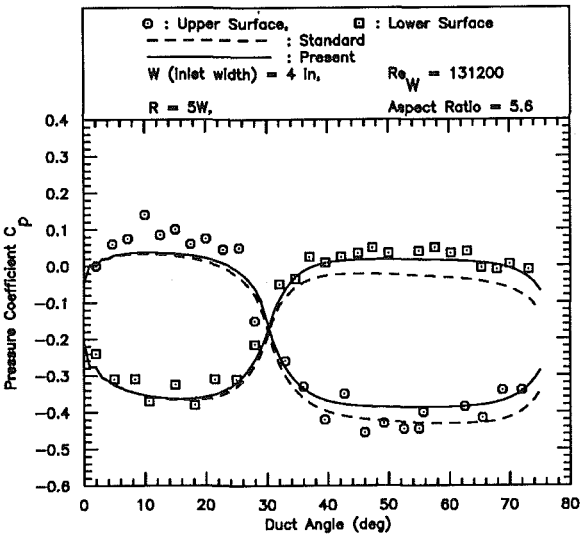

Fig. 7 Static pressure coefficient distribution for a 30-45 deg S-bend duct

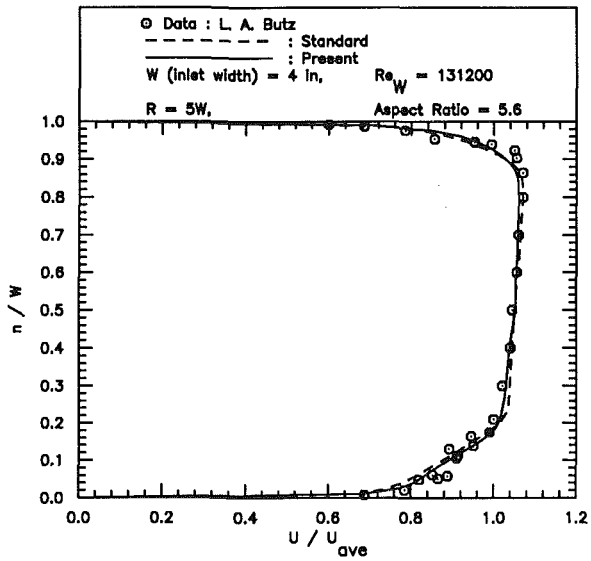

Fig. 8 Longitudinal velocity profile at the exit plane of a 30-45 deg S-bend duct

Conclusions

Algebraic Reynolds stress models with flux Richardson number parameter representing various curvature effects are proposed. Three curved flows are considered. In the backwardfacing step flow, the proposed model is indeed capable of dictating the effect of local curvature cause by flow separation. The present model, however, underpredicts the reattachment point. This problem is attributable to the effects of flow unsteadiness, large-scale eddy, and turbulence anisotropy in the recirculation zone. The flow unsteadiness can be accounted for by applying the present model to the 3-D configuration with the time-accurate numerical scheme, as long as the flow characteristics are the same (i.e., have the same dominant extra rate of strain). However, this needs to be further verified. In addition, the flow inside the recirculation zone is basically dominated by a large-scale eddy with low Reynolds number. This is a deficiency of the high-Reynolds-number $k-\epsilon$ model used in this study. It is also known that the anisotropic effect becomes dominant as the flow approaches the wall, thus the effect plays an important role near the reattachment region.

In the curved-duct flows, the present model demonstrates a good agreement with the measured data. The major success of the present model is to predict the flow separation in strongly curved ducts. Flows with transverse curvature, as in swirling flows, require a more sophisticated turbulence modeling.

Acknowledgment

The research presented in this paper is supported by NASA research grant NAG 3-841. The contributions of Dr. Charles

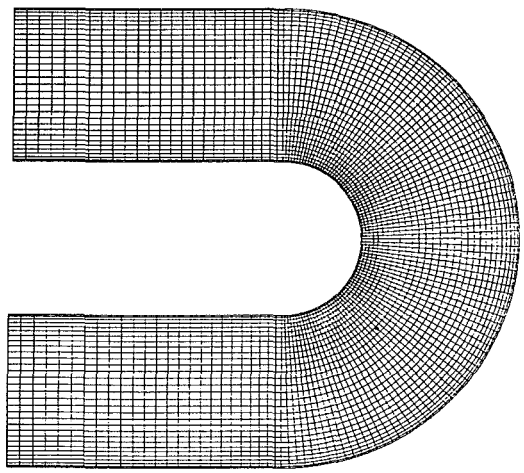

Fig. 9 Grid system for a two-dimensional 180 deg turn-around duct

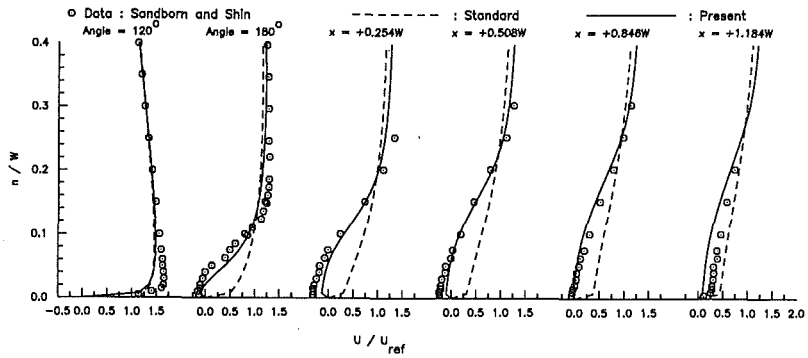

Fig. 10 Longitudinal velocity profiles in a 180 deg turn-around duct

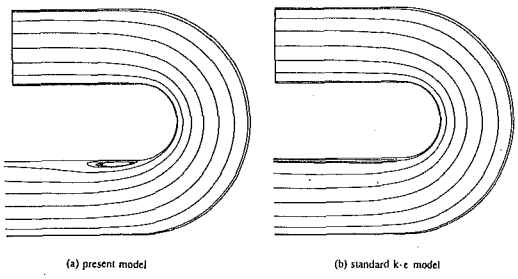

Fig. 11 Particle traces in a 180 deg turn-around duct

Towne of NASA-Lewis in the accomplishment of this research is greatly appreciated.

References

Bradshaw, P., 1973, "Effects of Streamline Curvature on Turbulent Flow," AGARDograph No. 169.

Butz, L. A., 1979, "Turbulent Flow in S-Shaped Ducts," M.S. thesis, Aeronautics and Astronautics Dept., Purdue University.

Chen, Y. S., January 1988a, "Viscous Flow Computations Using a Second-Order Upwind Differencing Scheme," AIAA Paper 88-0417, AIAA 26th Aerospace Science Meeting.

Chen, Y. S., 1988b, "3-D Stator-Rotor Interaction of the SSME," AIAA Paper 88-3059, AIAA 24th Joint Propulsion Conference.

Cheng, G. C., 1990, "The Effect of Streamline Curvature and Swirl on Turbulence Modeling in Curved Ducts," Ph.D. thesis, The University of Kansas, Lawrence, Kansas.

Driver, D. M., and Seegmiller, H., 1985, "Features of a Reattaching Turbulent Shear Layer in Divergent Channel Flow," *AIAA Journal*, Vol. 23, No. 2, pp. 163–171.

Galmes, J. M., and Lakshminarayana, B., 1984, "Turbulence Modeling for Three-Dimensional Shear Flows over Curved Rotating Bodies," *AIAA Journal*, Vol. 22, No. 10, pp. 1420–1428.

Gibson, M. M., and Launder, B. E., 1976, "On the Calculation of Horizontal Turbulent, Free Shear Flows under Gravitational Influence," ASME *Journal of Heat Transfer*, Vol. 98, pp. 81–87.

Gibson, M. M., and Launder, B. E., 1978, "Ground Effects on Pressure Fluctuations in the Atmospheric Boundary Layer," *Journal of Fluid Mechanics*, Vol. 86, pp. 491–511.

Gibson, M. M., and Rodi, W., 1981, "A Reynolds-Stress Closure Model of Turbulence Applied to the Calculation of a Highly Curved Mixing Layer," *Journal of Fluid Mechanics*, Vol. 103, pp. 161–182.

Gibson, M. M., and Younis, B. A., 1986, "Calculation of Swirling Jets with a Reynolds Stress Closure," *Physics of Fluids*, Vol. 29, pp. 38–48.

Hah, C., and Lakshminarayana, B, 1980, "Prediction of Two- and Three-Dimensional Asymmetrical Turbulent Wakes, Including Curvature and Rotation Effects," *AIAA Journal*, Vol. 18, No. 10, 1980, pp. 1196–1204.

Launder, B, E., and Spalding, D. B., 1972, *Mathematical Models of Turbulence*, Academic Press, London.

Launder, B. E., Reece, G. J., and Rodi, W., 1975, "Progress in the Development of a Reynolds-Stress Turbulence Closure," *Journal of Fluid Mechanics*, Vol. 68, Part 3, pp. 537–566.

Launder, B. E., Priddin, C. H., and Sharma, B. I., March 1977, "The Calculation of Turbulent Boundary Layers on Spinning and Curved Surfaces," ASME JOURNAL OF FLUIDS ENGINEERING, pp. 231–239.

Naot, D., and Rodi, W., August 1982, " Calculation of Secondary Currents in Channel Flow," *Journal of Hydraulics Division*, Vol. 108, No. HY8, pp. 948–968.

Pourahmadi, F., and Humphrey, J. A. C., 1983, "Prediction of Curved Channel Flow with an Extended $k-\epsilon$ Model of Turbulence," *AIAA Journal*, Vol. 21, No. 10, pp. 1365–1373.

Rodi, W., 1976, "A New Algebraic Relation for Calculating the Reynolds Stresses," *Zeitschrift für Angewandte Mathematik und Mechanik*, Vol. 56, pp. T219–T221.

Sandborn, V. A., and Shin, J. C., June 1989, "Water Flow Measurements in a 180 Degree Turn-Around Duct," Report Prepared under Contract No. NAS8-36354.

Warfield, M. J., and Lakshminarayana, B., 1987, "Computation of Rotating Turbulent Flow with an Algebraic Reynolds Stress Model," *AIAA Journal*, Vol. 25, No. 7, pp. 957–964.

R. H. Fashbaugh
Department of Mechanical Engineering,
University of Reno,
Reno, NV 89557

Inlet Boundary Conditions for Shock Wave Propagation Problems in Air Ducts

Introduction

Accurate prediction of shock waves propagating into air ducting systems is of interest in the design of military facilities. The solution of this problem is necessarily a numerical one in which fundamental differential equations are integrated utilizing a finite difference approach. For accurate solutions to be obtained it is necessary that viscous losses at the inlet to a duct be properly included in the solution. These losses have to be included in the solution empirically using experimental data, which is primarily from shock tube experiments. A considerable amount of experimental data are available that deals with shock wave attenuation at the entrance to an air duct. A summary of these data is given by Kriebel et al. (1972). The most comprehensive experiments were conducted at the Ballistic Research Laboratory (1962). Other contributions were by Zimmerman et al. (1970), Deckker and Male (1967) and Heilig (1975). The data used in this study were taken from the summary by Kriebel (1972). These data are put into a form here that facilitates its use in a numerical solution.

Various types of inlet junctions are possible in air ducting systems. The junction types for which experimental data are available are shown in Fig. 1. The bulk of the data is for small-scale junctions mounted in shock tubes with the incident shock wave essentially a flat-topped wave.

Duct Inlet Loss Simulation

The simulation of a duct entrance is achieved by evaluating the flow losses from a point s outside of the duct entrance to a point e inside of the entrance where the transmitted shock wave has formed. The point e can be one and one-half to ten diameters from the entrance depending on the type of entrance by Kriebel et al. (1972). The flow loss is measured by the increase in entropy ΔS from point s to point e. Assuming that the ratio of specific heats γ does not change significantly from point s to point e, the entropy change from the combined first and second law of thermodynamics can be shown to yield,

$$\Delta S = R\ ln\left[\left(\frac{T_e}{T_s}\right)^{\frac{\gamma}{\gamma-1}}\left(\frac{p_s}{p_e}\right)\right] \tag{1}$$

The equation of state for an ideal gas, $p = \rho RT$, has been assumed in deriving relation (1), and the combined first and second law used in the form, $Tds = dh + dp/\rho$. The entropy change can also be expressed in terms of stagnation variables as

Contributed by the Fluids Engineering Division for publication in the JOURNAL OF FLUIDS ENGINEERING. Manuscript received by the Fluids Engineering Division July 31, 1990.

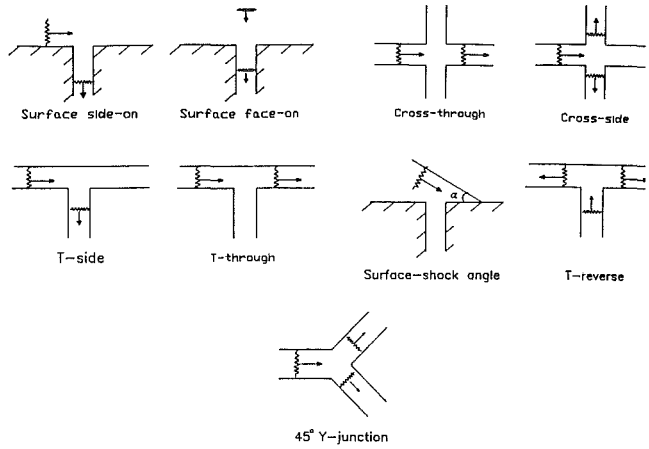

Fig. 1 Duct junction types considered in the study

$$\Delta S = R\ ln\left[\left(\frac{T_{te}}{T_{ts}}\right)^{\frac{\gamma}{\gamma-1}}\left(\frac{p_{ts}}{p_{te}}\right)\right] \tag{2}$$

Equating relations (1) and (2) will yield a relation (3) for the static pressure p_e at the point where the transmitted shock wave has formed in terms of the static pressure p_s behind the incident shock wave outside of the junction.

$$p_e = p_s\left(\frac{p_{te}}{p_{ts}}\right)\left[\left(\frac{T_e}{T_{te}}\right)\left(\frac{T_{ts}}{T_s}\right)\right]^{\frac{\gamma}{\gamma-1}} \tag{3}$$

Since the flow is adiabatic but not necessarily steady T_{te} is not equal to T_{ts}. The pressure p_e depends upon the stagnation pressure ratio p_{te}/p_{ts} which is determined from experimental data and p_e also depends upon the static to stagnation temperature ratios T_e/T_{te} and T_s/T_{ts} which are functions of the Mach numbers at point e and point s, respectively. By plotting the experimental data as p_{te}/p_{ts} versus M_s for each type of duct inlet shown in Fig. 1, it is found that the losses in any of the junctions can be expressed by the relation

$$\frac{p_{te}}{p_{ts}} = A_2 \exp(-A_1 M_s), \tag{4}$$

where A_1 and A_2 are constants which are different for each type of junction. A typical plot of experimental data is shown in Fig. 2 for a surface side-on type entrance. The curve is essentially linear for this semi-logarithmic plot. The values of the constants A_1 and A_2 were determined using the method of

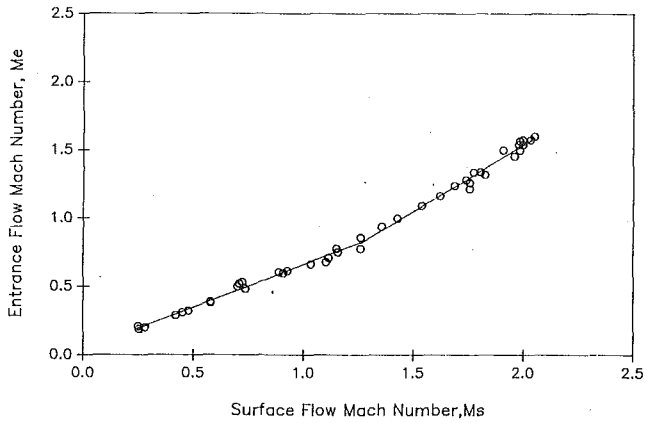

Fig. 2 Stagnation pressure ratio versus surface Mach number for side-on entrance (BRL data, 1962)

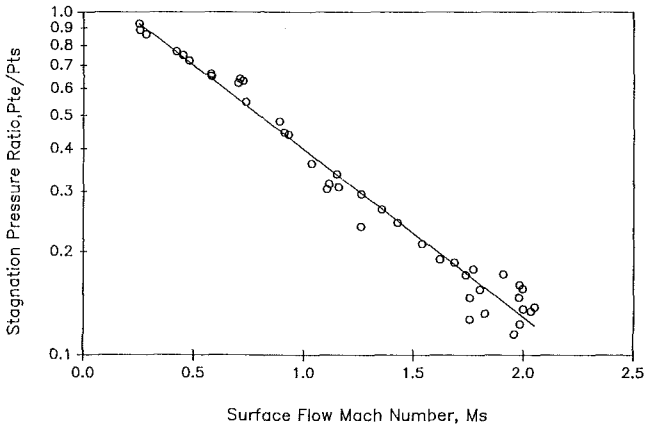

Fig. 3 Mach number, M_e, versus Mach number, M_s, for side-on entrance (BRL data, 1962)

Table 1 Duct inlet type and stagnation pressure parameters

Type of Inlet	Equation constants A_1	A_2	Corr. coeff. r
No inlet loss	0.00	1.00	
Surface side-on	1.129	1.24	0.99
Surface face-on	−0.140	1.30	0.36
T-junction, side trans.	1.210	1.13	0.97
T-junction, through trans.	0.341	0.99	0.63
T-junction, reverse trans.	0.570	1.07	0.88
45 degree Y-junction	0.610	1.00	0.96
Cross-junction, side trans.	1.200	1.02	0.98
Cross-junction, through trans.	0.260	0.93	0.88
Surface side-on, 50 deg	0.610	1.52	0.99
Surface side-on, 60 deg	0.510	1.61	0.98
Surface side-on, 70 deg	0.340	1.61	0.98
Surface side-on, 80 deg	0.120	1.56	0.78

Table 2 Duct inlet type and Mach number parameters

Type of inlet		Equation constants A_3	A_4	Corr. coeff. r
Surface side-on	$M_s \le 1.2$	0.615	0.0413	0.99
" "	$1.2 < M_s \le 1.8$	0.975	0.412	0.99
Surface face-on	$M_s \le 1.4$	0.964	0.163	0.99
T-junction, side trans.	$M_s \le 1.2$	0.615	0.041	0.97
" " "	$1.2 < M_s \le 1.7$	0.975	0.0412	0.98
T-junction, through trans.	$M_s \le 1.5$	0.940	−0.050	0.99
T-junction, reverse trans.	$M_s \le 1.6$	0.876	−0.025	0.99
45 degree Y-junction	$M_s \le 1.12$	0.832	−0.047	0.99
Cross-junction, side trans.	$M_s \le 1$	0.450	0.0	0.99
" " "	$1 < M_s \le 1.5$	1.133	−0.683	0.96
Cross-junction, through trans.	$M_s \le 1$	0.840	0.0	0.99
" " "	$1 < M_s \le 1.5$	1.220	−0.380	0.96
Surface side-on, 50 deg	$M_s \le 1.12$	0.780	0.154	0.99
Surface side-on, 60 deg	$M_s \le 1.12$	0.796	0.194	0.99
Surface side-on, 70 deg	$M_s \le 1.12$	0.830	0.213	0.99
Surface side-on, 80 deg	$M_s \le 1.12$	0.886	0.220	0.99

least-squares for each of the junction types shown in Fig. 1 through plots similar to Fig. 2. Values for A_1 and A_2 for all the junctions considered are tabulated in Table 1.

To complete the specification of the static pressure p_e behind the transmitted shock wave, the Mach number outside the inlet, M_s, and the Mach number inside the inlet, M_e, need to be known. Since M_s is specified, a relation between M_e and M_s is needed. This relation is obtained from the experimental shock tube data, also. A curve of M_e versus M_s for the surface side-on entrance is shown in Fig. 3. Similar curves were made for each of the junction types of Figure 1. The relationships for M_e in terms of M_s are of the form

$$M_e = A_3 M_s + A_4 \tag{5}$$

where A_3 and A_4 are constants with values given in Table 2 for each of the junction types considered. Constants A_3 and A_4 were determined using the method of least-squares. Having values for the Mach numbers M_e and M_s yields the static to stagnation temperature ratios required in relation (3).

Duct Entrance Mass Inflow Calculation

This method of specifying inlet losses has been used by the author in solutions using a Lagrangian finite difference method. The finite different zones are of fixed mass and move with the flowing fluid. Mass inflow into a duct therefore requires periodically establishing a new finite difference zone at the duct entrance. When a new inlet zone is created the internal energy of the new zone is determined by assuming the stagnation enthalpy does not change from point s outside the junction to point e inside the junction. This assumption yields the internal energy e_e as

$$e_e = \frac{1}{\gamma}\left(h_{ts} - \frac{1}{2}u_e^2\right) \tag{6}$$

Nomenclature

A_1 = empirical constant
A_2 = empirical constant
A_3 = empirical constant
A_4 = empirical constant
e = internal energy per unit mass
h = enthalpy per unit mass
M = flow Mach number
p = static pressure
p_t = stagnation pressure
R = gas constant for air
ΔS = entropy change per unit mass
T = static temperature
T_t = stagnation temperature
u = local flow velocity
ρ = mass density
γ = ratio of specific heats for air

Subscripts

s = point in flow upstream of a duct inlet junction
e = point in flow downstream of a duct inlet junction

where h_{ts} is the stagnation enthalpy behind the shock wave outside the inlet and an ideal gas has been assumed. The velocity u_e is the inlet interface velocity calculated at the time cycle just prior to creating the new inlet zone. The pressure p_e from relation (3) and the internal energy e_e from relation (6), with the velocity u_e, establishes the flow state in the new zone. The density, and therefore the mass of the new zone, are determined from the equation of state in the form

$$\rho_e = \frac{p_e}{e_e(\gamma - 1)} \tag{7}$$

Uncertainty of the Results

The uncertainty of the measurement results for the data used in this analysis and summarized in Kriebel (1972) is not available. Typically, data from shock tube experiments involve a fair amount of data scatter as can be noted in Fig. 2. A measure of how well the least-square curves represent the experimental data is established by the correlation coefficient r commonly used in a least-squares analysis. The value of the correlation coefficient for each of the junction loss curves is presented in Tables 1 and 2.

Conclusions

By utilizing the values given in Table 1 for the constants in relation (4), the stagnation pressure ratio through a duct inlet, p_{te}/p_{ts}, can be evaluated for any of the junction types shown in Fig. 1. The logarithm of this ratio varies linearly with the Mach number of the flow behind the incident shock wave, M_s, for all of the junction types considered. The static pressure inside the inlet, p_e, is established through the experimental data with knowledge of the Mach numbers of the incident and inlet flows, M_s and M_e using relation (5) and Table 2 constants.

To establish inflow to the duct it is necessary to assume a constant stagnation enthalpy through the inlet junction. Establishing inflow establishes a contact surface across which the pressure does not change but the temperature and density change abruptly.

References

Ballistic Research Laboratory Shock Tube Facility Staff, 1962, "*Information Summary of Blast Patterns in Tunnels and Chambers*," Memorandum Report No. 1390, Ballistic Research Laboratories, Aberdeen Proving Ground, MD.

Deckker, B. E. L., and Male, D. H., 1967, "Fluid Dynamic Aspects of Unsteady Flow in Branched Ducts," *Proceedings Institution of Mechanical Engineers*, Vol. 182, Part 3H, pp. 167–174.

Heilig, W. H., 1975, "Propagation of Shock Waves in Various Branched Ducts," *Proceedings Modern Development in Shock Tube Research*, pp. 273–283.

Kriebel, A. R., et al. 1972, *Air Blast in Tunnels and Chambers*, DASA 1200-II Supplement 1, pp. 5-13 through 5-40.

Zimmerman, A. W., et al., 1970, "Nonsteady Flow Past Duct Junctures," *AIAA Journal of Spacecraft*, Vol. 7, No. 3, pp. 344–347.

Pressure Oscillation in the Leakage Annulus Between a Shrouded Impeller and Its Housing Due to Impeller-Discharge-Pressure Disturbances

D. W. Childs
Turbomachinery Laboratories,
Mechanical Engineering Department,
Texas A&M University,
College Station, Texas 77843

An analysis is presented for the perturbed flow in the leakage path between a shrouded-pump impeller and its housing caused by oscillations in the impeller-discharge pressure. A bulk-flow model is used for the analysis consisting of the path-momentum, circumferential-momentum, and continuing equations. Shear stress at the impeller and housing surfaces are modeled according to Hirs' turbulent lubrication model. In the present analysis, perturbations of the impeller discharge pressure are used to excite the fluid annulus. The circumferential variation of the discharge pressure is expanded in a Fourier series up to order n_1, where n_1 is the number of impeller blades. A precession of the impeller wave pattern in the same direction or opposite to pump rotation is then assumed to completely define the disturbance excitation. Predictions show that the first (lowest-frequency) "centrifugal-acceleration" mode of the fluid within the annulus has its peak pressure amplitude near the wearing-ring seal. Pressure oscillations from the impeller can either be attenuated or (sharply) magnified depending on: (a) the tangential velocity ratio of the fluid entering the seal, (b) the order of the fourier coefficient, and (c) the closeness of the precessional frequency of the rotating pressure field to the first natural frequency of the fluid annulus, and (d) the clearance in the wearing-ring seal.

Introduction

The present work is stimulated by experiences with the SSME HPFTP (Space Shuttle Main Engine, High Pressure Fuel Turbopump) wearing-ring seals. A stepped, 3-cavity, tooth-on-rotor, labyrinth-seal design is used. The stator for the seal is made from KEL-F, a plastic that is somewhat similar to nylon. In some cases, post-test inspection of the stator element has revealed that interior points in the stator material have melted and then resolidified, despite being in contact with liquid hydrogen. One hypothesis for this exceptional outcome was that the material had been subjected to cyclical stresses which generated heat due to hysteresis. Because of poor conduction properties of the material, the heat could not be dissipated, the temperature rose, and melting resulted. "What pressure oscillations are driving the cyclical stresses?", is an obvious question in reviewing this scenario. The present analysis examines "centrifugal-acceleration" modes, arising between the impeller shroud and its housing and driven by pressure oscillations from the pump, as an answer to this question.

[1]The work reported herein was supported by NASA Marshall Space Flight Center under contract NAS 8-37821; contract technical monitor: James Cannon.
Contributed by the Fluids Engineering Division for publication in the JOURNAL OF FLUIDS ENGINEERING. Manuscript received by the Fluids Engineering Division August 20, 1990.

Figure 1 illustrates an impeller stage of a multi-stage centrifugal pump. Leakage along the front side of the impeller, from impeller discharge to inlet, is restricted by a wearing-ring seal, while leakage along the back side is restricted by either an interstage seal or a balance-piston discharge seal. The present analysis considers perturbed flow in the leakage paths between the impeller-shroud surface and its housing.

Prior analyses by the author of those annulli have been concerned with lateral (1987, 1989) and axial (1990a) reaction forces developed by the impeller shrouds as a consequence of harmonic clearance changes due to impeller motion. These analyses have been based on "bulk-flow" models which neglect the variation in the dependent variables across the fluid film. The model consists of the path and circumferential momentum equations and the continuity equations.

The analyses cited have yielded force and moment coefficients due to impeller motion but have also predicted "resonance" phenomena, which are caused by the centrifugal-acceleration body forces present in the path momentum equations. An algorithm was developed (1990b) to calculate the complex eigenvalues and eigenvectors associated with these resonances. In the present analysis, the harmonic response of the flow within the annulus is examined due to time and circumferential variations in the discharge pressure of the impeller.

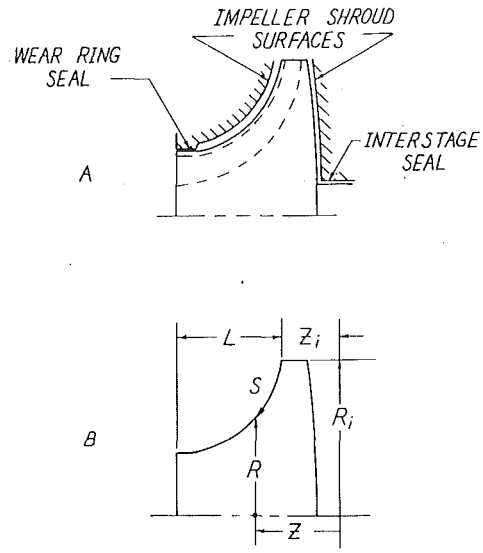

Fig. 1 Impeller leakage paths

Geometry and Kinematics

Figure 1 illustrates the annular leakage paths along the front and back sides of a typical shrouded impeller of a multistage centrifugal pump. The present discussion concentrates on the flow and pressure fields within the forward annulus; however, the analysis can also be applied to the rear annulus.[2] As illustrated in Fig. 2, the outer surface of the impeller is a surface of revolution formed by rotating the curve $R = R(Z)$ about the Z axis. A point on the surface may be located by the coordinates $Z, R(Z), \theta$. The length along the curve $R(Z)$ from

[2]Although the leakage flow is normally up the backside of all impellers except the last impeller, the governing equations would continue to be valid irrespective of the flow direction.

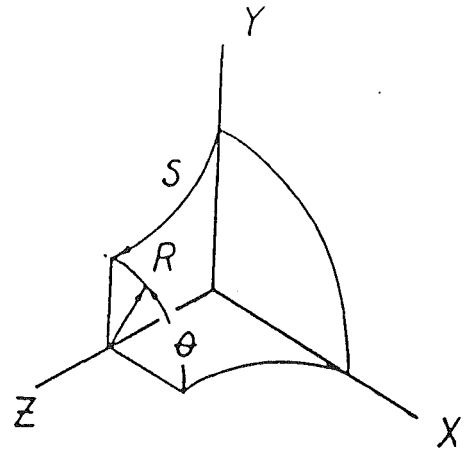

Fig. 2 Impeller surface geometry

the initial point R_i, Z_i to an arbitrary point R, Z is denoted by S and defined by

$$S = \int_{Z_i}^{Z} \sqrt{1 + \left(\frac{dR}{dZ}\right)^2}\, du = \int_{R_i}^{R} \sqrt{1 + \left(\frac{dZ}{dR}\right)^2}\, du \qquad (1)$$

In the equations which follow, the path coordinate S and angular coordinate θ are used as independent spatial variables. The coordinates Z, R defining the impeller surface are expressed as parametric functions of S, i.e., $Z(S)$, $R(S)$. The length of the leakage path along the impeller face is defined by

$$L_s = \int_{Z_i}^{Z_i+L} \sqrt{1 + \left(\frac{dR}{dZ}\right)^2}\, du \qquad (2)$$

Governing Equations

Returning to Fig. 2, the path coordinate S and circumferential coordinate $R\theta$ are used to locate a fluid differential

Nomenclature

A_{2s}, A_{3s}, $A_{2\theta}$, $A_{3\theta}$ = coefficients introduced in Eq. (12)
$b = V_i/R\omega$ = nondimensional velocity ratio
C_{de} = discharge coefficient for the exit wear-ring seal introduced in Eq. (7)
C_i = initial ($s = 0$) clearance (L)
C_r = exit seal clearance (L)
$f = \Omega/\omega$ = nondimensional precession frequency
f^* = nondimensionalized precession frequency yielding a maximum response pressure
$f^{+1} = \dfrac{n_1}{(n_1 - n_2)}$ = positive, dominant, nondimensional, precession frequency predicted for an impeller with n_1 blades in a diffuser with n_2 blades
$h = H/C_i$ = nondimensionalized clearance
H = clearance between impeller shroud and housing (L)
L_s = leakage-path length, defined by Eq. (2), (L)
n = order of Fourier coefficient, introduced in Eq. (13).
$p = P/\rho V_i^2$ = nondimensional static fluid pressure
$p_s(\theta,t)$ = prescribed annulus supply pressure (impeller exit pressure)
$p_e(\theta,t)$ = prescribed annulus exit pressure (impeller inlet pressure)
P = fluid static pressure (F/L^2)
R = radial coordinate (L)
R_i = initial ($s = 0$) radius (L)
$r = R/R_i$ = nondimensionalized radial coordinate
$R_s = 2HU_s/\nu$ = path-velocity Reynolds number
S = path coordinate introduced in Eq. (1), (L)
$s = S/L_s$ = nondimensionalized path length
$T = L_s/V_i$ = representative transit time for fluid traversing the leakage path (T)
$u_s = U_s/V_i$ = nondimensionalized path fluid velocity
$u_\theta = U_\theta/R_i\omega$ = nondimensionalized circumferential fluid velocity
V_i = initial ($s = 0$) path fluid velocity
ϵ = perturbation coefficient
ω = pump running speed (T^{-1})
Ω = excitation frequency (T^{-1})
ρ = fluid density (M/L^3)
θ = circumferential coordinate
σ_r, σ_s = normalized friction factors, defined by Eq. (11)
$\tau = \tau t$ = nondimensionalized time
ξ = entrance-loss coefficient introduced in Eq. (7)
ν = kinematic viscosity (L^2T^{-1})

Overbars denote complex variables; see Eq. (16). Subscripts 0 and 1 denote zeroth- and first-order solutions, respectively.

element of thickness $H(S, \theta, t)$. From Childs (1987), the continuity equation can be stated

$$\frac{\partial H}{\partial t}+\frac{\partial}{\partial S}(U_s H)+\frac{1}{R}\frac{\partial}{\partial \theta}(U_\theta H)+\left(\frac{H}{R}\right)\frac{\partial R}{\partial S}U_s=0 \quad (3a)$$

where U_s and U_θ are the path and circumferential bulk-velocity components, respectively. The path and circumferential momentum equations are stated

$$-H\frac{\partial P}{\partial S}=\tau_{ss}+\tau_{sr}-\rho H\frac{U_\theta^2}{R}\frac{dR}{dS}+\rho H\left(\frac{\partial U_s}{\partial t}+\frac{\partial U_s}{\partial \theta}\frac{U_\theta}{R}+\frac{\partial U_s}{\partial S}U_s\right) \quad (3b)$$

$$-\frac{H}{R}\frac{\partial P}{\partial \theta}=\tau_{\theta s}+\tau_{\theta r}+\rho H\left(\frac{\partial U_\theta}{\partial t}+\frac{\partial U_\theta}{\partial \theta}\frac{U_\theta}{R}+\frac{\partial U_\theta}{\partial S}U_s+\frac{U_\theta U_s}{R}\frac{\partial R}{\partial S}\right) \quad (3c)$$

Following Hirs' approach (1973), the wall shear-stress definitions in these equations can be stated

$$\tau_{ss}=\frac{ns}{2}\rho U_s^2 R_s^{ms}[1+(U_\theta/U_s)^2]^{\frac{ms+1}{2}}$$

$$\tau_{sr}=\frac{nr}{2}\rho U_s^2 R_s^{mr}\{1+[(U_\theta-R\omega)/U_s]^2\}^{\frac{mr+1}{2}}$$

$$\tau_{\theta s}=\frac{ns}{2}\rho U_\theta U_s R_s^{ms}[1+(U_\theta/U_s)^2]^{\frac{ms+1}{2}}$$

$$\tau_{\theta r}=\frac{nr}{2}\rho U_s(U_\theta-R\omega)R_s^{mr}\{1+[(U_\theta-R\omega)/U_s]^2\}^{\frac{mr+1}{2}} \quad (4)$$

where

$$R_s=2HU_s/\nu \quad (5)$$

Nondimensionalization and Perturbation Analysis

The governing equations define the bulk-flow velocity components (U_s, U_θ) and the pressure P as a function of the coordinates ($R\theta$, S) and time, t. They are conveniently nondimensionalized by introducing the following variables

$$u_s=U_s/V_i, \quad u_\theta=U_\theta/R_i\omega, \quad p=P/\rho V_i^2$$

$$s=S/L_s, \quad r=R/R_i, \quad b=V_i/R_i\omega$$

$$\tau=\omega t, \quad T=L_s/V_i \quad (6)$$

The present analysis examines the changes in (u_s, u_θ, p) due to changes in the impeller's discharge or inlet pressure. Following conventional notation, pressure drops at the annulus inlet and exit are stated

$$P_s(\theta,t)-P(0,\theta,t)=\rho(1+\xi)U_s^2(0,\theta,t)/2$$

$$P(L_s,\theta,t)-P_e(\theta,t)=\rho C_{de}U_s^2(L_s,\theta,t)/2 \quad (7)$$

Note specifically that the (upstream) supply and (downstream) exit pressure are now functions of time. Assume that the oscillations consist of a small perturbation of the form

$$P_s(\theta,t)=P_{s0}+\epsilon P_{s1}(\theta,t), P_e(\theta,t)=P_{e0}+\epsilon P_{e1}(\theta,t)$$

and introduce nondimensional variables to yield the following zeroth

$$p_0(0)=p_{s0}-(1-\xi)/2$$

$$p(1)=p_{es}+C_{de}u_{s0}^2(1)/2 \quad (8)$$

and first-order equations

$$p_{s1}(\theta,t)-p_1(0,\theta,t)=(1+\xi)u_{s1}(0,\theta,t)$$

$$p_1(1,\theta,t)-p_{e1}(\theta,t)=C_{de}u_{s0}(1)u_{s1}(1,\theta,t) \quad (9)$$

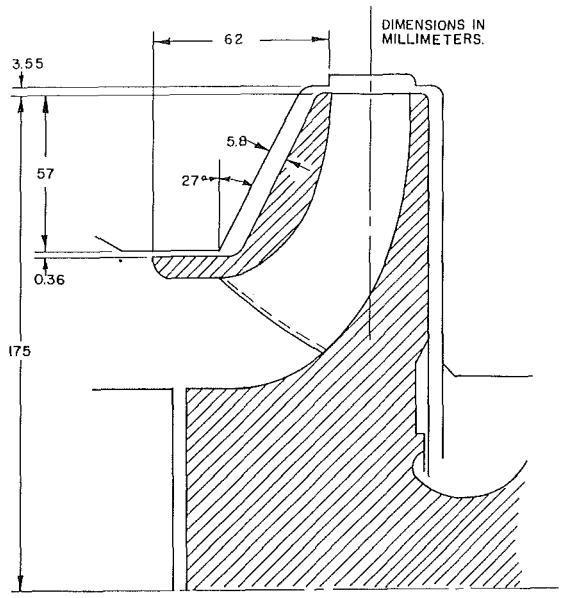

Fig. 3 Example impeller; Bolleter et al. (1987)

The perturbed supply and exit pressures $p_{s1}(\theta,t)$, $p_{e1}(\theta,t)$ can now be specified functions of time and provide excitation for the perturbed flowfield within the annulus.

Expansion of the dependent variables of Eq. (3) in perturbation equations yields:

Zeroth-Order Equations

(a) Path-Momentum Equation

$$\frac{dp_o}{ds}-\frac{1}{r}\left(\frac{dr}{ds}\right)\frac{u_{\theta o}^2}{b^2}+\left[\left(\frac{\sigma_r+\sigma_s}{2}\right)-\frac{1}{h_o}\frac{dh_o}{ds}-\frac{1}{r}\frac{dr}{ds}\right]u_{so}^2=0 \quad (10a)$$

(b) Circumferential-Momentum Equation

$$\frac{du_{\theta o}}{ds}+\frac{u_{\theta o}}{r}\frac{dr}{ds}+[\sigma_r(u_{\theta o}-r)+\sigma_s u_{\theta o}]/2=0 \quad (10b)$$

(c) Continuity Equation

$$rh_o u_{so}=1 \quad (10c)$$

The quantities σ_s and σ_r are defined by

$$\sigma_s=(L_s/H_o)\lambda_s, \quad \sigma_r=(L_s/H_o)\lambda_r \quad (11)$$

where λ_s and λ_r are the dimensionless stator and rotor friction factors:

$$\lambda_s=nsR_{so}^{ms}[1+(u_{\theta o}/bu_{so})^2]^{\frac{ms+1}{2}}$$

$$\lambda_r=nrR_{so}^{mr}\{1+[(u_{\theta o}-r)/bu_{so}]^2\}^{\frac{mr+1}{2}}$$

The continuity equation has been used to eliminate du_{so}/ds from Eq. (10a). The momentum equations define the pressure and velocity distributions for a centered impeller position. They are coupled and nonlinear and must be solved iteratively. The initial condition for $u_{\theta o}(0)$ is obtained from the exit flow condition of the impeller. Zeroth-order pressure boundary conditions are provided by Eq. (8).

Figure 3 illustrates the pump-impeller and shroud geometry used by Bolleter et al. (1987) in their test program for radial force coefficients. Their tests were at best efficiency point (BEP) with the pump running at 2000 rpm, while developing 68m of head and 130l/s of flow rate. The impeller has seven blades and an impeller exit angle of 22.5°. The test fluid is water at 26.6°C. For the present study, ΔP across the impeller is assumed to be 70 percent of the total head rise of the stage. Based on pitot-tube measurements, impeller-exit-tangential velocity is about 50 percent of the impeller discharge surface velocity; hence, $u_{\theta 0} \cong 0.5$.

Table 1 Zeroth-order-solution results; C_l = 3.5mm, C_r = 0.36mm

$u_{\theta o}(0)$	0.5	0.6	0.7
R_{s0}	9377	8907	8426
C_{de}	2.068	2.098	2.130
$\dot{m}$ (kg/sec)	4.448	4.225	3.997

Table 1 provides the zeroth-order solutions for new (original-clearance) exit wearing-ring seals. The R_{s0} values on the order of 10,000 are low in comparison to the circumferential Reynolds number $R_{\theta 0} = 2HU_{\theta 0}/\nu$ which varies along the path, but is on the order of 250,000. These leakage results were obtained iteratively starting with guessed values for the seal inlet values of pressure and tangential velocities and yielding an initial estimate for C_{de}. With this estimate for C_{de}, the leakage is calculated through the annulus which yields new inlet conditions for the seal. Solutions are "bounced" back and forth between the seal and the annulus until the same leakage value is obtained for both flow paths (four-place accuracy).

First-Order Equations

(a) Path-Momentum Equation

$$\frac{\partial p_1}{\partial s} + u_{\theta 1}A_{2s} + u_{s1}A_{3s} + \left[\omega T\frac{\partial u_{s1}}{\partial \tau} + \omega T\frac{u_{\theta o}}{r}\frac{\partial u_{s1}}{\partial \theta} + u_{so}\frac{\partial us_1}{\partial s}\right] = 0 \quad (12a)$$

(b) Circumferential-Momentum Equation

$$b\frac{L_s}{R_i}\frac{1}{r}\frac{\partial p_1}{\partial \theta} + u_{\theta 1}A_{2\theta} + u_{s1}A_{3\theta} + \left[\omega T\frac{\partial u_{\theta 1}}{\partial \tau} + \omega T\frac{u_{\theta o}}{r}\frac{\partial u_{\theta o}}{\partial \theta} + u_{so}\frac{\partial u_{\theta 1}}{\partial s}\right] = 0 \quad (12b)$$

(c) Continuity Equation

$$\frac{\partial u_{s1}}{\partial s} + \frac{\omega T}{r}\frac{\partial u_{\theta 1}}{\partial \theta} + u_{s1}\left(\frac{1}{r}\frac{dr}{ds} + \frac{1}{h_o}\frac{dh_o}{ds}\right) = 0 \quad (12c)$$

New coefficients in these equations are defined in, Childs (1987).

Solution Procedure: First-Order Equations

The functions $p_{s1}(\theta, t)$, $p_{e1}(\theta, t)$ provide the boundary excitation for the first-order equations. The general form for the excitation takes the form

$$p_{s1}(\theta,t) = e^{j\Omega t}(p_{s1c}\cos n\theta + p_{s1s}\sin n\theta)$$
$$p_{e1}(\theta,t) = e^{j\Omega t}(p_{e1c}\cos n\theta + p_{e1s}\sin n\theta) \quad (13)$$

where n can reasonably be expected to vary from zero (plane wave) upwards through multiples of the number of blades in the impeller. The form of Eq. (13) suggests that the θ variation in boundary pressures is defined in an impeller-fixed coordinate system, which is precessing at the frequency Ω.

The θ and time dependency of the dependent variables is eliminated by assuming the comparable, separation-of-variable, solution format

$$u_{s1} = e^{jf\tau}(u_{s1c}\cos n\theta + u_{s1s}\sin n\theta)$$
$$u_{\theta 1} = e^{jf\tau}(u_{\theta 1c}\cos n\theta + u_{\theta 1s}\sin n\theta)$$
$$p_1 = e^{jf\tau}(p_{1c}\cos n\theta + p_{1s}\sin n\theta) \quad (14)$$

where the coefficients are solely functions of s, and

$$f = \Omega/\omega \quad (15)$$

is the normalized precession frequency. Substituting into Eqs. (12) and equating like coefficients of cos $n\theta$ and sin $n\theta$ yields six first-order equations in s. Introducing the complex variables

$$\bar{u}_{s1} = u_{s1c} + ju_{s1s}, \quad \bar{u}_{\theta 1} = u_{\theta 1c} + ju_{\theta 1s} \quad \bar{p}_1 = p_{1c} + jp_{1s} \quad (16)$$

reduces these real equations to three, complex, ordinary differential equations

$$\frac{d}{ds}\begin{Bmatrix}\bar{u}_{s1}\\ \bar{u}_{\theta 1}\\ \bar{p}_1\end{Bmatrix} + [A(n,f,s)]\begin{Bmatrix}\bar{u}_{s1}\\ \bar{u}_{\theta 1}\\ \bar{p}_1\end{Bmatrix} = 0 \quad (17)$$

where

$$[A] = \begin{bmatrix} B & -jn\omega t/r & 0 \\ A_{3\theta}/u_{s0} & (A_{2\theta} + j\Gamma T)/u_{s0} & -j\dfrac{nb}{ru_{s0}}\left(\dfrac{Ls}{Ri}\right) \\ A_{3s} - Bu_{s0} + j\Gamma T & \left(A_{2s} + j\dfrac{n\omega T}{r}u_{s0}\right) & 0 \end{bmatrix} \quad (18)$$

$$B = \frac{1}{r}\frac{dr}{ds} + \frac{1}{h_0}\frac{dh_0}{ds}, \quad \Gamma = \omega\left(f - n\frac{u_{\theta 0}}{r}\right) \quad (19)$$

Since there is no right-hand side to Eq. (17), the homogeneous solution is the complete solution and can be stated as follows in terms of the transition matrix and initial conditions

$$\begin{Bmatrix}\bar{u}_{s1}\\ \bar{u}_{\theta 1}\\ \bar{p}_1\end{Bmatrix} = [\Phi(n,f,s)]\begin{Bmatrix}\bar{u}_{s1}(0)\\ \bar{u}_{\theta 1}(0)\\ \bar{p}_1(0)\end{Bmatrix} \quad (20)$$

The inlet initial condition $\bar{u}_{\theta 1}(0)$ is set equal to zero, and calculation of $\bar{u}_{s1}(0)$ and $\bar{p}_1(0)$ in terms of the specified boundary conditions is the immediate problem at hand. Substitution from Eqs. (13) and (14) into Eq. (9) yields

$$\bar{p}_{s1} - \bar{p}_1(0) = (1+\xi)\bar{u}_{s1}(0)$$
$$\bar{p}_1(1) - \bar{p}_{e1} = C_{de}u_{s0}(1)\bar{u}_{s1}(1) \quad (21)$$

where

$$\bar{p}_{s1} = p_{s1c} + jp_{s1s}$$
$$\bar{p}_{e1} = p_{e1c} + jp_{e1s} \quad (22)$$

From Eq. (20)

$$\bar{u}_{s1}(1) = \Phi_{11}(1)\bar{u}_{s1}(0) + \Phi_{13}(1)\bar{p}_1(0)$$
$$\bar{p}_1(1) = \Phi_{31}(1)\bar{u}_{s1}(0) + \Phi_{33}(1)\bar{p}_1(0) \quad (23)$$

Hence, from Eq. (21) one obtains

$$\begin{bmatrix} (1+\xi) & 1 \\ \Phi_{31}(1 - C_{de}u_{s0}(1)\Phi_{11}(1) & \Phi_{33}(1) - C_{de}u_{s0}(1)\Phi_{13}(1) \end{bmatrix} \times \begin{Bmatrix}\bar{u}_{s1}(0)\\ \bar{p}_1(0)\end{Bmatrix} = \begin{Bmatrix}\bar{p}_{s1}\\ \bar{p}_{e1}\end{Bmatrix} \quad (24)$$

Inversion of this equation yields

$$\begin{Bmatrix}\bar{u}_{s1}(0)\\ \bar{p}_1(0)\end{Bmatrix} = \begin{bmatrix} Z_{11} & Z_{12} \\ Z_{21} & Z_{22}\end{bmatrix}\begin{Bmatrix}\bar{p}_{s1}\\ \bar{p}_{e1}\end{Bmatrix} \quad (25)$$

$\bar{p}_{s1}$ and $\bar{p}_{e1}$ cannot be specified independently, and a relationship between the two cannot be established without a knowledge of the fluid system beyond the current terminating orifices. For the purposes of this discussion, the arbitrary choice

$$\bar{p}_{s1} = 1, \quad \bar{p}_{e1} = 0$$

is made to examine the influence of pressure perturbations at the impeller exit (annulus inlet). The resulting set of initial conditions for Eq. (20) is then

$$\begin{Bmatrix}\bar{u}_{s1}(0)\\ \bar{p}_1(0)\end{Bmatrix} = \begin{Bmatrix}Z_{11}\\ Z_{21}\end{Bmatrix}, \quad \bar{u}_{\theta 1}(0) = 0 \quad (26)$$

The complete solution along the impeller is found by evaluating Eq. (20) for $s \in [0, 1]$.

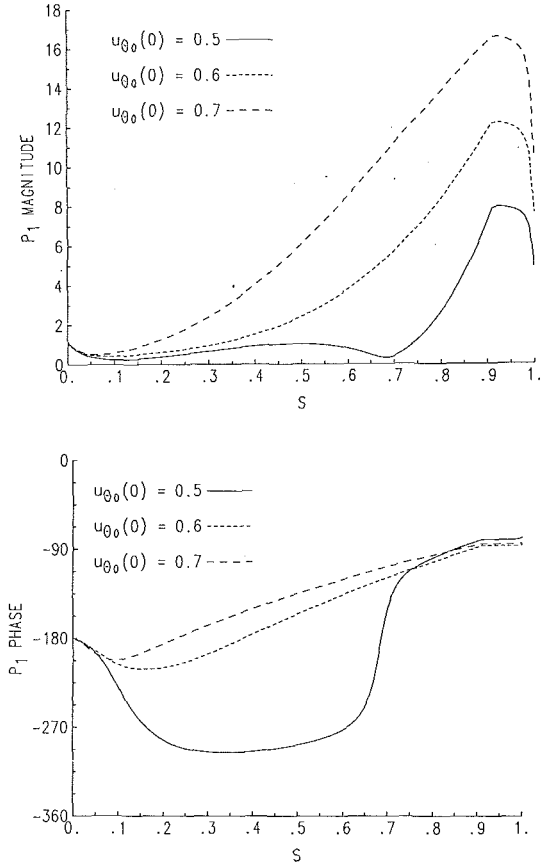

Fig. 4 $\bar{p}_1(s)$ complex eigenvector from Childs (1990b); $n = 1$

Numerical Results. Childs' (1990b) analysis yields complex eigenvalues $\bar{\alpha}$ and eigenvectors $\bar{u}_{s1}(s)$, $\bar{u}_{\theta 1}(s)$, $\bar{p}_1(s)$ for the system modeled by Eq. (12). Figure 4 illustrates the amplitude and phase for the first (lowest-natural-frequency) eigenvalue for $n = 1$; $u_{\theta 0}(0) = 0.5$, 0.6, and 0.7. Observe that the peak-pressure amplitudes lie near the wearing-ring seal, which is consistent with the internally-melted HPFTP wearing-ring-seal results cited earlier. Forced, harmonic-response solutions developed in this study due to impeller-discharge-pressure oscillations also show the largest pressure oscillations to occur near the wearing-ring seal ($s = 0.95$); hence, results presented here focus on $\bar{p}_1(0.95)$. This peak-pressure-oscillation location is very near the exit-wearing-ring seal of Fig. 3. The first question to be addressed here is, "How does $\bar{p}_1(0.95)$ depend on n, f, and C_r?"

Figure 5 illustrates the amplitude and phase of $\bar{p}_1(0.95)$ versus f for $C_r = 0.36$mm, $n = 5$, and $u_{\theta 0} = 0.5$. As will be explained later, the choice $n = 5$, arises because of the number of impeller and diffuser blades used in Bolleter et al.'s (1987) pump. The phase results indicate that numerous resonances exist for positive values of f. However, only the first resonance experiences significant amplification. The remaining fluid modes are heavily damped.

Figure 6 illustrates $|\bar{p}_1(0.95)|$ for $C_r = 0.36$mm, $n = 5$, and $u_{\theta 0}(0) = 0.5$, 0.6, and 0.7. The peak-response frequency increases as $u_{\theta 0}(0)$ is increased from 0.5 to 0.6, and a secondary peak appears around $f = 2.5$. Increasing $u_{\theta 0}(0)$ from 0.6 to 0.7 causes an additional peak to appear.

Figure 7 illustrates $|\bar{p}_1(0.95)|$ for $C_r = 0.36$mm, $u_{\theta 0}(0) = 0.5$, and $n = 0$, 1, 3, 5, and 7. The response is heavily damped for $n = 0$, rises sharply as n is increased to one, but then remains relatively constant as n ranges upwards over 3, 5, and 7. Figure 8 repeats the results of Fig. 7, except for worn clearances; i.e., $C_r = 0.72$mm. Comparisons of Figs. 7 and 8 show that doubling the clearances reduces pressure amplification and

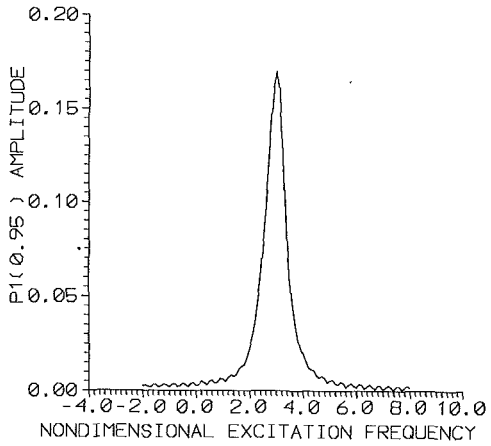

Fig. 5(*a*) $|\bar{p}_1(0.95)|$ versus f; $C_r = 0.36$mm, $u_{\theta 0}(0) = 0.5$, $n = 5$

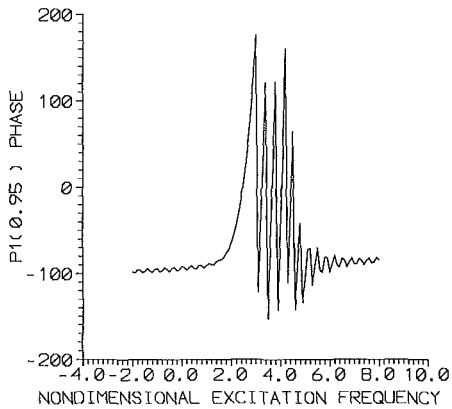

Fig. 5(*b*) Phase $\bar{p}_1(0.95)$ versus f; $C_r = 0.36$mm, $u_{\theta 0}(0) = 0.5$, $n = 5$

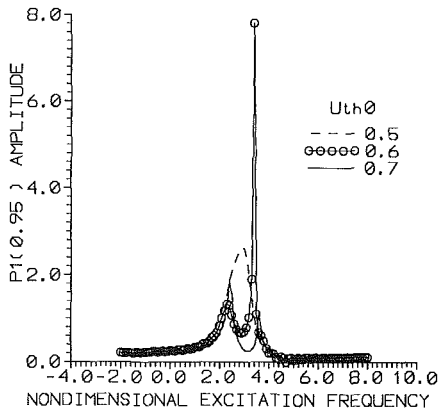

Fig. 6 $|\bar{p}_1(0.95)|$ versus f; $C_r = 0.36$mm, $n = 5$, and $u_{\theta 0}(0) = 0.5$, 0.6, and 0.7

slightly elevates the peak-amplitude-excitation frequency f^*. Table 2 shows f^* versus n for the new($C_r = 0.36$mm) and worn seals($C_r = 0.72$mm). Note that f^* increases more-or-less linearly with increasing n.

The questions which now arise are: **In a real pump, what value of n is likely to arise in impeller-pressure-discharge patterns, and what precession frequency is most likely to be present and dominant?** Answers to these questions have been provided by Bolleter (1988), who presents an analysis for the pressure waves developed by the interaction of impeller and diffuser vanes or impeller vanes and volutes. For an impeller with n_1 vanes and a diffuser with n_2 vanes, Bolleter shows that a rotating pressure wave is developed around the impeller exit with $n = |n_1 - n_2|$ diametral nodes. If $n_1 > n_2$ the pressure wave rotates in the direction of the pump with the frequency $n_1\omega/$

Table 2 f^* (peak-excitation-amplitude frequency) versus n for $u_{\theta 0}(0) = 0.5$

n	1	2	3	4	5	6	7
C_r = 0.36mm	0.3	0.8	1.4	2.1	2.9	3.6	4.2
C_r = 0.72mm	0.3	0.9	1.6	2.4	3.1	3.8	4.4

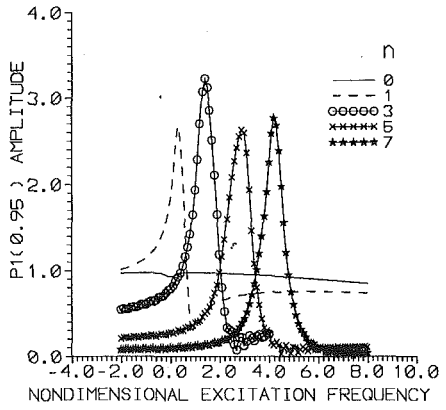

Fig. 7 $|\bar{p}_1(0.95)|$ versus f for n = 0, 1, 3, 5, 7; C_r = 0.36mm, and $u_{\theta 0}(0)$ = 0.5

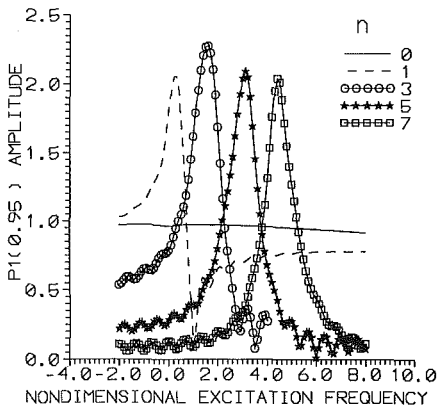

Fig. 8 $|\bar{p}_1(0.95)|$ versus f for n = 0, 1, 3, 5, 7; C_r = 0.72mm, and $u_{\theta 0}(0)$ = 0.5

n. If $n_1 < n_2$ the precessional frequency is $-n_1\omega/n$. Note that n, the number of diametral nodes, cited by Bolleter is the same n used in Eq. (13) for the pressure excitation. Further, in terms of Eq. (13), $\Omega = \pm n_1\omega/|n_1 - n_2|$. Tyler and Sofrin (1962) earlier developed this same result in analyzing the noise generated by the interaction of a rotor and stator in axial compressors of gas turbines.

Bolleter et al.'s pump (1987) used 12 diffuser blades, and the impeller of Fig. 3 has 7 blades. Hence, from Bolleter (1988), $n = |7 - 12| = 5$, and $\Omega = -7\omega/5 = -1.4\omega$. If the impeller were mounted in a double volute, $n = |7 - 2| = 5$, and $\Omega = 7\omega/5 = 1.4\omega$. From Fig. 5 ($n = 5$, $u_{\theta 0}(0) = 0.5$), amplification for $f = -1.4$ and 1.4 is 0.23 and 0.5, respectively. Hence, pressure disturbances from the impeller would generate pressure oscillations about twice as large in a double volute as in a 12-vaned diffuser. However, in either case, because the predominant frequency is well removed from the peak-amplitude-excitation frequency $f^* = 2.9$, impeller pressure disturbances would actually be attenuated by the annulus.

From Bolleter's equations, and the results of Figs. 5 through 7, significant amplification of impeller-discharge-pressure variations will only arise when the number of impeller blades exceeds the number of diffuser (or volute) blades, yielding a positive normalized precession frequency.

$$f^+ = n_1/n = n_1/(n_1 - n_2) \tag{27}$$

Table 3 Dominant normalized precession frequency f^+ and peak-excitation-amplitude frequency f^* versus n_1 and n_2; $u_{\theta 0}(0) = 0.5$

n_1	n_2	n	f^+	f^* (C_r=0.36mm)	f^* (C_r=0.72mm)
8	1	7	1.14	4.2	4.4
	2	6	1.33	3.6	3.8
	3	5	1.60	2.9	3.1
	4	4	2.0	2.1	2.4
	5	3	2.67	1.4	1.6
	6	2	4	0.8	0.9
	7	1	8	0.3	0.3
7	1	6	1.16	3.6	3.8
	2	5	1.40	2.9	3.1
	3	4	1.75	2.1	2.4
	4	3	2.33	1.4	1.6
	5	2	3.5	0.8	0.9
	6	1	7.0	0.3	0.3
6	1	5	1.2	2.9	3.1
	2	4	1.5	2.1	2.4
	3	3	2.0	1.4	1.6
	4	2	3.0	0.8	0.9
	5	1	6.0	0.3	0.3
5	1	4	1.25	2.1	2.4
	2	3	1.67	1.4	1.6
	3	2	2.5	0.8	0.9
	4	1	5.0	0.3	0.3

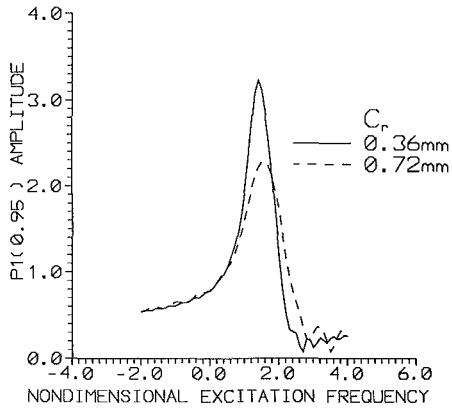

Fig. 9 $|\bar{p}_1(0.95)|$ versus f; n = 3, $u_{\theta 0}(0)$ = 0.5; C_r = 0.36 and 0.72mm

Moreover, for significant amplification within the leakage annulus, f^+ must lie near f^*, the peak-amplitude excitation frequency. Table 3 shows the variation of f^+ and f^* for various combinations of n_1 and n_2. The case of $n_1 = 8$ (eight-bladed impeller) and $n_2 = 4$ (four-bladed diffuser) yields a close proximity of $f^* = 2.1$, 2.4 to $f^+ = 2.0$; however, this is an unrealistic combination. For a practical configuration, the nondimensional frequencies $f^+ = 1.67$ and $f^* = 1.6$ are closest for $n_1 = 5$(five-bladed impeller) and $n_2 = 2$(double-discharge volute). Figure 9 illustrates $|\bar{p}_1(.95)|$ for $u_{\theta 0}(0) = 0.5$ and $n = 3$, confirming the predictions of Table 3. An amplification by a factor of 2.6 is predicted for new clearances and 3.2 for worn clearances.

Numerical Uncertainty. The numerical uncertainty issue for the results presented concerns the numerical integration of Eq. (17). The results presented were obtained with a fourth-order Runge-Kutta integrator package using 200 integration steps for the interval [0, 1]. Repeating these calculations with 400 integration steps yielded the same results to about three significant figures.

Summary and Conclusions

An analysis has been developed and results presented for the pressure oscillations in the leakage annulus between a shrouded pump impeller and its housing. These pressure oscillations are driven by a circumferential variation of the impeller discharge pressure which can precess either in the same or opposite to the direction of rotation. The circumferential variation can be modeled with a Fourier decomposition with each mode having n diametral nodes across the impeller. The peak-pressure oscillations within the impeller are predicted to occur near the exit wearing-ring seal in association with a centrifugal-acceleration-mode response of the fluid within the annulus (Childs, 1988, 1990b). The peak-amplitude-excitation frequency increases linearly with n. Using Bolleter's (1988) work which provides a dependency of n and the precessional frequency on the number of impeller (n_1) and diffuser (n_2) blades, situations are presented which can yield large amplifications (or significant attenuation) of impeller discharge variations. The occurrence and nature of the pressure oscillations are shown to depend on: (*a*) the tangential-velocity ratio of the fluid entering the seal, (*b*) the order of the Fourier coefficient, (*c*) the closeness of the precessional frequency of the rotating pressure field to the first natural frequency of the fluid annulus, and (*d*) the clearance of the wearing-ring seal.

The present results suggest an explanation for the internal melting observed on SSME HPFTP seal parts. However, given liquid hydrogen's significant compressibility, a more complete analysis, including fluid compressibility, is in order.

Bolleter, U., Wyss, A., Welte, Z., and Stürchler, R., 1987, "Measurement of Hydrodynamic Interaction Matrices of Boiler Feedpump Impellers," ASME *Journal of Vibrations, Stress, and Reliability in Design*, Vol. 109, pp. 144–151.

Bolleter, U., 1988, "Blade Passage Tones of Centrifugal Pumps," *Vibrations*, Vol. 4, No. 3.

Childs, D., 1987, "Fluid-Structure Interaction Forces at Pump-Impeller-Shroud Surfaces for Rotordynamic Calculations," *Rotating Machinery Dynamics*, Vol. II, ASME 1987, pp. 581–593.

Childs, D., 1989, "Fluid-Structure Interaction Forces at Pump-Impeller-Shroud Surfaces for Rotordynamic Calculations," ASME *Journal of Vibration, Acoustics, Stress, and Reliability in Design*, Vol. 111, July 1989, pp. 216–225.

Childs, D., 1990a, "Fluid-Structure Interaction Forces at Pump-Impeller-Shroud Surfaces for Axial Vibration Analysis," accepted for publication in ASME *Journal of Vibration and Acoustics*, May 1990.

Childs, D., 1990b, "Centrifugal-Acceleration Modes for Incompressible Fluid in the Leakage Annulus Between A Shrouded Pump Impeller and Its Housing," accepted for publication in ASME *Journal of Vibration and Acoustics*, May 1990.

Hirs, G., 1973, "A Bulk-Flow Theory for Turbulence in Lubricant Films," ASME *Journal of Lubrication Technology*, pp. 137–146.

Tyler, M. J., and Sofrin, T. A., 1962, "Axial Compressor Noise Studies," *SAE Trans.*, Vol. 70, pp. 309–332.

Flow Development and Analysis of MHD Generators and Seawater Thrusters

E. D. Doss
Argonne National Laboratory,
Argonne, Illinois 60439
Mem. ASME

G. D. Roy
Office of Naval Research,
Arlington, VA 22217
Mem. ASME

The flow characteristics inside magnetohydrodynamic (MHD) plasma generators and seawater thrusters are analyzed and are compared using a three-dimensional computer model that solves the governing partial differential equations for fluid flow and electrical fields. Calculations have been performed for a Faraday plasma generator and for a continuous electrode seawater thruster. The results of the calculations show that the effects caused by the interaction of the MHD forces with the fluid flow are strongly manifested in the case of the MHD generator as compared to the flow development in the MHD thruster. The existence of velocity overshoots over the sidewalls confirm previously published results for MHD generators with strong MHD interaction. For MHD thrusters, the velocity profile is found to be slightly flatter over the sidewall as compared to that over the electrode wall. As a result, distinct enhancement of the skin friction exists over the sidewalls of MHD generators in comparison to that of MHD thrusters. Plots of velocity profiles and skin friction distributions are presented to illustrate and compare the flow development in MHD generators and thrusters.

1 Introduction

Extensive work has been done on channel flow inside open-cycle MHD plasma generators (e.g., Roy and Wu, 1975; Doss and Curry, 1976; Doss et al., 1975, 1981; Ahluwalia and Doss, 1980; Doss and Ahluwalia, 1983; Vanka and Ahluwalia, 1982, 1983), but there has been minimal research effort on duct flow inside MHD seawater thrusters (e.g., Phillips, 1962; Doragh, 1963; Way, 1968; Saji, et al., 1978; Hummert, 1979; Cott et al., 1988). However, MHD flow inside those ducts is subject to $J \times B$ forces whether the duct is an MHD generator or an accelerator. For MHD generators, electrical power is extracted from the interaction of the fluid flow with the magnetic field. For MHD thrusters, energy is supplied to the duct by applying an external electrical field, and the resulting electrical currents interact with the magnetic field to produce a driving force that pushes the fluid through the duct. There are obviously some differences between the flow medium and the operating conditions between the two applications; however, the governing equations and the physical phenomena are quite similar. Figure 1 is a schematic diagram of the concept of MHD plasma generator and seawater thruster.

The literature on MHD channel flow for plasma open-cycle generators indicate that the flow and electrical fields in MHD generators are inherently three-dimensional for a variety of reasons. The interaction of the MHD electrical forces ($J \times B$) with the fluid flow leads to flow distortions (Vanka and Ahluwalia,1982, 1983; Doss and Ahluwalia, 1983). The cross-sectional nonuniformity of the axial component of the Lorentz force (J_yB) is directly responsible for the generation of velocity overshoots in the boundary layers. The nonuniformity in the magnetic field direction of the Lorentz force due to Hall current (J_xB) produces secondary flows which in turn leads to flow asymmetry.

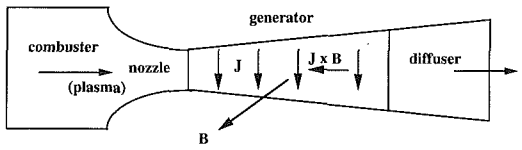

Fig. 1(*a*) A schematic diagram of an MHD generator

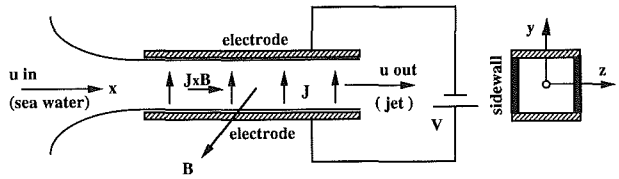

Fig. 1(*b*) A schematic diagram of an MHD generator

For MHD seawater thrusters, however, the electrical conductivity of seawater is expected to be practically uniform across and along the thruster provided the effect of bubbles formation, due to electrolysis, on the electrical conductivity is minimum. The Hall parameter for seawater thruster is also negligible. Therefore, one might anticipate that such flow nonuniformities would not be manifested strongly inside the ducts as much as in the case of plasma generators. In order to in-

Contributed by the Fluids Engineering Division for publication in the JOURNAL OF FLUIDS ENGINEERING. Manuscript received by the Fluids Engineering Division September 25, 1990.

vestigate the extent of such flow nonuniformities in the MHD thrusters, three-dimensional calculations of the flow and electrical fields have to be carried out.

The purpose of the present paper is to report the results of a comparative analysis performed using the three-dimensional flow model that has been previously developed, and to present a comparison of the development of the flow fields inside MHD generators and seawater thrusters.

2 MHD Three-Dimensional Generator and Thruster Model

A three-dimensional MHD generator model incorporating fully the interaction between the flow and the electrical fields inside the channel has been developed at Argonne National Laboratory and has been applied for several open-cycle MHD generators (Vanka and Ahluwalia, 1982, 1983; Doss and Ahluwalia, 1983).

Therefore, only a brief description of this model is given in this paper for completeness. The details of the model, flow equations, and their methods of solution are discussed in the references. (Vanka and Ahluwalia, 1982, 1983; Vanka et al., 1982). The flow fields are represented by the parabolic form of the three-dimensional compressible, turbulent Navier-Stokes equations and their solution is coupled to the solution of the electrical field in the cross-flow direction. The equations solved in this model consist of the mass conservation equation, the three momentum equations, the equations for enthalpy, turbulence kinetic energy and dissipation rate, the Maxwell and Ohms law equations. This set of coupled equations is solved by the use of a finite-difference calculation procedure. The turbulence is represented by a two-equation model of turbulence in which partial differential equations are solved for the turbulence kinetic energy and its dissipation rate.

The three-dimensional model has been adapted for the application of seawater thrusters. A continuous electrode configuration has been used in this application where the electric field along the flow direction is assumed to be zero. This assumption is reasonable since the Hall parameter for seawater is negligible. An applied electric field, in terms of a load factor, is specified as the boundary condition for the electrode walls. This assumption is also reasonable for seawater thruster of constant cross section, because the average axial velocity is constant at any cross section for mass conservation. The sidewalls are assumed to be insulators. The electrical fields are computed at each cross sectional plane perpendicular to the flow. Locally, the axial variation of the electrical fields and current densities are assumed to be negligible in comparison with their variations in the cross plane. This assumption may not be accurate where there are strong variations of the magnetic field and/or the flow velocity, or where there are abrupt changes in the boundary conditions. Such situations may exist near the ends of the MHD thrusters; however, they are beyond the scope of this paper.

3 Applications and Results

3.1 Operating Conditions. Computations have been performed using the three-dimensional model described in the previous section for an MHD plasma generator operating in the Faraday mode with insulating sidewalls, and for an MHD thruster operating in the continuous electrode mode with insulating sidewalls. The general operating parameters for the applications considered are listed in Table 1. The flow at the entrance of the generator and thruster is assumed to be a plug flow.

The physical properties of seawater are documented by Parker (1987) and the values used are for a temperature of 20°C, while those for plasma are obtained from the NASA-Lewis Chemical equilibrium code.

3.2 Grid Resolution and Sensitivity of the Predictions. For MHD generators, the theoretical predictions of the three-dimensional MHD model have been compared previously by Vanka and Ahluwalia (1983), for a generator operating in the Faraday mode. Excellent agreement was reported between the theory and experiments. For that particular application the calculations were made with a 29 × 29 finite-difference grid in the cross section and with a forward step of 2 cm.

In the current applications for MHD thrusters, the sensitivity of the predictions to the grid-size and to the forward step-size has been investigated. For example, for the same operating conditions of the thruster (magnetic field $B = 20$ T, load factor $K = 1.5$, flow velocity $u = 30$ m/s), several computer runs have been performed with 15 × 15, 29 × 29, and 39 × 39 finite-difference grids in the cross section and with a forward step of 4 cm. The grid-size distribution across the thruster has been defined using a power-law function with an exponent $py = 2$. [the distance away from the wall, $y(i) = (\text{height}/2) * (i/i_{cl})^{py}$, where $i = 0$ is at the wall and i_{cl} is the index of the grid at the centerline]. The initial step size away from the wall for the three above mentioned finite-difference grids is .0102, 0.00255, and 0.00139 m, respectively. Three variables have been used to investigate the sensitivity of the results using the different grids and those variables are the pressure rise along the 10 m thruster, the total frictional losses, and the total input power. It has been found that the predicted total input power and the pressure rise along the thruster remain practically the same, i.e., insensitive to the number of grids. For the total frictional losses, there is only 0.8 percent difference between the predictions using the 29 × 29 and the 39 × 39 grids and 5.3 percent between the predictions using the 15 × 15 and 39 × 39 grids.

Several other computations have been performed using 29 × 29 and 39 × 39 finite-difference grids and with forward

Table 1 Operating condition for the illustrated examples

	Generator	Thruster	
Geometry	rectangular	rectangular	
• length	10	10	m
• height × width (inlet)	0.5 × 0.5	1.0 × 1.0	m^2
• height × width (outlet)	1.0 × 1.0	1.0 × 1.0	m^2
• wall roughness	2.5	2.5	mm
Wall temperature	1800	300	K
Inlet fluid temperature	2760	300	K
Working fluid	Products of combustion of natural gas seeded with potassium	Seawater	
• electrical conductivity	7.2–5.1	4.8	S/m
Inlet flow velocity	770	30	m/s
Mass flow rate	75	30750	Kg/s
Magnetic field	6	20	T
Duct loading	Faraday with insulating sidewalls	continuous electrode with insulating sidewalls	
• average electric load factor	0.2–0.95	1–20	

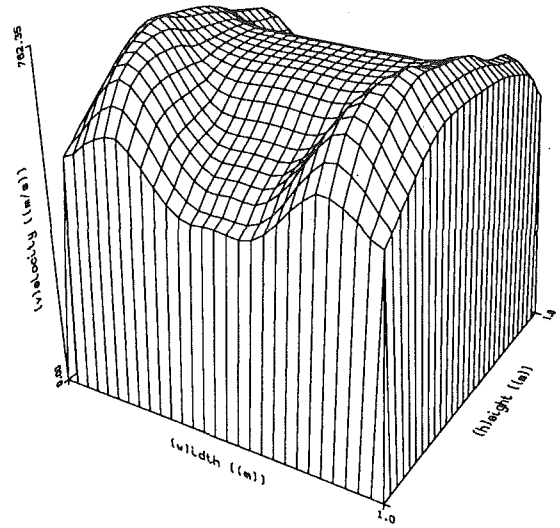

A. Generator

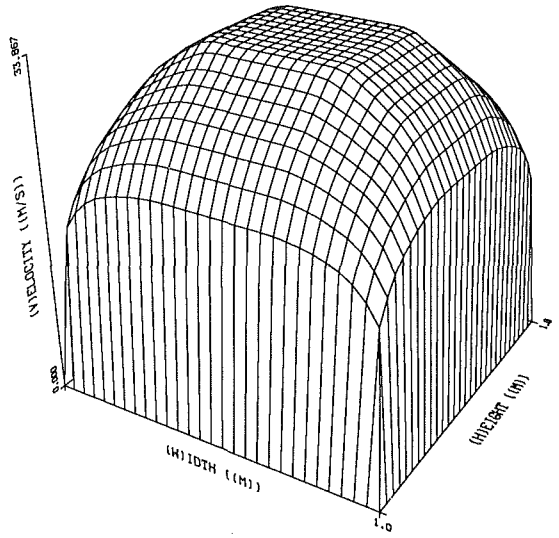

B. Thruster

Fig. 2 Surface plots of the axial velocity distribution at the exit of the MHD generator and thruster (x = 10 m)

step sizes of 10, 4, and 2 cm. For this particular application, where the magnetic field and the average flow velocity are constants along the thrusters, the predictions of the pressure rise, total frictional losses and input power are found to be practically the same (less than 0.8 percent difference) for the three quoted step sizes.

Based on these findings and using previous experience in analyzing the performance of MHD generators (Vanka and Ahluwalia, 1982, 1983; Vanka, et al., 1982), the following parametric study has been performed using a 29 × 29 finite-difference grid in the cross section and with a 4 cm forward step.

3.3 Flow Fields and Friction Factor. A Parametric study has been peformed by varying the average electric load factor ($K \equiv \langle E_y \rangle / \langle uB \rangle$ where E_y is the Faraday electric field) between 0.0 and 0.95 ($K < 1.0$) for the MHD generator and between 1 and 20 ($K > 1.0$) for the thruster. Sample results are presented and discussed in this paper for an MHD generator operating with $K = 0.75$ and for an MHD thruster operating with $K = 2$. More details can be found in Vanka and Ahluwalia (1983) and Doss and Roy (1991).

Figure 2 shows surface plots for the calculated axial velocity

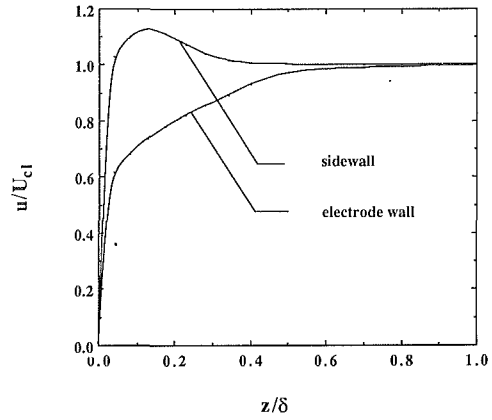

Fig. 3 Normalized velocity profiles across the MHD generator walls (x = 8 m)

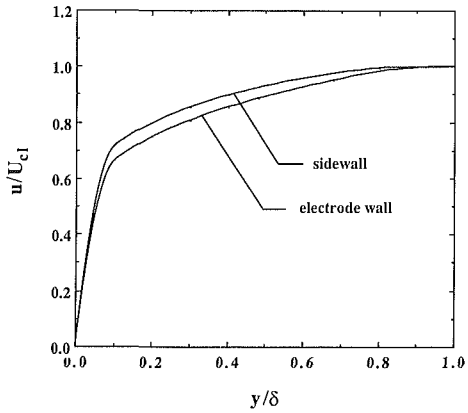

Fig. 4 Normalized velocity profiles across the MHD thruster walls (x = 8 m)

distributions at the exit cross-sections (x = 10m) of the MHD generator and thruster. As shown on Fig. 2, the three-dimensional effects, caused by the interaction of the Lorentz forces (J × B) with the fluid flow, are strongly manifested in the case of the MHD generator as compared to the flow development in the thruster. The axial component of the Lorentz force (J_yB) acts as a retarding force for the case of the generator, while it acts as an accelerating force for the case of the thruster. The J_yB force, however, is not uniform over the cross-section. As a result, velocity distortions exist and they are manifested strongly as velocity overshoots in the boundary layer for the MHD generator case. Furthermore, the perpendicular component of the Lorentz force (J_xB) produces cross stream transverse velocities leading to flow asymmetries. For MHD seawater thrusters, operating in the continuous electrode mode and with a negligible Hall parameter, the J_xB component is practically non-existent. Therefore, as shown in Fig. 2, the flow structure for the thruster is less complex than that for the generator.

Figures 3 and 4 present the corresponding axial velocity profiles in the boundary layer for the two devices. At first, one may think that the surface plot for the thruster (Fig. 2) is typical to normal non-MHD turbulent flow. However, as shown on Fig. 4, there is a difference between the shape of the axial velocity profile along the electrode wall and that along the sidewall. The velocity near the insulating wall (Hartmann boundary layers) is relatively higher than that near the electrode walls. For the generator, the disparity between the velocity profiles over the two walls is much larger where there is a distinct velocity overshoot in the boundary layers.

Figure 5 presents the corresponding variation of the J_y-com-

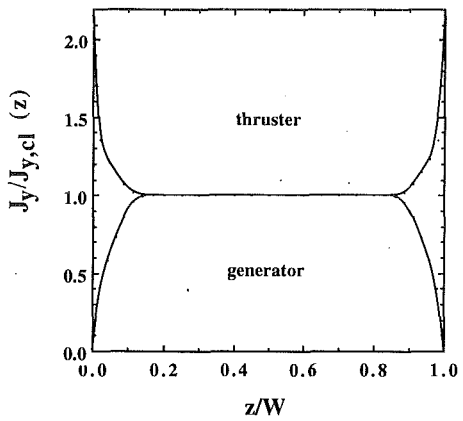

Fig. 5 Normalized current density across the sidewalls of the MHD generator and thruster (x = 8 m)

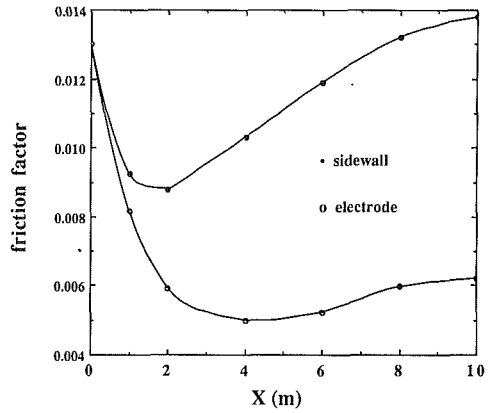

Fig. 6 Variation of the friction factor along the duct walls of the MHD generator

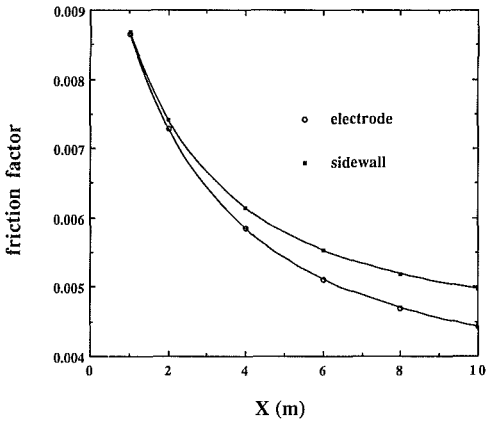

Fig. 7 Variation of the friction factor along the duct walls of the MHD thruster

ponent of the current density across the duct between the insulating walls for the MHD generator and thruster. The nonuniform J_y-distribution acts on the flow differently. For the case of the generator, where the electrical conductivity is very small in the boundary layers in comparison to the main flow, J_y is correspondingly very small compared to the core flow values. Accordingly, the retarding J_yB force exerts a less force on the sidewall (Hartmann) boundary layer. In a relative sense, the sidewall boundary layers are accelerated in relation to the central region. This relative acceleration of the sidewall boundary layers results in the observed velocity overshoots.

On the other hand, for the MHD thruster case, the seawater electrical conductivity is practically constant (neglecting the effects of bubble formation). Therefore, any change of the current density, J_y, in the sidewall (Hartmann) boundary layers will be caused by the nonuniformity of the velocity. For constant electrical potential between the cathode and the anode, the current density is larger in the sidewall boundary layers because of the smaller velocities. Therefore, a larger accelerating force (J_yB) will be felt on the flow in the sidewall boundary layers as compared to the main flow due to the increase of the current density component J_y as shown in Fig. 5. Consequently, the velocity profile is flatter over the sidewall in comparison to the velocity profile in the boundary layers over the electrode wall (Fig. 4).

As a result of such nonuniformities in the flow fields, nonuniform distribution of the skin friction is expected along the duct walls. Figures 6 and 7 present the variation of the friction factor (C_f) along the electrode wall and the sidewall of the MHD generator and thruster, respectively. The skin friction is higher on the sidewall for both applications but with a distinct difference for the generator case. Wall friction can have a strong adverse effect on the performance of both MHD devices (generator and thruster) in terms of their electrical efficiency. Such an important issue has been discussed recently in detail for MHD thrusters by Doss and Geyer (1990). Therefore greater attention should be given to the calculation of the flow fields and the frictional losses for those applications.

Summary and Conclusions

1. A three-dimensional MHD computer model has been applied to compare the flow characteristics inside MHD plasma generators with those inside seawater thrusters. Computations have been performed for a Faraday plasma generator operating with a 6 Tesla magnet and at a load factor K = 0.75, and for an MHD thruster operating in the Faraday mode with continuous electrodes with a 20 Tesla magnet and at a load factor K = 2.0.

2. The three-dimensional effects caused by the interaction of the Lorentz forces ($J \times B$) with the fluid flow are strongly manifested in the MHD generator as compared to the flow development in the thruster. Distinct velocity overshoots exist in the sidewall boundary layers for the case of the generators, whereas for the thruster a slightly flatter boundary layer velocity profile exists over the sidewall boundary layer as compared to the velocity profile over the electrode wall.

3. The flow velocity nonuniformities in both applications is caused basically by the nonuniformities of the component of the current density J_y in the Hartmann layers of the sidewalls of the MHD ducts. For MHD plasma generators the nonuniform J_y-distribution in the Hartmann layers is primarily caused by the strong variation of the electrical conductivity and secondarily by the nonuniformity of the velocity in the boundary layers. For MHD seawater thrusters, the electrical conductivity is uniform. Therefore, the nonuniformities of J_y in the sidewall boundary layers are caused primarily by the nonuniformities of the velocity in those layers.

4. As a result of such velocity nonuniformities, nonuniform distributions of the skin friction exist along the duct walls. The friction coefficient is higher on the sidewalls for both applications but with a distinct difference for the generator case.

Acknowledgment

This work has been sponsored by the Office of Naval Research, U.S., under Contract No. N00014-89-F-0064.

References

Ahluwalia, R. K., and Doss, E. D., 1980, "Quasi-Three Dimensional Modeling of Flow in MHD Channels," *Numerical Heat Transfer*, Vol. 3, pp. 67–87.

Cott, D. W., Daniel, V. W., Carrington, R. A., and Herring, J. S., 1988, "MHD Propulsion For Submarines," *CDIF External Report*, No. 2, DOE-MHD-D140, MSE Inc., Butte, Montana.

Doragh, R. A., 1963, "Magnetohydrodynamic Ship Propulsion Using Superconducting Magnets," *Proceedings of Naval Architects and Marine Engineers Transaction*, Vol. 71.

Doss, E. D., Argyropoulos, G. S., and Demetriades, S. T., 1975, "Two-Dimensional Flow Inside MHD Ducts with Transverse Asymmetries," *AIAA Journal*, Vol. 13, No. 5, pp. 545–546.

Doss, E. D., and Curry, B. P., 1976, "Studies of the 3-D Coupled Flows Between the Electrode and Sidewalls of MHD Channels," *AIAA Paper*, No. 76-311, AIAA 9th Fluid and Plasma Dynamics Conference.

Doss, E., Geyer, H., Ahluwalia, R. K., and Im, K., 1981, "Two-Dimensional Performance Analysis and Design of MHD Channels," ASME JOURNAL OF FLUIDS ENGINEERING, Vol. 103, pp. 307–314.

Doss, E. D., and Ahluwalia, R. K., 1983, "Three-Dimensional Flow Development In MHD Generators At Part Load," *Journal of Energy*, Vol. 7, No. 4, pp. 289–290.

Doss, E. D., and Geyer, H. K., 1990, "Effects of Friction and End Losses on MHD Thruster Efficiency," *Proceedings of the 28th Engineering Aspects of Magnetohydrodynamics*, Chicago, Ill., pp. III.2.1–III.2.8.

Doss, E. D., and Roy, G. D., 1991, "Flow Characteristics Inside MHD Seawater Thrusters," *Journal of Propulsion and Power*, Vol. 7, No. 4, pp. 635–641.

Hummert, G. T., 1979, "An Evaluation of Direct Current Electromagnetic Propulsion In Seawater," *Report ONR-CR168-007-1*, Westinghouse Research Laboratories, Pittsburgh, Pennsylvania.

Parker, S. P., ed., 1987, *McGraw-Hill Encyclopedia of Science and Technology*, McGraw-Hill, New York, 6th Edition, Vol. 16, pp. 144–178.

Phillips, O. M., 1962, "The Prospects for Magnetohydrodynamic Ship Propulsion," *Journal of Ship Research*, Vol. 43, pp. 43–51.

Roy, G. D., and Wu, Y. C. L., 1975, "Study of Pressure Distribution Along Supersonic Magnetohydrodynamic Generator Channel," *AIAA Journal*, Vol. 13, No. 9, pp. 1149–1153.

Saji, Y., Kitano, M., and Iwata, A., 1978, "Basic Study of Superconducting Electromagnetic Thrust Device for Propulsion in Sea Water, *Advances in Cryogenic Engineering*, Timmerhans, K. D., ed., Vol. 23, pp. 159–169.

Vanka, S. P., Ahluwalia, R. K., and Doss, E. D., 1982, "Three-Dimensional Analysis of MHD Generators and Diffusers," *Argonne National Laboratory*, Report No. ANL/MHD-82-4, Argonne, Ill.

Vanka, S. P., and Ahluwalia, R. K., 1982, "Three-Dimensional Flow and Thermal Development in Magnetohydrodynamic Channels," *Journal of Energy*, Vol. 6, No. 3, pp. 218–224.

Vanka, S. P., and Ahluwalia, R. K., 1983, "Coupled Three-Dimensional Flow and Electrical Calculations for Faraday MHD Generators," *Journal of Energy*, Vol. 7, No. 1, pp. 65–72.

Way, S., 1968, "Electromagnetic Propulsion for Cargo Submarines," *Journal of Hydraulics*, Vol. 2, No. 2, pp. 49–57.

B. A. Singer
High Technology Corporation Research Scientist.

P. G. Dinavahi
AS&M Research Scientist.
NASA Langley Research Center,
Hampton, VA 23665

Testing of Transition-Region Models

An approach for the comprehensive testing of transition-region models is described. This approach emphasizes the need to evaluate the models in all of the flow scenarios for which they are likely to be used. As an example of the procedure, seven different types of transitioning flows are described and experiments illustrating the different scenarios are discussed. Two transition-region models are used to predict mean-flow quantities for all of the cases and selected results are reported.

1 Introduction

The laminar-turbulent-transition zone presents special problems for the calculation of boundary-layer flows. Mean-flow quantities obey neither the fully laminar nor the fully turbulent correlations. In addition, local maxima in skin friction, wall temperature and heat transfer often occur near the end of the transition region. Traditionally, modeling this region has been important for the design of turbine blades, where the transition region is long relative to the chord length of the blade. More recently, the need for better transition-region models has been recognized by designers of hypersonic vehicles. Here the high Mach number, the low Reynolds number, and the low-disturbance flight environment emphasize the importance of the transition region. While numerous models have been proposed for the calculation of mean-flow quantities through the transition region, the models are rarely tested over the full range of flows for which they may be used. The proponents of a model typically present results for flows which are similar to the ones from which the model was calibrated. These tests show how well the model can perform, but do not show the model's limitations. In the more refined art of turbulence modeling, formal "Contests," such as the "Stanford Olympics" (Kline et al., 1968; Coles and Hirst, 1968; and Kline et al., 1981) have been organized to provide a rational basis for the comparison of various models. Since no such organized effort is expected for transition-region models in the near future, it is up to individual users of transition-region models to develop a framework for the fair evaluation of the models.

Unbiased testing of transition-region models has been undertaken by a few workers (Dinavahi, 1990; Abid, 1990; and Singer et al., 1991b) but all of these studies have focused on a small number of flows. The purpose of this paper is to present an approach to the thorough testing of transition-region models using a large variety of flows. In Section 2 we briefly discuss two transition-region models and the boundary-layer code in which they are implemented. We then give the testing procedure some structure and propose a set of test flows in Section 3. These flows include the most common instability mechanisms in aerodynamic applications. The choice of experiments with which to compare the predictions of the transition-region models and the results of the comparisons are discussed in Section 4. We summarize our work and offer some suggestions in Section 5.

2 The Models

Two different models are considered here. They are chosen to illustrate two different classes of models (see Narashimha (1985) for a complete classification of transition-region models). Our use of them here is intended neither to advocate nor discourage the use of any specific model.

We first consider the linear-combination model proposed by Dey and Narasimha (1988). In linear-combination models the mean flow in the transition region is a linear combination of the mean flows in the laminar and fully turbulent boundary layers. In the transition region, it is assumed that the laminar flow continues, but is intermittently replaced by patches of fully turbulent flow. The intermittency, γ, governs the appropriate proportions of the laminar and turbulent flows, i.e.,

$$\mathbf{U} = (1-\gamma)\mathbf{U}_{\text{lam}} + \gamma\mathbf{U}_{\text{turb}} \tag{1}$$

where $\mathbf{U}_{\text{lam}}$ is the calculated laminar flow field and $\mathbf{U}_{\text{turb}}$ is the calculated turbulent flow field. $\mathbf{U}_{\text{turb}}$ is initialized at the point where transition starts, x_t. This point coincides with the origin of the turbulent patches and the intermittency distribution. The intermittency relation used was first proposed by Dhawan and Narasimha (1958) and is given by:

$$\gamma = 1 - \exp(-0.411(x-x_t)^2/\lambda^2) \tag{2}$$

where λ is the streamwise distance between the points where $\gamma = 0.25$ and $\gamma = 0.75$. Since λ is not known *a priori*, it is calculated from:

$$\lambda = (0.411\text{Re}_\theta^3/N_2)^{1/2}\,\nu/U(x_{t2}) \tag{3}$$

where ν is the kinematic viscosity at the edge of the boundary-layer, $U(x_{t2})$ is the boundary-layer-edge velocity at x_{t2}, and Re_θ is the Reynolds number based on laminar momentum thickness at the point x_{t2}. For constant pressure flows x_{t2} is the same as x_t, the starting location of transition. When pressure gradients exist, Dey and Narasimha (1988) report the presence of subtransitions, or changes in the character of the flow. The point x_{t2} is the location of the last subtransition. As yet, Narasimha has not developed correlations for predicting x_{t2}, so here we use, $x_{t2} = x_t$ (though we keep x_{t2} in the appropriate

Contributed by the Fluids Engineering Division for publication in the JOURNAL OF FLUIDS ENGINEERING. Manuscript received by the Fluids Engineering Division March 16, 1991.

formulae in anticipation of future correlations). The factor N_2 is a nondimensional turbulent-spot-formation rate and is determined via the correlation:

$$N_2 = N_0(M, q) + 0.24L_{t2}^2 \quad for\ L_{t2} > 0 \tag{4}$$

or

$$N_2 = N_0(M, q) - 323L_{t2}^3 \quad for\ L_{t2} < 0 \tag{5}$$

where $N_0 = 0.7 \times 10^{-3}$ for boundary-layer-edge Mach number, M_e, less than 1.8 and with free-stream turbulent levels, q, greater than 0.2 percent and $L_{t2} = dU/dx\ \theta_L^2/\nu$ is a pressure gradient parameter. Both the free-stream velocity gradient, dU/dx, and the laminar momentum thickness, θ_L, are measured at x_{t2}. For compressible flows, the Mach number correction to N_0 given by Narasimha (1985) is used. Very low free-stream turbulence levels require a modified value of N_0. Our modification,

$$N_0 = -1.453 \times 10^{-3} \log q - 1.61 \times 10^{-3} \quad \text{for } q < 0.2\% \tag{6}$$

where q is the free-stream turbulence level in percent, comes from fitting a curve to the data in Figure 5.10 of Dey and Narasimha (1988). To compute the turbulent flow field, the model of Cebeci and Smith (1974), with modifications described by Singer et al. (1991a), has been used.

The next model we consider is an algebraic model developed at ONERA/CERT and is discussed briefly by Arnal (1986, 1988). In algebraic models one calculates the mean flow from a set of averaged equations in which the effective viscosity, μ_{eff}, is equal to the sum of the molecular viscosity, μ_{mol}, and the product of a transition function, ϵ_t, with a turbulent-eddy viscosity, μ_{turb}, such that:

$$\mu_{\text{eff}} = \mu_{\text{mol}} + \epsilon_t \mu_{\text{turb}}. \tag{7}$$

The Cebeci-Smith fully turbulent model is used to determine μ_{turb}. The transition function, ϵ_t, is not the intermittency of the flow, but is an empirically determined expression which governs the amount of turbulent-eddy viscosity used. ϵ_t is a function of a correlating parameter, χ_1, where

$$\chi_1 = (\theta/\theta_t - 1 + 0.005M_e^2)/(1 + 0.02M_e^2), \tag{8}$$

θ is the momentum thickness of the boundary layer, θ_t is the momentum thickness at the point where the model is started, and M_e is the Mach number at the edge of the boundary layer. This model does not account for any free-stream-turbulence effects. The expression for ϵ_t is piecewise continuous in the streamwise direction and is constant across the boundary layer. The algebraic expressions for ϵ_t used in this work are given by Arnal (private communication). The original expressions were developed from observations in low speed flows with zero and positive pressure gradients, but the more recent expressions reflect modifications necessary for the model to work in three-dimensional boundary layers which have both positive and negative pressure gradients (Arnal, 1986), and supersonic and hypersonic boundary layers (Arnal, 1988). For $0 < \chi_1 \le 0.25$,

$$\epsilon_t = 1 - \exp(-4.5(\chi_1(1 + 0.02M_e^2) - 0.005M_e^2)^2). \tag{9}$$

For $0.25 < \chi_1 \le 0.75$,

$$\epsilon_t = 18.628\chi_1^4 - 55.388\chi_1^3 + 52.369\chi_1^2 - 16.501\chi_1 + 1.893. \tag{10}$$

For $0.75 < \chi_1 \le 3$,

$$\epsilon_t = 1.25 - 0.25\sin(\pi(0.444\chi_1 - 0.833)). \tag{11}$$

For $\chi_1 > 3$,

$$\epsilon_t = 1. \tag{12}$$

The models are implemented in the three-dimensional boundary-layer code of Iyer (1990). This code is fourth-order accurate in the wall-normal direction and second-order accurate in the stream-surface directions. Numerous laminar-flow examples are given by Iyer (1990) to verify the accuracy and robustness of the code. Of particular interest to us are the examples of flows over flat plates, cones, and spheroids. The test cases we consider below are variations of these basic geometries, i.e., cases for which the code has already been proven accurate.

The performance of the Cebeci-Smith turbulence model in this code was documented by Singer et al. (1991a). There the predicted skin-friction distributions for five low-speed, fully turbulent flows were compared with data used for the 1968 Stanford Conference (Coles and Hirst, 1968). For favorable and zero pressure-gradient flows the computed values were in excellent agreement with the experimentally obtained ones. For a constant adverse pressure gradient the agreement was still very good, though for nonconstant deceleration, the calculation overpredicted the skin-friction coefficient, C_f, by as much as 20 percent. To assess the turbulent results for supersonic flow, a comparison with the boundary-layer code of Anderson and Lewis (1971) was performed for a five degree half-angle cone at zero angle of attack with adiabatic wall conditions and an edge Mach number of 1.46. The skin-friction coefficients and recovery factors computed by the two codes matched to within one percent at all stations.

In all cases, we adjusted the numerical resolution to ensure that the mean velocity at the point nearest the wall was less than five percent of the boundary-layer-edge velocity at all streamwise locations. For our cases, $C_f \ge 2 \times 10^{-4}$, so the point next to the wall was always within five viscous length scales of the wall. In this region the mean velocity profile is linear and improvements in resolution do not improve the results. As a check, we re-ran our case with the highest Reynolds number two additional times; in one run the five percent criterion was just satisfied, in the other, twice as many points were used. Both reproduced the wall shear and temperature to all four significant digits that were printed.

3 The Flows

The most important part of the testing procedure involves the choice of flow scenarios and the specific experiments which illustrate them. Here we describe a set of test flows which include most of the physical phenomena influencing the boundary-layer transition process for a high-speed aerodynamic vehicle. Our purpose is to help identify important effects that are not handled appropriately (either explicitly or implicitly) by the various models. Additional test flows ought to be included for certain applications (for instance, free shear layers), while other applications may not require a model to perform well in every test flow listed below. For any particular application the relevant physical phenomena that are likely to influence the transition process always should be identified regardless of whether there are experiments with which to compare the results. If there are flows for which no relevant experiments exist, extreme caution should be exercised in using the model and interpreting the obtained results.

Flow 1. The most basic transitional flow is that of a two-dimensional, incompressible, flat-plate boundary layer. Here transition is initiated by a viscous instability which grows, leading to secondary instabilities and localized breakdowns into turbulent patches which coalesce and eventually form the fully turbulent flow field. Mean-flow properties such as skin friction and wall heat transfer reach local maxima during the late stages of transition in this flow.

Flow 2. Pressure-gradient effects, even without boundary-layer separation, exert a strong influence on the transition process. Favorable pressure gradients tend to delay transition and often extend the transition region, while adverse pressure gradients result in a more rapid transition.

Flow 3. Compressibility effects are important in two ways. The Mach number influences the mean flow of a boundary layer, and also the character of the stability equations. At Mach

numbers greater than approximately 2, an inviscid instability can play an important role during transition and the characteristic sequence of events observed for incompressible flows may not occur here.

Flows 4 and 5. The typical viscous instability route to transition can be bypassed in the presence of strong free-stream turbulence or wall-roughness effects. While both effects lead to a transition process that is denoted by the term "bypass" transition, the actual bypass process is likely to be quite different since roughness affects the boundary layer near the wall while free-stream turbulence enters the boundary layer away from the wall. Both bypass mechanisms will be considered separately.

Flow 6. The Görtler instability which develops in regions of concave wall curvature is fundamentally different from the usual viscous instabilities which initiate transition on flat plates. Instead of streamwise traveling waves, the Görtler instability manifests itself as pairs of counter-rotating vortices which can significantly distort the time-averaged streamwise-velocity profile long before the flow can be considered turbulent. Important differences in the physics of the transition process are possible here.

Flow 7. Three-dimensional boundary layers are subject to inviscid crossflow instabilities which result in both stationary and traveling vortices in the flow. These instabilities are generally important near the leading edges of swept wings and on bodies of revolution at angles of attack.

4 Experiments and Comparison With Model Predictions

The evaluation of the models involves comparing the model's predictions with experimentally obtained results for the different flows. We start this section by giving some general guidelines governing our choices of the experiments. Then we will discuss specific experiments for each of our test flows.

In order that an experiment be useful to us, the experiment must measure some quantity that can be related to both the beginning and the end of transition. Ideally, measurements throughout the transition region are desired, although the locations of the beginning and end of transition, as determined by some well-defined criteria, are acceptable. Dey and Narasimha (1988) suggest that shear stress, temperature, and surface-pitot-tube pressure have local minima at a streamwise location x_{min} that is somewhat downstream of the zero-intermittency point, ($\gamma(x_{min}) \approx 0.15$) and that these quantities tend to have local maxima near the point where the flow is fully turbulent ($\gamma(x_{max}) \approx 0.985$). Many experiments use these local minima and maxima to determine the start and end of transition. Measurements of intermittency, shear stress, and surface temperature are highly desirable. Displacement and momentum thickness at different streamwise stations can be useful, although the locations of the start and the end of transition are not as well defined with these measurements.

Transition onset and end are often presented in terms of Reynolds numbers. Sometimes, the experimentally determined Reynolds numbers have been obtained by varying the flow velocity and/or viscosity with a measuring probe at a fixed streamwise location. Unfortunately, wind-tunnel characteristics often change with the flow velocity. Especially for compressible flows, a Reynolds number based on leading edge (or nose) bluntness can influence the transition Reynolds number. Since all the models predict the transitional behavior of a flow as one moves downstream, we require that the experiments with which we compare our results also provide measurements at multiple streamwise locations.

It is important to choose experiments that minimize extraneous effects that might influence the transition process. Here we stress simple geometries. This helps us to avoid numerical difficulties and allows us to isolate the physical phenomena at work. We also concentrate on experiments with low free-stream-turbulence levels. Free-stream turbulence is an important factor influencing transition. Dey and Narasimha (1988) identify three different regimes of free-stream-turbulence levels, q. For $q >$ four percent, transition begins at essentially the same Reynolds number, regardless of q. When 0.3 percent $< q <$ four percent, the onset location of transition varies with q and can be considered to be "turbulence driven." Except where we explicitly study the effects of free-stream turbulence, we have tried to choose experiments with $q < 0.3$ percent, below the range of turbulence driven transition.

Transition experiments are often sensitive to details of the flow that are not explicitly measured, such as very small scale surface roughness near the leading edge and length scale and spectrum of free-stream turbulence. The uncertainty in quantities that are often not explicitly measured is typically not reflected in the experimental uncertainty of the measurements. When possible, comparison with experiments performed in different facilities for the same flow type is useful for determining consistent trends.

Unless otherwise specified, the models are initiated at the point, x_t, which is approximated so that $1.1\ x_t = x_{min}$ where x_{min} is the point at which the measured surface quantity is a local minimum (Dey and Narasimha, 1988).

A summary of the results obtained for each of the flows is presented below. For those who wish to use some or all of our cases to test various models, extensive details regarding experimental conditions and our computational results for all of the cases used are contained in Singer et al. (1991a). The distributions of experimentally determined mean-flow quantities that we used for comparison are available in ASCII data files.

Flow 1. For two-dimensional, incompressible flow over a flat plate, we chose to compare our calculated results with the experiments of Schubauer and Klebanoff (1955). For free-stream-turbulence levels as low as 0.03 percent, they reported intermittency distributions as well as mean-flow profiles through the transition region. Dey and Narasimha (1988) deduced the experimental skin-friction coefficients from the velocity profiles. No uncertainty was reported in either reference. Our experience with digitizing and then differentiating the original authors' data suggests that C_f can vary by as much as 20 percent with different differentiation schemes.

The skin friction coefficient through the transition region is plotted against x-Reynolds number in Fig. 1. Since intermittency is reported, the models are started at the point at which the intermittency curve goes to zero. Both the ONERA/CERT model and Narasimha's model give reasonable fits to the available data. The ONERA/CERT model tends to overpredict the skin friction maximum while Narasimha's model slightly underpredicts this maximum. The sharp rise in C_f that occurs near the transition onset with Narasimha's model appears in several of our later cases. Results from a recent version of Dey and Narasimha's (1988) integral-momentum code (TRANZ3) are also included in Fig. 1. The rapid increase in C_f is also noticed in this code. TRANZ3 underpredicts the skin friction in the laminar boundary layer while our boundary-layer code agrees with the Blasius solution to within 1/2 percent. The discrepancy in the fully turbulent region is due to the turbulence modeling and is discussed more fully by Singer et al. (1991a).

Flow 2. Experiments with pressure gradients that had low free-stream-turbulence levels were hard to find. In order to try to isolate the pressure-gradient effect from the free-stream-turbulence effect, we chose two experimental conditions with different pressure gradients but with the same nominal free-stream-turbulence levels. The experiments were performed by

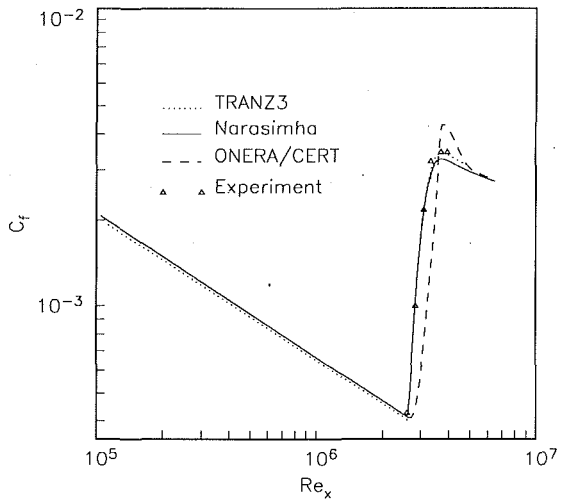

Fig. 1 Zero pressure gradient boundary layer

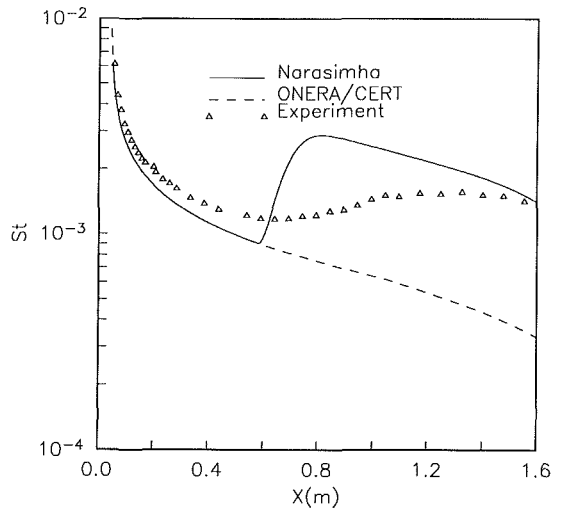

Fig. 2 Boundary layer with strong favorable pressure gradient

Blair and Werle (1981) on an almost uniform heat-flux flat plate. Local Stanton numbers were reported throughout the transition region. While the free-stream-turbulence levels varied somewhat with different pressure gradients (and with streamwise location), the values were similar enough that small deviations from an average value of 2 percent did not lead to different results for either of the models tested. The experimental uncertainty in the Stanton numbers was given as ±3 percent.

In Fig. 2 the results with the stronger pressure gradient are plotted. The models are initiated at 0.58 meters, slightly upstream of the minimum Stanton number location. The discrepancies with the experiments in the laminar region are probably due to the elevated free-stream-turbulence levels. This is discussed later with respect to Flow 4. The more serious problems occur after transition starts. Narasimha's model predicts a much shorter transition region than was observed experimentally. This also happens (although not so seriously) for the milder pressure gradient case. This deficiency with Narasimha's model may be corrected when appropriate correlations for x_{t2} become available. On the other hand, the ONERA/CERT model fails catastrophically. Because of the strong favorable pressure gradient, the laminar momentum thickness starts to decrease before the transition model is initiated. In a decreasing momentum-thickness environment, the ONERA/CERT model does not invoke the turbulence model and hence the predicted flow remains laminar.

Flow 3. The transition of a supersonic flow in a wind tunnel is often governed by the noise radiated from the turbulent boundary layers on the sidewalls of the tunnel (Laufer, 1961 and Pate and Schueler, 1969). To avoid this problem, we used data obtained from the flight tests of Fisher and Dougherty (1982) and from the Mach 3.5 Low-Disturbance Tunnel at NASA Langley Research Center (Chen et al. 1989). Both experiments were performed on five degree half-angle cones with adiabatic walls. The cones were maintained at zero angle of attack. Many other sources of flight data were found to be lacking crucial mean-flow information (e.g., angle of attack, nose bluntness, free-stream temperature and pressure, etc.). In the flight cases, the locations of the beginning and end of transition were reported as determined by the locations of local minima and maxima in surface-pitot-tube measurements. The specific flight cases chosen were examined by Malik (1984) to assess the usefulness of e^N methods for predicting the beginning of transition. In the Low-Disturbance Tunnel, transition criteria were based on the recovery factor,

$$r = \frac{T_{aw} - T_e}{T_0 - T_e} \tag{13}$$

where T_{aw} is the adiabatic wall temperature, T_0 is the stagnation temperature, and T_e is the boundary-layer-edge temperature. Unlike other wall quantities, the recovery factor does not have a local minimum near the start of the transition region, (the laminar value is constant), hence a different criterion is needed to locate the point at which the models are initiated. The experiments report a Reynolds number for the beginning of transition which is based on the intersection of a line faired through the transitional zone and one through the laminar data. This streamwise position is identified as $x_{\min}$; the relation, $1.1\ x_t = x_{\min}$ is then used to find the starting location for the models. The experimental recovery factors which we plot have been obtained by digitizing the data from Fig. 3 of Chen et al. (1989). Dr. Chen provided us with more readable plots of the data than those in his original publication and he estimated the uncertainty in the recovery factors to be ±1.5 percent.

For the flight cases there is no clear trend in either the models or the experimental data regarding the extent of transition with Mach number for Mach numbers from 1.16 to 1.86. Narasimha's model usually gives shorter transition extents than both the ONERA/CERT model and the experiments.

All of the data taken in the Langley Low-Disturbance Wind Tunnel have a Mach number of 3.36 at the boundary-layer edge. The experimental data indicate a slight tendency for the transition region to shorten, in terms of x-Reynolds number extent (although it lengthens in terms of physical distance), with decreasing stagnation pressure (and hence unit Reynolds number). The experimentally obtained recovery factors in the turbulent region are typically below 0.87. This is a very low value for a turbulent flow as can be seen by comparing it to the collected data of recovery factors on cones in Fig. 23.5 of Schlichting (1979). Dr. Chen has suggested that this may be due to heat transfer to the base of the cone. The boundary-layer-code predictions are qualitatively similar for all cases. Figure 3 illustrates the case with the intermediate stagnation pressure. Here the transition region is in the center of the instrumented portion of the cone. The agreement is excellent in the laminar region and poor in the turbulent region. The experimental data reach their fully turbulent values before the models do. The computed fully-turbulent recovery factors do not reach an asymptotic value; this may be due to the constant turbulent Prandtl number assumption that we used.

Flow 4. We chose two sets of experiments providing transition information with different levels of free-stream turbulence. Schubauer and Skramstad (1948) provided onset and end Reynolds numbers of transition for incompressible flow over a flat plate with free-stream-turbulence levels less than

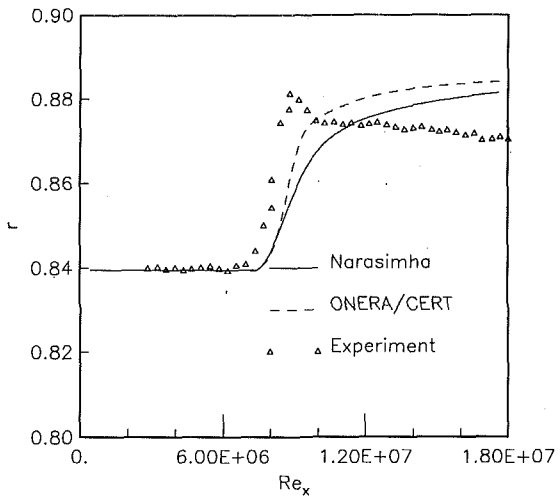

Fig. 3 Supersonic flow over 5 deg half-angle cone

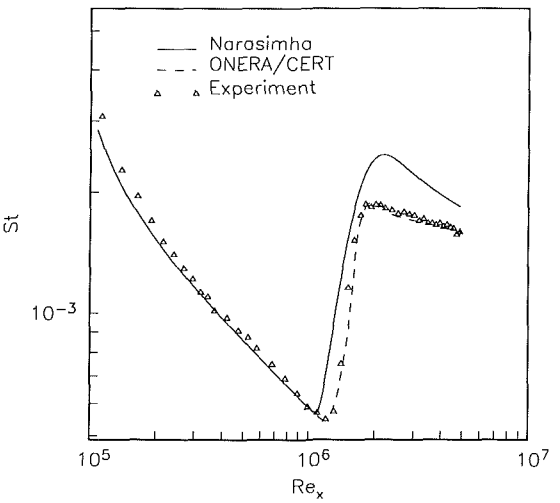

Fig. 4 Zero pressure gradient boundary layer with 0.25 percent free-stream turbulence

0.35 percent. These locations were determined from the local minima and maxima of surface-pitot-tube pressures.

For these experiments, the ONERA/CERT model tends to underpredict the length of transition by increasing amounts as the free-stream turbulence increases from 0.042 percent to 0.342 percent. Narashimha's model does quite well at the end of transition, where the predicted skin-friction maximum occurs close to the experimentally determined end of transition, but near the beginning of transition, the skin-friction minimum often occurs sooner than expected. Because this sequence of experiments forms the basis for the low free-stream-turbulence correction in Narasimha's model, the good agreement is not surprising. Recall that free-stream turbulence is not a parameter in the ONERA/CERT model.

For larger levels of free-stream turbulence (0.25 percent $< q <$ 2 percent), Stanton numbers through the transition region on a constant heat-flux flat plate were given by Blair (1983). Tabulated Stanton number data were obtained from Dr. Blair (personal communication). Uncertainties in the Stanton number were estimated to be ± 2.5 percent.

As seen in Fig. 4, the ONERA/CERT model gives an excellent prediction for the case with a free-stream-turbulence level of 0.25 percent. Narasimha's model does not perform quite so well on this case, overpredicting both the length of transition as well as the magnitude of the overshoot. For a comparable free-stream-turbulence level in the Schubauer and Skramstad experiments, Narasimha's model does somewhat better than the ONERA/CERT model in determining the transition-region length. The difference might be facility dependent, or it might be due to differences in the thermal and momentum boundary layers during transition. As the free-stream-turbulence level increases, up to 2 percent, the Stanton numbers in the laminar and early transition regions are noticeably underpredicted by both models. This is possibly due to buffeting of the boundary layer by the free-stream turbulence, a phenomena that neither model was designed to predict. A similar buffeting problem may have been present in Flow 2 as well.

Flow 5. The transition region over a rough surface was studied by Feindt (1956). Unfortunately, we were unable to find a translation of this work into English and we felt that the chance of misinterpreting some aspect of the experiment was too great for us to consider using this as a test case. As an alternative, Meier, et al. (1983) studied the development of the shear stress downstream of a thin strip of sandpaper roughness on a prolate spheroid. Calibrated surface hot films in a V configuration were used to determine the shear-stress magnitude and direction. The streamwise extent of the roughness strip was 0.020 meters and it was positioned 0.48 meters from the nose of the 2.4 meter long spheroid. For sufficiently high free-stream velocities, transition either started somewhat downstream of the roughness, or at the roughness strip. While this experiment did not address the issue of transition in the roughness region, the data showed the effects of the roughness strip. Detailed data dealing with this experiment were provided to the authors by Dr. Kreplin (personal communication). Dr. Kreplin estimated the uncertainty in C_f to be ± 5 percent in the fully laminar and fully turbulent regions and ± 10 percent in the transitional flow regime.

In comparing the experimental data to the model predictions one should note that neither model accounts for roughness except in how the roughness affects the location of the beginning of transition. Because of the geometry, pressure-gradient effects are also present. Two free-stream velocities are considered; at each velocity there is one case with the roughness strip and one without it. The qualitative behavior of both models does not seem to be sensitive to the free-stream speed. The results plotted in Fig. 5 are for the higher velocity case. The ONERA/CERT model overpredicts the maximum in skin friction regardless of the presence of the roughness strip. Narasimha's model underestimates the maximum in skin friction. Both models seem to perform slightly better with the roughness strip than without it. This might be a consequence of the fact that the roughness strip triggers transition in a favorable pressure gradient region while without the roughness, transition starts in an adverse pressure gradient region.

Flow 6. Swearingen and Blackwelder (1987) performed experiments on a concave wall in a wind tunnel with the free-stream turbulence level less than 0.07 percent. The experimental conditions were such that the boundary layer was stable to Tollmien-Schlichting waves; only the Görtler vortex instability was operative. Shear stress was determined from velocity-profile measurements extrapolated to the wall. The shear-stress measurements were reported at two separate spanwise locations, one where the Görtler vortices brought high-speed fluid nearer to the wall, the other where the vortices moved low-speed fluid away from the wall. Near the end of transition the shear stresses at these two locations came together and the fluctuating velocity signals indicated that the flow was essentially turbulent. Tabulated data from this experiment were provided by Dr. Swearingen (personal communication). He estimated the experimental uncertainty in C_f to be ± 5 percent at the first streamwise measurement station and assumed that it would increase linearly to ± 30 percent at the last station.

Neither transition-region model is designed to deal with flows

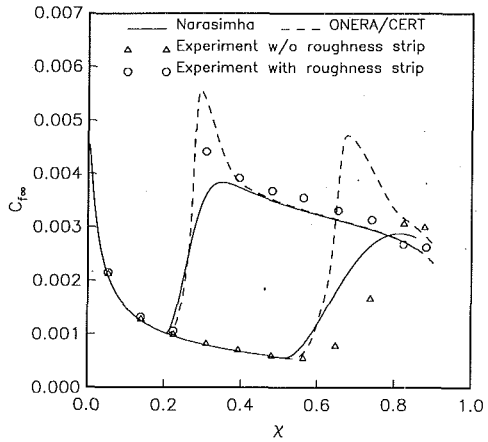

Fig. 5 Flow over a prolate spheroid at zero angle of attack. Major axis is 2 α

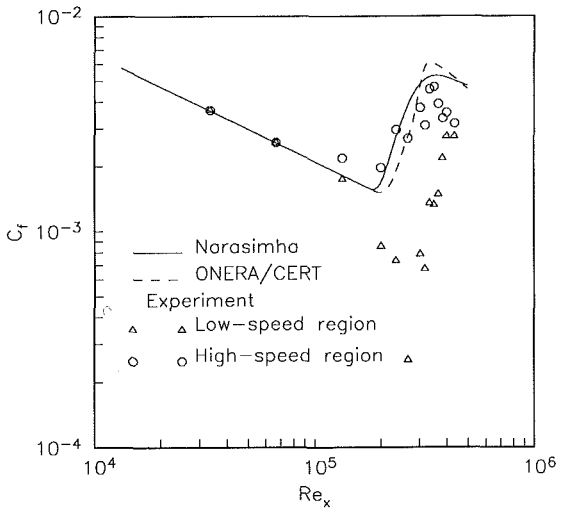

Fig. 6 Flow over a concave wall

dominated by streamwise vortices. Since it is probably more important to estimate the maximum shear stress, here we locate x_{min} at the minimum shear-stress location of the high-speed region. In Fig. 6 we see that the minimum value of C_f in the high-speed region is greater than the value of C_f in the calculated laminar flow. This is because the effects of the vortices are not considered in the calculation. In spite of this, the location of the skin-friction maximum is predicted reasonably well by both models.

Flow 7. As an example of three-dimensional boundary-layer transition, we considered the experiments of Meier and Kreplin (1980) on a prolate spheroid at angle of attack. Their wind tunnel had a free-stream-turbulence level of less than 0.2 percent. They used calibrated V-formation surface hot films to measure the wall shear stress at several axial stations at numerous circumferential angles. For angles of attack at 2.5 and 5 degrees, separation occurred only very near the aft of the body. At an angle of attack of 10 degrees, the separated flow region extended far forward and would invalidate our use of the analytical potential flow solution for the boundary-layer edge conditions, hence we restricted our comparisons to the two smaller angles of attack. Detailed tabulated data were provided by Dr. Kreplin (personal communication). He estimated the uncertainty in C_f to be $\pm$ 5 percent in the laminar and fully turbulent regions, $\pm$ 10 percent in the transitional flow zone.

For an angle of attack of 5 degrees, the laminar flow (U_{lam} in Eq. (1)) separates in the transition region, hence Narasimha's

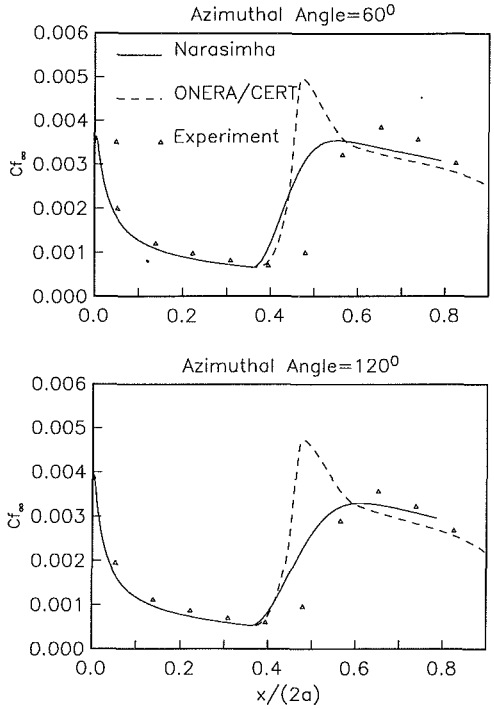

Fig. 7 Flow over a prolate spheroid at 2.5 degrees angle of attack. Major axis is 2 α.

model cannot be used. Even if this were not a problem, it would be difficult to initiate the fully turbulent boundary layer required by Narasimha's model in the code because x_t varies strongly with azimuthal location. A special grid would be required to ensure that information from transitional and turbulent zones does not propagate into laminar zones. In Fig. 7 we see the results for the smaller angle of attack at two azimuthal stations. Here a constant x_t is a satisfactory approximation. As in the case of the spheroid at zero angle of attack, (see Flow 5), the peak shear stress predicted by the ONERA/CERT model is too high.

5 Summary and Suggestions

We described a framework for the thorough testing of transition-region models. The procedure involves:

1. identifying the major flow types for which the model will be used,
2. finding appropriate experiments that illustrate the important physics, and
3. comparing the model predictions with the experimental data.

To illustrate this process, we studied the behavior of two different transition-region models for seven distinct types of flows. During the course of the tests we discovered a few serious problems that might not have been noted if the testing were more limited. For instance:

1. The ONERA/CERT model failed to predict any transition for a strong favorable pressure-gradient case (Flow 2).
2. Narasimha's model could not be used for the case of a prolate spheroid with an angle of attack of 5.0 degrees (Flow 7) because the laminar flow would have separated.
3. When using Narasimha's model, a turbulent boundary layer that started with zero thickness at x_t was required. This would have been difficult to do for the case of a prolate spheroid with an angle of attack of 5.0 degrees (Flow 7) because x_t varies strongly with the spanwise coordinate.

Item 1 is a problem specific to the ONERA/CERT model while items 2 and 3 are difficulties inherent in all linear-combination models.

Additional issues that we found to be important in determining the accuracy of the models are summarized below.

The transitional flow results depend on the turbulence model used. Deficiencies in a turbulence model that is incorporated into a transition-region model will be noticed in the transitional-flow region. More reasonable methods for initiating the transitional-flow model need to be developed. In our results, there were several cases where the agreement could have been improved if x_t were chosen differently. For Narasimha's model, a correlation to determine x_{t2} must also be developed. In the heat-transfer experiments, Narasimha's model consistently overpredicts the maximum Stanton number. Separate intermittency distributions may be needed for the momentum and thermal boundary layers.

Both free-stream turbulence and free-stream acoustic disturbances need to be included in the models. This was attempted by Shamroth and McDonald (1972); future transition models might extend this aspect of their work. Free-stream turbulence-levels greater than 1 percent seem to influence the skin friction in the laminar region long before the minimum skin-friction location is reached. It may be necessary to include a "pre-transition" model in the transition-region model in order to correctly predict these elevated skin-friction levels. Similarly, large scale vortices (like those due to the Görtler instability in Flow 6) also result in large deviations in the skin friction (and presumably the heat transfer) in the laminar flow. A "pre-transition" model that includes some results of stability theory may be needed.

The extensive testing procedure also revealed the need for additional carefully performed experiments. There needs to be additional overlap between experiments in order for us to resolve anomalies, like the very low turbulent recovery factor found in the NASA Langley Low-Disturbance Wind Tunnel. More experiments at supersonic speeds as well as experiments studying the effects of distributed roughness on the transition region are needed. There is also a need for low-free-stream-turbulence experiments studying the transition region in both favorable and adverse pressure gradients. If both favorable and adverse pressure-gradient flows were studied in the same facility it would be easier to sort out differences caused by the pressure gradient and differences caused by variations in the facilities.

There is plenty of room for improvements in transition-region modeling. One possible approach might be the conglomerate model, consisting of sets of submodels, each one designed to perform well for a specific flow situation. Intelligent users, or perhaps a sophisticated expert system would choose an appropriate submodel for the each type of flow. The comprehensive evaluation procedure described here will help guide the development and the use of all future models.

Acknowledgments

The authors would like to thank Dr. V. S. Iyer for his considerable help in using his boundary layer code. The detailed data provided by Drs. Blair, Chen, Kreplin, and Swearingen were greatly appreciated. Prof. Narasimha gave some useful suggestions and provided us with the TRANZ3 computer program. We thank Prof. Reshotko for his views on the future of transition-region models. The Theoretical Flow Physics Branch at NASA Langley Research Center Supported this work under contracts NAS1-18240 and NAS1-18599.

References

Abid, R., 1990, "A Study of Turbulence Models for Prediction of Transitional Boundary Layers," *Instability and Transition*, eds., Hussaini, M. Y. and Voigt, R. G., Springer, New York, Vol. 2, pp. 335–351.

Anderson, C., and Lewis, C. H, 1971, "Laminar or Turbulent Boundary-Layer Flows of Perfect Gases or Reacting Gas Mixtures in Chemical Equilibrium," NASA CR-1893.

Arnal, D., 1986, "Three-Dimensional Boundary Layers: Laminar-Turbulent Transition," AGARD-FDP-VKI Special Course on *Calcul Des Limites Tridimensionnelles Avec Ou Sans Decollement*, 14–18 April.

Arnal, D., 1988, "Laminar-Turbulent Transition Problems in Supersonic and Hypersonic Flows," AGARD—FDP—VKI Special Course on *Aerothermodynamics of Hypersonic Vehicles*, 30 May–3 June.

Blair, M. F,. 1983, "Influence of Free-Stream Turbulence on Boundary Layer Heat Transfer and Mean Profile Development, Part 1—Experimental Data," ASME *Journal of Heat Transfer*, Vol. 105, pp. 33–40.

Blair, M. F., and Werle, M. J., 1981, "Combined Influence of Free-Stream Turbulence and Favorable Pressure Gradients on Boundary Layer Transition and Heat Transfer," United Technologies Report No. R81-914388-17.

Cebeci, T. and Smith, A. M. O., 1974, "Analysis of Turbulent Boundary Layers," *Applied Mathematics and Mechanics*, Vol. 15, Academic Press, New York.

Chen, F.-J.; Malik, M. R., and Beckwith, I. E., 1989, "Boundary-Layer Transition on a Cone and Flat Plate at Mach 3.5," *AIAA J.*, Vol. 27, pp. 687–693.

Coles, D. E., and Hirst, E. A., 1968, Vol. 2, *Proc. Comput. Turbul. Boundary-Layers*, Mechanical Engineering Department, Stanford Univ., Stanford, CA.

Dey, J. and Narasimham, R., 1988, "An Integral Method for the Calculation of 2D Transitional Boundary Layers," Report 88 FM 7, Department of Aerospace Engineering, Indian Institute of Science, Bangalore, India.

Dhawan, S., and Narasimha, R., 1958, "Some Properties of Boundary Layer Flow During the Transition from Laminar to Turbulent Motion," *J. Fluid Mech.*, Vol. 3, p. 418–436.

Dinavahi, S., 1990, "Comparison of Two Transition Models," *Instability and Transition*, eds., Hussaini, M. Y. and Voigt, R. G., Springer, New York, Vol. 2, pp. 453–462.

Feindt, E. G., 1956, "Untersuchungen über die Abhängigkeit des Umschlages laminar-turbulent von der Oberflächenrauhigkeit und der Drukverteilung," Diss. Braunschweig, DFL 12-S 1345.

Fisher, D. F., and Dougherty, N. S., 1982, "Transition Measurements on a 10° Cone at Mach Numbers from 0.5 to 2.0," NASA Technical Paper 1971.

Iyer, V. S., 1990, "Computation of Three-Dimensional Compressible Boundary Layers to Fourth Order Accuracy on Wings and Fuselages," NASA Contractor Report 4269.

Kline, S. J., Cantwell, B. J., and Lilley, G. M., 1981, "The 1980–1981 AFOSR-HTTM-Stanford Conference on Complex Turbulent Flows: Comparison of Computation and Experiment," Thermosciences Division, Mechanical Engineering Department, Stanford University, Stanford, CA.

Kline, S. J., Cockrell, D. J., Morkovin, M. V., and Sovran, G., 1968, Vol. 1, *Proc. Comput. Turbul. Boundary-Layers*, Mechanical Engineering Department, Stanford Univ., Stanford, CA.

Laufer, J., 1961, "Aerodynamic Noise in Supersonic Wind Tunnels," *J. Aerosp. Sci.*, Vol. 28, No. 9, pp. 685–692.

Malik, M. R., 1984, "Instability and Transition in Supersonic Boundary Layers," Proceedings of Energy Sources Technology Conference, New Orleans, Feb. 12–16, in *ASME Fluids Engineering Division*, Vol. 11, pp. 139–147.

Meier, H. L., and Kreplin, H. P., 1980, "Experimental Investigation of the Boundary Layer Transition and Separation on a Body of Revolution," *Z. Flugwiss. Weltraumforsch.*, Vol. 4, pp. 65–71.

Meier, H. L., Kreplin, H. P., and Ming, X., 1983, "Problems Associated with Artificial Boundary Layer Transition," AIAA Paper No. 83-1673.

Narasimha, R., 1985, "The Laminar-Turbulent Transition Zone in the Boundary Layer," *Prog. Aerospace Sci.*, Vol. 22, pp. 29–80.

Pate, S. R., and Schueler, C. J, 1969, "Radiated Aerodynamic Noise Effects on Boundary-Layer Transition in Supersonic and Hypersonic Wind Tunnels," *AIAA J.*, Vol. 7, No. 3, pp. 450–457.

Schlichting, H., 1979, *Boundary Layer Theory*, 7th Edition, McGraw-Hill, New York, p. 714.

Schubauer, G. B., and Skramstad, H. K., 1948, "Laminar-Boundary-Layer Oscillations and Transition on a Flat Plate," NACA Report No. 909.

Schubauer, G. B., and Klebanoff, P. S., 1955, "Contributions on the Mechanics of Boundary-Layer Transition," NASA TN 3489.

Shamroth, S., and McDonald, H., 1972, "Assessment of a Transitional Boundary Layer Theory at Low Hypersonic Mach Numbers," NASA CR-2131.

Singer, B. A., Dinavahi, S. P. G., and Iyer, V. S., 1991a, "Testing of Transition-Region Models—Test Cases and Data," NASA CR 4371.

Singer, B. A., Dinavahi, S., and Zang, T. A., 1991b, "Evaluation of a Compressible Flow Transition Model," NASP CR-1109.

Swearingen, J. D., and Blackwelder, R. F., 1987, "The Growth and Breakdown of Streamwise Vortices in the Presence of a Wall," *J. Fluid Mech.*, Vol. 182, pp. 255–290.

A. Salhi
Assistant Professor,
Laboratoire de Mécanique des Fluides,
Faculté des Sciences de Tunis,
Campus Universitaire,
1060 Tunis, Tunisia

C. Rey
Professor.

J. M. Rosant
Research Scientist.

Laboratoire de Mécanique des Fluides,
D.M.E., CNRS U.R.A. 1217,
ECN, 44072 NANTES Cedex 03, France

Pressure Drop in Single-Phase and Two-Phase Couette-Poiseuille Flow

This paper is concerned with axial pressure gradient in single-phase and two-phase flow at low void fraction in a narrow annular space between two concentric cylinders, the inner one rotating. From experimental results, the coupling function (inertial forces/centrifugal forces) is parameterized by Taylor or Rossby numbers for two values of the intercylindrical width (clearance). The results are discussed with regard to different flow regimes and it is shown in particular that transition from the turbulent vorticed regime to the turbulent regime occurs at $Ro \simeq 1$. The proposed correlation agrees in a satisfactory manner to all the regimes studied in our experiments and in those given in the bibliography. In addition, original tests with a two-phase liquid/gas flow at 5 percent G.O.R. (gas oil ratio), for a finely dispersed gas phase are also reported. These results indicate a similar behavior to single-phase flows, justifying the transposition of the same correlation in the framework of the homogeneous model.

1 Introduction

The flow in an annulus formed by two concentric cylinders with rotation of the inner cylinder and forced axial flow rate, the so-called Couette-Poiseuille flow, has in recent years been the subject of fundamental research concerning stability problems (Hugues and Reid, 1968; Frene, 1974; Hasoon and Martin, 1977; Takeuchi and Jankowski, 1981; Di Prima and Stuart, 1983). The practical difficulty of instrumentation in standard metrology due to the confinement of the geometry, is a handicap for the local exploration of such flows. A comparison between the results now available and theoretical approaches reveals considerable and even contradictory differences depending on the authors. In general, four principal regimes have been identified (Kaye and Elgar, 1958): the laminar, laminar vortex, turbulent vortex, and turbulent flows. According to Kataoka et al. (1977) Legrand and Coeuret (1982), Legrand et al. (1983), secondary regimes can be observed in the vortex regimes, which issue essentially from the complexity of the structures in the Taylor vortices. Besides the laminar regime, which is characterized by the absence of any interaction between the two components (axial and azimuthal), the wall friction was studied (Yamada et al., 1969; Simmers and Coney, 1979), but the knowledge of the corresponding interaction is actually insufficient for all flow regimes.

From an engineering point of view, the design of industrial machinery, rotating at high angular velocity, raises various technological problems. Therefore, for industrial projects in which machinery must operate at 8000 rpm, a better understanding of the behavior of the bearing (labyrinth) is necessary. This might be qualified by the relationship between the feed pressure and flow rate as a function of the shaft rotation velocity. The present experimental investigation is concerned with the measurements of the axial pressure gradient for a given flow rate and an angular velocity. It was conducted in order to explore a relatively wide range of Taylor and Reynolds numbers, $Ta \leq 4500$ and $720 \leq Re \leq 18000$. An example in case, is one in which the fluid circulating in the labyrinth is of the two-phase type (oil + gas). Here, the investigation was limited to low void fraction.

2 Experimental Procedures

The schematic diagram of the experimental apparatus used is shown in Fig. 1. The labyrinth is simulated by an annular space between two concentric cylinders having a horizontal axis and with the interior rotating cylinder (rotor) and the exterior cylinder fixed (stator). The rotor shaft is set in rotation by a DC motor capable of reaching angular velocities of 10000 rpm, accurate to ±5 rpm by a tachometer. Two geometries

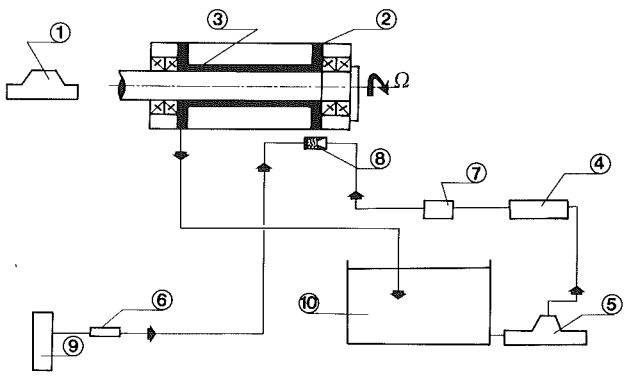

Fig. 1 General arrangement of the apparatus

Contributed by the Fluids Engineering Division for publication in the JOURNAL OF FLUIDS ENGINEERING. Manuscript received by the Fluids Engineering Division October 23, 1989.

Table 1 Geometries of the bearing and experimental conditions

e/R_1	0.02	0.04
L_1/R_1	9.	9.28
Ta	0 – 1620	0 – 4500
Re	720 – 8. 10^5	10^3 – 1.8 10^4
Ro (Re > 4000)	0. – 3.55	0. – 8.27
G.O.R.	0.	0., 0.05

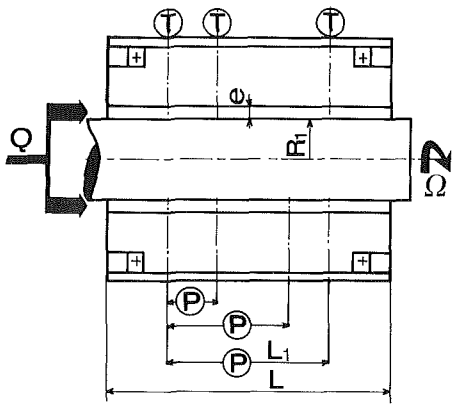

Fig. 2 Measurements in the test cell P: pressure sensor; T: thermocouple

are tested with a diameter of 50 mm for the rotor and radial clearances of 0.5 and 1. mm. The length of the bearing is always 312 mm (Table 1). For a flow circulating in the labyrinth, the pressure profile is determined along the test cell. Four pressure taps have been drilled along the bearing (Fig. 2), which are connected to differential sensors having measuring ranges of 10^4 to 5.10^5 Pa with a full-scale accuracy of 2 percent. The temperature variation, ΔT, is also determined by two thermocouples mounted in opposition at the bearing inlet and outlet by using a third thermocouple as a reference. In disadvantageous conditions, i.e., high liquid flow rate with various rotation velocities, it was noticed that pressure decreases in a linear fashion from the tape at the inlet bearing and at the outlet. Later on in the experiment, for presented results, differential pressure measurements are taken between the first tap and the last one, spaced a distance L_1 apart.

The working fluid is composed of 95 percent water and 5 percent soluble oil. The choice of this fluid was made to avoid oxidation of some bearing steel components and to preserve the wall roughness (smooth walls). Physical properties of the mixture were determined in the IFP Laboratory. The density

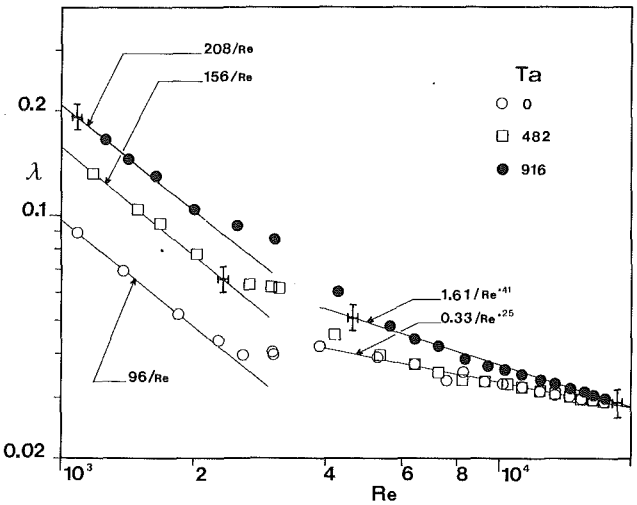

Fig. 3 Rotation effect on the pressure drop coefficient λ versus Re at Ta fixed for $e/R_1 = 0.04$

remains close to that of water and viscosity of the mixture varies like that of water with temperature. The heat exchanger in the loop allows a constant temperature to be maintained in the test cell, close to 21°C. There, in this temperature-range, the relative viscosity (compared to water) is about 1.13. For two-phase flow tests, gas is injected through a sintered-metal element situated at the inlet of the bearing. A venturi effect system is used to measure the nitrogen flow rate with an accuracy of about 5 percent (see Salhi, 1986a). At the outlet of the test cell a sample of the flow is taken, the slip velocity of bubbles in the steady liquid is evaluated and gives an estimated medium diameter of 30 μm for the nitrogen bubbles; this value is confirmed by photographic pictures.

3 Results and Discussion

Figure 3, obtained from the 0.04 value of the ratio e/R_1, shows the experimental evolution of (the pressure drop coefficient) λ, in relation to (the axial Reynolds number) Re, at a fixed value of (the Taylor number) Ta. It can be seen, on the one hand that these experimental data satisfy the following relationship, written in a general form:

$$\lambda = C\,\mathrm{Re}^{-n}$$

On the other hand, they have different shapes depending on whether the value of the Reynolds number is less than or greater than approximately 2100. Therefore, the experimental results are interpreted using only as sole reference the Poiseuille flow (annular axial flow without rotation) and the influence of the centrifugal forces on the axial pressure drop can be expressed by a coupling function,

Nomenclature

A_0, A, C = numerical coefficients
e = $R_2 - R_1$, annual space width (clearance)
f = $\Delta p/\Delta p_p$, coupling function
G = mass flow rate
L = length of the bearing
L_1 = distance between pressure taps
Q = volumetric flow rate
R_1 = radius of inner cylinder
R_2 = radius of outer cylinder
Re = $2e\rho Q/\mu S$, Reynolds number
Re* = modified Reynolds number
Ro = $\Omega R_1 S/Q$, Rossby number
S = $\pi e(R_2 + R_1)$, cross-sectional area
Ta = $(\Omega R_1 e\rho/\mu)\sqrt{e/R_1}$, Taylor number
T = temperature
α = void fraction at the inlet of the bearing
Δp = axial pressure drop
λ = $4eS^2\Delta p/(\rho Q^2 L_1)$, axial pressure drop coefficient
μ = dynamic viscosity
ρ = density
Ω = angular velocity of inner cylinder

Subscripts

m = mixture
p = Poiseuille flow alone
g = gas phase
c = critical value
cal = calculated value
exp = experimental value

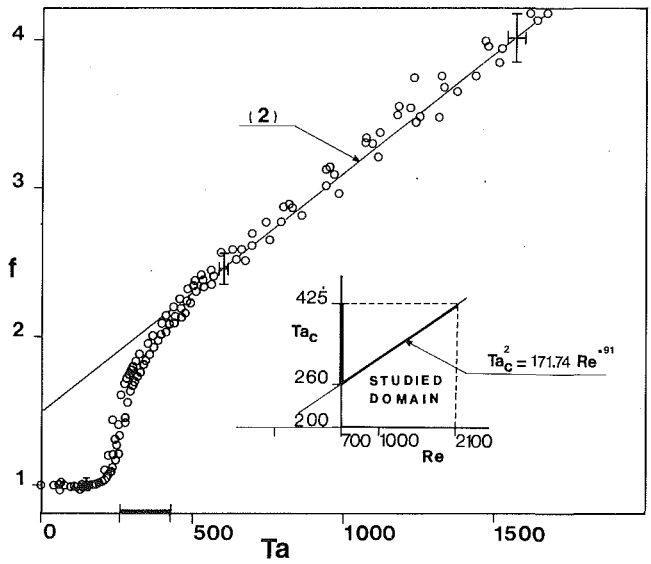

Fig. 4 Variation of coupling function versus Taylor number for $720 \leq Re \leq 2100$ and $e/R_1 = 0.02$

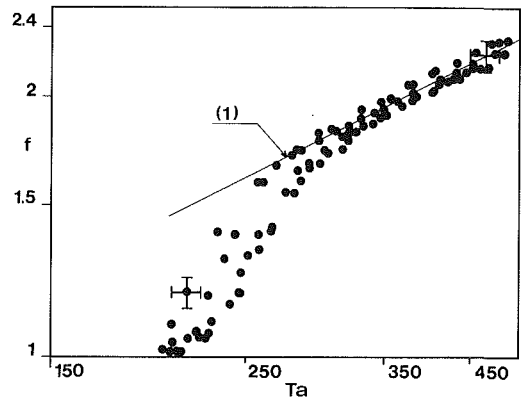

Fig. 5 Transition between laminar and laminar vortex flows $e/R_1 = 0.02$ $720 \leq Re \leq 2100$

$$f = \Delta p/\Delta p_p = \lambda/\lambda_p$$

where λ_p, the pressure drop coefficient for the Poiseuille flow, may be estimated using the following classical expressions for narrow gaps (Salhi, 1986b):

$$\lambda_p = 96/Re \quad \text{if } Re \leq 2100$$
$$\lambda_p = 0.33/Re^{0.25} \quad \text{if } Re \geq 4000$$

3.1 Range of Reynolds Numbers $Re \leq 2100$. The combination of an inner cylinder rotation and a forced axial flow rate give rise to an increased axial pressure drop. The experimental evolution of the pressure drop coefficient verifies a similar law describing a laminar regime of the Poiseuille flow in the same conditions, $\lambda = C(Ta)/Re$. The effect of the rotation on the axial pressure drop coefficient is described by the C parameter. It can be seen that the evolution of the coupling function ($f = \Delta p/\Delta p_p = C/96$) versus the Taylor number presents three shapes as shown in Fig. 4 obtained for the 0.02 value of the ratio e/R_1. Thus the existence of three zones can be noticed:

- the first one defined by $Ta \leq 250$, where f remains constant ($f \simeq 1$),
- the second one defined by $250 \leq Ta \leq 450$, where f can be estimated by the empirical relationship (Fig. 5):

$$f = 0.1\ Ta^{0.5} \quad (1)$$

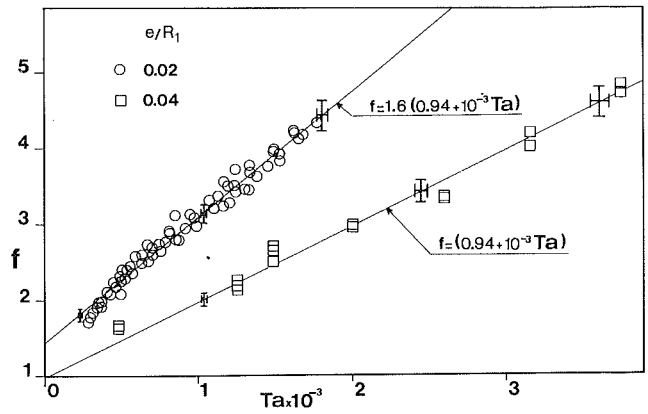

Fig. 6 Vortex laminar regime; f versus Ta for $720 \leq Re \leq 2100$ $e/R_1 = 0.02$ and $e/R_1 = 0.04$

- the third one begins at $Ta \geq 450$, where the following relation is in good agreement with our measurements for the two tested gaps, $e/R_1 = 0.02$ and $e/R_1 = 0.04$ (Fig. 6):

$$f = C/96 = A_0\ (0.94 + 10^{-3}\ Ta) \quad (2)$$

the parameter A_0 depends on the ratio e/R_1,

$$A_0 = 1.6 \quad \text{if} \quad e/R_1 = 0.02$$
$$A_0 = 1.0 \quad \text{if} \quad e/R_1 = 0.04$$

Legrand and Coeuret (1983) indicate that in the domain they studied ($Re \leq 820$ and $135 \leq Ta \leq 3700$), the critical Reynolds value $Re = 300$ characterizes the transition from laminary vortex to turbulent vortex flow. According to Kreith (1968), the regime always remains a laminar vortex flow even when $Re \geq 300$, but the size of the vortices is not uniform. According to the criterion proposed by other authors, the range $Ta \leq 4500$ and $720 \leq Re \leq 18000$—our study domain—, can be divided into two or three flow regimes:

- the turbulent with vortices and turbulent regimes (Kaye and Elgar, 1958; Astill, 1964),
- the laminar with vortices, turbulent with vortices and turbulent regimes (Becker and Kaye, 1962).

The various flow regimes are not well-defined in the literature, so that it is difficult to deduce exactly from the coupling function expression the different regimes corresponding to the range $Ta \leq 4500$ and $720 \leq Re \leq 2100$. It can be noted that the form of the coupling function f in the third zone—$f = A_0\ (0.94 + 10^{-3}\ Ta)$—implies that the probable vortices state of the azimuthal component is convected by the axial motion, without any disturbance. Our deduction is in agreement with the analysis of Legrand et al. (1983). From the expression of the coupling function and other works, zones and regimes can be related as follows:

- the first zone ($f \simeq 1$) corresponds probably to the laminar regime,
- the third zone ($f = A_0\ (0.94 + 10^{-3}\ Ta)$) corresponds to a laminar regime with vortices,
- the second zone ($f = 0.1\ Ta^{0.5}$) corresponds to the transition between these two regimes, so if we refer to the couple values of (Ta_c, Re) reported by Simmers and Coney (1979) and empirically fitted by Legrand and Coeuret (1982):

$$Ta_c^2 = 171.74\ Re^{0.91} \text{ for } 300 \leq Re \leq 1600 \quad (3)$$

we can observe that the critical value of the Taylor number corresponding to the Reynolds number as $720 \leq Re \leq 2100$ (the relation (3) is extended) belongs to this zone.

3.2 Range of Reynolds Numbers $Re \geq 4000$. In this range the increase of the axial pressure drop depends simultaneously on the two components of the motion. We can obviously in-

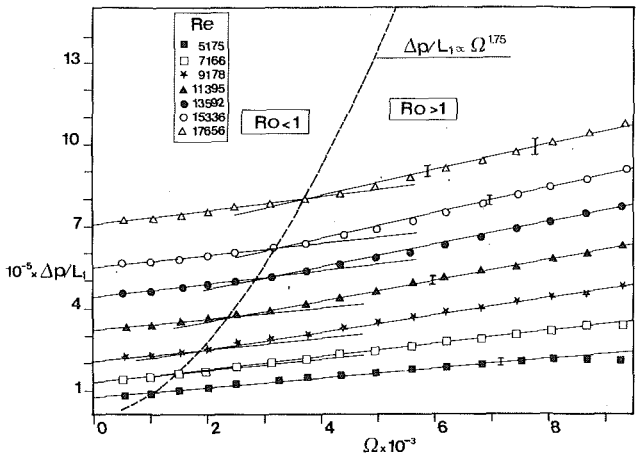

Fig. 7 Rotation effect on the pressure drop: $\Delta p/L_1$ (Pa/m) versus Ω (rpm) at Re fixed for $e/R_1 = 0.04$ ——— curve corresponding to Ro = 1 ($Q/S = \Omega R_1$; $\Delta p \propto \Omega^{1.75}$)

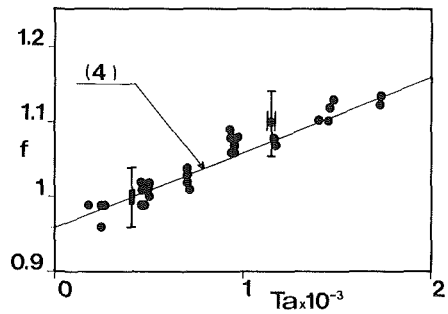

Fig. 8 f versus Ta for $e/R_1 = 0.04$; $4000 \le Re \le 18000$ and $Ro < 1$. Turbulent regime flow

troduce the Rossby number ($Ro = 2\sqrt{R_1/e}\ Ta/Re = \Omega R_1 S/Q$, if R_1 is the chosen characteristic length scale) which is the ratio of centrifugal forces to inertial forces, to improve our measurement of these two effects. The equality of centrifugal and inertial forces, i.e., Ro = 1, can be used for the definition of two regions as observed in the Fig. 7. The experimental data belonging to the zone where Ro < 1 can be grouped in the representation (f, Ta) and the following relation is obtained for 0.04 value of the ratio e/R_1 (Fig. 8):

$$f = 0.96 + 10^{-5}\ Ro.Re = 0.96 + 10^{-4}\ Ta \qquad (4)$$

Consequently, in this case (Ro < 1) the increase of axial pressure drop depends only on the centrifugal forces and one can observe that $0.96 \le f \le 1.05$ (see Fig. 8). This variation is therefore not significant in regard to the experimental uncertainty. Indeed it may be proposed $f = 1$ in explanation, the fact that the vortice structure (resulting from the centrifugal forces) cannot persist because of a strong turbulent intensity induced by the inertial forces. The experimental data, belonging to the zone where Ro > 1 satisfy the following relation, for our two values of the ratio e/R_1 (Fig. 9):

$$f = 0.94 + 0.23\ Ro \qquad (5)$$

In this zone the centrifugal forces are greater than those of the inertial forces. When the Reynolds number is fixed and when the Rossby number increases, then the flow regime is controlled by the azimuthal component which leads to an increase in the wall friction.

For the Ro > 1 and $Re \ge 4000$ range, our data and those collected from Viano (1970) verify the following classical relationship:

$$\lambda = A\ Re^{*-n} \qquad (6)$$

where Re* is a modified Reynolds number, $Re^* = Re/(0.94 + 0.23\ Ro)^4$; numerical coefficients A and n are parameters depending on the ratio e/R_1. The experimental data can be fitted with the following analytical functions (see Salhi, 1986a, Salhi et al., 1987):

$$A = 0.1\ (e/R_1)^{-0.37}$$
$$n = 0.15\ (e/R_1)^{-0.16}$$

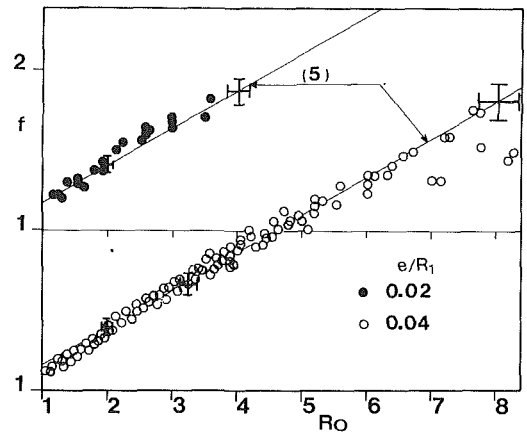

Fig. 9 f versus Ro for $e/R_1 = 0.04$; $4000 \le Re \le 18000$ and $Ro > 1$. Turbulent vortex flow

Figure 10 shows the comparison between the experimental pressure drop coefficient and pressure drop coefficient deduced from the correlation (6) for $e/R_1 \le 0.02$.

The two typical zones correspond respectively to a turbulent regime (Ro < 1) and a vortex turbulent regime (Ro > 1). The transition between these regimes corresponds to the $Ro \simeq 1$ value and the pressure drop coefficient satisfies the relationship:

$$\lambda = 0.20\ Ta^{-0.25} = 0.36\ Re^{-0.25}$$
$$\text{i.e., } \Delta p \propto \Omega^{1.75} \qquad (7)$$

It can be seen in Fig. 9, that the experimental data which fall in the range ($Ro \ge 5$) and ($Re \ge 4000$) show a discrepancy with Eq. (5), but we do not have enough data to conclude whether this value, Ro = 5, implies a transition or not. It can be noted that the rotation has the same quantitative effect in the cases of the homogeneous or inhomogeneous flows; Jacquin et al. (1987) have observed transitions, which are associated with particular values of the macroscopic Rossby number characterizing a turbulent rotating homogeneous flow (see also Hopfinger et al., 1982). The experimental evolution of the coupling function for $2100 \le Re \le 4000$ and $Ta \le 4500$ is spread in (f, Ta) or (f, Ro) appropriate representations.

The rise in temperature between the bearing inlet and outlet was not felt to be significant enough during runs ($\Delta T \le 1°C$) to be the subject of a particular investigation.

4 Two-Phase Flow Experiments

Two-phase flow experiments are performed only for the gap $e = 1$. mm and for $Re_m \ge 4000$, while the gas/oil ratio (G.O.R.) remains constant and equal to 5 percent. The experimental results confirm that the pressure drop in the labyrinth increases in the presence of the gas phase and this increase is more significant when the forced axial rate is important. This effect can be taken into account with a homogeneous model (Wallis, 1969). The definition of dimensionless numbers is modified as follows:

$$Re_m = 2e\ G/\mu_m$$
$$Ta_m = \frac{\rho_m\ \mu}{\rho\ \mu_m} Ta$$

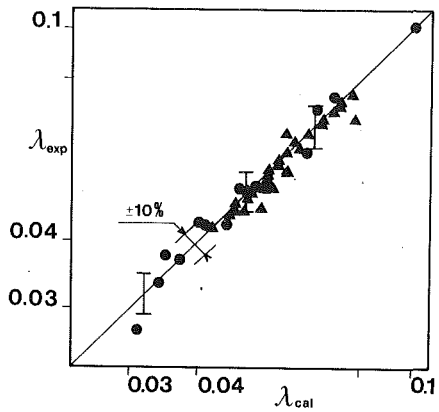

Fig. 10 Comparison between correlation results and experimental data for $e/R_1 \leq 0.02$ $Re \geq 4000$; λ_{exp} versus λ_{cal} • Viano (1970) ▲ Salhi (1986b)

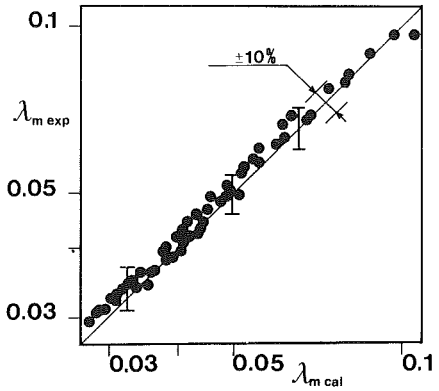

Fig. 11 Two-phase flow tests. Comparison between present results and the homogeneous model, for $e/R_1 = 0.04$ and $Re_m \geq 4000$; $\lambda_{m\ exp}$ versus $\lambda_{m\ cal}$

Using a scheme for the mixture viscosity $\mu_m = \mu\ \rho_m/\rho$, deduced from the fact that the gas phase plays a principal role in the increase of the bulk velocity ($Re_m = \rho/\rho_m\ Re$; $Ta_m = Ta$). The value 1 for Ro_m is always characteristic for the definition of two zones, and the transposition of the correlation established from single-phase flow (relations (4) and (5)) to the two-phase flow gives a good agreement with our measurements:

$$\lambda_m = 0.33\ (0.96 + 10^{-4}\ Ta) \text{ if } Ro_m < 1 \text{ and } Re_m \geq 4000$$

$$\lambda_m = 0.33\ (0.94 + 0.23\ Ro_m) Re_m^{-0.25} \text{ if } Ro_m > 1 \text{ and } Re_m \geq 4000$$

Figure 11 shows the comparison between the experimental pressure drop coefficient of the mixture and the pressure drop coefficient calculated with the present correlation. The interpretation of our measurements is consistent with the homogeneous model. This allows a justification of the hypothesis that the gas remains dispersed in the annular space. The separation favored by the rotation would be limited by the turbulent intensity and eventually stopped by the bubble coalescence time.

5 Conclusions

The present results contribute to an improvement in the modelling of the Couette-Poiseuille flow with single-phase and two-phase (with a low void fraction) configurations. Our measurements complete the experimental data base and our analysis leads to a correlation which includes parameters that can be used for a relatively wide range of flow rate and angular velocity.

More precisely, the parameters such as Taylor and Rossby numbers take into account the rotation/convection coupling using a coupling function which clearly shows the different flow regimes: laminar, laminar vortex, turbulent vortex and turbulent flows. The Rossby number appears as the fundamental parameter of the transition having a universal character when a rotation is added to developing turbulence. Finally, regarding the liquid/gas flows with low void fraction, in spite of the possible rotation effects, the validity of the homogeneous model seems to be experimentally proved.

Acknowledgments

The authors are grateful to the Institut Français de Pétrole, where this experimental work was conducted.

References

Astill, K. N., 1964, "Studies of the Developing Flow Between Concentric Cylinders with the Inner Cylinder Rotating," ASME *Journal of Heat Transfer*, Vol. 86, pp. 383-392.

Becker, K. M., and Kaye, J., 1962, "Measurements of Diabatic Flow in an Annulus with an Inner Rotating Cylinder," ASME *Journal of Heat Transfer*, Vol. 84, pp. 97-105.

Di Prima, R. C., and Stuart, J. T., 1983, "Hydrodynamic Stability," *Journal of Applied Physics*, Vol. 50, pp. 983-991.

Frene, F., 1974, "Régimes d'écoulement non laminaire en films minces. Application aux paliers lisses," Thèse Docteur-ès-Sciences, Université Claude Bernard, Lyon.

Hasoon, M. A., and Martin, B. W., 1977, "The Stability of Viscous Axial Flow in an Annulus with a Rotating Inner Cylinder," *Proc. Roy. Soc. London*, Vol. A. 352, pp. 351-380.

Hopfinger, E. J., Browand, F. K., and Gagne, Y. D. J., 1982, "Turbulence and Waves in a Rotating Tank," *Journal of Fluid Mechanics*, Vol. 125, pp. 505-534.

Hugues, T. H., and Reid, W. H., 1968, "The Stability of Spiral Flow Between Rotating Cylinders," *Phil. Trans. Roy. Soc. London*, Vol. A 263, pp. 57-91.

Jacquin, L., Leuchter, O., and Geffroy, P., 1987, "Experimental Study of Homogeneous Turbulent in the Presence of Rotation," *Proc. 6th Symp. on Turbulent Shear Flow*, Toulouse, pp. 351-356.

Kataoka, K., Doi, H., and Komai, T., 1977, "Heat/Mass Transfer in Taylor Vortex Flow with Constant Axial Flow Rates," *Int. J. Heat Mass Transfer*, Vol. 20, pp. 57-63.

Kaye, J., and Elgar, E. C., 1958, "Modes of Adiabatic and Diabatic Fluid Flow in an Annulus with an Inner Rotating Cylinder," *Trans. ASME*, Vol. 80, pp. 753-765.

Kreith, F., 1968, "Convection Heat Transfer in Rotating Systems," *Adv. Heat Transfer*, Vol. 5, p. 129.

Legrand, J., and Coeuret, F., 1982, "Transfert de matière global liquide-paroi pour des écoulements associant tourbillons de Taylor et circulation axiale forcée," *Int. J. Heat Mass Transfer*, Vol. 25, pp. 345-351.

Legrand, J., Coeuret, F., and Billon, M., 1983, "Structure dynamique et transfert de matière liquide-paroi dans le cas de l'écoulement laminaire tourbillonaire de Couette-Poiseuille," *Int. J. Heat Mass Transfer*, Vol. 26, pp. 1075-1085.

Salhi, A., 1986a, "Flow in Rotating Space," Two-phase transfer Poseidon Activity Report, Ref. 33 758 A, Institut Français du Pétrole, Paris.

Salhi, A., 1986b, "Etude de l'écoulement de Couette-Poiseuille, liquide et liquide/gaz, dans un espace annulaire réduit," Thèse Docteur-Ingénieur, Université de Nantes.

Salhi, A., Rosant, J. M., and Rey, C., 1987, "Débit de fuite dans les paliers longs en fonctionnement monophasique et diphasique," *Proc. 11th Canadian Congress of Applied Mechanics*, Edmonton, pp. B 84-85.

Simmers, D. A., and Coney, J. E. R., 1979, "A Reynolds Analogy Solution for the Heat Transfer Characteristics of Combined Taylor Vortex and Axial Flows," *Int. J. Heat Mass Transfer*, Vol. 22, pp. 679-689.

Viano, M., 1970, "Pertes dans les labyrinthes cylindriques lisses. Considérations et essais sur les labyrinthes cylindriques lisses des machines hydrauliques," *La Houille Blanche*, No. 1, pp. 55-61.

Takeuchi, D. I., and Jankowski, D. F., 1981, "A Numerical and Experimental Investigation of the Stability of Spiral Poiseuille Flow," *Journal of Fluid Mechanics*, Vol. 102, pp. 101-126.

Wallis, G. B., 1969, *One Dimensional Two-Phase Flow*, McGraw-Hill.

Yamada, Y., Nakabayashi, K., and Maeda, K., 1969, "Pressure Drop Measurements of the Flow Through Eccentric Cylinders with Rotating Inner Cylinders," *Bulletin of JSME*, Vol. 12, No. 53, pp. 1032-1040.

Studies on Cavitation Inception Process in Separated Flows

S. G. Milton

V. H. Arakeri

Department of Mechanical Engineering,
Indian Institute of Science,
Bangalore 560012, India

Studies related to cavitation inception process in separated flows are reported. Experimental observations of bubble appearance in grooves with laminar or turbulent boundary layer over them have clearly shown that gaseous diffusion process is significantly enhanced in turbulent flow. This process can lead to local nuclei size modification in environment similar to that of flow over a groove, like laminar separation "bubbles." Cavitation inception modeling including this aspect is carried out for predicting inception conditions associated with "bubble-ring" cavitation commonly observed on hemispherically nosed axisymmetric body. Qualitative dependence of predicted inception numbers with velocity is found to agree very well with experimental observations of Carroll (1981).

1 Introduction

It is now a well established fact that certain features of viscous flow past a body significantly affect its cavitation inception characteristics. Arakeri and Acosta (1973) were the first to convincingly demonstrate this fact for axisymmetric bodies which possess laminar separation. Subsequent studies by Van der Muelen (1976), Gates and Acosta (1978), Katz (1981), and Carroll (1981) have all confirmed these findings.

Modeling of inception has been carried out by many investigators and much of the work before 1969 has been reviewed comprehensively by Holl (1969). However, only Parkin's later work (Parkin, 1979) has incorporated the new findings for flows with laminar separation and the following sequence of events has been proposed. A typical nucleus as it travels along the surface of the body first grows vaporously due to low pressures around the minimum pressure point upstream of laminar separation. It then becomes stabilized in the laminar separation bubble where it may grow by gaseous diffusion. When its size becomes large enough it interacts with the free shear layer and is carried downstream to the turbulent reattachment region where because of low pressures in the turbulent eddies it experiences a second short period of vaporous growth. This growth does not continue for a long time but due to turbulent shearing motions the bubble is torn apart and forms a part of the frothy narrow band of cavitation which appears at the downstream end of the separation bubble. This final frothy band of extremely small bubbles is identified as the bubble-ring cavitation. It is admitted by Parkin (1979) that even though the above events are enumerated to provide a reasonably complete picture of inception process, the assumption is made that once the nucleus becomes stabilized in the laminar separation bubble the subsequent events will occur automatically. A theory is then built which centers around the growth of the nucleus in response to the minimum pressures upstream of separation to a size large enough to either interact with the free shear layer or grow by gaseous diffusion. This theory which was a pioneering effort in this direction, however, is not complete for the reasons indicated below. The potential role of turbulent fluctuations due to turbulent transition before reattachment is not considered in the actual analysis and also any effect of the actual growth rates of nuclei in the separated region is not incorporated.

Here we include both of these effects in the modeling of inception process. The flow around the hemispherical nosed body on which bubble-ring cavitation occurs can be divided into three distinct regions: 1) the minimum pressure region upstream of separation; 2) the separation region; and 3) the reattachment region. In general, one would expect cavitation to start occurring in the minimum pressure region. But the peculiarity with the bubble-ring cavitation is that it does not occur in the minimum pressure region but, downstream, in the reattachment region. We conjectured that this may be due to the nuclei in the free stream being too small to respond to low pressures in the minimum pressure region but that they get entrained in the separated region and grow there by gaseous diffusion and then are carried downstream into the reattachment region. Here they grow and collapse vaporously under the action of turbulent pressure fluctuations resulting in the observed bubble-ring cavitation. The gaseous growth in the separated region has very important role to play in that the nuclei which failed to respond earlier to the low pressures in the minimum pressure region now respond to the turbulent pressure fluctuations only because they have grown to sufficiently large size by diffusion. This is true over a considerable range of velocities and is the main thrust of the paper. Experiments were conducted to see what is the important mechanism of growth of bubbles in separated flows and to obtain the order-of-magnitude values for the residence time of the bubbles in such flows. The experimental studies are described here briefly first. A complete description of the experimental studies and the modeling is contained in a thesis by Milton (1989).

2 Background Experiments

As indicated, some experimental work was undertaken to

Contributed by the Fluids Engineering Division for publication in the JOURNAL OF FLUIDS ENGINEERING. Manuscript received by the Fluids Engineering Division March 5, 1991.

investigate if the diffusion process is influenced by the type of flow surrounding the nucleus like laminar or turbulent. At the outset it became clear that this issue could not be resolved by studying or observing bubble growth patterns in naturally separated regions since, in this case, the nuclei are likely to experience both laminar and turbulent flow conditions. Therefore, an experimental configuration had to be thought of where some of the properties of the separated regions like the long residence time are simulated, at the same time having the possibility of subjecting the trapped liquid sample to the desired flow conditions. It was felt that this could be achieved by trapping a liquid sample in a groove placed on an axisymmetric body with its axial location suitably selected.

Experiments were conducted in the High Speed Water Tunnel at the Indian Institute of Science (Arakeri et al., 1987). Axisymmetric grooves were placed at different axial locations on different models, all having a 1.5 caliber ogive for their nose profile. The aspect ratio of the grooves, namely the depth-to-width ratio was 1. The groove locations were such that the boundary layer flow approaching a groove was either only laminar or turbulent depending on its location for the velocity range of 6 m/s to 15 m/s employed in the present studies. The selection of the groove locations was based on schlieren flow visualization and fluctuating pressure measurements. A diagram of one of the models used in the present studies, and indicating the groove locations, is shown in Fig. 1. Tests were conducted for inception in the grooves; the procedure for these tests was as follows. First the desired test velocity was established and the tunnel was run for a few minutes, like fifteen, at a pressure much higher than that required for inception. Then the test section pressure was slowly lowered until bubbles became visible in either of the grooves. In all cases the bubbles first appeared in the turbulent groove; after recording the pressure for inception there, the pressure was further lowered until visible bubbles appeared in the laminar groove and the corresponding pressure was also noted. From these the inception cavitation number, K_i, for each groove could be computed now as

$$K_i = \frac{p_{\infty i} - p_v}{1/2\rho U_\infty^2}$$

where, $p_{\infty i}$ is the test section static pressure at inception and the other parameters are defined in the nomenclature. The tests were repeated for the range of velocities indicated earlier. The nominal water temperature for the present tests was $28(\pm 0.5)°C$ and the dissolved gas content was maintained at about $75(\pm 4)$ percent of saturation at STP.

The significant findings from the experimental work relevant to the present scope of work are indicated below. Some results

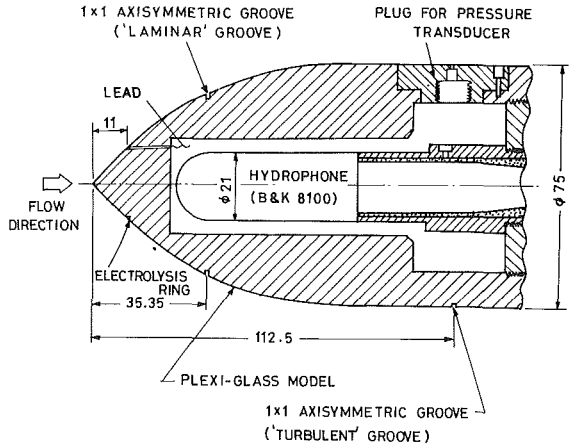

Fig. 1 Schematic sketch of one of the test models used in the present work. Note: All dimensions are in mm

Nomenclature

B = universal gas constant
C = a constant
C_0 = gas concentration in liquid at infinity
C_s = gas concentration in liquid at the liquid-gas interface
C_p = nondimensional pressure coefficient, $(p-p_\infty)/(1/2\rho U_\infty^2)$
C_p' = pressure coefficient corresponding to the amplitude of the fluctuating component, $p_a'/(1/2\rho U_\infty^2)$
C_{ps} = pressure coefficient at the separation point, $(p_s-p_\infty)/(1/2\rho U_\infty^2)$
D = diameter of the model
$\mathfrak{D}$ = diffusion coefficient
f = frequency
H = height of the separation bubble
j = an index
k = Henry's constant
K = cavitation number, $(p_\infty-p_v)/(1/2\rho U_\infty^2)$
K_i = inception cavitation number or inception number
L = length scale
m = mass of gas
M = molecular weight of gas
p = pressure
p_i = gas saturation pressure
p' = fluctuating component of pressure
p_a' = amplitude of the fluctuating component of pressure
p_{rms}' = rms value of the fluctuating component of pressure
p_s = static pressure in the separation region
p_v = vapor pressure
p_∞ = free-stream pressure
$p_{\infty i}$ = free-stream pressure corresponding to inception
R = bubble radius
R_{01} = bubble radius at the beginning of the first phase of growth
R_{12} = bubble radius at the end of the first phase of growth and also the initial size for the second phase of growth
R_{23} = bubble radius at the end of the second phase of growth and also the initial size for the third phase of growth
Re_D = Reynolds number based on body diameter, $U_\infty D/\nu$
$\dot{R}, \ddot{R}$ = bubble wall velocity and acceleration, respectively
s = arc distance along the model surface
s_0 = arc distance corresponding to a fixed point
S = surface tension of the liquid
t = time
t' = time local to one cycle in surface renewal theory
t^* = nondimensional time, tD/U_∞
t_R = residence time
T = temperature
U = velocity
U_∞ = free-stream velocity
V_{01} = bubble wall velocity at the beginning of the first phase of growth
V_{23} = bubble wall velocity at the end of the second phase of growth and also the initial velocity for the third phase of growth
x = axial distance
ν = kinematic viscosity of the liquid
ρ = liquid density
τ = renewal time

have been presented earlier by Arakeri et al. (1984) and, as indicated previously, further details may be found in Milton (1989). When the present experimental work was started very few inception results were available for inception in grooves at normal air content levels. But recently Cimbala and Billet (1989) have carried out extensive tests for inception in grooves under turbulent boundary layer conditions. In addition, they have carried out extensive measurements to characterize the flow in the groove in the form of velocity surveys and static pressure measurements. Certain questions have been raised regarding the effect of the ratio of shear layer thickness to groove width on inception. In the present studies we have made inception tests on grooves with aspect ratio of 1 and the boundary layer thickness approaching the turbulent groove is estimated to have the same order of thickness as the groove width, namely 1 mm. However, in the present studies our interest has been to directly compare the inception results for grooves under laminar and turbulent conditions subjecting them to the same free stream conditions such as the dissolved air content, nuclei population etc.

Inception results for the groove in turbulent region ($x/D = 1.5$) showed a clear difference from those for the groove in laminar region ($x/D = 0.47$); the inception indices were higher for the former compared to those for the latter. Also, at inception, one could observe inside the turbulent groove a ring of bubbles while only a few, usually 2 or 3, were observed inside the laminar groove. The inception results are presented in Fig. 2. There appears to be a jump in the inception values for the turbulent groove at a velocity between 10 m/s and 11 m/s. The reasons for this are not known but it is tempting to suspect that the boundary layer above the turbulent groove becomes fully turbulent only in the interval noted above though there is no other evidence to support this conjecture. Apart from the above observation the inception numbers for the turbulent groove are significantly higher even for velocities lower than 10 m/s. Also, included in the figure is a curve representing the threshold for static/turbulent diffusion. The inception results for the turbulent groove are seen to approach this threshold curve (presumably due to their fast growth) while those for the laminar groove do not. It should be pointed out here that the mean pressure coefficient, C_p at the present laminar and turbulent groove locations on a smooth model is nearly the same and is approximately equal to -0.1. All the K_i values in Fig. 2 exceed the negative value of this C_p and hence we can infer that the observed inception, in particular, for the turbulent groove was gaseous in nature. We do not expect the local excursions in static pressures to be so high as to over ride this conjecture. In addition, the bubble activity in the turbulent groove was uniform and continuous and hence unlikely to be dominated by static pressure excursions leading to vaporous cavitation. Further, there was no audible sound which is typical of vaporous cavitation. Cimbala and Billet (1989) also have arrived at the same conclusions from their experimental findings.

The time nuclei spend in the grooves is an important factor in determining the size to which they grow. If the growth rate of bubbles trapped in groove-like flows is to be estimated then the characteristic residence time is an important parameter. An order of magnitude estimate of this time was presently obtained using an experimental technique developed for this purpose. A laser beam was focussed in the groove at the top of the axisymmetric model and the scattered light was collected with the receiving optics of DISA Laser Doppler Anemometer (LDA) set-up. The signal from the photomultiplier tube was displayed on a digital storage oscilloscope screen. It was not possible to make any residence time measurements with naturally occurring nuclei or bubbles in the flow. Instead, measurements were possible with electrolysis bubbles generated from a flush mounted electrode whose location is shown in Fig. 1. Shanmuganathan (1985) has reported typical size of bubbles

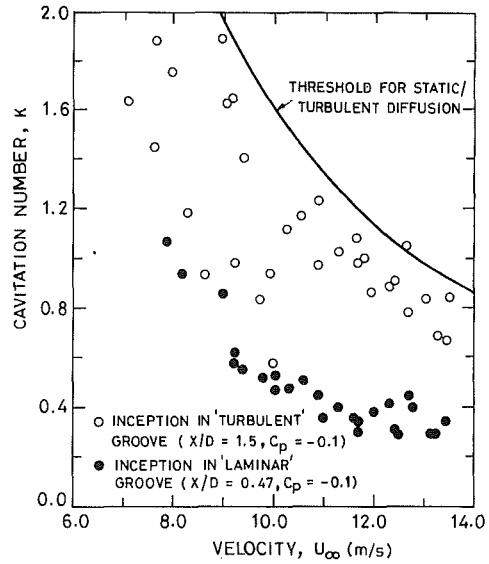

Fig. 2 Inception results for the grooves. Also shown is the threshold for static/turbulent gaseous diffusion. (Uncertainty in inception number is ±6 percent and in velocity it is ±1.5 percent at 20:1 odds)

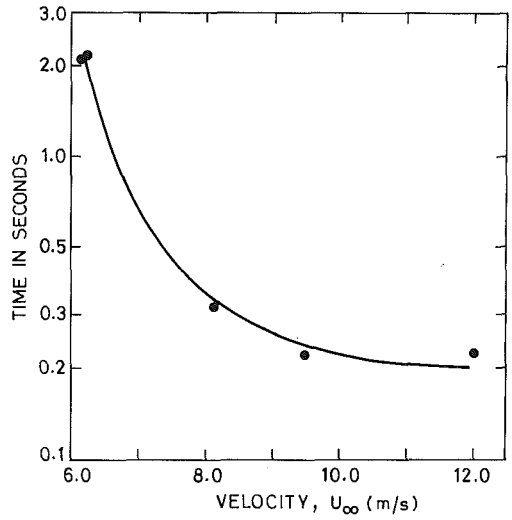

Fig. 3 Measured residence times for the laminar groove. (Uncertainty in residence time is ±44 percent and in velocity it is ±1.5 percent at 20:1 odds)

thus generated being in the range of 20–50 μm. The photomultiplier signal as displayed on the oscilloscope screen showed clear distinction in amplitude and in the number of pulses registered on the screen when the electrolysis bubbles were present in the groove as compared to when they were absent. This fact enabled us to make the residence time measurements following the procedure indicated next. First the electrolysis voltage was switched on and the steady state was established. Then when the voltage was switched off, at that instant the storage operation is triggered and the signal on the screen is frozen showing the details of the signal before and after the trigger. The residence time is then read off from the screen from the triggered point to the appropriate portion where the pulses have disappeared and the signal has returned to the normal state i.e., when the bubbles are not present in the groove. The results for the laminar groove are presented in Fig. 3 where an average of ten readings is reported as residence time. The results are quite accurate (with the uncertainity indicated in the figure caption) but we were not as confident about the measurements in the turbulent groove and hence the

results are not presented; there is definite scope for further improvement of the technique.

It appears from the experimental results presented that the growth of bubbles in the grooves is due to gaseous diffusion and among the various forms of diffusion possible, the turbulent diffusion is more effective in enhancing the bubble growth rates and that the residence time of the nuclei in the grooves is small. Bubble appearance in the turbulent groove was so distinct as compared to that in the laminar groove that we were lead to one of the conclusions indicated above. However, the actual bubble growth rates were not measured and the conclusion is a conjecture but, we believe, a logical one. In addition, there is potential for bubble growth by coalescence. Typical nuclei density measurements in water tunnels (see Billet, 1986) indicate that it is not likely to be an important factor, since average distance between the nuclei is estimated to be quite large in a relative sense. Similarly, we do not believe that the differences observed between turbulent and laminar grooves are related to other factors like cleanliness of the groove surfaces etc. since same experimental procedures were followed for both. Some of the important conclusions from the experimental study will be utilized in modeling the inception process in separated flows which is described next.

3 Modeling of Cavitation Inception

3.1 Preliminary Considerations. We wish to model the inception process of the particular type of cavitation known as bubble-ring cavitation (see Holl and Carroll, 1981; Parkin, 1979). It has been found that this form of cavitation, in general, is associated with headforms exhibiting laminar separation such as the hemispherical nosed body. On this body, laminar boundary layer separation has been found to exist upto a Reynolds number of 1.17×10^6 while theoretical calculations predict its existence even upto a Reynolds number of 5×10^6. The separation zone consists of two regions, namely, 1) the separation bubble region, 2) the transition and reattachment region. The separation bubble region is characterized by recirculating fluid close to the model surface, the pressure being nearly constant throughout the separation bubble region. Transition and reattachment occur at the end of the separation region, the reattachment region being characterized by large turbulent pressure fluctuations (Arakeri, 1975; Huang and Hannan, 1975; and Katz, 1981). We expect certain features of fluid flow characteristics in the bubble region to be similar to those occurring for flow within a groove. Observation of the bubble activity by Parkin and Kermeen (1953) and Arakeri (1973) indicate a close relationship with the viscous flow characteristics just described. The first visible macroscopic cavitation i.e., the bubble-ring cavitation is found to occur in the reattachment region of the separated zone (Arakeri and Acosta, 1973). High speed motion pictures indicated that the macroscopic cavitation was sustained by microscopic bubbles which grew, presumably, by gaseous diffusion in the separated region. The microscopic bubbles had a residence time of the order of a few milliseconds. These observations are further supported from our present findings with respect to inception process in the flow over grooves.

3.2 Equations Governing the Growth of a Nucleus. In the modeling of inception we consider three different phases of growth on the hemispherical nosed body corresponding to the three distinct regions mentioned earlier. A schematic sketch showing the trajectory of a typical nucleus with a demarcation of the regions of various phases of growth is given in Fig. 4. Also shown in the figure are respective initial conditions for various phases of growth. Next, we formulate the details of each phase of growth and this is followed by an indication of the methodology for inception prediction. It should be pointed out here that the second phase of growth has been included

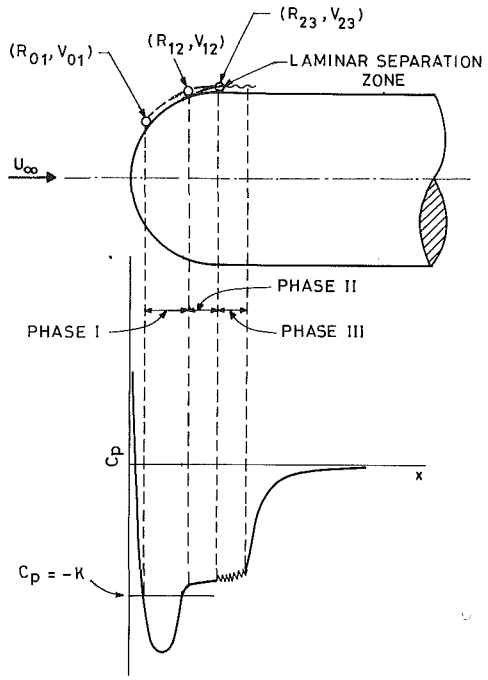

Fig. 4 Schematic diagram indicating the bubble trajectory and some details related to various phases of growth considered in inception modeling

in the present model based solely on our observations of inception process in the flow over a groove.

3.2.1 Phase I—Growth Due to Low Pressure Upstream of Separation. The growth of a nucleus in this phase is governed by the Rayleigh-Plesset bubble dynamics equation. For isothermal behavior of gas inside the bubble it takes the following form,

$$R\ddot{R}+\frac{3}{2}\dot{R}^2=\frac{1}{\rho}\left(\frac{C}{R^3}+p_v-\frac{2S}{R}-p(t)\right) \tag{1}$$

with $R(0)=R_{01}$ and $\dot{R}(0)=V_{01}$ (refer to Fig. 4). We put $p(0)=p_v$ and $V_{01}=0$. Therefore R_{01} corresponds to the bubble size corresponding to the vapor pressure p_v; this happens to be a convenient reference state in the present problem. Also, it can be shown that $C=2SR_{01}^2$. For $p(t)$ we have the following relations

$$p(t)=(C_p(t)+K)\frac{1}{2}\rho U_\infty^2+p_v \tag{2}$$

and

$$t=\frac{1}{U_\infty}\int_{s_0}^{s}\frac{ds}{\sqrt{1-C_p(s)}}\,. \tag{3}$$

The theoretical pressure distribution, C_p, computed by Carroll (1981) for hemispherical nose without any blockage effects has been used for the present growth calculations.

3.2.2 Phase II—Growth Due to Turbulent Diffusion. For estimating the growth rates of nuclei/bubbles by turbulent diffusion we will apply surface renewal theory (see Danckwerts (1970) for a review). We will use the form of model suggested by Higbie (1935), since it has been found to be reasonably accurate when compared to others and at the same time simple. In the presently adopted model due to Higbie (1935) a bubble surface is assumed to be exposed to fresh liquid samples repeatedly with a constant time interval of τ. A schematic diagram in Fig. 5 illustrates the basic features of the surface renewal theory as applied presently. At time $t'=0$ there is a step jump in concentration from C_0 to C_s across the in-

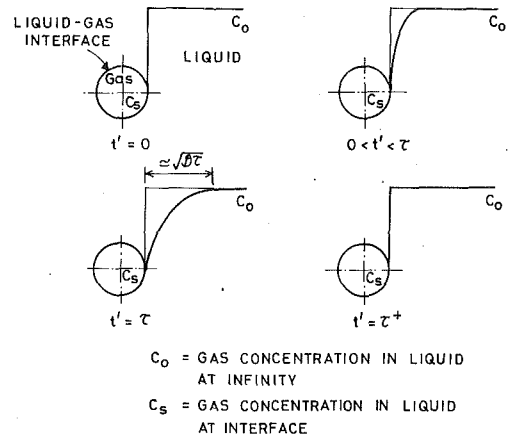

Fig. 5 Schematic diagram illustrating the variation of concentration profiles during a typical cycle of surface renewal

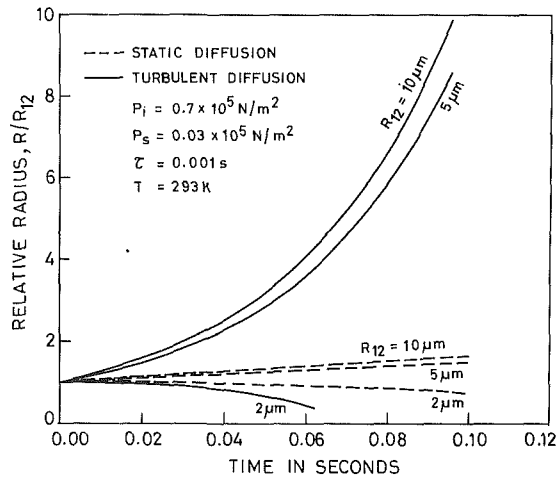

Fig. 6 Computed rates of growth of nuclei by turbulent diffusion and static diffusion for typical conditions. R_{12} here is the initial size

terface. Subsequently, for $t' > 0$ the rate of diffusion of gas is the same as that would exist under static conditions up to a time interval of τ. At the end of this interval the surface is renewed with a fresh liquid sample of concentration C_0 (by turbulent eddies) and the cycle is repeated, now, with a new initial radius. Epstein and Plesset's theory (Epstein and Plesset, 1950) is used for estimating the growth rates in each cycle. Then, for the jth cycle of renewal we have,

$$\frac{dR(j)}{dt'} = \frac{\mathfrak{D}k^{-1}}{(M/BT)} \frac{\left(p_i - \left(p_s - p_v + \frac{2S}{R(j)}\right)\right)}{\left(p_s - p_v + \frac{4S}{3R(j)}\right)} \left(\frac{1}{R(j)} + \frac{1}{(\pi \mathfrak{D} t')^{1/2}}\right) \tag{4}$$

for $0 < t' \leq \tau$, with $R(j)(t' = 0) = R(j-1)(t' = \tau)$ and $R(j=1)(t' = 0) = R_{12}$. Here t' represents the time local to one cycle. The relation between t' and the global time t is

$$t = (j-1)\tau + t' \text{ for the } j\text{th cycle.}$$

It should be noted that even though $\mathfrak{D}$ signifying molecular diffusion appears in Eq. (4) above, the enhancement of rates of diffusion due to turbulence is accounted for by the renewal of the bubble surface with fresh liquid samples at intervals of τ, with the accompanied high initial rates of mass transfer in each cycle.

Some solutions to the above equation are presented in Fig. 6 for one value of pressure in the separation region and for different values of the initial radius R_{12}. Solutions for static diffusion growth also are presented in the same figure for comparison. For these calculations the renewal time τ was given a value of 0.001 seconds which is within the range to be encountered later in the inception calculations. The saturation pressure p_i was taken as 0.7×10^5 N/m^2 while $\mathfrak{D}$ has been taken as 2.0×10^{-9} m^2/s for diffusion of air in water and, the other properties of liquid and gas have been assigned standard values as applicable to water and air. For solving the above equation fourth-order Runge-Kutta-Gill algorithm was used. It can be seen from the figure that after a fixed time interval the predicted growth by turbulent diffusion is, in general, many times greater than growth by static diffusion. It is also apparent that both growth and dissolution are enhanced by turbulent diffusion.

3.2.3 Phase III—Vaporous Growth Due to Turbulent Pressure Fluctuations. Here we assume that the complex interaction of a bubble with turbulent eddies can be represented by a function of the form

$$p(t) = p_s - p_a' \sin 2\pi f t \tag{5}$$

where, f is the dominant frequency of the fluctuations. During this phase of growth we assume that there is no diffusion of gas into the bubble. The bubble dynamics equation for this case will be

$$\rho\left(R\ddot{R} + \frac{3}{2}\dot{R}^2\right) = C/R^3 - (C_{ps} + K)\frac{1}{2}\rho U_\infty^2 - 2S/R + C_p' \frac{1}{2}\rho U_\infty^2 \sin 2\pi f t \tag{6}$$

with initial conditions $R(0) = R_{23}$ and $\dot{R}(0) = V_{23}$ (refer to Fig. 4). The constant C is obtained from the previous phase of growth as

$$C = \frac{3\pi}{4}(m/M)BT \tag{7}$$

knowing the mass, m, of the gas inside the bubble at the end of that phase of growth.

3.3 Assumptions Made in Relation to Various Parameters. The assumptions made regarding the magnitude and the variation of the parameters involved in the computation of the inception number K_i are given below.

(i) Amplitude of pressure fluctuations and its variation with velocity.

Katz (1981) has measured rms value of pressure fluctuations p_{rms}' on a hemispherical nosed body to be 5.5 percent of the dynamic pressure. Since, here we assume a simple sinusoidal variation of pressure fluctuations, this gives the amplitude p_a' as 8 percent. In the present study this was rounded off by taking p_a' as 10 percent of the dynamic pressure. Also, we assume $p_{peak}' \propto 1/2\,\rho U_\infty^2$ which gives $C_p' = 0.1$.

(ii) Dominant frequency of pressure fluctuations and its variation with velocity.

Katz's (1981) measurements on the hemispherical nosed body showed that the frequency at which the rms pressure spectra showed a peak varied as $U_\infty^{3/2}$. We also assume the same dependence, namely $f \propto U_\infty^{3/2}$. As regards the base value for frequency scaling, we will assume a representative value of 2000 Hz at a velocity of 21.34 m/s (70 ft/s) which is of the same order of magnitude as measured values (Katz, 1981).

(iii) Renewal time, τ.

The renewal time τ will be assumed to be numerically equal to the inverse of dominant frequency of the pressure fluctuations at a given velocity i.e., $\tau \propto 1/f$.

(iv) Residence time, t_R.

The residence time t_R will be assumed to vary as $t_R \propto L$ and $t_R \propto U^{-1}$; where, L and U are characteristic length and velocity in the separation zone, respectively. Assuming $L \propto U_\infty^{-1/2}$ and $U \propto U_\infty$, we have for t_R, $t_R \propto U_\infty^{-3/2}$. We assume some base

value for the residence time and then scale according to the above scaling relation. Finally, the base value of residence time will be treated as a parameter, since the present experiments indicated only an order of magnitude and that too only in the laminar groove. However, based on these observations, t_R is taken to be of the order of tens of milliseconds.

3.4 Scheme of Calculations for Inception Prediction. The condition for inception prediction is that the maximum size attained by a bubble during a growth phase be such that it is visible to the naked eye under normal stroboscopic lighting. In the present case we have three phases of growth and, so, if the maximum radius attained by the bubble during any of the phases of growth exceeds a prescribed size determined by the conditions of visibility, inception can be said to occur. Following Holl and Kornhauser (1970) we will take this size to be 250 μm. For a given velocity the problem, then, is to find the cavitation number K for which the bubble just attains this value of radius of a nucleus of given size. The cavitation number thus obtained represents the inception number, K_i, corresponding to that nucleus size and velocity. The steps followed are outlined below.

Essentially, the size of the nucleus and the velocity for which inception number is to be calculated are prescribed and initially even the cavitation number K is prescribed and the following procedure of calculations is then followed.

(i) To start with, the first phase of growth is considered. The C_p distribution as a function of the non-dimensional time t^* is given as input along with other relevant parameters. The computation of radius as a function of time starts at the point $C_p = -K$, when the time is initialized. The calculation is continued till the separation point is reached. At separation point the calculation is stopped.

(ii) If the bubble diameter at the end of the first phase of growth is smaller than the separation height, then the calculations for growth by turbulent diffusion are carried out. This is the second phase of growth. The growth of the bubble in this phase ends when either the bubble has completed its residence time or if at any stage of its gaseous growth its diameter exceeds the height of separation region.

(iii) If the diameter of the bubble at the end of the first phase of growth is equal to or larger than the separation height, then the second phase of growth is skipped and the third phase of growth is initiated. The separation height is calculated from the analytical approximation given by Parkin (1979) viz.,

$$H = 111.0\, D/\mathrm{Re}_D^{0.79}. \tag{8}$$

(iv) The bubble undergoes the third phase of growth either at the end of the second phase of growth or at the end of the first phase if the condition in (iii) is true. During the collapse stage in this phase calculations are ended when the demand on accuracy is too high.

(v) The cavitation number K is now modified according to whether the maximum radius attained is greater than or less than 250 μm and the value of K which gives a maximum radius close to 250 μm within a prescribed accuracy is taken as the inception number K_i. These computations are repeated for different free stream velocities and nuclei sizes.

Certain times we may skip the first phase of growth, replacing it by just an isothermal change of nucleus size from a value of R_{0i} to a value corresponding to the separation pressure p_s. In other cases second phase is skipped to highlight the influence of turbulent diffusion on K_i.

In addition to the above we also calculated the inception numbers for travelling bubble cavitation on the hemispherical nosed body. We used potential pressure distribution around this body for the purpose of these calculations. We followed through the growth and collapse of a typical nucleus under the action of potential pressure distribution alone. This amounts to inception of travelling bubble on a tripped hemispherical nosed body.

3.5 Presentation and Discussion of Inception Results. In the present scheme of inception predictions, the initial nuclei can either respond to the minimum pressures upstream of separation or to the local minimum in the reattachment region. In the present model, the latter can occur either with the possibility of turbulent diffusion or without it being included. When the nuclei respond to the minimum pressure upstream of separation it is nothing but the classical travelling bubble cavitation inception. As indicated in the results presented in Fig. 7, this is the type which is predicted to dominate when the possible growth of nuclei in the separation region by turbulent diffusion is not included. This suggests that the inception in the absence of nuclei modification by turbulent diffusion is controlled by the first phase of vaporous growth. The turbulent pressure fluctuations in the transition/reattachment region do not play a significant role in such a situation, at least, for the pressure fluctuation levels assumed in the present model.

In Fig. 8 we compare the predicted inception results with

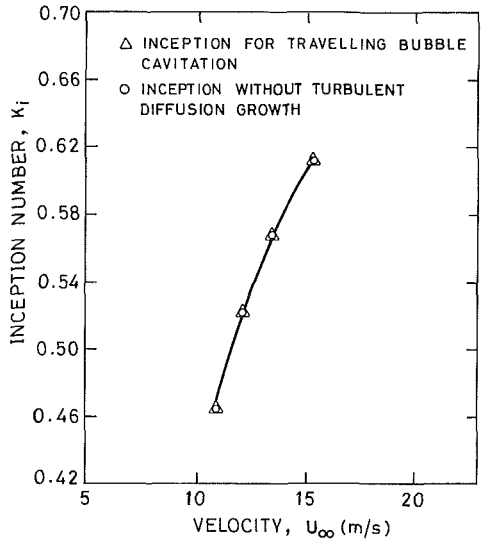

Fig. 7 Comparison of computed inception results without the inclusion of turbulent diffusion growth with the computed inception numbers for travelling bubble cavitation (initial nucleus size = 3 μm)

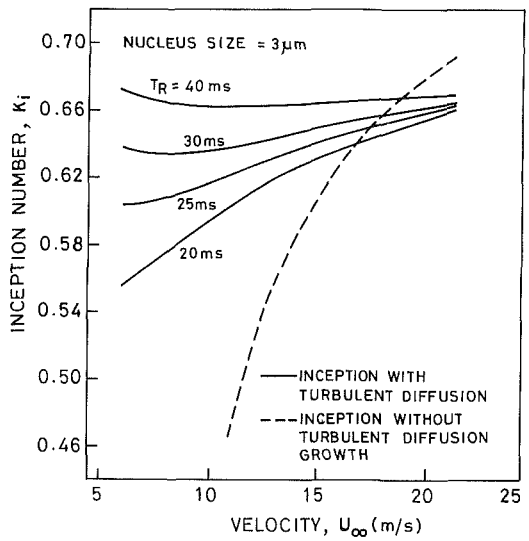

Fig. 8 Computed inception results for the cases with and without the inclusion of turbulent diffusion growth. For the former various residence time values have been considered

the inclusion of turbulent diffusion and without the inclusion of turbulent diffusion; the latter, incidentally, are the same as those for the travelling bubble type of cavitation inception. The former are shown for various values of residence time, t_R, and, as noted earlier, these refer to a fixed base value at $U_\infty = 21.34$ m/s and then scaled by $t_R \propto U_\infty^{-3/2}$ at other velocities. It should be noted that the measured residence time values at higher velocities for the laminar groove (Fig. 4) when scaled according to $t_R \propto U_\infty^{-3/2}$ yield a base value of about 80 ms at 21.34 m/s. Since for the separation bubble on the hemispherical nosed body the vertical dimensions are smaller than the groove dimensions and turbulent conditions prevail at the downstream end of the separation bubble, it is expected that the t_R values for this case will be lower than 80 ms. In view of this, we have made inception calculations over a range of base values of t_R from 20 ms to 40 ms. It is clear from the results shown in Fig. 8 that the inception results are sensitively dependent on the assumed base value of t_R, in particular, at lower velocities. Another parameter which was varied in the inception prediction was the initial nuclei size, and the results of which are not presented here since the qualitative behavior for the other nuclei sizes in the range of 2 μm to 10 μm was similar to the results presented in Fig. 8 for the initial nuclei size of 3 μm.

One important observation to be made from Fig. 8 is that considerable difference exists between the results for the cases with and without the inclusion of turbulent diffusion (TD) growth, at lower velocities. The results seem to indicate that inception can take place without a previous phase of vaporous growth for these velocities when TD growth is included. This can easily be verified from threshold calculations for vaporous growth for 3 μm initial size bubble and comparing them with the predicted K_i values when *TD* is included. At the same time tensions are predicted at the minimum pressure point since the present K_i values are much lower than the negative value of $C_{p\min}$ (≈ -0.775); a 3 μm size nucleus is too small to respond to the tensions at the $C_{p\min}$ point, at least for lower velocities.

The results presented in Fig. 7 and Fig. 8 clearly bring to focus the significance of the separated region and nuclei growth by *TD* in that the turbulent pressure fluctuations which do not play any important role in inception in the absence of *TD* growth assume significance and control inception when *TD* growth is included. For inception calculations in Fig. 8 the prescribed maximum size is 250 μm. Prescription of such a size even for bubble-ring cavitation may be justified since photographs of bubble-ring cavitation do show discreet bubbles (Carroll, 1981 and Van der Muelen, 1976). A photograph from Carroll (1981) shows some discreet bubbles of about 125 μm in size. We repeated the inception calculations taking this as the maximum size to see how this would affect the results. It was found that the inception numbers for the case with *TD* growth differ only in their third decimal place for 125 μm and 250 μm.

At higher velocities above the crossing point of the two curves in Fig. 8, the situation is different. Here the first phase is expected to dominate. (In fact, beyond the crossing point the extension of the results with the inclusion of turbulent diffusion has been made possible only by suppressing the vaporous growth in the first phase in a manner indicated earlier). This is in contrast to Carroll's (1981) observations, who found bubble-ring type of cavitation inception even at velocities higher than 20 m/s. This may be due to the fact that at higher velocities, where the system pressures in the facility are expected to be large at inception, availability of nuclei of even 3 μm size may be questioned. Arakeri et al. (1986) have recently discussed this point about nuclei starvation at higher velocities. This is a matter of detail and we would not like to pursue this further at this point. What is important and illustrated in Fig. 9 is the excellent qualitative agreement of present results when turbulent diffusion is included with the experimental observations of Carroll (1981). The quantitative agreement is also good, but we cannot stress on this point since there is no justification for the use of initial nuclei size of 3 μm and the t_R of 25 ms for the base value of residence time in the calculations presented in the Fig. 9 except to say that they are definitely realistic (see Carroll (1981) for nuclei size involved in inception). It should be pointed out that the trend of travelling bubble cavitation inception number dependence on velocity does not change for other initial nuclei sizes. Therefore, on the basis of the agreement in Fig. 9, we can justifiably claim that the scope for nuclei size modification by turbulent diffusion process is a definite possibility in flows with separation bubbles and should be accounted for in the analytical modeling of inception process in such flows. The only other theoretical results for the separation induced bubble-ring cavitation inception are due to Parkin (1979) and he finds, generally, good agreement with the experimental results of Carroll (1981). But here we do not propose to compare our results with those of Parkin (1979) as we like to emphasize only the qualitative agreement of our results with the experimental results rather than the quantitative agreement.

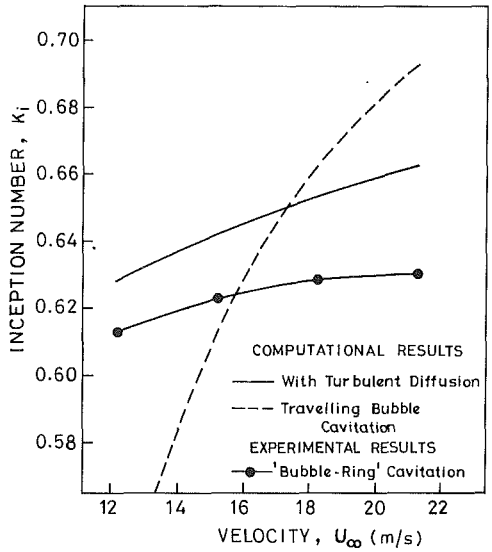

Fig. 9 Comparison of present computational results with the experimental results of Carroll (1981)

Conclusions

The main conclusion from the present study is that gaseous bubble growth by turbulent diffusion can locally modify nuclei sizes from those existing in the free stream. In particular this can occur in zones of flow where potential nuclei residence times can be large, like in laminar separation bubbles. Presently this has been demonstrated by experimental studies on grooves, simulating separated flow, and theoretical modeling of cavitation inception process on a hemispherical nosed body.

Acknowledgments

We would like to thank Drs R. Kumar and K. S. Gandhi of Chemical Engineering Department for introducing us to the surface renewal theory and for many helpful discussions we had with them. We would also like to thank Dr. J. Srinivasan of Mechanical Engineering Department for many helpful discussions we had with him on the topic. We would also like to thank Dr. S. D. Sharma for his assistance in carrying out some of the experimental work reported here. Finally, we would like to thank the reviewers for their suggestions which have resulted in considerable improvement of the original manuscript.

References

Arakeri, V. H., 1973, "Viscous Effects in Inception and Development of Cavitation on Axi-symmetric Bodies," Ph.D. dissertation, California Institute of Technology, pp. 40–43.

Arakeri, V. H., 1975, "A Note on the Transition Observations on an Axi-symmetric Body and Some Related Fluctuating Wall Pressure Measurement," ASME JOURNAL OF FLUIDS ENGINEERING, Vol. 97, pp. 82–86.

Arakeri, V. H., and Acosta, A. J., 1973, "Viscous Effects in the Inception of Cavitation on Axi-symmetric Bodies," ASME JOURNAL OF FLUIDS ENGINEERING, Vol. 95, pp. 519–527.

Arakeri, V. H., Higuchi, H., and Arndt, R. E. A., 1986, "Analysis of Recent Tip Vortex Cavitation Inception Data," *Proc. of the 21st American Towing Tank Conference*, Washington, D. C., August 5–7.

Arakeri, V. H., Milton, S. G., and Sharma, S. D., 1984, "Role of Unsteady Pressure Fields in Cavitation Inception," *International Symposium on Cavitation Inception-1984*, Ed., Parkin, B. R., and Morgan, W. B., ASME, New Orleans.

Arakeri, V. H., Sharma, S. D., Mani, K., and Govinda Ram, H. S., 1987, "The High Speed Water Tunnel Facility at the Indian Institute of Science," *International Symposium on Cavitation Facilities and Techniques-1987*, FED-Vol. 57, ASME, pp. 27–36.

Billet, M. L., 1986, "The Importance and Measurement of Cavitation Nuclei," *Adv. in Aero. Fluid Mech. and Hydraulics*, Eds., Arndt, R. E. A., et al., ASCE, pp. 967–988.

Carroll, J. A., 1981, "Observations of the Effect of Boundary Layer and Nuclei on Cavitation of Axi-symmetric Bodies," TM 81-60, Pennsylvania State University.

Cimbala, J. M., and Billet, M. L., 1989, "Cavitation Inception and Pressure Measurement in Rectangular Slots," *Third International Symposium on Cavitation Inception-1989*, FED-Vol. 89, ASME, pp. 35–44.

Danckwerts, P. V., 1970, *Gas-Liquid Reactions*, McGraw-Hill, pp. 96–103.

Epstein, P. S., and Plesset, M. S., 1950, "On the Stability of Gas Bubbles in Liquid-Gas Solutions," *J. Chem. Phys.*, Vol. 18, pp. 1505–1509.

Gates, M., and Acosta, A. J., 1978, "Some Effects of Several Free Stream Factors on Cavitation Inception on Axi-symmetric Bodies," *12th Symp. Naval Hydrodynamics*, Washington, D. C.

Higbie, R., 1935, "The Rate of Absorption of Pure Gas into a Still Liquid During Short Periods of Exposure," *Trans. Am. Inst. of Chem. Engrs.*, Vol. 35, p. 365.

Holl, J. W., 1969, "Limited Cavitation," *Cavitation State of Knowledge*, ASME, pp. 26–63.

Holl, J. W., and Carroll, J. A., 1981, "Observations of the Various Types of Limited Cavitation on Axi-symmetric Bodies," ASME JOURNAL OF FLUIDS ENGINEERING, Vol. 103, p. 415.

Holl, J. W., and Kornhauser, A. L., 1970, "Thermodynamic Effects on Desinent Cavitation on Hemispherical Nosed Bodies in Water from 80°F to 260°F," ASME *Journal of Basic Engineering*, Vol. 92, pp. 44–58.

Huang, T. T., and Hannan, D. F., 1975, "Pressure Fluctuations in the Regions of Flow Separation," Rep. No. 4723, David Taylor Naval Ship Research and Development Center.

Katz, J., 1981, "Cavitation Inception in Separated Flows," Ph.D. dissertation, California Institute of Technology.

Milton, S. G., 1989, "Studies on Cavitation Inception Process in Separated Flows," Ph.D. thesis, Indian Institute of Science, Bangalore.

Parkin, B. R., 1979, "A Theory for Cavitation in a Flow Having Laminar Separation," TM 79-198, ARL, Pennsylvania State University.

Parkin, B. R., and Kermeen, R. W., 1953, "Incipient Cavitation and Boundary-Layer Interaction on a Streamlined Body," Rep. No. E-35.2, Hydrodynamics Laboratory, California Institute of Technology.

Shanmuganathan, V., 1985, "Experimental Studies on Travelling Bubble Cavitation Noise," Ph.D. thesis, Indian Institute of Science, Bangalore.

Van der Muelen, J. H. J., 1976, "A Holographic Study of Cavitation on Axi-symmetric Bodies and the Influence of Polymer Additives," Publication No. 509, Netherlands Ship Model Basin, Wageningen, The Netherlands.

Dynamics of Attached Cavities on Bodies of Revolution

S. L. Ceccio[1]

C. E. Brennen

California Institute of Technology,
Pasadena, CA 91125

Attached cavitation was generated on two axisymmetric bodies, a Schiebe body and a modified ellipsoidal body (the I. T. T. C. body), both with a 50.8 mm diameter. Tests were conducted for a range of cavitation numbers and for Reynolds numbers in the range of $Re = 4.4 \times 10^5$ to 4.8×10^5. Partially stable cavities were observed. The steady and dynamic volume fluctuations of the cavities were recorded through measurements of the local fluid impedance near the cavitating surface suing a series of flush mounted electrodes. These data were combined with photographic observations. On the Schiebe body, the cavitation was observed to form a series of incipient spot cavities which developed into a single cavity as the cavitation number was lowered. The incipient cavities were observed to fluctuate at distinct frequencies. Cavities on the I. T. T. C. started as a single patch on the upper surface of the body which grew to envelope the entire circumference of the body as the cavitation number was lowered. These cavities also fluctuated at distinct frequencies associated with oscillations of the cavity closure region. The cavities fluctuated with Strouhal numbers (based on the mean cavity thickness) in the range of $St = 0.002$ to 0.02, which are approximately one tenth the value of Strouhal numbers associated with Kármán vortex shedding. The fluctuation of these stabilized partial cavities may be related to periodic break off and filling in the cavity closure region and to periodic entrainment of the cavity vapor. Cavities on both headforms exhibited surface striations in the streamwise direction near the point of cavity formation, and a frothy mixture of vapor and liquid was detected under the turbulent cavity surface. As the cavities became fully developed, the signal generated by the frothy mixture increased in magnitude with frequencies in the range of 0 to 50 Hz.

1 Introduction

"Fixed" or "attached" cavitation occurs when a liquid flow detaches from the rigid boundary of an immersed body or flow passage to form a cavity, and this cavity may exist indefinitely with a quasi-steady geometry. Attached cavitation may negatively affect the performance of hydromechanic surfaces, as in the case of propeller thrust breakdown (Emerson and Sinclair 1967). It is associated with cavitation erosion damage in hydraulic turbomachinery and marine propellers (Knapp et al., 1970), and is responsible for dangerous ship propeller/hull interactions (Weitendorf, 1989) and unwanted acoustic emissions (Blake et al., 1977). All of these phenomena are influenced by cavity dynamics, but studies of cavity fluctuations have been hampered by the lack of simple, nonintrusive cavity volume measurement techniques.

Previous researchers have used high speed films (Knapp, 1955 and Lush and Skipp, 1986) and near cavity LDA measurements (Avellan et al., 1988) to observe cavity dynamics. Presented here are the initial results of a different method to study the time averaged and unsteady nature of attached cavities using electrical impedance measurements of the near-surface fluid with flush mounted electrodes. This technique has recently been used to study travelling bubble cavitation (Ceccio and Brennen, 1991), and the same experimental setup and techniques were employed by this study.

2 Experimental Methods

Attached cavities were produced on three axisymmetric headforms made of lucite: one Schiebe body and two modified ellipsoid bodies (known as I. T. T. C. headforms), which are described below. The experiments were conducted in the Low Turbulence Water Tunnel (LTWT) at the California Institute of Technology. (Gates 1977). The free-stream velocity, U, for these tests was varied from 8.3 to 9.5 m/s, and for all tests, the velocity of the tunnel was maintained constant. The test section pressure, P, was slowly reduced until the desired operating point was reached. The controlled air content of the water was 6–7 ppm for these tests.

The Schiebe headform used in the experiment had a maximum diameter of 51.4 mm and a minimum pressure coefficient, C_P, of -0.75 (Gates et al., 1979). The actual final diameter of the body, D, is 50.8 mm due to some truncation of the after body. The body was constructed of lucite and was instrumented with three surface electrodes made of silver epoxy. The electrodes were circumferential rings and located at positions $s/D = 0.608$, 0.645, and 0.691, where s is the streamwise coordinate measured along the body surface from the stagnation point. The electrodes had a thickness of 0.76 mm. Both

[1]Currently at the Department of Mechanical Engineering and Applied Mechanics, University of Michigan, Ann Arbor, Mich.

Contributed by the Fluids Engineering Division for publication in the JOURNAL OF FLUIDS ENGINEERING. Manuscript received by the Fluids Engineering Division April 13, 1991.

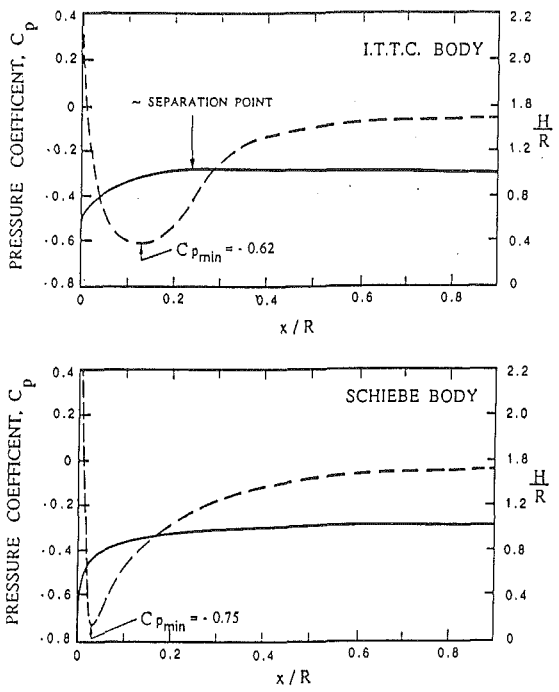

Fig. 1 Profile and surface pressure distribution on the Schiebe and I. T. T. C. bodies

I. T. T. C. bodies (Lingren and Johnsson, 1966) were of identical shape but were instrumented with different electrode geometries. The minimum pressure coefficient for the I. T. T. C. body is -0.62, and the diameter of the bodies was 50.4 mm. The first I. T. T. C. body was instrument with sixteen circumferential electrodes of thickness 0.76 mm and equally spaced 2.54 mm apart in the longitudinal direction starting at $s/D = 0.68$ and ending at $s/D = 1.37$. The second I. T. T. C. headform had rectangular patch electrodes of width 1.14 mm in the streamwise direction and length 5.72 mm in the circumferential direction. They were equally spaced 2.54 mm apart in the longitudinal direction starting at $s/D = 0.68$ and ending at $s/D = 1.37$. The surface of the bodies, including the electrode-lucite interface, was highly polished, and no surface cavitation was observed to consistently form on the electrode/lucite interface which would have implied significant local roughness. The headform profiles and surface pressure distributions are presented in Fig. 1.

The electrodes were used to measure both the mean volume and volume fluctuations of the attached cavities. An alternating potential of fixed amplitude is applied to each electrode, and neighboring electrodes have voltage signals which are 180 degrees out of phase. Changes in the emitted current are measured for each electrode. When a void or cavity is present over a portion of the electrode, the fluid impedance is increased, decreasing the emitted current. In the case of attached cavitation, changes in the electrode signal are the result of two separate effects. First, the percentage of the electrode surface area which will freely conduct electricity is reduced, and hence the magnitude of the output current decreases. This is the primary effect detected by the electrode system. There may also be a secondary effect due to changes in conductivity of the cavity content, which consists of a liquid and vapor mixture; the conductivity of this mixture will clearly differ from that of water.

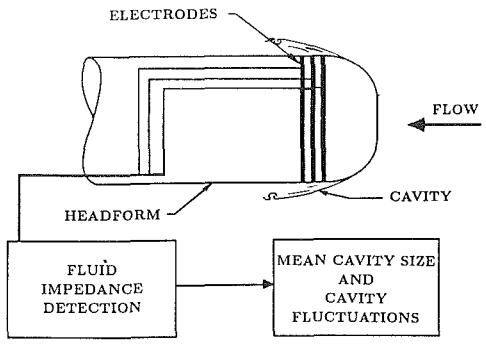

Fig. 2 Schematic diagram of fluid impedance measuring system

The dynamic response of the electrode signal processor is on the order of 10 kHz, and the signal to electrical noise ratio was at least 45 dB for all the experiments. A complete description of the electrode system is provided by Ceccio (1990). The Fourier transforms of the electrode signal were performed digitally with a windowed FFT algorithm, and the error estimates which accompany the FFTs were derived from baseline measurements. In addition to the electrical measurements, high speed still photographs of the attached cavities were taken for each operating condition. From these photographs, the mean cavity thickness and length could be measured, and the cavitation present over each electrode could be recorded. A schematic diagram of the electrode system is shown in Fig. 2.

3 Experimental Results-Schiebe Body Measurements

Originally the Schiebe body shape was designed to avoid the occurrence of laminar separation (Schiebe, 1972) which has been associated with the presence of attached cavities (Arakeri and Acosta, 1973). The experiments were conducted in a fairly narrow range of Reynolds number ($\mathrm{Re} = 4.4\times10^5 - 4.8\times10^5$, based on the body diameter, D). The cavitation formation index, defined as the first appearance of attached cavitation anywhere on the headform, was about $\sigma_{ia} = 0.40$ for all experiments. The leading edge cavitation was located at about $s/D = 0.45$. The cavitation disappearance index, which was always greater than the formation index, was about $\sigma_{da} = 0.42$.

Nomenclature

C_P = pressure coefficient $(P_S - P)/(1/2\rho U^2)$
D = diameter of the axisymmetric body
E = electrode signal voltage
f = frequency
H = local radius of headform
L = mean cavity length
P = freestream pressure
P_S = pressure on surface of body
P_v = water vapor pressure
R = radius of headform
Re = Reynolds number (UD/ν)
s = streamwise coordinate measured along the body surface from the stagnation point
St = Strouhal number $(f\delta_c/U)$
U = freestream velocity
x = coordinate along centerline of body
δ_c = mean cavity thickness
ν = kinematic viscosity of water
ρ = density of water
σ = cavitation number $(P - P_v)/(1/2\rho U^2)$
σ_{ia} = attached cavitation formation index
σ_{da} = attached cavitation desinence index

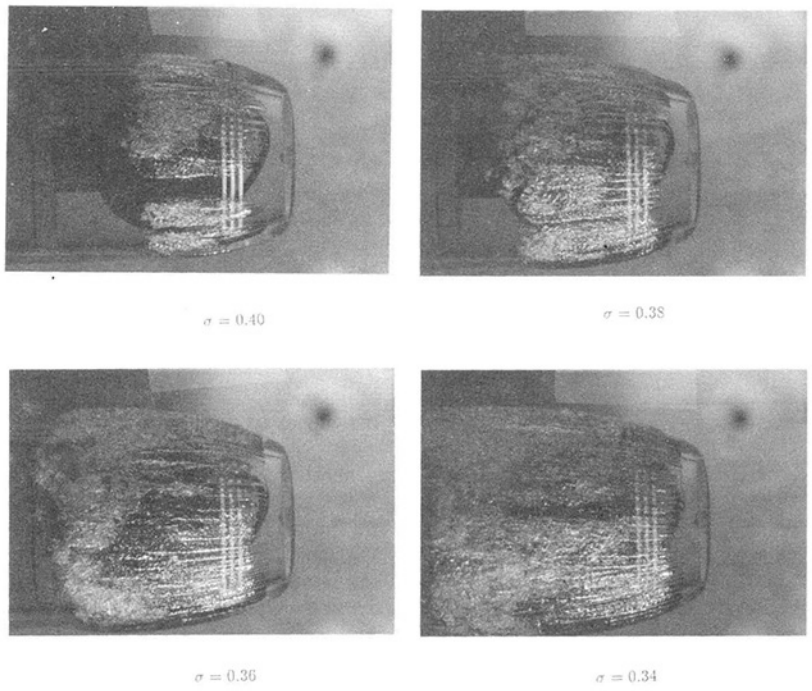

Fig. 3 Examples of attached cavities on the Schiebe body for cavitation numbers σ = 0.40, 0.38, 0.36, and 0.34 at a free-stream velocity U = 9 m/s

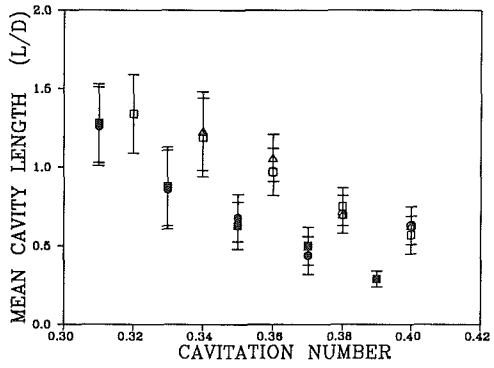

Fig. 4 Mean cavity length plotted against the cavitation number, σ, for the Schiebe body (open symbols) and the I. T. T. C. body (filled symbols). U = 8.75 m/s (○), U = 9 m/s (△), and U = 9.5 m/s (□). The error bars represent the minimum and maximum cavity length measured from the photographs. The value for the I. T. T. C. body at σ = 0.39 is the maximum length of the partial cavity.

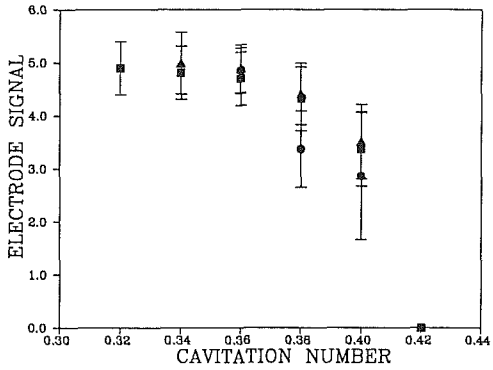

Fig. 5 Mean and standard deviation of the electrode signal, E, from cavitation on the Schiebe body plotted against cavitation number, σ. Vertical scale is arbitrary. U = 8.75 m/s (○), U = 9 m/s (△), and U = 9.5 m/s (□).

Photographs taken at each operating point were used as a reference for the electrode data, and examples are presented for the Schiebe body in Fig. 3, with U = 9 m/s and σ = 0.40, 0.38, 0.36, 0.34. At the first formation of cavities, the circumference of the headform was only about half covered with attached patch cavities, or "finger" cavities, some of which were temporally intermittent. At lower cavitation numbers these finger cavities combined to cover the entire circumference of the body. Further decreases in cavitation number increased the mean length of the cavity, L, which is plotted against cavitation number in Fig. 4. The surface of the cavity shows a transition from a smooth laminar interface to a wavy and then turbulent surface in a manner similar to the growth of Tollmein-Schlichting waves in an unstable boundary layer (Brennen, 1970). The point of transition on the cavity surface was about one half the total cavity length in all cases.

Both the mean and fluctuating components of the electrode output contain interesting information. First, the mean level of the electrode signal, E, indicates the percentage of the electrode which is covered by the cavity, and this is presented as a function of the cavitation number in Fig. 5. As the cavitation number decreases, the percentage of the circumference covered by the cavity grows, and hence the electrode signal voltage increases. The signal levels off as the cavity become fully developed. The large uncertainty associated with the measurements at higher cavitation numbers is due to the temporal intermittency of the cavitation. Once the cavity is fully developed, the uncertainty decreases. The high frequency portion of the signal is associated with churning of the two-phase mixture inside the cavity and fluctuations of the cavity boundary. The relative contribution of these effects to the signal is small when compared to the portion of the signal resulting from the presence or absence of the cavity. Consequently, the ordinate in Fig. 5 may be transposed into a quantitative measurement of the covered surface when the mean signal is considered.

Secondly, the fluctuating components of the electrode signals were analyzed. Initial spectra obtained without filtering indicated that there were no frequencies of significant magnitude above 500 Hz. Therefore, the fluctuating signal was

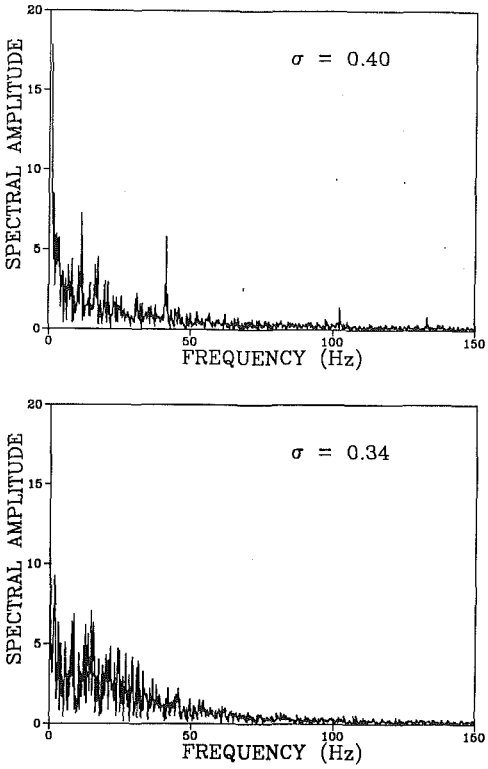

Fig. 6 Electrode signal spectra for cavitation on the Schiebe body. Cavitation number σ = 0.40 and 0.34 at free-stream velocity U = 9 m/s. Vertical scale is arbitrary and the uncertainty of the spectral coefficients is ± 0.20.

low pass filtered with a cutoff frequency of 1 kHz and was digitally sampled at 2 kHz. This filtering eliminated the signals produced by travelling bubbles which may pass over portions of the uncovered electrodes. Figure 6 represents two typical spectra. They have similar shapes with large amplitudes at low frequency and a uniform rolloff to approximately 500 Hz.

At the higher cavitation numbers, the frequencies below 1 Hz are dominant, since the temporal intermittency associated with the partially developed cavities produces this low frequency component. A series of dominant spectral peaks at intermediate frequencies were detected for the partially developed cavities. As seen in Fig. 6, the spectra for σ = 0.40 and U = 9 m/s has distinct frequency peaks at f = 10, 40, 103, and 133 Hz. These peaks are not due to line noise, are repeatable, and disappear after the cavities became fully developed. Since they occur only when the cavities are partially developed, they may be due to pulsation of the finger cavities in the circumferential direction (see Fig. 7). Note that the electrode location is upstream of the cavity collapse region, which also fluctuates. The Strouhal number, St, based on the cavity mean thickness, δ_c, and upstream velocity, U, for the observed dominant frequencies would be St = 0.002, 0.006, 0.015, and 0.019, respectively. The cavity thicknesses were derived from the photographs. The error associated with the Strouhal number measurement is approximately ± 20 percent for the cavities with $\sigma > 0.37$ (thin cavities) and ± 25 percent for the cavities with $\sigma < 0.37$ (thick cavities).

As the cavities become fully developed, the magnitudes of frequency component below 1 Hz decrease with increases at higher frequencies, as seen in Fig. 6 for the case of σ = 0.34. The electrodes on the Schiebe body were located under a portion of the finger cavities which contained only vapor (that is, before complete transition to a turbulent cavity interface). Given the absence of a frothy mixture over the electrodes, two other mechanisms can be cited for the perturbation of the electrode signal. First, the fully developed cavity consists of a

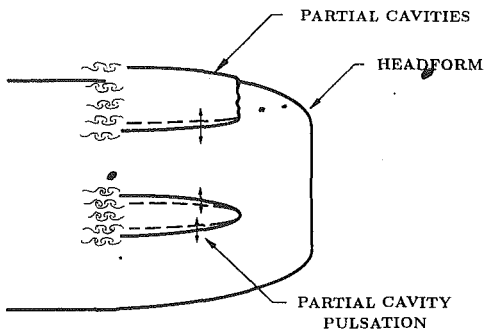

Fig. 7 One possible mode of cavity oscillation

collection of finger cavities whose boundaries may wet the electrode surface. As these boundaries fluctuate, a signal is generated. Secondly, the cavity surface may intermittently collapse, wetting the surface and producing a signal. Fluctuations on the cavity surface due to the presence of Tollmein-Schlichting waves have been estimated to occur with frequencies in the range of 5–10 kHz (Brennen, 1970); signals in this frequency range were not observed. The spectra due to the fully developed cavities revealed no dominant frequencies.

4 Experimental Results-I. T. T. C. Body Measurements

The I. T. T. C. body is known to possess a region of laminar separation which is associated with the formation of stable attached cavities (Arakeri and Acosta, 1973). These cavities originate within the laminar separation bubble. A single cavity first formed at the upper portion of the headform in the region of laminar separation and grew to envelope the entire circumference of the headform as the cavitation number was lowered. This "top to bottom" cavity formation was caused by the slight pressure difference across the headform resulting from gravity, an effect which was not as noticeable on the Schiebe body due to the finger cavity intermittency. The experiments were conducted over a narrow range Reynolds numbers (Re = $4.4 \times 10^5 - 4.8 \times 10^5$) which resulted in a fairly constant cavity formation index of σ_{ia} = 0.41. The cavitation disappearance index was σ_{da} = 0.42. The leading edge of the cavity first appears at approximately s/D = 0.75, and the location of the leading edge moved forward as the cavitation number decreased.

The mean cavity length in the streamwise direction presented as a function of cavitation number in Fig. 4. The ratio of cavity length to body diameter (L/D) for the I. T. T. C. headform is consistently lower that for the Schiebe body at higher cavitation numbers. This is due to the process of cavity formation. In the case of the Schiebe body, the cavities are not promoted by the presence of a laminar separation region and take the form of long cavities close to the headform surface. Cavities on the I. T. T. C. headform first form in the separated recirculating region and are initially confined there at higher cavitation numbers. As the cavitation number decreases, the cavities grow and begin to dominate the flow near headform surface. At this point, the detailed shape of the headform has less influence on the cavity size, hence the ratio (L/D) begins to converge for both axisymmetric bodies.

As in the case of the Schiebe body, the cavity near the separation point consisted of a series of finger cavities or surface striations which, at lower cavitation numbers, combined to cover the circumference of the body. Figure 8 presents photographs of cavitation on this body for the case of free-stream velocity U = 8.7 m/s and for cavitation numbers of σ = 0.37, 0.35, 0.33, 0.31. The finger cavities were less well defined than those of the Schiebe body. This may be due to the relatively short distance from the leading edge of the cavity to the point of surface turbulent transition as well as to the

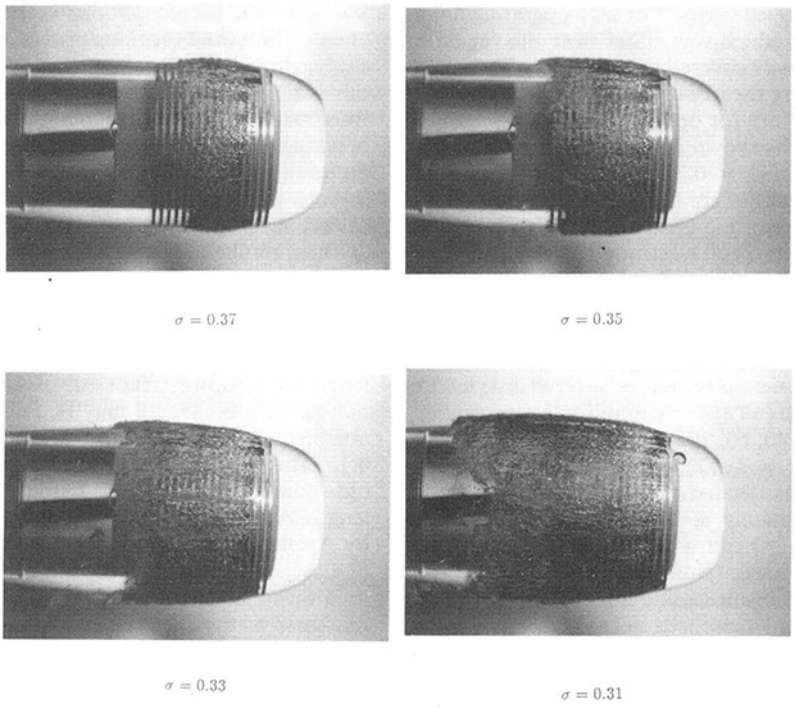

Fig. 8 Examples of attached cavities on the I. T. T. C. body for cavitation numbers σ = 0.37, 0.35, 0.33, and 0.31 at a free-stream velocity of U = 8.7 m/s

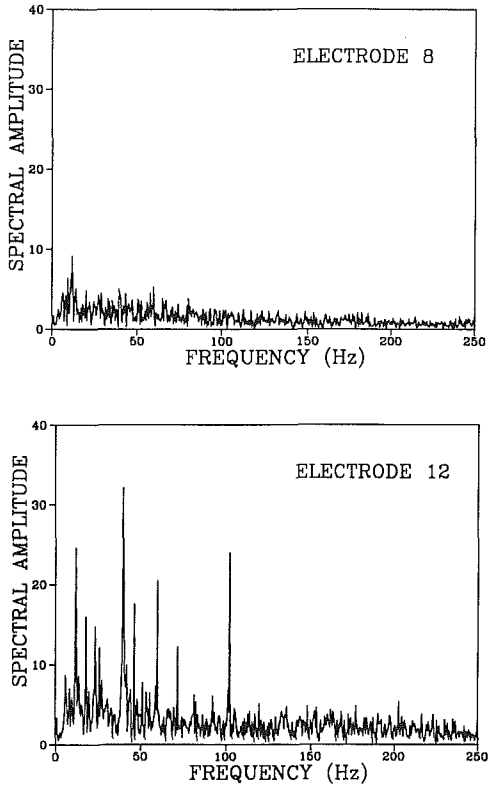

Fig. 9 Electrode signal spectra for cavitation on the I. T. T. C. body with circular electrodes. Cavitation number σ = 0.37 at freestream velocity U = 8.75 m/s. The signals were taken from electrode 8 and 12. Vertical scale is arbitrary, and the uncertainty of the spectral coefficients is ± 0.25.

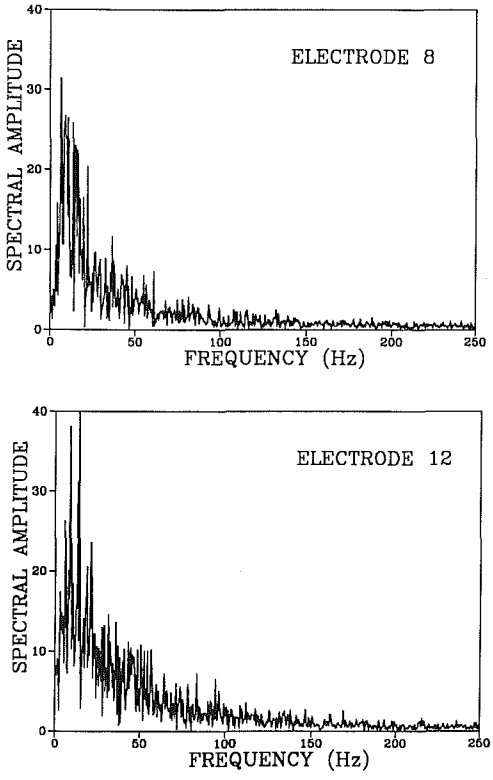

Fig. 10 Electrode signal spectra for cavitation on the I. T. T. C. body with circular electrodes. Cavitation number σ = 0.31 at free-stream velocity U = 8.75 m/s. The signals were taken from electrode 8 and 12. Vertical scale is arbitrary, and the uncertainty of the spectral coefficients is ± 0.25.

presence of the laminar separation. The first I. T. T. C. body tested was instrumented with sixteen circumferential electrodes, and in order to eliminate any signal which may be due to circumferential oscillations, all the electrode data was taken for fully developed cavitation which covered the entire circumference.

During the electrical impedance measurements with the I. T. T. C. bodies, attention was focused on the downstream

portion of the fully developed cavity. For each operating point, an electrode was chosen which was either near the region of cavity closure, or completely covered by the cavity. The signals from these electrodes were then Fourier analyzed. The sample spectra in Figs. 9 and 10 are for operating points represented by two of the photographs shown in Fig. 8. Two spectra corresponding to the case of $\sigma = 0.37$ and $U_\infty = 8.75$ m/s are shown in Fig. 9. The signals were taken from electrode 8 (as counted from the first electrode upstream), which was completely covered by the cavity, and electrode 12, which was near the cavity reattachment point. The signal from the completely covered electrode exhibits some distinct frequencies, which may be due to cavity surface fluctuations, but these features do not dominate the spectra. Near the cavity closure region, however, the spectra is characterized by several distinct frequencies, with the four largest spectral amplitudes corresponding to frequencies of 12, 40, 60, 102 Hz. These correspond the Strouhal numbers of St = 0.002, 0.007, 0.010, and 0.017, respectively. The error associated with the Strouhal number measurement is approximately ± 20 percent for the cavities with $\sigma > 0.37$ (thin cavities) and ± 25 percent for the cavities with $\sigma < 0.37$ (thick cavities). (Note that the 60 Hz peak was determined not to be the result of line noise). In general, the frequencies of fluctuations measured near the closure region were repeatable over the range of freestream velocities and cavitation numbers tested.

For the case of $\sigma = 0.31$ presented in Fig. 10, both electrodes 8 and 12 were covered by the cavity. These spectra are dominated by low frequencies and do not exhibit any dominant features. As in the case of the Schiebe body, these low frequency fluctuations are in the range of 0 to 50 Hz. These measurements were from the electrode covered by the fully turbulent region of the cavity, and the principle cause of these signals is the churning of the frothy mixture inside the cavity. The magnitude of the low frequency oscillations increased with decreasing cavitation number and the associated increase in cavity thickness at the location of the electrode. With increasing cavity thickness, the two-phase mixture inside the cavity may begin to churn with a coherent, low-frequency motion. This may not be possible in thin cavities.

The range of frequencies associated with the longitudinal fluctuations of the Schiebe body cavities are quite similar to those measured in the cavity closure region of the I. T. T. C. body. This suggests that similar pulsation mechanisms are present for the two headforms. Furthermore, a I. T. T. C. body with patch electrodes was used to measure the oscillation of the cavity closure region at a specific point on the body surface, and these data were compared to those measurements taken with the circumferential electrodes. The patch electrode spectra were similar to those from the circular electrode data presented above. Similar dominant frequencies were detected near the cavity closure region, although the relative magnitude of the spectral peaks were reduced. This result suggests that the pulsation mechanism operates in a similar way over the entire surface of the cavity.

The cavities observed on the I. T. T. C. body (as well as the Schiebe body) had relatively constant lengths and have been referred to as "stabilized partial cavities" (Knapp et al., 1970). Previous observations of these cavities have revealed the presence of local, periodic fluctuations near the cavity closure region (Knapp, 1955). These oscillations have been attributed to a reentrant jet which cause the cavity to undergo a process of filling and break-off. At the free-stream velocities of this study, the cavities did not undergoe large scale filling and breaking, since the re-entrant jet may not be able to penetrate far upstream in the cavity. Instead, premature growth and break-off may occur. Knapp observed that large scale shedding occurred at frequencies on the order of 50 to 130 Hz on a 2 in. diameter, hemisphere shaped axisymmetric bodies, for various velocities and cavitation numbers. As the velocity was lowered, periodic vapor entrainment became noticable, and the filling and breaking process was reduced. In the present study, the measured frequencies of cavity oscillation were on the same order as those measured previously, although the freestream velocities were much lower. Small scale filling and breaking along with periodic entrainment of vapor would cause the cavity to oscillate in size, leading to periodic fluctuations in both the lateral boundaries and the closure region of the cavity, such as those observed here.

These results may also be compared to the shedding of cavitation vortices in the wake of a bluff body. Young and Holl (1966) observed that cavitation vortices were shed from a symmetric wedge with Strouhal numbers on the order of 0.26, based on the shedding frequency, freestream velocity, and the length of the downstream side of the wedge. For a thin wedge, one half of this length may be related to the thickness of an attached cavity resulting in a modified Strouhal number of 0.13. These measurements were conducted at an average Reynolds number of 1.7×10^5 based on the characteristic wedge length. A result similar to that of Young and Holl was obtained by Avellan et al., (1988) who measured the vortex shedding of attached cavities on two dimensional hydrofoils. The measured Strouhal number was 0.147 (based on the displacement thickness of the shear layer above the cavity), at a Reynolds number 2×10^6 (based on the cord length). These Strouhal numbers are approximately ten times greater that the values presented in this study, suggesting that the oscillations in the cavity closure region of stable cavities may not be the result of fully developed Kármán vortex shedding.

5 Conclusions

The fluid impedance measurement described in this paper allow determination of both the average size and the dynamic fluctuations of attached cavities. Cavity size may be inferred from the average electrode signal, and with the proper electrode geometry, the total cavity area may be measured. The dynamics of the attached cavity may also be detected through processing of the unsteady component of the electrode signal.

Limited cavitation on the Schiebe body consisted of a series of both steady and intermittent partial cavities. As the cavitation number decreases, the cavities merge to cover the circumference of the headform. These finger cavities fluctuate with distinct frequencies corresponding to Strouhal numbers in the range St = 0.002 to 0.02, and these fluctuations may be caused by cavity oscillations in the circumferential direction. Fully developed cavities produced signals which fluctuate in the frequency range of 0 to 50 Hz, and these oscillations may be the result of intermittent contact of finger cavity boundaries or by churning of a frothy mixture of vapor and liquid inside the cavity.

Cavitation on the I. T. T. C. body started as a single patch on the upper surface of the headform. This grew to cover the entire circumference of the headform as the cavitation number was reduced. The closure region was found to oscillate with distinct frequencies corresponding to Strouhal numbers ranging from St = 0.002 to 0.02. These values are approximately one tenth of the Strouhal numbers associated with Kármán vortex shedding. The cavity in many instances was not evacuated but contained a mixture of vapor and fluid which churned inside the cavity, producing low frequency electrode signals in the frequency range of 0 to 50 Hz. As the cavity became fully developed, the magnitude of the low frequency oscillations increased.

All the cavities of this study had relatively constant lengths and have been referred to as "stabilized partial cavities." The present study has emphasized that these cavities undergo localized fluctuations in the lateral boundaries and the closure region. These fluctuations may be due to the periodic entrainment of cavity vapor and the presence of a small re-entrant

jet which enters the downstream portion of the cavity, causing a process of filling and shedding. In contrast, many cavities exhibit large scale break-off (Knapp, 1955) and (Lush and Skipp, 1986). Cavitation erosion may be related to the shedding of vortices formed over the cavity surface which carry away vapor filaments from the closure region (Avellan et al., 1988). These vapor filaments later collapse in the high pressure region downstream of the cavity causing cavitation erosion. Large scale cavity fluctuations and vapor shedding usually occur at higher Reynolds numbers and were not observed in this study.

Acknowledgments

The authors thank the Office of Naval Research for their support under contract N00014-85-K-0397. The assistance of Yan Kuhn de Chizelle and Sanjay Kumar is gratefully acknowledged, and the authors with to thank the reviewers for their helpful comments.

References

Arakeri, V. H. and Acosta, A. J., 1973, "Viscous Effects on the Inception of Cavitation on Axisymmetric Bodies," ASME JOURNAL OF FLUIDS ENGINEERING, Vol. 95, pp. 519–527.

Avellan, F., Dupont, P., and Ryhming, I., 1988, "Generation Mechanisms and Dynamics of Cavitation Vortices Downstream of a Fixed Leading Edge Cavity," *Proc. Seventeenth Symp. on Naval Hydrodynamics*, The Hague, pp. 317–329.

Blake, W. K., Wolpert, M. J., and Geib, F. E., 1977, "Cavitation Noise and Inception as Influenced by Boundary Layer Development on a Hydrofoil," *J. of Fluid Mechanics*, Vol. 80, pp. 617–640.

Brennen, C. E., 1970, "Cavity Surface Wave Patterns and General Appearance," *J. of Fluid Mechanics*, Vol. 80, pp. 617–640.

Ceccio, S. L., 1990, "Observations of the Dynamics and Acoustics of Travelling Bubble Cavitation," Caltech Div. Engineering and Applied Science Rep. No. ENG249.11.

Ceccio, S. L. and Brennen, C. E., 1991, "Observations of the Dynamics and Acoustics of Travelling Bubble Cavitation," accepted for publication in the *J. of Fluid Mechanics*.

Emerson, A., and Sinclair, L., 1967, "Propeller Cavitation: Systematic Series Tests on 5– and 6– Bladed Model Propellers," *SNAME Trans.*, Vol. 75, pp. 224–267.

Gates, E. M., 1977, "The Influence of Freestream Turbulence, Freestream Nuclei Populations, and Drag-Reducing Polymer on Cavitation Inception on Two Axisymmetric Bodies," Caltech Div. Engineering and Applied Science Rep. No. E182-2.

Gates, E. M., Billet, M. L., Katz, J., Ooi, K. K., Holl, W., and Acosta, A. J., 1979, "Cavitation Inception and Nuclei Distribution- Joint ARL-CIT Experiments," Caltech Div. Engineering and Applied Science Rep. No. E244.1.

Knapp, R. T., 1955, "Recent Investigations of the Mechanisms of Cavitation and Cavitation Damage," *Trans. ASME*, Vol. 77, pp. 1045–1055.

Knapp, R. T., Daily, J. W., and Hammitt, F. G., 1970, *Cavitation*, McGraw-Hill.

Lingren, H. and Johnsson, C. A., 1966, "Cavitation Inception on Headforms: I. T. T. C. Comparative Experiments," *Proc. Eleventh Int. Towing Tank Conf.*, Tokyo.

Lush, P. A. and Skipp, S. R., 1986, "High Speed Cine Observations of Cavitating Flow in a Duct," *Int. J. of Heat and Fluid Flow*, Vol. 7, pp. 283–290.

Schiebe, F. R., 1972, "Measurement of the Cavitation Susceptibility of Water Using Standard Bodies," U. of Minnesota St. Anthony Falls Hydraulic Lab. Rep. No. 118.

Weitendorf, E. A., 1989, "25 Years of Research on Propeller Excited Pressure Fluctuations and Cavitation," *Proc. Third Int. ASME Symp. on Cavitation Noise and Erosion in Fluid Systems*, San Francisco, pp. 1–10.

Young, J. O. and Hall, J. W., 1966, "Effects of Cavitation on Periodic Wakes Behind Symmetric Wedges," *Trans. ASME.*, Vol. 88, pp. 163–176

Numerical Simulation of Heavy Particle Dispersion Time Step and Nonlinear Drag Considerations

Lian-Ping Wang[1]

D. E. Stock

Department of Mechanical and Materials Engineering, Washington State University, Pullman, WA 99164-2920

Numerical experiments can be used to study heavy particle dispersion by tracking particles through a numerically generated instantaneous turbulent flow field. In this manner, data can be generated to supplement physical experiments. To perform the numerical experiments efficiently and accurately, the time step used when tracking the particles through the fluid must be chosen correctly. After finding a suitable time step for one particular simulation, the time step must be reduced as the total integration time increases and as the free-fall velocity of the particle increases. Based on the numerical calculations, we suggest that the nonlinear drag be included in a numerical simulation if the ratio of the particle's Stokes free-fall velocity to the fluid rms velocity is greater than two.

Introduction

Numerical experiments enable us to advance our understanding of particle motion in a turbulent flow. While physical experiments are vital, they are difficult to carry out and often do not provide all the information we seek. For example, particle motion is easiest to express and simulate in terms of Lagrangian statistics, but this information is very difficult to obtain experimentally. Numerical experiments must be performed carefully to ensure that the resulting data represent reality, and they must also be done efficiently to allow numerous parameters to be examined. The purpose of the work described here was to provide some guidelines to help researchers doing numerical experiments for gas-particle flows decide what time step to use and when Stokes drag can no longer be used.

Numerical experiments for gas-particle flows involve tracking the particles through a simulated turbulent flow. The instantaneous turbulent field can be found by solving the Navier–Stokes equations. This can be done by direct numerical simulation (e.g., Squires and Eaton 1989; Ueda et al. 1983). Unfortunately, direct simulations are still limited to very low Reynolds numbers and are often prohibitively time consuming. There are many alternative techniques (e.g., Monte-Carlo procedure, random flight model, Brown-Hutchinson (1979) model) to generate instantaneous turbulent flow and then simulate particle dispersion. These alternative techniques are stochastic models and can give reasonable agreement with experimental data, but they require that certain assumptions be made about the fluid-particle interaction and use empirical coefficients such as a diffusion coefficient or Lagrangian time and length scales.

In this paper, we apply the model proposed by Kraichnan (1970) in which a stationary Gaussian velocity field is generated by means of a linear superposition of a large number of random Fourier modes. This model falls between the very complicated techniques of direct simulation and the simplified approach of the more common stochastic techniques. Unlike direct simulations, there is no limitation on Reynolds number for this model. All the parameters involved are Eulerian and the spectrum and autocorrelation of the flow can be specified. Kraichnan's model is very efficient for this particular simulation because it computes the velocity at the time and location required, and interpolation is not required as it is with direct simulation. While Kraichnan's model is limited to isotropic and homogeneous turbulence, which is an idealized situation, many regions of a flow field are closely represented by this flow.

Particle velocities and trajectories are found by numerically integrating the Lagrangian equations describing the particle motion with inertia and external body forces included in the equations of motion for the particle. All the statistics of the particle's motion are evaluated by ensemble averaging over a large number of realizations of individual particles.

Simulation of the Turbulent Flow Field

The stochastic model for the Gaussian random velocity field proposed by Kraichnan (1970) has been widely used to simulate stationary homogeneous turbulence (e.g., Maxey 1987; Reeks 1980). Recently this model has been extended by Drummond et al. (1984) and others to incorporate more turbulent characteristics into the model. For the purpose of the present work, the original model is sufficient and requires less information about the flow being simulated. In Kraichnan's method, the flow field is represented by the following equation, which is a linear superposition of a large number of Fourier modes with random amplitudes and phases:

$$u_i(x_i,t)/u_0 = \sum_{n=1}^{N} \{ b_i^{(n)} \cos(\mathbf{k}^{(n)} \cdot \mathbf{x} + \omega^{(n)} t) + c_i^{(n)} \sin(\mathbf{k}^{(n)} \cdot \mathbf{x} + \omega^{(n)} t) \}. \quad (1)$$

[1]Current Address: Center for Fluid Mechanics, Turbulence, and Computation, Brown University, Providence R.I., 02912.

Contributed by the Fluids Engineering Division for publication in the JOURNAL OF FLUIDS ENGINEERING. Manuscript received by the Fluids Engineering Division September 21, 1989.

This equation is equivalent to the discretization of a Fourier transform of the velocity field over space and time. Here N is the number of modes and u_0 is the rms fluctuation velocity. The mean velocity is zero, and the velocity field is understood to represent the velocity field in a frame of reference moving with the mean velocity of the flow. Using the definitions given in Wang and Stock (1988), Eq. (1) gives the velocity field in the moving Eulerian system. For each n, $k_i^{(n)}$ and $\omega^{(n)}$ are chosen independently from Gaussian random numbers of zero mean with standard deviations of k_0 and ω_0, respectively. Real coefficients $b_i^{(n)}$ and $c_i^{(n)}$ are also independent Gaussian random variables that have been filtered such that $\mathbf{b}^{(n)}\cdot\mathbf{k}^{(n)}$ and $\mathbf{c}^{(n)}\cdot\mathbf{k}^{(n)}$ vanish, making the overall flow field incompressible. The ensemble-averaged two-point correlation of this random flow field is (Maxey, 1987)

$$R_{ij}(\mathbf{r},\tau)/u_0^2 = N\int_{-\infty}^{\infty} d^3\mathbf{k}\int_{-\infty}^{\infty} d\omega \times P_1(\mathbf{k})P_2(\omega)\Gamma^2(\mathbf{k},\omega)\left[\delta_{ij}-\frac{k_ik_j}{k^2}\right]\cos(\mathbf{k}\cdot\mathbf{r}+\omega\tau) \quad (2)$$

where P_1 and P_2 are Gaussian probability functions and $\Gamma(k,\omega)$ is the scaling function. $\Gamma(k,\omega)$ allows the flow field to be generated with any prescribed two-point correlation function. If we assume Γ is only a function of $k = \sqrt{k_1^2+k_2^2+k_3^2}$, then

$$R_{ij}(\mathbf{r},\tau)/u_0^2 = \frac{N}{(2\pi)^{3/2}\mathbf{k}_0^3}\int_{-\infty}^{\infty} d^3\mathbf{k}\Gamma^2(k)\left[\delta_{ij}-\frac{k_ik_j}{k^2}\right]\cos(\mathbf{k}\cdot\mathbf{r})e^{-\frac{k^2}{2k_0^2}}\exp\left(-\frac{\omega_0^2\tau^2}{2}\right). \quad (3)$$

The scalar energy-spectrum function associated with this flow field is

$$E(k) = \sqrt{\frac{2}{\pi}}\frac{k^2}{k_0^3}\Gamma^2(k)\exp\left(-\frac{k^2}{2k_0^2}\right). \quad (4)$$

In this work, the scaling function Γ was chosen to be

$$\Gamma(k,\omega) = \frac{k}{\sqrt{2N}k_0}, \quad (5)$$

which makes the energy spectrum function

$$E(k) = \frac{u_0^2}{\sqrt{2\pi}}\frac{k^4}{k_0^5}\exp\left(-\frac{k^2}{2k_0^2}\right). \quad (6)$$

This form of the energy spectrum has also been used by Kraichnan (1970) and Maxey (1987). The function in Eq. (6) has a maximum at $k = 2k_0$. The Eulerian one-point time correlation in the moving coordinate system is

$$D(\tau) = \exp\left(-\frac{\omega_0^2\tau^2}{2}\right), \quad (7)$$

and Eulerian integral time scale in the moving coordinate system is

$$T_{mE} = \frac{\sqrt{2\pi}}{2\omega_0}. \quad (8)$$

The flow field generated by this method is governed by three parameters, u_0, k_0, and ω_0, where u_0 is the rms fluctuation velocity, k_0 is the characteristic wave number which depends on the integral length scale of the turbulence, and ω_0 is related to the one-point integral time scale. Wang and Stock (1988) discussed how these three parameters can be related to the flow field found in grid generated turbulence.

Simulation of Heavy Particle Motion

The general Lagrangian equations for particle motion in an unsteady flow are known as the BBO (Bassett-Boussinesq-Oseen) equation (Maxey and Riley, 1983) in which Stokes drag, virtual mass, pressure gradient, Basset history term, and buoyancy effects are included. In the present study, we assume that the particles are much denser than the gas and that the particulate phase is dilute. The pressure gradient force, the virtual mass force, and the Basset force can be neglected because of the large difference between the density of the gas and the density of the particles. Therefore the equations of motion for a particle can be written as

$$\frac{dv_i}{dt} = \frac{(u_i(\mathbf{y},t)-v_i)f}{\tau_a} - q\delta_{i3}, \quad (9)$$

Nomenclature

b_i, c_i = random coefficients
d_p = diameter of particle
$D(\tau)$ = one-point fluid velocity correlation in the moving Eulerian frame
$E(k)$ = scalar energy spectrum function
f = the ratio of drag coefficient to Stokes drag
q = external body force acting on particle
$\mathbf{k}$ = wave number
k_0 = characteristic wave number
m = $k_0u_0T_{mE}$
N = the number of Fourier modes
$\mathbf{r}$ = space separation
$R_{ij}(\mathbf{r},\tau)$ = fluid velocity correlation
Re_0 = d_pu_0/ν
Re_p = particle Reynolds number
St = Stokes number
t = time
T_{mE} = integral time scale of Eulerian fluid correlation in the moving Eulerian frame
T_L = Lagrangian integral time scale of particle
$\mathbf{u}$ = flow velocity
u_0 = fluid rms fluctuation velocity
$\mathbf{v}$ = particle velocity
v_{i0} = ith component of particle rms fluctuation velocity
v_d = Stokes drift velocity of particle = τ_aq
$\mathbf{x}$ = Eulerian coordinate
$\mathbf{y}$ = particle's location
δ_{ij} = Kronecker delta
ϵ_{ij}^p = particle diffusivity tensor
γ = v_d/u_0
Γ = the scaling function, Eq. (2)
ν = fluid kinematic viscosity
ω = frequency
ω_0 = characteristic frequency
ρ = fluid density
ρ_p = particle density
τ = time delay
τ_a = particle aerodynamic response time

Superscripts

(j) = j^{th} mode
$*$ = dimensionless variables

Subscripts

1,2 or x,y = horizontal directions
3 or z = vertical direction
e = effective parameter
i = i^{th} component

$$\frac{dy_i}{dt} = v_i, \tag{10}$$

where v_i is the particle velocity and q is the body force per unit mass. $u_i(\mathbf{y},t)$ is the fluid velocity at the location of the particle, $\mathbf{y}(t)$. τ_a is the aerodynamic response time for the linear Stokes drag, namely,

$$\tau_a = \frac{\rho_p d_p^2}{18\mu}, \tag{11}$$

where d_p is the diameter of particle, μ is the dynamic viscosity of the fluid, and ρ_p is the material density of the particle. The factor f is the ratio of the drag coefficient to Stokes drag which is well represented for Reynolds number up to 1000 by the empirical expression

$$f = 1 + 0.15\ \mathrm{Re}_p^{0.687}, \tag{12}$$

where Re_p is the particle Reynolds number based on the relative velocity between the particle and the fluid. Equations (9) and (10) can be put into dimensionless form to give

$$\frac{dv_i^*}{dt^*} = \frac{(u_i^*(\mathbf{y}^*,t^*) - v_i^*)f}{\mathrm{St}} - \frac{\gamma\delta_{i3}}{\mathrm{St}}, \tag{13}$$

$$\frac{dy_i^*}{dt^*} = v_i^*, \tag{14}$$

where the dimensionless variables are defined as $v_i^* = v_i/u_0$, $u_i^* = u_i/u_0$, $y_i^* = y_i/(u_0 T_{mE})$ and $t^* = t/T_{mE}$. St is the Stokes number defined as τ_a/T_{mE}, the ratio of the particle's aerodynamic response time (based on Stokes drag) to a characteristic time scale of the flow. The Stokes number is a measure of the relative importance of inertia since τ_a increases with particle mass. The parameter γ is defined as $\tau_a q/u_0 = v_d/u_0$. It is the ratio of the particle's Stokes velocity to the rms fluid fluctuating velocity.

The initial conditions for the equations of motion of the particles are

$$y_i^*(t^* = 0) = 0, \tag{15}$$

$$v_i^*(t^* = 0) = u_i^*(0,0) - \gamma\delta_{i3}. \tag{16}$$

These conditions are probably not realistic for particles being emitted from a point source, but in this study the numerical computation of particle dispersion was started at some later time, e.g., $t^* = 2$ to allow the initial conditions to have sufficient time to decay. Thus any spurious effects of the initial conditions on the long-time dispersion of the particles were eliminated.

Particles trajectories are found by numerically integrating the equations of motion for the particles, Eqs. (13) and (14), using fluid velocities from Eq. (1). The Gaussian random numbers used in Eq. (1) are determined by the functional routine RNNOF of the IMSL STAT/LIBRARY which is available on the IBM 3090 of Washington State University's Computer Center. The routine generates a Gaussian distribution by an inverse CDF technique. At each point on a particle trajectory where the fluid velocity is required it is computed using

$$u_i^*(\mathbf{y}^*,t^*) = \sum_{n=1}^{N} \{b_i^{(n)} \cos(\mathbf{k}^{(n)*}\cdot\mathbf{y}^* + \omega^{(n)*}t^*) + c_i^{(n)} \sin(\mathbf{k}^{(n)*}\cdot\mathbf{y}^* + \omega^{(n)*}t^*)\}, \tag{17}$$

where $k_i^{(n)*}$ and $\omega^{(n)*}$ are nondimensional Gaussian random numbers with zero mean and with standard deviations of $m \equiv k_0 T_{mE} u_0$ and 1.2533 (or $\sqrt{\pi/2}$), respectively. Then Eqs. (13) and (14) are integrated by the fourth-order, stable predictor-corrector scheme known as the Hamming method. The values for the first four steps are computed using the fourth-order Runge-Kutta method three times. The numerical error in the integration increased exponentially with time. Therefore, it is critical to use a time step Δt^* small enough to satisfy a global tolerance accuracy but as large as possible to save time.

Integration Time Step Size Considerations

The time step considered here is that used to numerically integrate the Lagrangian motion of a heavy particle, given that the instantaneous flow is a continuous function of space and time. Intuitively we know that the size of the time step for a given numerical accuracy is governed by the character of the turbulence, most likely the integral time scale, the particle's inertia, and the particle's free fall velocity. We carried out some tests to determine the relative importance of these three parameters.

Figure 1 shows typical trajectories in a $y-z$ plane for a single particle with different inertia parameters (St = 0.1, 0.4, 1.0, 5.0) and γ equal to zero. As the St number increases, the particle tends not to respond to the acceleration of the surrounding fluid, but instead follows a trajectory quite different than that of the fluid. From this figure it is difficult to guess if smaller time steps are required for a particle that follows the flow or one that is very sluggish. Figure 2 shows typical trajectories in a $y-z$ plane for a single particle with different nondimensional free fall velocities, γ (γ = 0.0, 0.4, 1.0, 2.0), for a St of 0.2. For small γ, the particle shows no preferred direction, but as γ increases the particle drifts in the direction of the body force. Again it is difficult to guess which case will require the smallest time step to hold the overall error at a constant value.

To quantify the effect of St number and γ on the size of the time step required to maintain a given overall tolerance, simulations were run and the error in the particle's displacement and velocity were compiled. Figure 3 shows the result of one such simulation. The errors were calculated relative to an almost *exact* trajectory obtained by a nondimensional time step of $\Delta t^* = 0.01$. The flow field used in this simulation is typical of that found in low speed gas-particle flows.[2] The error in the particle location grows exponentially with time. No matter how small the time step the error in the particle's location will ultimately start to increase in a manner similar to that shown in Fig. 3, except that the smaller the time step, the longer it will take for the error to become significant.

If the long-time diffusivities are to be calculated, one would like to have very low error in the particle trajectories after several Lagrangian integral times. Simulations were made for a range of Stokes numbers and γ to find the time step that would give a one percent error in particle location after a total integration time of $4T_L^*$.[3] Table 1 lists the time step size, Δt^*, that will give an average error of one percent in the particle's location after a total integration time of $4T_L^*$. The results clearly show that a smaller time step is required with increasing Stokes number and γ. The decrease in the length of the time step with increasing Stokes number (particle mass) is mostly due to the increase in the Lagrangian integral time. The decrease in time step with increasing γ (free-fall velocity) is caused by the increase in distance traveled by the particle.

If one is interested in the behavior of particle trajectories at a given time after release (e.g., for particles in a combustion chamber), then the time-step size limit should be determined for a fixed total integration time. Table 2 shows the time-step

[2]The rms fluctuation velocity of the flow, u_0, was 20 cm/s and the integral time scale, T_{mE}, was 14.4 ms. The Reynolds number based on these scales ($T_{mE}u_0^2/\nu$) was about 50. These values are typical for grid-generated flow of air (e.g., Wells and Stock, 1983).

[3]$T_L^* = T_L/T_{mE}$. T_L is the Lagrangian integral time scale for the motion of heavy particles. It is a strong function of St and a weak function of γ. Larger St results in larger T_L because of the sluggish response of particles to the flow. On the other hand, larger γ gives slightly smaller T_L because of the crossing trajectory effect (Reeks, 1977).

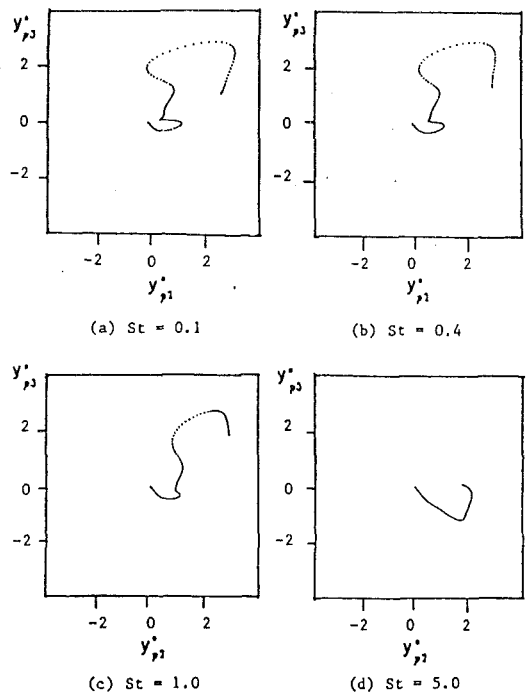

Fig. 1 Typical trajectories of a particle in a $y-z$ plane ($x = 0$) for different inertia parameters with zero fall velocity and $k_0u_0T_{mE} = 0.2710$. $y_2^* = y_2/(u_0T_{mE})$, $y_3^* = y_3/(u_0T_{mE})$.

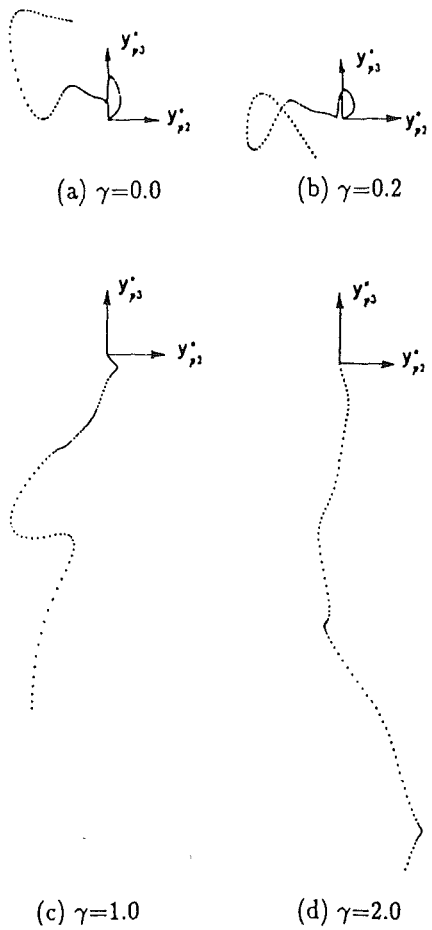

Fig. 2 Typical trajectories of a particle in a $y-z$ plane ($x = 0$) for different fall velocity γ, given St = 0.2 and $k_0u_0T_{mE} = 0.2710$. $y_2^* = y_2/(u_0T_{mE})$, $y_3^* = y_3/(u_0T_{mE})$.

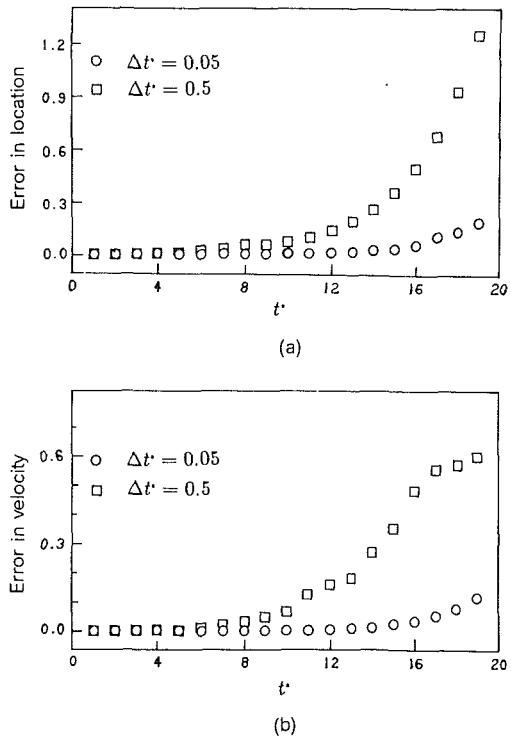

Fig. 3 Nondimensionalized global errors in the integration of equations of motion based on $\Delta t^* = 0.01$. Parameters are: St = 0.8, $k_0u_0T_{mE} = 0.6265$, $\gamma = 1.0$. The corresponding Lagrangian integral time of particle T_L^* is about 1.3. The number of Fourier modes $N = 80$. (*a*) Error in location; (*b*) error in velocity.

Table 1 Dimensionless time steps for one percent error in location at $t^* = 4T_L^*$ ($k_0u_0T_{mE} = 0.62665$)

	$\gamma=0$	$\gamma=0.4$	$\gamma=1.0$	$\gamma=2.0$
St = 0.1	0.2	0.2	0.1	0.1
St = 0.4	0.1	0.1	0.08	0.06
St = 1.0	0.08	0.06	0.05	0.04
St = 5.0	0.05	0.04	0.03	0.02

Table 2 Dimensionless time steps for one percent error in location at $t^* = 2$ ($k_0u_0T_{mE} = 0.62665$)

	$\gamma=0$	$\gamma=0.4$	$\gamma=1.0$	$\gamma=2.0$
St = 0.1	0.2	0.2	0.2	0.2
St = 0.4	0.3	0.3	0.3	0.3
St = 1.0	0.5	0.5	0.5	0.5
St = 5.0	1.0	1.0	0.8	0.8

size that will give an average error of one percent in the particle location after a total integration time of 2. In this case, larger time steps can be used for particles with larger inertia (larger St number), because the trajectories are less random.

Kraichnan's random Gaussian velocity field, Eq. (1), was used to provide the fluid velocity field used in the simulation. In all the simulations we used 80 Fourier modes and expected that the number of modes used in the calculations would not influence the average error in particle trajectory calculations,[4] because the integral scales of the velocity fields do not change when N is changed. To determine if our intuition was correct, we repeated the same simulation, but used a different number of Fourier modes in each calculation. Figure 4 shows the result of this set of calculations. Beyond 40 modes we see little change in the results when more modes are used.

The time required to accomplish a simulation for heavy

[4]To achieve the same uncertainty for the dispersion coefficient, the mean square displacement, or the Lagrangian velocity correlation, either a small number of Fourier modes and a large number of flow realizations or a large number of Fourier modes and smaller number of flow realizations can be used.

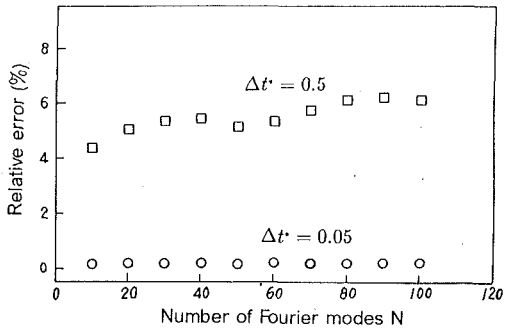

Fig. 4 The relative error in particle's location (averaged over 100 realizations of the flow) at $t^* = 4T_L^*$ (or about 5) as a function of the number of Fourier modes. Parameters are: St = 0.8, γ = 1.0, $k_0u_0T_{mE}$ = 0.6265.

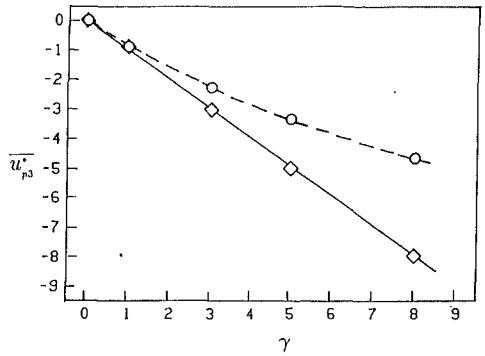

Fig. 5 Mean vertical fall velocity of a heavy particle, $\overline{v_3^*}$, as a function of γ for St = 0.8 and $k_0u_0T_{mE}$ = 0.62665. Key: —, f = 1 in still fluid (analysis); ◇ ◇ ◇, f = 1 in turbulent flow (simulation); - - -, f = 1 + 0.15 $Re_p^{0.687}$ in still fluid (analysis); ○ ○ ○, f = 1 + 0.15 $Re_p^{0.687}$ in turbulent flow (simulation).

particle dispersion depends on the total integration time, the size of the time step, the number of Fourier modes used to simulate the fluid, and the number of particle trajectories computed. In the dispersion simulation presented in this paper, 2000 particle trajectories were calculated and 80 Fourier modes were used. The computing time on an IBM 3090 computer ranged from 2500 and 8000 seconds.

Effect of Nonlinear Drag

When particles move with a low relative Reynolds number, the viscous drag on the particle is directly proportional to the difference in velocity between the particle and the fluid (the Stokes drag). However, when the relative Reynolds number approaches one, the drag starts to depend on the relative velocity raised to some power (the nonlinear drag). The ratio of the actual drag coefficient to the Stokes drag coefficient is called f and is given by Eq. (12). Numerical simulation is much simpler if Stokes drag can be assumed, because then each velocity component can be treated separately and the total velocity magnitude need not be computed at each time step. Before starting a simulation, one must decide if Stokes drag can be used or if the total relative velocity must be computed at each time step. One would expect that the relative velocity between the particle and the fluid would increase as the Stokes number (inertia) and γ (free fall velocity) increase. It would be useful to have some guidelines to help decide when nonlinear drag effects must be taken into account.

To incorporate nonlinear drag into the simulation, Re_p must be computed and updated after each time step. To calculate the Re_p we have to specify the type of particles and fluid. In our computations we assumed that the particles were glass beads (ρ_p = 2500 kg/m^3) and that the fluid was air with a density ρ = 1.22kg/m^3, kinematic viscosity $\nu = 1.25\times10^{-5}$ m^2/s. For the flow field we assumed u_0 = 0.2 m/s, T_{mE} = 0.01438 s, and q = 9.8 m/s^2 for the acceleration of gravity. Then

$$\mathrm{Re}_p = \mathrm{Re}_0 \cdot \frac{[\mathbf{v}-\mathbf{u}]}{u_0}, \tag{18}$$

where $Re_0 = d_pu_0/\nu$. For our particles and fluid this becomes

$$\mathrm{Re}_0 = \sqrt{\frac{\rho}{\rho_p}\frac{18u_0^3}{\nu q}}\,\gamma = 0.701\gamma^{0.5}. \tag{19}$$

As the relative velocity between the particle and the fluid increases, the particle free fall velocity will be less than a similar particle falling under the influence of only Stokes drag. Figure 5 shows the mean vertical particle velocity calculated from a simulation using the nonlinear drag and a simulation using the Stokes drag. The solid lines are the analytically calculated vertical velocities of particles falling in still air. From Fig. 5 we can see that nonlinear drag effect should be considered when determining the free-fall velocity for larger γ (say, $\gamma > 2$).

On the other hand, we found that the Stokes number had very little effect on the free-fall velocity. A very close approximation to a particle's free-fall velocity in a turbulent flow can be calculated by assuming the particle is falling through still air. Maxey (1987) found that the average settling velocity of particles in turbulent flow was larger than the free fall velocity. However, the maximum difference was about 10 percent in the extreme case of $T_{mE}\to\infty$. For the simulation in Fig. 5, we used $k_0u_0T_{mE}$ = 0.62665, which is equivalent to a nondimensionalized ω_0 of 1.0 in Maxey's work. Maxey's Fig. 3 shows that the turbulence will increase the settling velocity by less than two percent. Thus our results as shown in Fig. 5 are in good agreement with Maxey's work.

The question of how large γ can be before nonlinear drag must be used in a simulation still remains. We were interested in how the simulation computed with the nonlinear drag differs from a simulation computed using Stokes drag. Therefore, we computed the ratios of the particle fluctuation velocity and diffusivity with nonlinear drag to their respective value with linear drag. We first ran some simulations at fixed γ and varied the Stokes number. These tests showed that the Stokes number had little effect on the computed diffusivity ratio or particle fluctuating velocity ratio for a given γ. The results of a computation using a Stokes number of 0.8 and a range of γ are shown in Figs. 6 and 7. These figures show both the fluctuation velocity ratio and the diffusivity ratio increase with increasing γ. From these figures we can see that nonlinear drag should be considered when γ is greater than two to keep the relative increase in the diffusivity due to the nonlinear drag less than 10 percent.

These findings can be explained by examining the equations of motion for the particles. If we define an effective Stokes number as $St_e = St/f$, and an effective drift parameter as $\gamma_e = \gamma/f$, the equations of motion for a particle with nonlinear drag (Eq. (13)) in terms of the effective parameters have the same form as the equations of motion for a particle under Stokes drag. Since f increases with particle free-fall velocity and is always larger than one, the effect of the nonlinear drag is to decrease the inertia and the fall velocity. Decreasing γ increases the dispersion coefficient and decreasing St increases the rms fluctuation velocity. Therefore, we would expect the ratios shown in Figs. 6 and 7 to increase with γ. Further, f is almost (not exactly) independent of the Stokes number, we thus expect St to have no influence on the ratios shown in Figs. 6 and 7.

We quantified the relative importance of the nonlinear drag in terms of γ, the ratio of the free fall velocity to the turbulence fluctuation velocity, rather than the particle's Reynolds number based on the fall velocity. We believe γ is a more proper parameter, because the relative velocity between a particle and

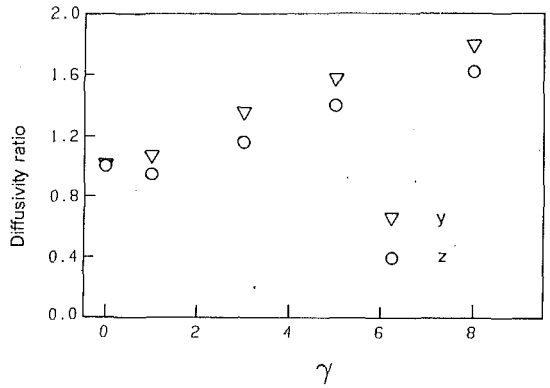

Fig. 6 The ratio of particle diffusivity with nonlinear drag to the particle diffusivity with linear drag. Parameters are: St = 0.8, $k_0 u_0 T_{mE}$ = 0.62665.

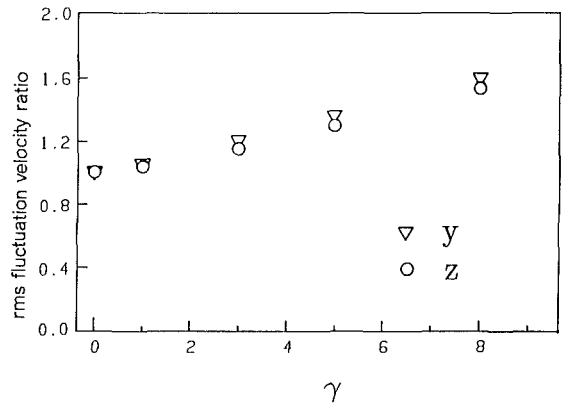

Fig. 7 The ratio of particle rms fluctuating velocity with nonlinear drag to the fluctuating velocity with linear drag. Parameters are: St = 0.8, $k_0 u_0 T_{mE}$ = 0.62665. *y* and *z* refer to transverse direction and vertical direction, respectively.

the flow depends on both the free-fall velocity of the particle and the fluid rms velocity, u_0.

Comparison With Analytical Techniques

Reeks (1977) developed an approximate solution for the dispersion of particles in an isotropic, homogeneous turbulent flow using second order iteration (Phythian, 1975). The second-order iteration technique is known to give good results for dispersion of fluid particles. Reeks extended the technique to heavy particles by assuming the particle motion was governed by Stokes drag. Based on the results of the simulation presented in the last section, we would expect the approximate analysis to be valid for γ of two or less. In this section, we will present direct comparisons between the simulation using nonlinear drag and the analysis, which uses Stokes drag, and determine the largest γ that can be used with the analytical technique.

The flow field used by Reeks and the one we use in the simulation, Eq. (1), are both governed by three parameters. However, the parameters are not the same and before showing results the relationship between the parameters is needed. We used the Stokes number, γ, and m as the three independent parameters. Reeks used the following three parameters in his study:

$$\gamma_0 = \frac{0.62665}{m}, \tag{20}$$

$$\beta = \frac{1}{2 \cdot \mathrm{St} \cdot m}, \tag{21}$$

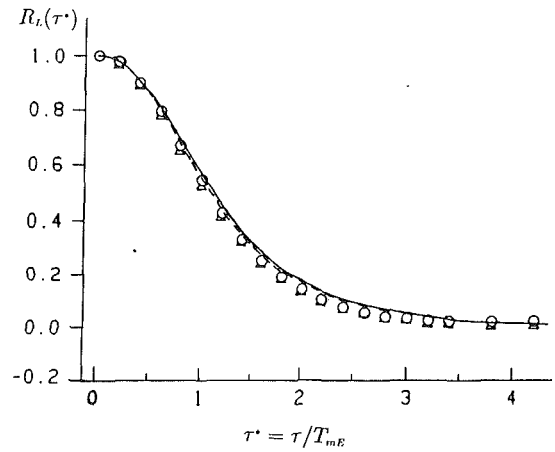

Fig. 8 Comparison of Lagrangian velocity correlations of particle for γ = 1.0, St = 0.8, $k_0 u_0 T_{mE}$ = 0.62665. Key: - - -, f = 1 in transverse direction (analysis); —, f = 1 in vertical direction (analysis); △ △ △, $f = 1 + 0.15 \times \mathrm{Re}_p^{0.687}$ in transverse direction (simulation); ○ ○ ○, $f = 1 + 0.15\ \mathrm{Re}_p^{0.687}$ in vertical direction (simulation).

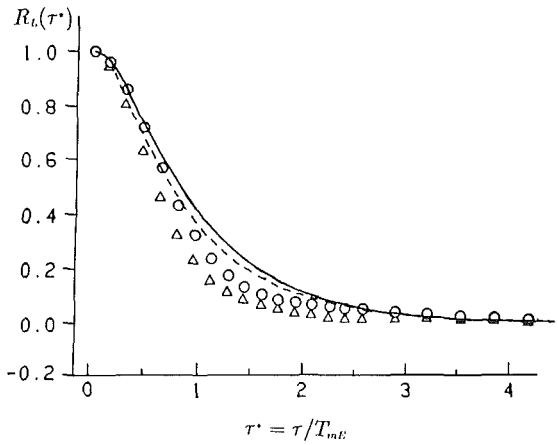

Fig. 9 Comparison of Lagrangian velocity correlations of particle for γ = 5.0, St = 0.8, $k_0 u_0 T_{mE}$ = 0.62665. Key: - - -, f = 1 in transverse direction (analysis); —, f = 1 in vertical direction (analysis); △ △ △, $f = 1 + 0.15 \times \mathrm{Re}_p^{0.687}$ in transverse direction (simulation); ○ ○ ○, $f = 1 + 0.15\ \mathrm{Re}_p^{0.687}$ in vertical direction (simulation).

$$F_g = \frac{2 \cdot \mathrm{St} \cdot m}{\gamma}. \tag{22}$$

To determine when the effects of nonlinear drag become significant and therefore when the analytical, second-order iteration method can no longer be used, we compared the simulation using nonlinear drag with the analysis using linear drag for a range of Stokes numbers and γ. All the computations were done for m = 0.62665, which is the same as used by Reeks. Figures 8 and 9 show the computed Lagrangian velocity correlations for γ of 1 and 5 with the Stokes number equal to 0.8 in both cases. Comparing the two plots we see that at γ = 1 the simulation and analysis give similar results and at γ = 5 there is considerable difference. Closer examination of the computed results show a relative decrease of 6 percent in the integral time scale T_L when the nonlinear drag is used at γ = 1; while a relative decrease of 38 percent in T_L when the nonlinear drag is used at γ = 5. Similar calculations performed at γ = 1 and Stokes numbers between 0.4 and 2.0 showed no additional change in the relative decrease of the integral time scale with the use of the nonlinear drag. The decrease in the integral time scale, T_L, when the nonlinear drag is used is due to the change in the effective inertia which dominates the value of T_L, as discussed earlier. We also compared the long time diffusivities determined by the simulation and the analysis and

found that the two methods agree reasonably well (within 10 percent) for γ of two or less and also found this result to be independent of the Stokes number.

Conclusions

Although numerical simulation of heavy particle dispersion is very useful, performing the computations requires making decisions on the time step. With the instantaneous velocity field known, heavy particle motion can be computed by tracking the particles through the flow field by integrating the particle's equations of motion over small time steps. Since the particle's equations of motion are strongly nonlinear, one would expect the particle trajectories to be very sensitive to small numerical errors. We found that the numerical errors tended to grow exponentially, a well-known feature of a chaotic system. Although the size of the time step will depend on the integration scheme and on the number of bits being carried by the computer, we have developed some general guidelines for the effect of the particle free-fall velocity and inertia. We found that the longer the total integration time or the larger the drift parameter, γ, the smaller the time step that must be used to maintain the same average error in the total displacement of a particle. If the integration is over a fixed number of Lagrangian integral time scales, then the time step must be reduced as γ or the Stokes number increases.

We also provided some guidelines for situations where it might be necessary to include the effects of nonlinear drag when computing particle motion. For typical gas-particle flows, we found that for γ greater than two, nonlinear drag must be taken into account. We also found that the value of the Stokes number did not affect the relative importance of the nonlinear drag (namely, the ratios of the results based on the nonlinear drag to their respective results based on the Stokes drag). These same results were also found when we compared the computed diffusivity from the simulation with the analytical results of a second-order iteration scheme (Reeks, 1977).

References

Brown, D. J., and Hutchinson, P., 1979, "The Interaction of Solid or Liquid Particles and Turbulence Fluid Flow Fields-A Numerical Simulation," ASME JOURNAL OF FLUID ENGINEERING, Vol. 101, pp. 265–269.

Drummond, I. T., Duane, S., and Horgan, R. R., 1984, "Scalar Diffusion in Simulated Helical Turbulence with Molecular Diffusivity," *J. Fluid Mech.*, Vol. 138, pp. 75–91.

Kraichnan, R. H., 1970, "Diffusion by Random Velocity Fields," *Phys. Fluids*, Vol. 13, No. 1, pp. 22–31.

Maxey, M. R., 1987, "The Gravitational Settling of Aerosol Particles in Homogeneous Turbulence and Random Flow Fields," *J. Fluids Mech.*, Vol. 174, pp. 441–465.

Maxey, M. R., and Riley, J. J., 1983, "The Equation of Motion for Small Rigid Particle Sphere in a Nonuniform Flow," *Phys. Fluids*, Vol. 26, pp. 883–889.

Phythian, R., 1975, "Dispersion by Random Velocity Fields," *J. Fluid Mech.*, Vol. 67, pp. 145–153.

Reeks, M. W., 1977, "On the Dispersion of Small Particles Suspended in an Isotropic Turbulent Field," *J. Fluid Mech.*, Vol. 83, pp. 529–546.

Reek, M. W., 1980, "Eulerian Direct Interaction Applied to the Statistical Motion of Particles in a Turbulent Field," *J. Fluid Mech.*, Vol. 97, pp. 569–590.

Squires, K. D., and Eaton, J. K., 1989, "Study of the Effects of Particle Loading on Homogeneous Turbulence Using Direct Numerical Simulation," *Turbulence Modification in Dispersed Multiphase Flows*, ed. E. E. Michaelides and D. E. Stock, ASME FED-Vol. 80, New York, 71 pages.

Ueda, T., Jinno, K., Momii, K., and Maehama, K., 1983. "Numerical Study of Diffusivity of Settling Particles in Homogeneous Isotropic Turbulence," *Trans. JSCE*, Vol. 15, pp. 293–296.

Wang, L. P., and Stock, D. E., 1988, "Theoretical Method for Obtaining Lagrangian Statistics from Measurable Eulerian Statistics for Homogeneous Turbulence," *Proc. 11th Symp. on Turbulence*, Rolla, Mo, pp. B14.1–B14.12.

Wells, M. R., and Stock, D. E., 1983, "The Effects of Crossing Trajectories on the Dispersion of Particles in a Turbulent Flow," *J. Fluid Mech.*, Vol. 136, pp. 31–62.

D. I. Driscoll
Research Associate,
School of Mechanical Engineering,
Purdue University,
West Lafayette, IN 47907

R. L. Schmitt
Senior Member of the Technical Staff,
Combustion Research Facility,
Sandia National Laboratories,
Livermore, CA 94550

W. H. Stevenson
Professor,
School of Mechanical Engineering,
Purdue University,
West Lafayette, IN 47907

Thin Flowing Liquid Film Thickness Measurement by Laser Induced Fluorescence

An optical technique is described for determining, in a physically nondisturbing manner, the thickness of a thin flowing liquid film. The technique is based on measurement of the fluorescent emission induced in the liquid film by absorption of a focused laser beam. Although the technique was developed for measuring liquid film thicknesses on the prefilming surface of an airblast fuel atomizer, it is not limited to this application.

Introduction

Measurement of thin flowing liquid films, which is of interest in many fields, has been performed using various techniques including surface contact devices, electrical resistance and capacitance, light absorption and scattering, and fluorescent emission. Fluorescent emission measurement is an attractive method for performing in-situ determination of film thickness because it can be performed without physically disturbing the flowfield and without interference from background light. The study of prefilming airblast atomizers is one application for such a technique. The effect of film thickness at the prefilming surface of an airblast atomizer on droplet size has been shown by many investigations (Lefebvre, 1983). It is especially desirable to obtain information on the spatial and temporal uniformity of the liquid film.

The technique described in this paper is suitable for measuring both steady and unsteady variations in film thickness. An earlier study by Schmitt (1980 and 1982) developed the basic theory and tested its feasibility using an optical system similar to the one used in this work. The primary objectives of the present work were to perfect the method used to calibrate the system, develop a method to correct raw calibration and nozzle data, and ensure the repeatability of results.

Experimental Airblast Atomizer

The airblast atomizing nozzle differs from the more conventional pressure type atomizer in which the fluid is discharged through a small orifice into a relatively stagnant mass of air. Figure 1 presents a cross-sectional view of the experimental double-swirler airblast atomizing nozzle used in this study. The fuel, or test fluid in this case (water + fluorescein dye), flows at low pressure through an annulus region and through eight circumferential swirler orifices prior to flowing

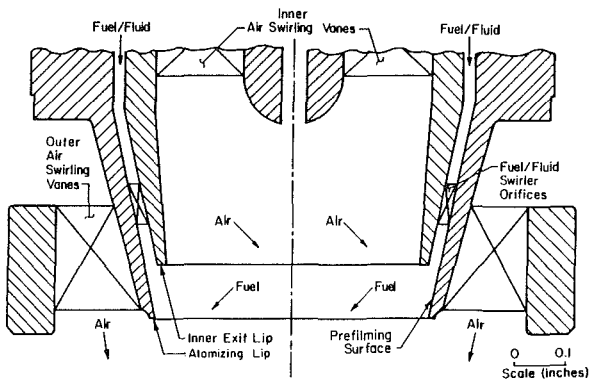

Fig. 1 Cross-section of the experimental airblast atomizing nozzle

across the prefilming surface of the atomizer. There are eight inner air swirling vanes and 16 outer air swirling vanes. The outer air swirling vanes induce a rotation of the airflow which is opposite that of the inner airflow. Initially one side of the fluid sheet is exposed to high velocity air flow at the prefilming surface, and then both sides are exposed to high velocity air as the liquid leaves the surface. The interfacial shearing action between the slow moving fluid and the opposed air flows disintegrate the sheet into small droplets.

For more detailed information and a complete list of references on atomization and atomizer design, the interested reader should refer to the work of Lefebvre (1983).

Theory

Fluorescence is the term for a process in which, under suitable circumstances, radiation is emitted by atoms or molecules that have been excited by the absorption of radiation. The emitted radiation generally has a longer wavelength than the absorbed (Stoke's fluorescence). When the excitation radiation is discontinued, the decay time is on the order of 10^{-7} to 10^{-10} seconds for fluorescence. More detailed information on flu-

Contributed by the Fluids Engineering Division for publication in the JOURNAL OF FLUIDS ENGINEERING. Manuscript received by the Fluids Engineering Division April 30, 1991.

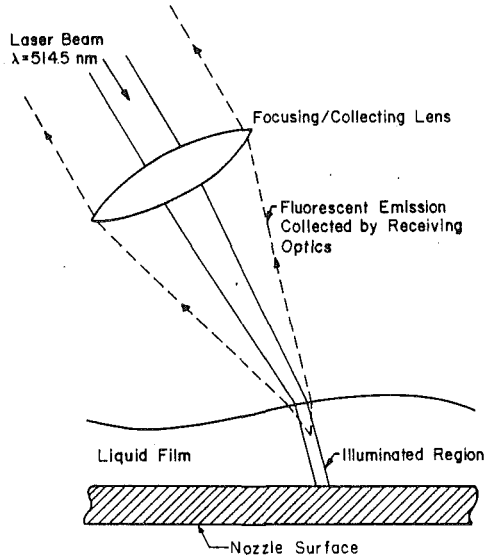

Fig. 2 Illumination configuration of the fluid film

orescence can be obtained from Becker (1969), Hercules (1966), Hieftje (1981), Guilbault (1967), and Parker (1968).

The laser induced fluorescence technique relies on measurement of the intensity of fluorescent radiation emitted from a narrow column of fluid illuminated by a focused laser beam. Figure 2 illustrates the illumination configuration at the atomizing nozzle prefilming surface. The intensity of the fluorescent light collected from the illuminated column is related to the column height and thus is a measure of the thickness of the liquid film.

As a basis for analysis, assume a parallel monochromatic beam traveling in air which is incident perpendicular to an absorbing fluorescent dye solution. A relationship can be readily obtained which relates the fluorescent power to the length of the illuminated column in the liquid. As light passes through any nontransparent medium it will be partially absorbed according to the relation

$$dI = -I\alpha\, dx \tag{1}$$

where

I = intensity of the light
dI = differential change in intensity of the excitation light
α = absorption coefficient
dx = differential pathlength through the absorbing medium

The intensity of transmitted light, after the beam has traversed a finite pathlength x, is found by integrating Eq. (1) to obtain

$$I_t = I_o e^{-\alpha x} \tag{2}$$

Equation (2) is the well-known Beer-Lambert law, where I_t is the intensity of the transmitted light and I_o is the intensity of the incident light in the absorbing medium at $x=0$. The decrease in beam intensity due to absorption in the dye solution is then

$$I_a = I_o - I_t = I_o(1 - e^{-\alpha x}) \tag{3}$$

The total absorbed power, P_a, in the fluid/dye solution is thus

$$P_a = \int I_o(1 - e^{-\alpha x})\, dA \tag{4}$$

Since the absorption coefficient, α, is constant, Eq. (4) can be rewritten as

$$P_a = (1 - e^{-\alpha x}) \int I_o\, dA = (1 - e^{-\alpha x}) P_o \tag{5}$$

where P_o is the power of the incident excitation beam (a focused laser beam) at the air/fluid interface.

The fluorescent power, P_f, emitted from the column of illuminated fluid/dye solution is directly proportional to the power absorbed from the excitation beam, thus

$$P_f = \eta P_a = \eta(1 - e^{-\alpha x}) P_o \tag{6}$$

Here η is the quantum efficiency of the fluorescent molecule, i.e., the probability that the absorption of a photon by a fluorescent molecule will result in the re-emission of a photon at some later time. This equation neglects self-absorption and power saturation effects. For low dye concentrations, self-absorption effects are negligible (see Santos, 1977) and tests were performed to ensure that power saturation did not occur.

Since the angle of incidence of the excitation beam may change unpredictably due to fluid surface angle variations, corrections to Eq. (6) are required. A geometrical correction is required to account for an illuminated column of fluid which is not perpendicular to the nozzle surface and a reflection correction is also required to account for reflection losses at the air/liquid interface.

Reflection of the incident beam at the prefilming metal surface is another possible source of error. This results in fluorescent emission from a region outside the illuminated column considered in the analysis. It is difficult to quantify this in general, but the instrument calibration procedure described in a later section should account for this effect—provided the angle of incidence does not deviate significantly from that used in the calibration.

Geometrical Correction

Consider the generalized illumination geometry of Fig. 3. The excitation beam is incident to the nozzle filming surface at some angle ϕ which is fixed by geometrical constraints. Thus, ϕ would be the angle of incidence on the air/liquid interface if the fluid surface were flat and parallel to the nozzle surface ($\xi = 0$). The excitation beam is refracted at the interface such that the length of the illuminated column is d rather than t where t is the actual liquid film thickness at the point where the excitation beam is incident on the liquid surface. Since d is the hypotenuse of the triangle that includes t as one of its sides, an equation can be readily obtained which relates t to d as a function of the fluid surface angle ξ.

Equation (6) predicts the fluorescent power output for an illuminated column of length x. In this case, the length of the illuminated column of fluid, d, is the quantity directly measured. Therefore, Eq. (6) becomes

$$P_f = \eta(1 - e^{-\alpha d}) P_o \tag{7}$$

Using Snell's law and geometrical relationships, an equation for the illuminated column length can be obtained of the form

$$d = C_g(\xi)\, t \tag{8}$$

where C_g is a function of the surface angle (ξ), and is termed the geometrical correction coefficient.

Interface Reflection Correction

When light is incident on the boundary between two dielectrics, a portion of the light is reflected while the remainder is transmitted. The proportion transmitted depends on the angle of incidence, the state of polarization, and the indices of refraction on both sides of the boundary.

First, consider the incident excitation beam. I_o is the intensity of the refracted portion of the excitation beam at the air/fluid interface. Given the polarization state of the excitation beam, the Fresnel equations and Snell's law can be used to obtain a transmission coefficient, T_o, as a function of surface angle ξ. The refracted excitation beam power is then given by

$$P_o = T_o(\xi) P_e \tag{9}$$

where P_e is the power of the excitation beam incident on the air/fluid interface.

The collected fluorescent radiation will also vary with fluid

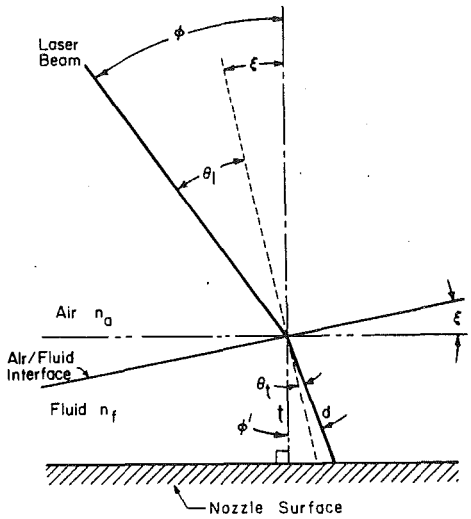

Fig. 3 Generalized illumination geometry

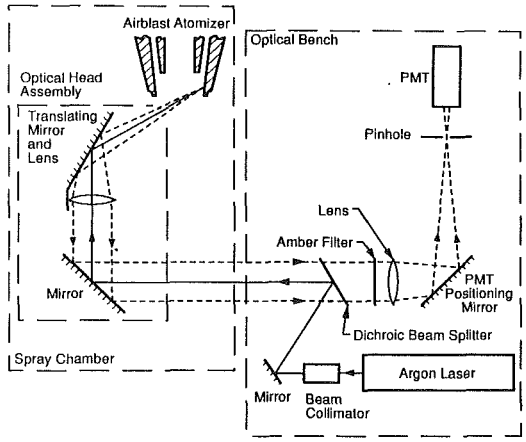

Fig. 4 Configuration of the optical system

surface angle, ξ, due to reflection at the interface. To simplify the derivation, it is assumed that all fluorescent radiation emitted from the illuminated fluid column is incident on the fluid/air interface at the same angle. This is reasonable, since the system f-number is such that the receiving optics will only collect light from a very small solid angle.

In general, for solutions of low viscosity, the fluorescent radiation will be nearly isotropic and unpolarized—even when the incident radiation is completely polarized. With this assumption, the Fresnel equations and Snell's law can again be used to obtain a transmission coefficient, T_c, for the collected fluorescent radiation as a function of surface angle ξ. The general expression for the fluorescent power collected by the optical system is thus

$$P_c = K T_c(\xi) P_f \tag{10}$$

where K is a constant that depends on the f-number of the optical system and is proportional to the solid angle defined by the light collection optics. Using Eqs. (7), (8), (9), and (10), the collected fluorescent radiation power can be expressed as

$$P_c = K\eta[1 - e^{-C_g(\xi)\alpha t}] C_r(\xi) P_e \tag{11}$$

where C_r is a combined correction coefficient given by

$$C_r(\xi) = T_o(\xi)\, T_c(\xi) \tag{12}$$

C_r accounts for reflection losses in both the excitation beam and the collected fluorescent radiation.

Optical System

Functionally, the optical system is composed of the illumination optics and the collection optics, with some optical elements shared. Since the fluorescent radiation is of a longer wavelength than that of the excitation beam, wavelength separating elements can be used to separate or unite the two beams as desired. Figure 4 illustrates the physical layout of the system.

The excitation beam originates from an argon ion laser operating on the 514.5 nm green line and is p-polarized at the liquid film (i.e., its plane of polarization is parallel to the plane defined by the incident and refracted beams). Optical elements of the system are positioned such that the collected fluorescent light travels back through the system as a nearly collimated beam. To achieve this, the illuminated fluorescent volume is positioned on the prefilming surface at the focal point of the translating lens. It is also desirable to have the prefilming surface exactly at the minimum waist of the focused beam, because this provides the best spatial resolution. Thus, the excitation beam also needs to be collimated so that the minimum waist will coincide with the focal plane of the translating lens. An excitation beam collimator was added to the system to achieve this.

After the excitation beam passes through the beam collimator, it is turned by a mirror and directed toward a dichroic beam splitter, which reflects most of the light at 514.5 nm and directs it to the optical head assembly inside the spray chamber. Once inside the optical head assembly, the beam is reflected toward the translating lens and focused on the atomizer prefilming surface. The focused beam diameter (minimum waist) at the prefilming surface was calculated to be approximately 40 μm (0.0016 in.). The Rayleigh depth of focus was calculated to be approximately 4800 μm (0.19 in.).

Fluorescent radiation emerging from the illuminated fluid layer is collected by the translating lens and travels as a nearly collimated beam toward the dichroic beam splitter. Nearly all of the flourescent light will be transmitted through the beam splitter. An amber filter is used to absorb any scattered radiation at the laser wavelength which might pass through the splitter. The collimated fluorescent light passes through the focusing lens and is turned by a positioning mirror toward a pinhole mounted in the front of the photomultiplier tube (PMT).

The pinhole acts as a field stop for the optical system by limiting the size of the object field detected by the PMT. In this case the object is the illuminated column of fluid in the liquid film. Thus, the pinhole significantly reduces unwanted fluorescent radiation that could reach the PMT after reflection from the solid prefilming surface.

Figure 5 illustrates the more salient features of the optical head assembly which is located inside the spray chamber. The head assembly serves as an illumination and collection beam positioning mechanism and isolates the light paths from the adverse environment. The translating lens, a mirror, and a nitrogen purge cone assembly all share a common translating base and thus move in unison. A stepping motor is used to move the translating base. The stepping motor is mounted in a separate compartment to isolate it from the beam path, since the motor generates a significant amount of heat. A purge cone is used to break through one side of the fluid sheet leaving the prefilming surface, and provide an unobstructed optical path to the lip on the opposite side, as illustrated in Fig. 6. Nitrogen flows into the purge cone assembly and exits through the tip along with the excitation beam. This purge flow prevents liquid from collecting at the tip opening and also prevents droplets from entering the cone assembly and depositing on the internal glass window. Since the nitrogen jet exiting the purge cone can disturb the film surface at the measurement point, the effect of the purge flow on measured film thickness was investigated.

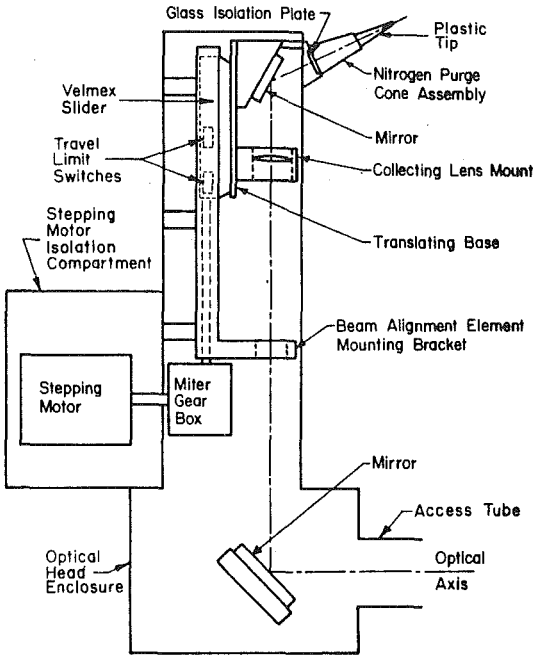

Fig. 5 Optical head assembly features

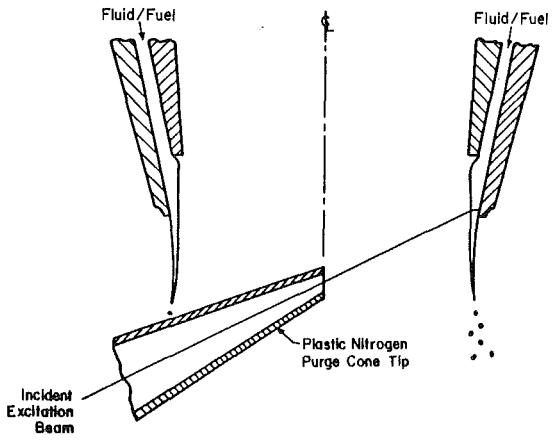

Fig. 6 Orientation of the nitrogen purge cone assembly

Optical System Calibration

Calibration of the system is a critical aspect of the work, since it permits verification of the theoretical results and provides the information required to obtain absolute film thickness.

A dynamic calibration nozzle was designed which provides access to varied thicknesses of a flowing fluid/dye solution. Calibration with a static fluid is not possible due to excessive buildup of dye molecules in the triplet state (a long-lived phosphorescence state) and dye degradation (photo-decomposition) which occur when the dye solution is continuously illuminated by a laser. The calibration nozzle, illustrated in Fig. 7, has a glass cover plate inclined with respect to the stainless steel base of the calibration nozzle to form a wedge shape. A mounting bracket allows the calibration nozzle to be placed in the same relative position in the spray chamber as the airblast atomizing nozzle. Except for a stainless steel insert, the calibration nozzle is made of aluminum. The stainless steel insert provides a finish similar to the atomizing nozzle filming surface and is not prone to oxidation effects. The nozzle was designed such that the flow area was the same at any axial cross-section which provides the same exposure time to the excitation beam for a fluorescent molecule entering the illuminated probe volume

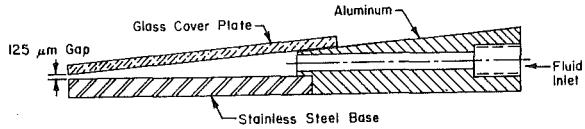

Fig. 7 Cross-section of the calibration nozzle

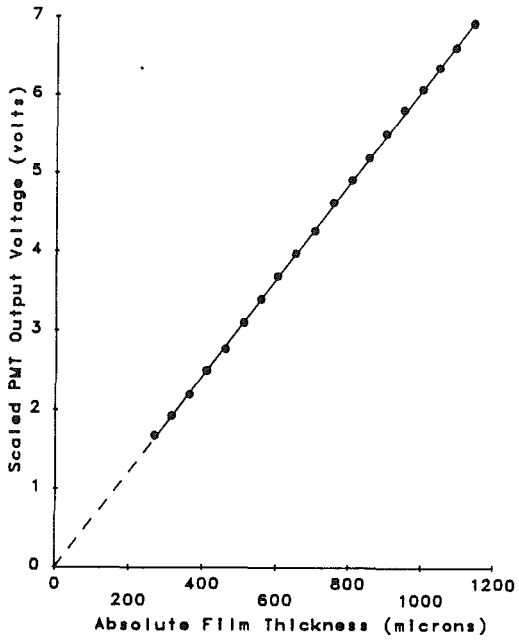

Fig. 8 System calibration results

anywhere on the nozzle. The glass plate introduces extra reflections not encountered with the airblast atomizing nozzle and the data is corrected for these.

Equation (11) predicts that the optical system calibration will be governed by the exponential equation of the form

$$V_i = B[1 - e^{(-A t_i)}] \tag{13}$$

where

V_i = scaled PMT output voltage at excitation beam measurement location i
B = constant which depends on the system operating parameters
A = apparent absorption coefficient
t_i = absolute thickness of the liquid normal to the calibration nozzle surface at excitation beam measurement location i

Typical calibration results are presented in Fig. 8. In this case, as would be expected for low values of $A\,t_i$, the calibration is nearly a linear function. The unknown coefficients A and B are determined using a least squares curve fit of the data presented in Fig. 8. Studies were performed to ensure that the calibration results were repeatable and independent of the fluid/dye solution mass flow rate. The standard deviation for the calibration results was less than 5 μm with a maximum deviation of less than 10 μm.

Once the unknown coefficients A and B are determined from the calibration results, the absolute thickness of the fluid film normal to the atomizing nozzle filming surface is given by

$$t_i = -\frac{C_{gc}}{C_g(\xi_i)A}\ln\left[1 - \frac{C_{rc}V_i}{C_r(\xi_i)B}\right] \tag{14}$$

where C_{gc} and C_{rc} are geometrical and reflection correction coefficients which modify A and B to account for the effect of the flat glass plate on the calibration nozzle. Unfortunately, the fluid surface angle (ξ_i) in Eq. (14) is not a known quantity. The fluid is not confined on the atomizing nozzle and therefore

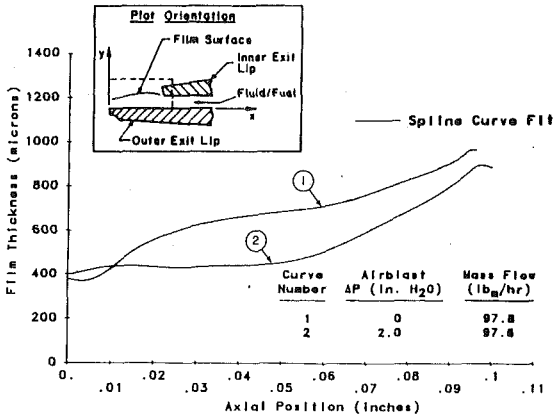

Fig. 9 Corrected data obtained at an azimuthal reference angle of 30 degrees

the fluid film surface angle may continually vary with axial measurement position. Thus, a special method is required to determine the corrected or actual film thickness (t_i). Initially, apparent film thickness data is obtained on the atomizing nozzle assuming $\xi_i = 0$ in Eq. (14). Once all the apparent film thickness data is obtained, an iterative technique (based on the apparent surface slope at the initial measurement position) is used to determine the actual fluid surface angle (ξ_i) and film thickness (t_i) at location i. This procedure will account for common wave induced variations in the free surface angle, but may be inadequate for extremely steep or breaking waves. Details of this and other aspects of the analysis may be found in Driscoll (1986).

Experimental Results

Preliminary experimental studies were performed to determine any direct or indirect effects on the measured liquid film thickness which might be caused by variations in such parameters as laser power, fluid/dye solution temperature, and nitrogen purge cone pressure. The scaled PMT output voltage was found to be a linear function of the laser beam power, at a fixed film thickness, which supports the assumption made in Eq. (11) that power saturation effects are negligible. The effect of the fluid/dye (water/Fluorescein) solution temperature was found to be very large (approximately a 1 percent change in the fluorescent power per degree F)—which necessitated the use of a heat exchanger to maintain a constant fluid/dye solution temperature. Varying the nitrogen purge cone pressure confirmed that a suitable range of purge pressure existed where the purge flow was adequate and no significant variation in measured film thickness occurred.

The film thickness data presented here was obtained using the experimental atomizing nozzle (illustrated in Fig. 1) with airblast pressure drops of both zero and two inches of water and a fluid/dye mass flow rate near 100 lb_m/hr. Measurements were made at seventeen axial positions for each azimuthal angle. At each position six measurements were taken in approximately a one second period and the computed standard deviations were found to be less than one percent corresponding to a maximum thickness deviation of 10 μm. Figure 9 presents film thickness results at an azimuthal reference angle of 30 degrees. The curves in Fig. 9 represent spline fits of the thickness data along the prefilming surface.

Axial scans, such as the one presented in Fig. 9, were obtained in 10 degree increments for azimuthal reference angles of 0 to 90 degrees. Since the nozzle is symmetric, with eight inner air swirling vanes and eight fuel/fluid inlet swirler orifices, data are presented here for only a quarter of the prefilming surface area. Figures 10 and 11 present three dimensional surface plots of the corrected data obtained by

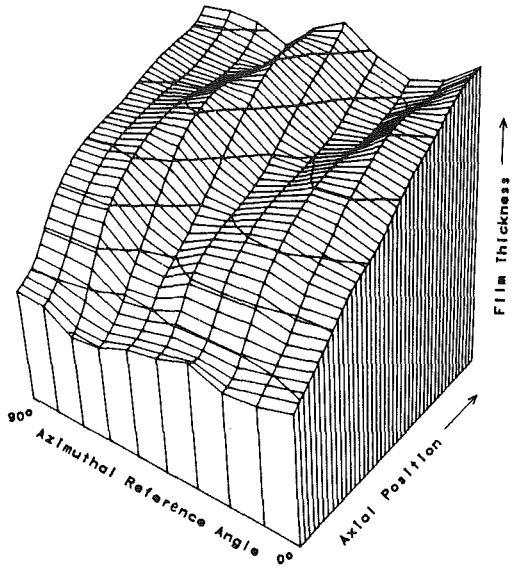

Fig. 10 Film surface structure without airblast

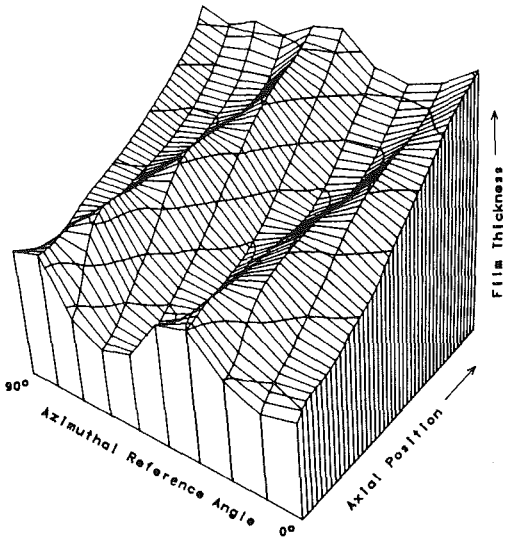

Fig. 11 Film surface structure with two inch airblast

combining axial scans. These figures depict the fluid surface as if a quarter of the conical film surface were cut away, laid out on a flat surface, and viewed from above. Figure 10 presents the film surface structure without airblast. Note the two slight ridges in the film caused by the two swirler orifices present in this quarter of the total filming area. Figure 11 presents the film surface structure with two-inch water-pressure airblast. The ridges or spokes are much more pronounced and are in the same general direction as the fuel/fluid swirler orifices (see Fig. 1). The periodic variation in film thickness will have a profound influence on the drop size distribution produced by the atomizer. Recent studies at the Parker-Hannifin Corporation have confirmed the usefulness of this method for studying airblast atomizers (Sun and Melvin, 1990).

Conclusions

A technique has been developed and perfected which allows accurate noncontact determination of liquid film thickness on the prefilming surface of an airblast atomizer. The repeatability of the technique based on both calibration and atomizer measurements is better than $+/-$ 10 μm. Spatial resolution of the system is also excellent, since the focused excitation beam diameter is 40 μm whereas the scanning range on the atomizer

lip is on the order of 2500 μm. A modification of the detection electronics would permit a system temporal resolution on the order of megahertz for time varying film thickness measurements, although this was not investigated during this work.

Although the laser induced fluorescence method developed here has been employed for the specific purpose of measuring liquid film thicknesses on an airblast atomizer, it could easily be adapted to other applications as well. Also, it should be possible to modify the method to obtain thickness measurements for a thin liquid sheet which is confined by air on both sides, rather than the current case where the sheet is confined by air on one side and a solid surface on the other.

References

Becker, R. S., 1969, *Theory and Interpretation of Fluorescence and Phosphorescence*, Wiley Interscience, New York.

Driscoll, D. A., 1986, "Liquid Film Thickness Measurement by Laser Induced Fluorescence," M.S. thesis, Purdue University, West Lafayette, IN.

Guilbault, G. G., ed., 1967, *Fluorescence-Theory, Instrumentation, and Practice*, Marcel Dekker, Inc., New York.

Hercules, D. M., ed., 1966, *Fluorescence and Phosphorescence Analysis*, John Wiley, New York.

Hieftje, G. M., et al., 1981, *Laser in Chemical Analysis*, The Humana Press, Clifton, New Jersey.

Lefebvre, A. H., 1983, *Gas Turbine Combustion*, McGraw-Hill, New York.

Parker, C. A., 1968, *Photoluminescence of Solutions*, Elsevier, New York.

Santos, R. D., 1977, "Flow Field and Particle Diagnostics with Fluorescent Aerosols," Ph.D. thesis, School of Mechanical Engineering, Purdue University, W. Lafayette, IN.

Schmitt, R. L., 1980, "Optical Measurement of Liquid Film Thickness in Airblast Atomizers," M.S. thesis, Purdue University, West Lafayette, IN, December.

Schmitt, R. L., Stevenson, W. H., and Simmons, H. C., 1982, "Optical Measurement of Liquid Film Thickness," *Proceedings of the International Congress on Applications of Lasers and Electro-Optics*, Vol. 33, pp. 31–35, Laser Institute of America.

Sun, F. T.-Y., and Melvin, J., 1990, "Effects of Inner Atomization Air on the Liquid Film Thickness of a Gas Turbine Fuel Nozzle," *Extended Abstracts of the Institute of Liquid Atomization and Spray Systems*, 4th Annual Conference, May 21–23, Hartford, CT.

Airblast Atomization of Viscous Newtonian Liquids Using Twin-Fluid Jet Atomizers of Various Designs

S. C. Tsai

B. Viers

Department of Chemical Engineering,
California State University,
Long Beach, CA 90840

Airblast atomization of viscous Newtonian liquids is carried out using coaxial twin-fluid jet atomizers of different nozzle sizes, slit angles, and slit cross sections for air flow. As the atomizing air swirls downstream along the liquid jet, waves form on the surface of the liquid jet. As a result, the liquid jet sheds ligaments which rapidly collapse into small drops. The atomized drop sizes can be described in terms of three dimensionless groups, namely, liquid-to-air mass ratio (M_L/M_A), Weber number (We), and Ohnesorge number (Z) in simple forms whose exponents and coefficients are determined by the best least square fit to the experimental results using the generalized inverse method. In addition, we found that the atomized drop sizes substantially decrease as the atomizing air pressure exceeds a threshold value which varies from less than 170 to 220 kPa depending on the nozzle size and the slit cross section.

Introduction

Airblast or twin-fluid atomization has been widely used in slurry combustion and suspension spray drying (Dombrowski and Munday, 1968; Marshall, 1954; Laskowski and Ranz, 1970). Twin-fluid atomizers have a number of advantages over pressure atomizers including lower slurry pressure and finer spray. Unfortunately, the process of airblast atomization is very complex and its physical mechanisms are not yet fully understood (Lefebvre, 1980). Moreover, conventional fuels, which must be broken into fine drops in order to be burned efficiently, are Newtonian liquids with relatively low viscosities (<0.5 P). In contrast, concentrated pseudoplastic suspensions such as coal water slurry (Tsai and Zammouri, 1988; Tsai and Knell, 1986) are much more viscous with viscosities up to 20 P at moderate shear rates. Whether or not the classical wave mechanism and the empirical models reported for airblast atomization of low viscosity liquids (Lefebvre, 1989) are applicable to airblast atomization of such viscous liquids is yet to be determined.

This paper describes the theoretical basis of several models which give the best least square fit to the experimental data for airblast atomization of Newtonian liquids with viscosities up to 10 P, and compares them with existing models for low viscosity liquids. The effects of atomizer design such as nozzle discharge diameter, slit angle and slit cross section of a distributor are also presented.

Experimental Methods and Atomizer Design

Airblast atomization of viscous Newtonian liquids (glycerol and its aqueous solutions) with viscosities ranging from 9.8 P to 2.9 P is carried out in a bench scale unit using a twin-fluid jet atomizer. The viscosity and the surface tension of the liquids are measured using Haake viscometer RV2 and Fisher surface tensiometer, respectively. They are in good agreement (± 5 percent) with the values reported in the *CRC Handbook of Chemistry and Physics*. The bench scale unit consists of a Malvern Particle Sizer Series 2600C, an atomization chamber, a pressure sample cylinder connected via an adaptor to the top of the twin-fluid atomizer, and a control panel for flow rate and pressure measurements.

The Malvern 2600C Particle Sizer measures the droplet size distribution of the spray through diffractive scattering (Fraunhöffer diffraction) of laser light (Mao et al., 1987; Switchenbank et al., 1976; Cameron et al., 1988). The overall spray is characterized by the Mass Median Diameter (MMD) of the droplets, which corresponds to the 50 percent point on the cumulative weight distribution curve, and the Volume Mean Diameter (VMD). Repeated experiments show that the experimental error in the droplet MMD is less than 5 μm. The particle size is calibrated using known particle size and size distribution standards provided by Advanced Particle Measurement, California.

The twin-fluid atomizer, as shown in Fig. 1, consists of a nozzle and a distributor (see Fig. 1 for the end view) assembled as a coaxial jet atomizer. It is a modified commercial atomizer from Delavan Corporation, South Carolina, which has been used in slurry combustion (Knell and Mansour, 1983; Tsai and Vu, 1987). Liquid passes axially through the center of the distributor, and the atomizing air passes through the angled slits drilled in the 45 deg taper of the distributor. A nozzle tip with a single discharge port is positioned 0.254 cm downstream

Contributed by the Fluids Engineering Division for publication in the JOURNAL OF FLUIDS ENGINEERING. Manuscript received by the Fluids Engineering Division May 25, 1990.

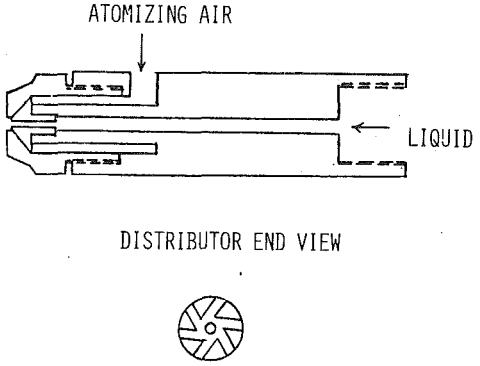

Fig. 1 Atomizer design

from the distributor tip. The diameters of the discharge ports of the three nozzles used are 0.249, 0.178, and 0.305 cm, which are larger than the diameter (0.152 cm) of the distributor for liquid passage. This design minimizes erosion of the nozzle tip during slurry atomization. The three distributors used have central openings of the same diameter (0.152 cm) but different slit dimensions: two have six slits 0.16 cm × 0.097 cm, angled at 15 and 5 deg, and one has four slits 0.24 cm × 0.076 cm, angled at 15 deg. As shown in Table 1, the total cross section of the four-slit distributor for air passage is smaller than that of the six-slit distributors. The slit angle facilitates swirling of the atomizing air which can be seen from the swirling of the liquid jet near the nozzle tip at low atomizing air pressure. Detailed experimental procedures and setup are described elsewhere (Tsai et al., 1988).

Wave Mechanism

Atomization is a process whereby a volume of liquid is converted into waves, ligaments, and ultimately into a multiplicity of small drops (Weber, 1931; Dombrowski and Johns, 1963; Bogy, 1979). The waves are initiated by factors such as pressure fluctuation or turbulence in the gas stream or the liquid stream (Adelberg, 1967; Adelberg, 1968). They continue as capillary waves if surface tension predominates, and as acceleration waves if pressure forces dominate. When the dynamic pressure ($\rho_A V_A^2/2$) of the air stream in airblast atomization is large enough, the amplitude of the surface waves will grow if their wavelength (λ) exceeds a minimum value (Adelberg, 1967; Adelberg, 1968; Jeffreys, 1925; Mayer, 1961). When the amplitude becomes sufficiently large, the waves shed ligaments which rapidly collapse, forming drops. The amplitude (A) of the surface waves on the liquid jet is described by the following differential equation (Jeffreys, 1925):

$$dA/dt = A\left[\frac{\pi\beta\rho_A(V_A-u)^2}{\lambda\rho_L u} - \frac{8\pi^2\mu_L}{\rho_L\lambda^2}\right] \tag{1}$$

Table 1 Atomizer dimensions

Nozzle tip no.	Discharge diameter cm	Cross section cm^2
1	0.249	4.866×10^{-2}
2	0.178	2.483×10^{-2}
3	0.305	7.306×10^{-2}

Distributor* no.	Slit-design no.-cm × cm-deg	Cross section, cm^2 liquid	air
1	6-0.16 × 0.097-15	1.815×10^{-2}	9.312×10^{-2}
2	4-0.24 × 0.076-15	1.815×10^{-2}	7.354×10^{-2}
3	6-0.16 × 0.097- 5	1.815×10^{-2}	9.312×10^{-2}

*Diameter of the central opening for liquid flow is 0.152 cm.

In this equation, we see that the amplitude, damped by the liquid viscous force, increases as the relative air velocity increases. When both the aerodynamic pressure and the surface tension forces are significant, the wave velocity u is given (Adelberg, 1968) by

$$u = [(a\lambda/2\pi) + (2\pi\sigma/\lambda\rho_L)]^{1/2} \tag{2}$$

where the acceleration (a) is caused by the aerodynamic drag on the liquid jet and is represented by

$$a = (4C_{Do}\sin^2\theta/\pi D\rho_L)\bar{\rho}_A\bar{V}_A^2/2 \tag{3}$$

where C_{Do} is the drag coefficient, D is the diameter of the liquid jet, θ is the angle between the air and the liquid stream, and $\bar{\rho}_A\bar{V}_A^2/2$ is the free stream aerodynamic pressure. Substituting Eq. (2) to Eq. (1) and assuming $V_A \gg u$ lead to the following equation:

$$dA/dt = A\left[\frac{\pi\beta\rho_A V_A^2}{\lambda\rho_L[(a\lambda/2\pi)+(2\pi\sigma/\lambda\rho_L)]^{1/2}} - \frac{8\pi^2\mu_L}{\rho_L\lambda^2}\right] \tag{4}$$

Equation (4) clearly shows that the amplitude growth is resisted by the surface tension (σ). Note that in this study the liquid flows at a velocity two orders of magnitude lower than the air velocity.

The minimum wavelength λ_m, above which the amplitude grows exponentially with time, may be estimated by setting $dA/dt = 0$. This results in the following cubic expression for λ_m:

$$\lambda_m^3 - \lambda_a\lambda_m^2 - \lambda_\sigma^3 = 0 \tag{5}$$

where

$$\frac{\lambda_\sigma}{D} = \frac{2\pi(16)^{1/3}}{\beta^{2/3}}(Z/\mathrm{We})^{2/3} \tag{5a}$$

$$\frac{\lambda_a}{D} = \frac{64C_{Do}\sin^2\theta}{n\beta^2\pi}(Z^2/\mathrm{We}) \tag{5b}$$

where λ_a and λ_σ are the wavelengths of the acceleration wave and the capillary wave, respectively, the Weber number (We) equals $\rho_A V_A^2 D/\sigma$, representing the ratio of aerodynamic force

Nomenclature

a = acceleration
A = amplitude of the surface waves on the liquid jet
A_o = area of flowing air stream
C_{Do} = drag coefficient
d_o = discharge port diameter
D = diameter of liquid jet or atomizer distributor diameter
L_c = characteristic length
MMD = mass median diameter of drops
$\dot{M}$ = mass flow rate
n = shock dynamic pressure ratio
P = pressure or poise
P^* = static pressure at a location where the flow is sonic
SMD = sauter mean diameter
u = wave velocity
V = velocity or average velocity
VMD = volume mean diameter
We = Weber number $\rho_A V_A^2 D/\sigma$
Z = Ohnesorge number, $\mu_L/(\rho_L\sigma D)^{1/2}$
ρ = density
μ = viscosity
σ = surface tension
λ = wavelength
β = Jeffreys' sheltering parameter having a value between 0 and 1
θ = angle between the jet axis and the free-stream gas velocity

Subscripts

A = atomizing air
L = liquid

to surface tension, the Ohnesorge number (Z) equals $\mu_L/(\rho_L\sigma D)^{1/2}$, and the shock dynamic pressure ratio (n) equals $\rho_A V_A^2/\bar{\rho}_A \bar{V}_A^2$.

When the aerodynamic pressure force predominates, waves propagate as acceleration waves at a minimum velocity of $(a\lambda_m/2\pi)^{1/2}$. In this case, $\lambda_a \ll \lambda_\sigma$, and one solution to Eq. (5) is $\lambda_m = \lambda_\sigma$ which is governed by $(Z/\mathrm{We})^{2/3}$ as shown in Eq. (5*a*). In contrast, when the surface tension predominates, waves propagate as capillary waves at a minimum velocity of $(2\pi\sigma/\lambda_m\rho_L)^{1/2}$. Since $\lambda_\sigma \ll \lambda_a$, one solution to Eq. (5) is $\lambda_m = \lambda_a$, which is governed by (Z^2/We) as shown in Eq. (5*b*). Therefore, both We and Z, with the exponent of Z-dependency equal to or twice that of We^{-1}-dependency, are included in our modeling of drop sizes for airblast atomization of viscous Newtonian liquids. Note that the nondimensional wavenumber that dictates the growth rate of Rayleigh-Taylor interface instability (Daly, 1969; Rangel and Sirignano, 1988) is equivalent to Z^2/We if the instability is caused by the acceleration generated by aerodynamic pressure force.

Semi-Empirical Models

Based on the aforementioned wave mechanism, the following three-parameter models are proposed along with the basic drop size equation for airblast atomizer (Lefebvre, 1980).

$$\mathrm{SMD}/L_c = (1+\dot{M}_L/\dot{M}_A)\{A\cdot \mathrm{We}^{-0.5} + B\cdot Z^{1.0}\} \quad (6)$$

$$\mathrm{MMD}/D = (1+\dot{M}_L/\dot{M}_A)\{x2\cdot \mathrm{We}^{-x1} + x3\cdot Z^{x1}\} \quad (7a)$$

$$\mathrm{MMD}/D = (1+\dot{M}_L/\dot{M}_A)\{x2\cdot \mathrm{We}^{-x1} + x3\cdot Z^{2\cdot x1}\} \quad (7b)$$

$$\mathrm{MMD}/D = (1+\dot{M}_L/\dot{M}_A)\{x2(Z/\mathrm{We})^{x1} + x3\} \quad (7c)$$

$$\mathrm{MMD}/D = (1+\dot{M}_L/\dot{M}_A)\{x2(Z^2/\mathrm{We})^{x1} + x3\} \quad (7d)$$

where L_c is a characteristic dimension that represents the scale of the atomizer, and is taken as the jet diameter. The linear dependency on $(1+\dot{M}_L/\dot{M}_A)$ is based on momentum balance and energy consideration (Tsai et al., 1991). $x3$ is included in Eqs. (7*c*) and (7*d*) because drop MMD remains finite as Z/We or Z^2/We approaches zero. The exponents and the coefficients are determined by the best least squares fit of these equations to more than 70 experimental data points using the generalized inverse method (Fletcher, 1968).

Iterative computation is used to obtain the best least squares solution to the set of m nonlinear equations in n unknown variables in the following form for example:

$$f(x) = (1+\dot{M}_L/\dot{M}_A)\{x2\mathrm{We}^{-x1} + x3Z^{x1}\} - \mathrm{MMD}/D$$

where x designates the set of three unknown variables $x1$, $x2$, and $x3$, and m is the number of experiments. Specifically,

(i) given x, set $k=1$

(ii) compute f_k, J_k, and $s_k = -J_k^+ f_k$

(iii) set $x_{k+1} = x_k + \alpha_k s_k$ choosing $\alpha_k > 0$ so that $F(x_{k+1})$ is the minimum of $F(x)$ in the direction s_k through x_k.

(iv) set $k = k+1$ and repeat from (ii) until convergence.

The Jacobian J is a $m \times n$ matrix of the first partial derivatives of $f(x)$ with elements $J_{ij} = \partial f_i/\partial x_j$ where $i=1$ to m and $j=1$ to n. J^+ is a $n \times m$ matrix, called the generalized inverse of J. In the case where $m > n$ and $\mathrm{rank}(J) = n$, J^+ becomes $(J'J)^{-1}J'$, where J' is the transpose of J. $F(x)$ is the least squares norm of the residuals, namely,

$$F(x) = f'(x)f(x) = f_1(x)^2 + f_2(x)^2 + \ldots + f_m(x)^2.$$

Wide ranges of the aforementioned dimensionless groups are covered:

$1+\dot{M}_L/\dot{M}_A$	We	Z
1.30–7.50	65–550	0.83–2.81

The two-parameter model, Eq. (6), gives very poor coefficients of correlation (0.57–0.61). The coefficients of correlation of Eqs. (7*a*) and (7*b*) were found to be 0.93–0.94 while those of Eqs. (7*c*) and (7*d*) range from 0.85 to 0.92. Therefore, only the best least squares solutions of the three unknown variables $x1$, $x2$, and $x3$ of Eqs. (7*a*) and (7*b*) are included in Table 2. Figures 2 and 3 demonstrate the agreement between the proposed 3-parameter models (Eqs. (7*a*) and (7*b*)) with the best least squares solutions listed in Table 2 and the experimental data. The agreement is considered excellent in view of the diverse nozzle designs and liquid properties. Also given in Table 2 are the 95 percent confidence intervals (Freund, 1979) of the correlation coefficients from which the ± deviations of $x1$, $x2$, and $x3$ are calculated. The power-dependency on $(1+\dot{M}_L/\dot{M}_A)$ is further examined by a logarithmic plot using We as a parameter for atomization of glycerol ($Z=2.81$) in Fig. 4. It should be noted that the slope of the lines in this figure is unity. Therefore the power of $(1+\dot{M}_L/\dot{M}_A)$ should be unity.

Table 2 Semi-empirical models for airblast atomization of glycerol and its aqueous solutions

$$\mathrm{MMD}/D = (1+\dot{M}_L/\dot{M}_A)\{x2\cdot \mathrm{We}^{-x1} + x3\cdot Z^{x1}\}\cdot 10^{-2} \quad (1)\#$$

$$\mathrm{MMD}/D = (1+\dot{M}_L/\dot{M}_A)\{x2\cdot \mathrm{We}^{-x1} + x3\cdot Z^{2\cdot x1}\}\cdot 10^{-2} \quad (2)\#$$

	$x1$	$x2$	$x3$	c.o.c.*	95 percent conf. interval	Equation
(*a*)	0.47 ±0.04	7.9 ±0.8	1.38 ±0.14	0.94	0.88–0.97	(1)
(*b*)	0.60 ±0.04	12.0 ±1.0	1.10 ±0.04	0.93	0.87–0.97	(1)
(*a*)	0.30 ±0.02	5.0 ±0.5	1.0 ±0.1	0.94	0.88–0.97	(2)
(*b*)	0.38 ±0.03	6.0 ±0.6	0.80 ±0.03	0.93	0.87–0.97	(2)

* Coefficient of correlation

\# D equals 0.152 cm.

(*a*) 32 data for atomization at air pressures below the threshold value.

(*b*) 40 data for atomization at air pressures above the threshold value, and MMD is replaced by VMD.

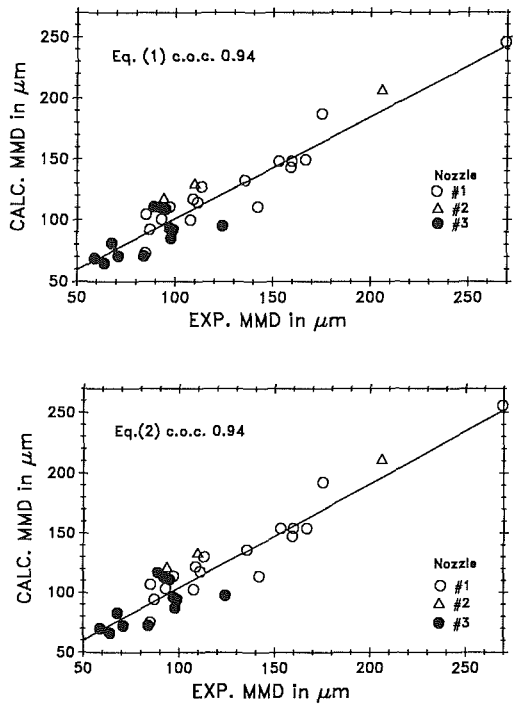

Fig. 2 Correlation between experimental and calculated drop mass median diameter (MMD) using Eqs. (1) and (2) of Table 2 for glycerol atomization at inlet air pressures below the threshold value

Discussions

Atomization results from interactions of disruptive aerodynamic force with consolidating liquid surface tension and viscous forces. The effects of liquid atomization on the flow

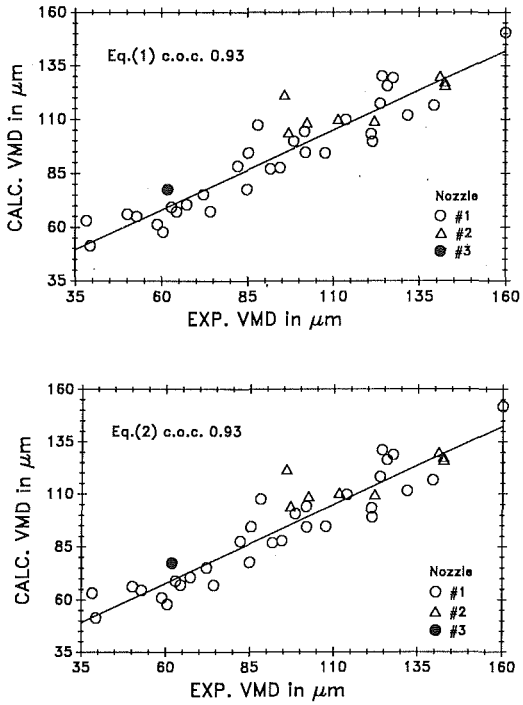

Fig. 3 Correlation between experimental and calculated drop volume mean diameter (VMD) using Eqs. (1) and (2) of Table 2 for glycerol atomization at inlet air pressures above the threshold value

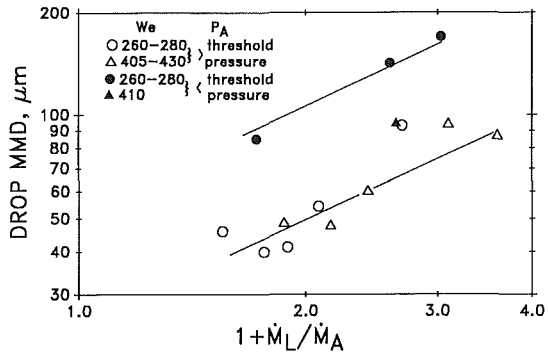

Fig. 4 Dependence of drop MMD on $1 + \dot{M}_L/\dot{M}_A$ in glycerol atomization using a twin-fluid jet atomizer (solid and open points for inlet atomizing air pressures below and above the threshold value, respectively)

of the atomizing air are shown in Fig. 5. The solid points in Fig. 5 represent the air mass flow rates during liquid atomization, while the open points represent those in the absence of liquid flow except for nozzle #3 where only the air mass flow rates during liquid atomization are given. In the absence of liquid flow, the air mass flow rate increases as the inlet air pressure increases because of the increasing density and velocity. The increase is slowed and saturation appears as the discharge port diameter is reduced (nozzle #2 versus nozzle #1). Likewise, the air mass flow rate is slowed and approaches saturation when the inlet air pressure exceeds 190 kPa during atomization of glycerol using nozzle #1. The saturated mass flow rate of the atomizing air and the inlet air pressure at which saturation occurs decrease as the liquid viscosity decreases. This finding indicates that the area for air passage in atomization of a less viscous liquid is reduced because of the resulting larger spray angle.

Liquid atomization behavior appears to be strongly dependent on the inlet pressure, the velocity, and the mass flow rate of the atomizing air. Atomization behavior varies with the inlet air pressure in differing degrees when the inlet air pressure exceeds a threshold pressure.

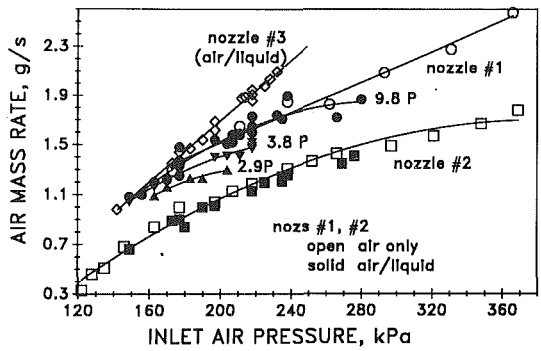

Fig. 5 Atomizing air mass flow rate using a twin-fluid atomizer consisting of distributor #1 and nozzles of various discharge diameters in the absence of liquid flow (open circles and open squares) and during the atomization of glycerol and its aqueous solutions with viscosities of 9.8 P (solid circles, solid squares, and open diamonds), 3.8 P (solid inverted triangles) and 2.9 P (solid triangles)

Effects of Threshold Air Pressure. Regressional analysis using the aforementioned models indicates the existence of a threshold inlet air pressure (see Table 2). As shown in Fig. 4, the drop MMD at inlet air pressures below the threshold value is considerably larger than those at inlet pressures above the threshold value. The effects of the threshold pressure are further demonstrated in Table 3. The drop MMD obtained using nozzle #1 becomes considerably smaller when the atomizing air pressure exceeds the threshold value which lies between 177 and 209 kPa. Note that the MMDs given in parenthesis in Table 3 are calculated using Eq. (7*a*) for inlet air pressures below the threshold pressure. This threshold pressure lies within the inlet air pressures at which saturation of the air mass flow rate occurs. It appears to be slightly higher (>220 kPa) when nozzle #1 is replaced by nozzle #3 that has a larger discharge diameter.

Similar to reduction in the saturated air mass flow rate, the aforementioned threshold pressure decreases as the liquid viscosity decreases from 9.8 P (glycerol) to 2.9 P (glycerol/water mixture). This threshold pressure in the atomization of glycerol also decreases (from 177–209 kPa to 177 kPa) when distributor #1 is replaced by distributor #2 that has a smaller cross sectional area (also see Table 3). Note that a larger spray angle was observed when using distributor #2 which provides a higher air velocity than distributor #1. It should be noted that the maximum inlet pressure (P_o) required of the critical pressure ratio of $P^*/P_o = 0.528$ when the isentropic air flow reaches the sonic velocity (Kihm and Chigier, 1989) at the atomizer tip is 190 kPa if P^* is taken as atmospheric pressure (McCabe et al., 1985).

For atomization at inlet air pressures below the threshold value, Eqs. (7*a*) and (7*b*) are in excellent agreement (coefficient of correlation of 0.94) with the experimental data (see Fig. 2). As the inlet air pressure exceeds the threshold pressure, new bands of small drops with average diameters of 6 μm and 20 μm are formed as shown in Fig. 6, which may have resulted from breakup of the primary drops (secondary atomization). The coefficient of correlation between the experimental MMD data and Eq. (7*a*) was found to be 0.88. Since small drops are weighted less in volume mean diameter (VMD) than MMD, VMD should better represent the primary atomization drop sizes. We found that the coefficient of correlation indeed improves from 0.88 to 0.93 as MMD in Eqs. (7*a*) and (7*b*) is replaced by VMD (see Fig. 3). The exponents of the power dependencies on We^{-1} and Z in this case are greater than those at inlet air pressures below the threshold value (see Table 2).

Comparison with the Reported Models of Airblast Atomization of Low Viscosity Liquids. Equations (7*a*) and (7*b*) are compared with the following empirical models reported in the

Table 3 Effect of threshold inlet air pressure on glycerol atomization

Noz. no.	Dtr. no.	$1+\dot{M}_L/\dot{M}_A$	P_A kPa	We	Z	MMD μm	VMD μm	SMD μm
1	1	(*a*) 1.72	177	278	2.81	85	118	49
1	1	(*b*) 1.76	211	263	2.81	40 (75)*	50	19
1	1	2.28	170	197	2.81	93	131	56
1	1	2.32	209	249	2.81	64 (81)*	95	31
1	1	2.54	177	222	2.81	97	129	53
1	1	2.78	232	293	2.81	64 (118)*	121	32
1	2	2.42	177	415	2.81	60 (100)*	92	29
1	2	3.00	156	301	2.81	113	141	54
1	2	3.10	183	406	2.81	94 (128)*	132	38
1	2	2.81	204	502	2.81	74 (114)*	121	27
2	1	2.72	177	102	2.81	110	139	72
2	1	2.70	238	149	2.81	71 (123)*	102	39
3	1	2.23	218	390	2.81	87	119	36
3	1	2.16	232	425	2.81	48 (89)*	62	21

*Values calculated using the following equation for atomization at inlet air pressures below the threshold pressure:

$$\mathrm{MMD}/D=(1+\dot{M}_L/\dot{M}_A)\{7.9\cdot \mathrm{We}^{-0.47}+1.38\cdot Z^{0.47}\}10^{-2}.$$

(*a*) and (*b*) The size distributions of atomized drops obtained at these conditions are shown in Fig. 6.

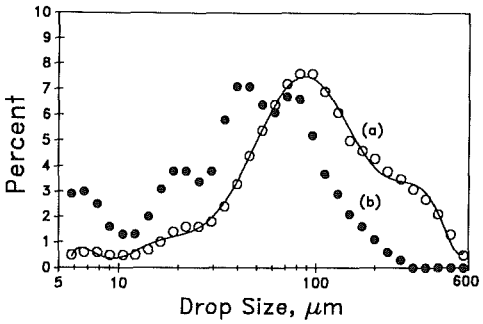

Fig. 6 Comparison of drop size distributions of glycerol atomization at inlet air pressure (*a*) below and (*b*) above the threshold pressure (other conditions are indicated in Table 3)

literature for airblast atomization of low viscosity liquids using a twin-fluid jet atomizer of various designs:

$$\mathrm{SMD}=0.585\{\sigma/(\rho_L V_R^2)\}^{0.5}+53\{\mu_L^2/(\sigma\rho_L\}^{0.225}(\dot{Q}_L/\dot{Q}_A)^{1.5} \quad (8a)$$

$$\mathrm{MMD}=5.36\times10^{-3}(\sigma^{0.41}\mu_L^{0.32})/\{(\rho_A V_R^2)^{0.57}A_o^{0.36}\rho_L^{0.16}\}+3.44\times10^{-3}\{\mu_L^2/(\rho_L\sigma)\}^{0.17}(\dot{M}_L/\dot{M}_A)V_R^{-0.54} \quad (8b)$$

$$\mathrm{SMD}=2.2\times10^{-2}\{\sigma/(\rho_A V_A^2)\}^{0.45}(1+\dot{M}_L/\dot{M}_A)^{0.5}+1.43\times10^{-3}\{\mu_L^2/(\sigma\rho_L)\}^{0.4}(1+\dot{M}_L/\dot{M}_A)^{0.8} \quad (8c)$$

$$\mathrm{SMD}/D=0.48\{\sigma/(\rho_A V_R^2 D)\}^{0.4}(1+\dot{M}_L/\dot{M}_A)^{0.4}+0.15\{\mu_L^2/(\sigma\rho_L D)\}^{0.5}(1+\dot{M}_L/\dot{M}_A) \quad (8d)$$

$$\mathrm{SMD}=0.95\{(\sigma\dot{M}_L)^{0.33}/(\rho_L^{0.37}\rho_A^{0.30}V_R)\}(1+\dot{M}_L/\dot{M}_A)^{1.7}+0.13\{\mu_L^2 D/(\sigma\rho_L)\}^{0.5}(1+\dot{M}_L/\dot{M}_A)^{1.7} \quad (8e)$$

where SMD is the Sauter Mean Diameter, V_R is the air velocity relative to the liquid jet, A_o is the flow area of atomizing air stream, and $\dot{Q}$ is the volumetric flow rate. Eq. (8*a*) is for atomization of liquids with viscosities up to 0.3 P using an internally mixed single-port twin-fluid jet atomizer (Nukiyama and Tanasawa, 1939). Equation (8*b*) is for atomization of liquids with viscosities up to 0.5 P using an externally mixed convergent-type twin-fluid jet atomizer (Kim and Marshall, 1971). Equation (8*c*) is for plain-jet airblast atomizer with which the liquid fuel such as kerosene flows through a number of radially-drilled circular holes in the form of discrete jets and enters a swirling airstream (Jasuja, 1982). Both Eqs. (8*d*) and (8*e*) are for plain-jet airblast atomizer (Rizk and Lefebvre, 1984; Lorenzetto and Lefebvre, 1977). Table 4 summarizes the

Table 4 Comparison of power dependencies of drop MMD obtained using plain-jet atomizer of various designs

	Exponent of variable indicated			
Eq.	μ_L	σ	$(1+\dot{M}_L/\dot{M}_A)$	Reference
(8*a*)	0.5	0.45	1.5[*a*]	Nukiyama and Tansawa (1939)
(8*b*)	0.41	0.34	1.0[*b*]	Kim and Marshall (1971)
(8*c*)	0.8	0.45	0.5-0.8	Jasuja (1982)
(8*d*)	1.0	0.4	0.4-1.0	Rizk and Lefebvre (1984)
(8*e*)	1.0	0.33	1.7	Lorenzetto and Lefebvre (1977)
(6)	1.0	0.5	1.0	Lefebvre (1980)
(7*a*)	0.47-0.60	0.47-0.60	1.0	This study
(7*b*)	0.60-0.76	0.30-0.38	1.0	This study

(*a*) Liquid-to-air volumetric flow rate ratio was used.
(*b*) $\dot{M}_L/\dot{M}_A$ instead of $(1+\dot{M}_L/\dot{M}_A)$ was used.

Table 5 Effect of nozzle discharge diameter on glycerol atomization using distributor #1

Noz#	dia. cm	$1+\dot{M}_L/\dot{M}_A$	P_A kPa	We	MMD μm	VMD μm	SMD μm
1	0.249	1.76	211	263	40 (75)*	50	19
1	0.249	1.72	177	278	85 (73)*	118	49
3	0.305	1.70	218	355	71 (71)*	98	33
1	0.249	2.52	197	269	68 (107)*	108	32
1	0.249	2.54	177	222	97 (111)*	129	53
3	0.305	2.52	218	373	85 (105)*	108	32
3	0.305	2.17	197	296	99 (92)*	137	42

*Values calculated using the following equation for atomization at inlet air pressures below the threshold pressure:

$$\mathrm{MMD}/D=(1+\dot{M}_L/\dot{M}_A)\{7.9\cdot \mathrm{We}^{-0.47}+1.38\cdot Z^{0.47}\}\cdot10^{-2}.$$

exponents of the power dependencies of the drop sizes on $(1+\dot{M}_L/\dot{M}_A)$, the liquid viscosity (μ_L), and the surface tension (σ) of these empirical models along with the wave mechanism-based models, Eqs. (7*a*) and (7*b*). This table shows that the exponents of these wave mechanism-based simple equations are remarkably similar to those of Eqs. (8*a*) and (8*b*). Like Eq. (6), the exponents of the power dependency on $(1+\dot{M}_L/\dot{M}_A)$ is unity. The exponent of the power dependency on surface tension (σ) in Eq. (7*a*) is also in excellent agreement with that in Eq. (6). However, Eq. (7*a*) shows power dependency on Z/We while Eq. (6) shows a power dependency on Z^2/We. Equations (7*b*), and (6) show power dependency on Z^2/We but to significantly different degrees.

Effects of Atomizer Design. As shown in Fig. 5, the atomizing air mass flow rate at a constant air pressure increases as the nozzle discharge diameter increases. However, as mentioned earlier, the threshold pressure effecting a significant improvement in atomization increases as well. As a result, the drop MMDs for nozzle #3 are significantly larger when atomization air pressures are just above the threshold value for nozzle #1 (see Table 5). Note that nozzle #3 is larger in discharge diameter than nozzle #1.

A slight increase in the air mass flow rate is seen in Fig. 7 either as the slit cross sectional area of the distributor decreases (distributor #2 vs #1) or as the slit angle decreases from 15 to 5 deg (distributor #3 vs #1). Reducing the slit cross section (distributor #2 vs #1, both angled at 15 deg) also results in increased Weber number and, thus, better atomization. In contrast, reducing the slit angle from 15 to 5 deg results in larger atomized drops as shown in Table 6. This table also shows that the inlet air pressure for glycerol atomizations with the use of distributor #3 angled at 5 deg has to exceed the threshold pressure in order to achieve drop sizes (in parenthesis) comparable to those obtained at inlet air pressures below the threshold value using the distributors angled at 15 deg.

Table 6 Effect of slit angle on glycerol atomization using nozzle #1

Dtr. no.	Slit Angle deg	$1+\dot{M}_L/\dot{M}_A$	P_A kPa	We	MMD μm	VMD μm	SMD μm
1	15	1.76	211	263	40 (75)*	50	19
1	15	1.72	177	278	85 (73)*	118	49
3	5	1.93	177	241	133 (83)*	181	61
3	5	1.76	177	249	121 (76)*	162	48
3	5	1.46	225	339	54 (61)*	77	23
3	5	1.93	204	293	74 (81)*	106	32
1	15	2.09	218	278	56 (87)*	85	26
1	15	2.28	170	197	93 (101)*	131	56
3	5	2.33	149	202	175 (103)*	201	96
3	5	2.09	232	339	74 (87)*	98	32

*Values calculated using the following equation for atomization at inlet air pressures below the threshold pressure:

$$\mathrm{MMD}/D=(1+\dot{M}_L/\dot{M}_A)\{7.9\cdot \mathrm{We}^{-0.47}+1.38\cdot Z^{0.47}\}\cdot 10^{-2}.$$

Conclusions

This study indicates the accuracy of the wave mechanism in depicting primary atomization of viscous Newtonian liquids with viscosities up to 10 P using a twin-fluid jet atomizer. The exponents of the power dependencies of the wave mechanism-based simple models are comparable to their counterparts reported for atomization of less viscous liquids with viscosities up to 0.5 P using twin-fluid jet atomizer.

As the inlet air pressure increases, the air mass flow rate increases and becomes saturated at a threshold pressure. Concurrently, the air velocity increases and approaches the maximum value (sonic velocity) at the atomizer tip. When the inlet pressure of the atomizing air exceeds this threshold pressure, the atomized drop sizes are considerably smaller, and new bands of small drops with average diameters of 6 μm and 20 μm are formed. These results may be attributed to the drop breakup by the sudden expansion at the nozzle tip. The threshold inlet air pressure above which better atomization results varies with the atomizer design such as nozzle discharge diameter, slit angle and slit cross section. Optimum atomizer design for airblast atomization of viscous liquids requires optimization of discharge diameter, slit angle, and slit cross sectional area.

Acknowledgments

The support of this work by a grant from the National Science Foundation (CBT-8613050), under the Particulate and Multiphase Program in the Division of Chemical, Biochemical and Thermal Engineering, is gratefully acknowledged. Partial support from the Department of Energy under the University Coal Research Program (DE-FG22-88PC88912) and the California State University Long Beach Foundation is also acknowledged. One of the authors (SCT) would like to acknowledge Frank Niu for computer programming, and Dale Botts for assistance in experimentation.

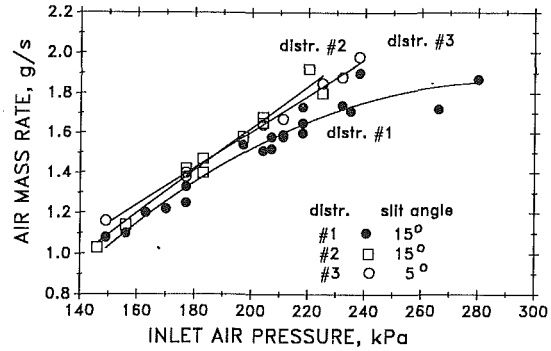

Fig. 7 Effect of distributor design on atomizing air mass flow rate through nozzle #1

References

Adelberg, M., 1967, "Breakup Rate and Penetration of a Liquid Jet in a Gas Stream," *AIAA J.*, Vol. 5, pp. 1408–1415.

Adelberg, M., 1968, "Mean Drop Size Resulting from the Injection of a Liquid Jet into a High-Speed Gas Stream," *AIAA J.*, pp. 1143–1147.

Bogy, D. B., 1979, "Drop Formation in A Circular Liquid Jet," *Ann. Rev. Fluid Mech.*, Vol. 11, pp. 207–228.

Cameron, C. D., Brouwer, J., and Samuelsen, G. S., 1988, "A Comparison of Spray Characterization in an Isothermal Chamber and in a Model Gas Turbine Combustor," *Proceedings of the 4th International Conference on Liquid Atomization and Spray Systems*, pp. 145–152.

Daly, B. J., 1969, "Numerical Study of the Effect of Surface Tension on Interface Instability," *Phys. Fluids*, Vol. 12, pp. 1340–1354.

Dowbrowski, N., and Johns, W. R., 1963, "The Aerodynamic Instability and Disintegration of Viscous Liquid Sheets," *Chem. Eng. Science*, Vol. 18, pp. 203–214.

Dowbrowski, N., and Munday, G., 1968, "Spray Drying," Ch. 16, *Bio-chemical and Biological Engineering Science*, edited by N. Blakebrough, Academic Press, London and New York.

Jasuja, A. K., 1982, "Plain-jet Airblast Atomization of Alternative Liquid Petroleum Fuels Under High Ambient Air Pressure Conditions," ASME Paper No. 82-GT-32.

Jeffreys, H., 1925, "On the Formation of Water Waves by Wind," *Roy. Soc. Proc.*, Series A, Vol. 107, pp. 189–206.

Fletcher, R., 1968, "Generalized Inverse Methods for the Best Least Squares Solution of Systems of Non-linear Equations," *Computer J.*, Vol. 10, pp. 392–399.

Freund, J. E., 1979, *Modern Elementary Statistics*, 5th edition, Ch. 15 "The Coefficient of Correlation," Prentice-Hall, Inc., Englewood Cliffs, NJ, pp. 392–400.

Kihm, K. D., and Chigier, N., 1989, "The Influence of Sonic Air Flows on Liquid Atomization of Airblast Atomizers," *Extended Abstracts, The 3rd Annual Conference of Institute of Liquid Atomization and Spray Systems*, Irvine, CA, pp. 131–135.

Kim, K. Y., and Marshall, W. R., Jr., 1971, "Drop Size Distributions from Pneumatic Atomizers," *AIChE J.*, Vol. 17, pp. 575–584.

Knell, W., and Mansour, M. N., 1983, *Proceedings of the 5th International Symposium on Coal Slurry Combustion Technology*, Apr., Tampa, FL, pp. 25–27.

Laskowski, J. J., and Ranz, W. E., 1970, "Spray Quenching," *AIChE J.*, Vol. 16, pp. 802–816.

Lefebvre, A., 1980, "Airblast Atomization," *Progress Energy Combustion Science*, Vol. 6, pp. 233–261.

Lefebvre, A. H., 1989, *Atomization and Sprays*, Ch. 6, "Atomizer Performance," Hemisphere Publishing Corp., New York, pp. 201–267.

Lorenzetto, G. E., and Lefebvre, A. H., 1977, "Measurements of Drop Size on a Plain Jet Airblast Atomizer," *AIAA J.*, Vol. 15, pp. 1006–1010.

Mao, C. P., Oechsle, V., and Chigier, N., 1987, "Drop Size Distribution and Air Velocity Measurements in Air Assist Swirl Atomizer Sprays," ASME JOURNAL OF FLUIDS ENGINEERING, Vol. 109, pp. 64–69.

Marshall, W. R., 1954, "Atomization and Spray Drying," *AIChE Chemical Engineering Progress*, Monograph Series 2, Vol. 50.

Mayer, E., 1961, "Theory of Liquid Atomization in High Velocity Gas Streams," *ARS J.*, pp. 1783–1785.

McCabe, W. L., Smith, J. C., and Harriott, P., 1985, *Unit Operations of Chemical Engineering*, 4th edition, McGraw Hill, New York, pp. 112–118.

Nukiyama, S., and Tanasawa, Y., 1939, "An Experiment on the Atomization of Liquid," *Trans. Soc. Mech. Eng., Japan, 4-6 Rept. 1-6*, pp. 68–75.

Rangel, R. H., and Sirignano, W. A., 1988, "Nonlinear Growth of Kelvin-Helmholtz Instability: Effect of Surface Tension and Density Ratio," *Phys. Fluids*, Vol. 31, pp. 1845–1855.

Rizk, N. K., and Lefebvre, A. H., 1984, "Spray Characteristics of Plain-Jet Airblast Atomizers," ASME *Journal of Eng. Gas Turbines Power*, Vol. 106, pp. 639–644.

Swithenbank, J., Beer, J. M., Abbott, D., and McCreath, G. C., 1976, "A Laser Diagnostic Technique for the Measurement of Droplet and Particle Size Distribution," *AIAA* paper 76-79, 14th Aerospace Sciences Meeting, Washington, D.C., Jan. 16–18.

Tsai, S. C., and Knell, E., 1986, "Viscometry and Rheology of Coal Water Slurry," *Fuel*, Vol. 65, pp. 566–571.

Tsai, S. C., and Vu, T., 1987, "Atomization of Coal Water Slurry Using Twin-fluid Jet Atomizer," *Fuel*, Vol. 66, pp. 1596–1602.

Tsai, S. C., Viers, B., and Botts, D., 1988, "Effects of Pseudoplastic Behavior on Airblast Atomization of Viscous Liquids," *Proceedings of the ASME 3rd International Symposium on Liquid-Solid Flows*, Vol. FED-75, pp. 225–231.

Tsai, S. C., and Zammouri, K., 1988, "Role of Interparticular Van Der Waals Force in Rheology of Concentrated Suspensions," *J. of Rheology*, Vol. 32, pp. 737–750.

Tsai, S. C., Ghazimorad, K., and Viers, B., 1991, "Airblast Atomization of Micronized Coal Slurries Using Twin-fluid Jet Atomizer," *Fuel*, Vol. 70, pp. 483–490.

Weber, C., 1931, "Zum Zerfall Einez Flussigkeitsstrahles," *Zischr. F. aqnew. Math. and Mech.*, Band 11, Heft 2, English Translation, University of Colorado Library, pp. 136–154.

Journal of Fluids Engineering

Technical Briefs

Eddy Correlations for Laminar Axisymmetric Sudden Expansion Flows

D. Badekas[1] and D. D. Knight[2]

1 Introduction

The laminar axisymmetric sudden expansion (Fig. 1) flowfield is governed by two dimensionless parameters: the Reynolds number $\mathrm{Re} = U_o d/\nu$ based upon the mean inflow velocity U_o, the inlet diameter d, and the fluid kinematic viscosity ν; and the expansion ratio $E = D/d$, where D is the outflow diameter.

Both experimental and theoretical (computational and analytical) studies as those of Back and Roshke (1972), Macagno and Hung (1967) and Monnet et al. (1982) have demonstrated that the flow remains laminar for $\mathrm{Re} \leq 200$. Unsteady effects have been observed for $200 < \mathrm{Re} < 400$, with turbulent flow (Back and Roshke, 1972) occurring for $\mathrm{Re} > 400$. Theoretical (computational) results in the laminar regime have been obtained using the full Navier-Stokes equations and a variety of computational algorithms. The first comprehensive investigation was performed by Macagno and Hung (1967) using a finite difference formulation for the stream-function vorticity formulation of the Navier-Stokes equations. Results were obtained at $E = 2$ for $\mathrm{Re} \leq 200$. Fletcher et al. (1985) employed a finite element algorithm and extended the investigation to $E = 6$ at a fixed $\mathrm{Re} = 200$. Scott and Mirza (1986) also employed a finite element method and examined the flow for $50 \leq \mathrm{Re} \leq 200$ and $1.5 \leq E \leq 4$. Good agreement between prediction and experiment was achieved in all of these studies, confirming the accuracy of the numerical methods. Analytical results have been obtained for the limiting cases of creeping flow (Monnet et al., 1982) and large Re (Milos and Acrivos, 1986).

These investigations in the laminar regime at $E \leq 4$ have demonstrated that the length of the eddy varies linearly with Reynolds number. This would appear to be rather unusual in view of the nonlinear nature of the Navier-Stokes equations. It is natural to inquire whether this behavior extends to higher values of E. The analysis of this question is the first objective of the present research wherein the flowfield is examined at $E = 6$ for $50 \leq \mathrm{Re} \leq 200$. A second objective is the development of correlations for the eddy characteristics as a function of E and Re. These characteristics, shown in Fig. 1, include the eddy reattachment length l_r, the relative eddy intensity V defined as the maximum reverse volume flux within the eddy normalized by the inlet volume flux, and the location of the eddy center l_c.

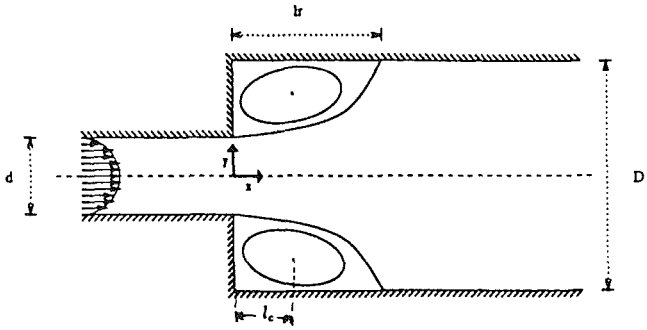

Fig. 1 Axisymmetric expansion

2 Method of Solution

In the present study, numerical solutions were obtained for the full axisymmetric incompressible Navier-Stokes equations (Batchelor, 1967) in primitive variables using the well known SIMPLE algorithm (Patankar, 1972). Details of the numerical method are presented in Badekas (1989) and Badekas and Knight (1991).

At the upstream boundary, a fully developed velocity profile was specified. On the wall boundaries, $u = v = 0$. At the downstream boundary, fully developed flow was also specified by setting zero radial velocity ($v = 0$) and no change to the axial velocity ($\partial u/\partial x = 0$). The upstream and downstream boundary conditions were applied sufficiently far from the expansion to insure that the computed solutions were independent of the location of application of these boundary conditions (Badekas, 1989 and Badekas and Knight, 1991).

A typical computation at $E = 6$ employed a grid size of 211×73 points and required 9 to 13 hr on the Convex C-1.

A detailed study of numerical accuracy was performed. As discussed by Badekas (1989), and Badekas and Knight (1991), the accuracy of the numerical solutions was established directly by a grid refinement study, and indirectly by comparison with previous published solutions in the range $1 \leq \mathrm{Re} \leq 200$ and $2 \leq E \leq 6$. On the basis of these, the accuracy of the eddy characteristic reattachment length (l_r), center location (l_c), and relative eddy intensity (V), is, ± 3, ± 1, and ± 5 percent, respectively.

3 Results and Discussion

3.1 Eddy Reattachment Length. The eddy that is generated at the step extends a large distance downstream (compared to the inlet size), because of the large expansion ratio. As the Reynolds number is increased, the eddy is proportionally stretched downstream.

[1]Graduate Assistant, Department of Mechanical and Aerospace Engineering, Rutgers University, New Brunswick, NJ 08903.

[2]Professor, Department of Mechanical and Aerospace Engineering, Rutgers University, New Brunswick, NJ 08903.

Contributed by the Fluids Engineering Division of The American Society of Mechanical Engineers. Manuscript received by the Fluids Engineering Division February 21, 1991.

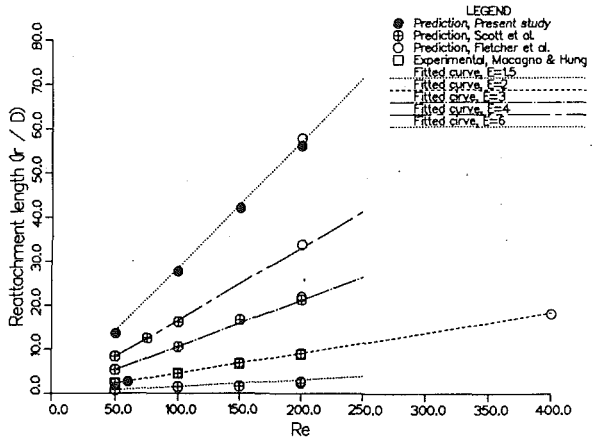

Fig. 2 Reattachment length (l_r) versus Reynolds number

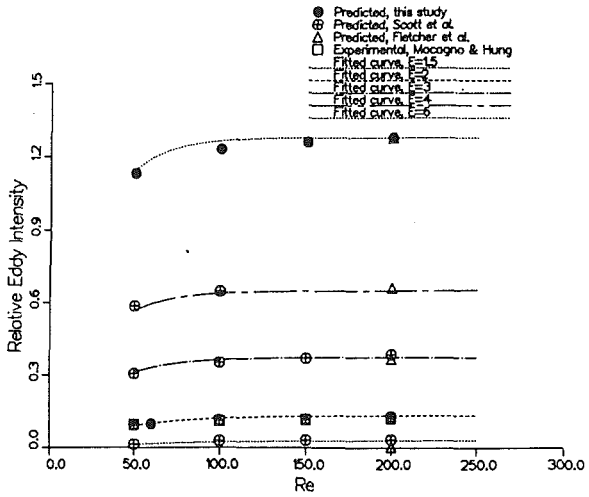

Fig. 3 Relative eddy intensity versus Reynolds number

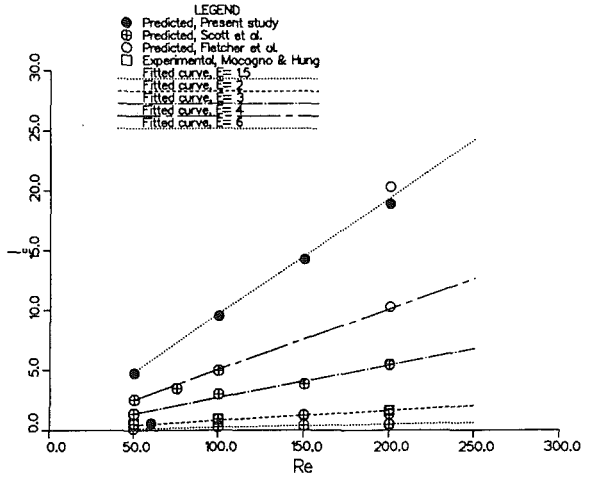

Fig. 4 Location of eddy center l_c versus Re

Figure 2 is a comprehensive plot of the reattachment length l_r vs Re, for various expansion ratios. The data in Fig. 2 agree well at the depicted expansion ratios among them, particularly so for $E=2$.

All the results seem to be very well fitted by a linear curve of the form:

$$\frac{l_r}{d}=\alpha \mathrm{Re} \tag{1}$$

where α is a parameter that depends on the expansion ratio. In the present study, the parameter α was found to be approximated by:

$$\alpha=0.0603(E-1)-0.0147 \tag{2}$$

The correlation Eqs. (1) and (2) were found to fit the data very well for $1.5\le E\le 6$ and $50\le \mathrm{Re}\le 200$ as shown in Fig. 2. The fact that α was not zero for a smooth pipe ($E=1$), is due to the non-linear effects evident when the circulation region is very small (Monnet et al., 1982). Therefore, the added constant part to the coefficient α can be viewed as a correction that accounts for this initial nonlinear behavior. Equations (1) and (2) have a maximum error of about 13 percent for an expansion ratio of $E=1.5$. The accuracy is improved for the larger expansion ratios. For example for $E=6$ the error is less than 3 percent.

Equation (1) is a very simple relation which well approximates the reattachment length for a wide range of expansion ratios as long as the flow can be considered laminar and steady state. This relation is not valid for $\mathrm{Re}<50$.

3.2 Relative Eddy Intensity. The relative eddy intensity V is defined as the ratio of the maximum amount of backflow in the recirculation region to the inlet mass flow. Figure 3 shows the dependence of the relative eddy intensity on the Reynolds number for various expansion ratios. An excellent agreement is seen for the relative eddy intensity between the results of Fletcher et al. (1985) and of the present calculations at $\mathrm{Re}=200$ and $E=6$.

The relative eddy intensity seems to be an exponential function of Re, and as proposed by Scott and Mirza (1986) the following form was assumed:

$$V=\theta[1-e^{(-\epsilon \mathrm{Re})}] \tag{3}$$

where the dimensionless coefficients θ and ϵ are functions of the expansion ratio.

In the present study, the following relations were developed to approximate the observed behavior of θ and ϵ:

$$\theta=a_1(E-1)^{a_2}+a_3 \tag{4}$$

$$\epsilon=b_1[1-e^{-b_2(E-1)}]+b_3 \tag{5}$$

where the coefficients were found to be: $a_1=0.17$; $a_2=1.27$, $a_3=-.037$, $b_1=0.054$, $b_2=0.86$, $b_3=-.008$.

Figure 3 shows that the correlation Eqs. (3)–(5) accurately approximate the observed behavior of V. Equation (3) has a maximum error of 12 percent for $E=1.5$. Again, as was true for the correlation for the reattachment length, the accuracy is improved for larger expansion ratios. At $E=2$, the error is less than 5 percent and for $E=6$ the error is less than 3 percent.

3.3 Location of the Eddy Center. The location of the eddy center l_c has been observed previously to vary linearly with the Reynolds number. Scott and Mirza (1986) provides an expression which is a linear function of Re, but does not indicate an explicit dependence on E. In the present study, the following correlation was developed:

$$a\,\frac{l_c}{d}=\beta \mathrm{Re} \tag{6}$$

where β is a function of E given by:

$$\beta=a_1[e^{a_2(E-1)^{a_3}}-1] \tag{7}$$

where $a_1=26$, $a_2=4\times 10^{-4}$, and $a_3=1.4$. Figure 4 indicates that the correlation Eqs. (6)–(7) provide an accurate approximation for the location of the eddy center.

4 Conclusions

The laminar axisymmetric sudden expansion has been examined numerically for $50\le \mathrm{Re}\le 200$ and $1.5\le E\le 6$ using the

full axisymmetric Navier-Stokes equations and the SIMPLE algorithm based upon primitive variables. The accuracy of the numerical algorithm was established through a grid refinement study and comparison with previous numerical results for a range of Re and E.

The principal results of this study are:

- Accurate flowfield solutions were obtained at $E=6$ for $50 \le \mathrm{Re} \le 200$. These results extend the range of numerical solutions which have previously been limited to $E \le 4$ with the exception of a single prior laminar computation at $E=6$.
- The reattachment length l_r was observed to be a linear function of Re at $E=6$ for $50 \le \mathrm{Re} \le 200$, similar to the observed linear behavior at lower E.
- Complete correlation equations were developed for the dimensionless reattachment length l_r/d, location of the eddy center l_c/d, and eddy intensity V as functions of the Reynolds number Re and expansion ratio E. The correlation equations provide good approximations in the range $50 \le \mathrm{Re} \le 200$ and $1.5 \le E \le 6$.

5 Acknowledgments

This research was supported by the Office of Naval research under Contract No. N00014-85-K-0238 and the National Science Foundation through supercomputer time awarded at the John von Neumann National Supercomputer Center. The authors also acknowledge the support of the Rutgers University Supercomputer Remote Access and Graphics Facility, funded by the New Jersey Commission on Science and Technology and Rutgers University.

References

Back, L., and Roshke, E., 1972, "Shear-layer Regimes and Wave Instabilities and Reattachment Lengths Downstream of an Abrupt Circular Channel Expansion," *Journal of Applied Mechanics*, pp. 677–681.

Badekas, D., 1989, "Navier-Stokes Solutions for Axisymmetric Sudden Expansion Flows at a Large Expansion Ratio," Master's thesis, Dept. of Mechanical and Aerospace Engineering, Rutgers University.

Badekas, D., and Knight, D., 1991, "Eddy Correlations for Laminar Axisymmetric Sudden Expansion Flows," Technical Report RU-TR-179-MAE-F, Rutgers University.

Batchelor, G. K., 1967, *Fluid Dynamics*, Cambridge University Press.

Fletcher, D., Maskel, S., and Patrick, M., 1985, "Heat and Mass Transfer Computations for Laminar Flow in an Axisymmetric Sudden Expansion," *Computers and Fluids*, Vol. 13, pp. 207–221.

Macagno, E., and Hung, T.-K., 1967, "Computational and Experimental Study of a Captive Annular Eddy," *Journal of Fluid Mechanics*, Vol. 28, pp. 43–64.

Milos, F., and Acrivos, A., 1986, "Steady Flow Past Sudden Expansions at Large Reynolds Number," *Physics of Fluids*, Vol. 29, pp. 1353–1357.

Monnet, P., Menard, C., and Sigli, D., 1982, "Some New Aspects to the Slow Flow of a Viscous Fluid Through an Axisymmetric Duct Expansion or Contraction. II—Experimental Part," *Applied Scientific Research*, Vol. 39, pp. 233–248.

Scott, P., and Mirza, F., 1986, "A Finite Element Analysis of Laminar Flows Through Planar and Axisymmetric Abrupt Expansions," *Computers and Fluids*, Vol. 14, pp. 423–432.

Patankar, S. V., 1972, *Numerical Heat Transfer and Fluid Flow*, Hemisphere.

The Effect of Friction on Flow Distribution in Dividing and Combining Flow Manifolds

P. I. Shen[1]

An analytical solution was obtained to evaluate the effect of friction on flow distribution in both dividing and combining flow manifolds. The governing equation follows the derivation given by Bajura (1971). A constant cross-sectional area of the manifold header and a constant friction factor along the manifold were assumed in order to obtain the analytical solution, expressed in terms of the lateral flow distribution as a function of two performance parameters, α (the friction parameter) and β (momentum loss parameter). Numerical results show that friction always increases flow imbalance in the combining flow configuration, but it may either increase or decrease flow imbalance in the dividing flow configuration, depending on the ratio of the lateral area to the cross-sectional area of the manifold.

1 Introduction

The flow manifold has various industrial applications, such as heat exchangers, pipe burners, irrigation systems, and other chemical processing streams. Recently, the flow manifold was used to analyze flow distribution of the air cooling of vertex detectors in the super-conducting super-collider. As a result, flow distribution in the flow manifold was subjected to extensive investigation. This study derived an analytical solution that describes the effect of friction on the lateral flow distribution in both combining and dividing flow manifolds. The method of deriving the solution may apply equally to other flow configurations, such as parallel and reverse flows, but only solutions of combining flow and dividing flow configurations are presented. The basic assumptions under which the analysis is valid are:

1. Flow along the manifold is incompressible.
2. The manifold has a constant cross-sectional area.
3. Flow is one-dimensional and the friction factor does not vary along the manifold.

In practice, the friction factor must vary along the manifold because of varying flow velocity. For a turbulent flow along the manifold, however, the friction factor varies only to the 1/4th power of the flow velocity along the manifold, and a constant friction factor may be a good approximation. Because the turbulent flow occurs in most practical cases, the manifold designer may use the simple solution obtained here as a convenient mathematical tool to perform quick performance trade evaluations. The analytical solution can also reduce the complexity of the flow network analysis, when multiple serial and parallel manifolds are required in the design.

2 Analytical Solution

The flow schematics of the manifold for both dividing and combining flow configurations are shown in Fig. 1. In the dividing flow configuration, the axial flow along the manifold has inlet velocity u_o, and the flow exits the manifold laterally

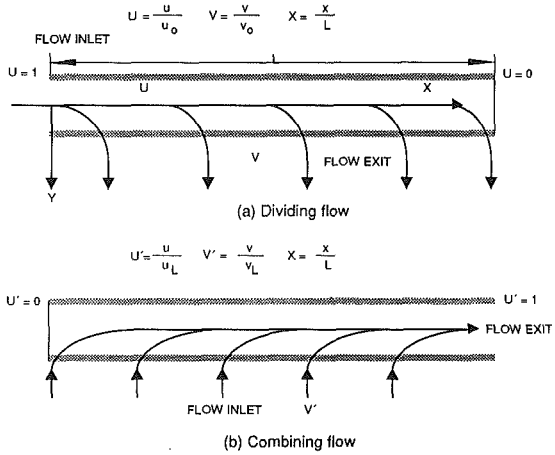

Fig. 1 Flow schematics

[1]Hughes Aircraft Company, El Segundo, CA 90245.

Contributed by the Fluids Engineering Division of THE AMERICAN SOCIETY OF MECHANICAL ENGINEERS. Manuscript received by the Fluids Engineering Division, February 10, 1991.

full axisymmetric Navier-Stokes equations and the SIMPLE algorithm based upon primitive variables. The accuracy of the numerical algorithm was established through a grid refinement study and comparison with previous numerical results for a range of Re and E.

The principal results of this study are:

- Accurate flowfield solutions were obtained at $E=6$ for $50 \le \mathrm{Re} \le 200$. These results extend the range of numerical solutions which have previously been limited to $E \le 4$ with the exception of a single prior laminar computation at $E=6$.
- The reattachment length l_r was observed to be a linear function of Re at $E=6$ for $50 \le \mathrm{Re} \le 200$, similar to the observed linear behavior at lower E.
- Complete correlation equations were developed for the dimensionless reattachment length l_r/d, location of the eddy center l_c/d, and eddy intensity V as functions of the Reynolds number Re and expansion ratio E. The correlation equations provide good approximations in the range $50 \le \mathrm{Re} \le 200$ and $1.5 \le E \le 6$.

5 Acknowledgments

This research was supported by the Office of Naval research under Contract No. N00014-85-K-0238 and the National Science Foundation through supercomputer time awarded at the John von Neumann National Supercomputer Center. The authors also acknowledge the support of the Rutgers University Supercomputer Remote Access and Graphics Facility, funded by the New Jersey Commission on Science and Technology and Rutgers University.

References

Back, L., and Roshke, E., 1972, "Shear-layer Regimes and Wave Instabilities and Reattachment Lengths Downstream of an Abrupt Circular Channel Expansion," *Journal of Applied Mechanics*, pp. 677–681.

Badekas, D., 1989, "Navier-Stokes Solutions for Axisymmetric Sudden Expansion Flows at a Large Expansion Ratio," Master's thesis, Dept. of Mechanical and Aerospace Engineering, Rutgers University.

Badekas, D., and Knight, D., 1991, "Eddy Correlations for Laminar Axisymmetric Sudden Expansion Flows," Technical Report RU-TR-179-MAE-F, Rutgers University.

Batchelor, G. K., 1967, *Fluid Dynamics*, Cambridge University Press.

Fletcher, D., Maskel, S., and Patrick, M., 1985, "Heat and Mass Transfer Computations for Laminar Flow in an Axisymmetric Sudden Expansion," *Computers and Fluids*, Vol. 13, pp. 207–221.

Macagno, E., and Hung, T.-K., 1967, "Computational and Experimental Study of a Captive Annular Eddy," *Journal of Fluid Mechanics*, Vol. 28, pp. 43–64.

Milos, F., and Acrivos, A., 1986, "Steady Flow Past Sudden Expansions at Large Reynolds Number," *Physics of Fluids*, Vol. 29, pp. 1353–1357.

Monnet, P., Menard, C., and Sigli, D., 1982, "Some New Aspects to the Slow Flow of a Viscous Fluid Through an Axisymmetric Duct Expansion or Contraction. II—Experimental Part," *Applied Scientific Research*, Vol. 39, pp. 233–248.

Scott, P., and Mirza, F., 1986, "A Finite Element Analysis of Laminar Flows Through Planar and Axisymmetric Abrupt Expansions," *Computers and Fluids*, Vol. 14, pp. 423–432.

Patankar, S. V., 1972, *Numerical Heat Transfer and Fluid Flow*, Hemisphere.

The Effect of Friction on Flow Distribution in Dividing and Combining Flow Manifolds

P. I. Shen[1]

An analytical solution was obtained to evaluate the effect of friction on flow distribution in both dividing and combining flow manifolds. The governing equation follows the derivation given by Bajura (1971). A constant cross-sectional area of the manifold header and a constant friction factor along the manifold were assumed in order to obtain the analytical solution, expressed in terms of the lateral flow distribution as a function of two performance parameters, α (the friction parameter) and β (momentum loss parameter). Numerical results show that friction always increases flow imbalance in the combining flow configuration, but it may either increase or decrease flow imbalance in the dividing flow configuration, depending on the ratio of the lateral area to the cross-sectional area of the manifold.

1 Introduction

The flow manifold has various industrial applications, such as heat exchangers, pipe burners, irrigation systems, and other chemical processing streams. Recently, the flow manifold was used to analyze flow distribution of the air cooling of vertex detectors in the super-conducting super-collider. As a result, flow distribution in the flow manifold was subjected to extensive investigation. This study derived an analytical solution that describes the effect of friction on the lateral flow distribution in both combining and dividing flow manifolds. The method of deriving the solution may apply equally to other flow configurations, such as parallel and reverse flows, but only solutions of combining flow and dividing flow configurations are presented. The basic assumptions under which the analysis is valid are:

1. Flow along the manifold is incompressible.
2. The manifold has a constant cross-sectional area.
3. Flow is one-dimensional and the friction factor does not vary along the manifold.

In practice, the friction factor must vary along the manifold because of varying flow velocity. For a turbulent flow along the manifold, however, the friction factor varies only to the 1/4th power of the flow velocity along the manifold, and a constant friction factor may be a good approximation. Because the turbulent flow occurs in most practical cases, the manifold designer may use the simple solution obtained here as a convenient mathematical tool to perform quick performance trade evaluations. The analytical solution can also reduce the complexity of the flow network analysis, when multiple serial and parallel manifolds are required in the design.

2 Analytical Solution

The flow schematics of the manifold for both dividing and combining flow configurations are shown in Fig. 1. In the dividing flow configuration, the axial flow along the manifold has inlet velocity u_o, and the flow exits the manifold laterally

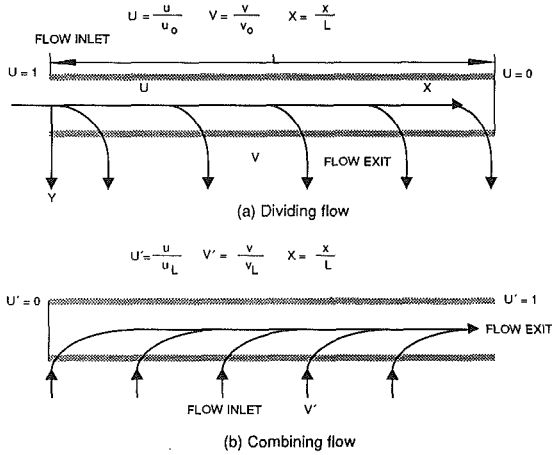

Fig. 1 Flow schematics

[1]Hughes Aircraft Company, El Segundo, CA 90245.

Contributed by the Fluids Engineering Division of THE AMERICAN SOCIETY OF MECHANICAL ENGINEERS. Manuscript received by the Fluids Engineering Division, February 10, 1991.

at velocity v. The axial flow velocity at $x = L$ (dead end) is zero. In the combining flow configuration, flow enters the manifold laterally and exits at the end of the manifold at $x = L$. The axial flow velocity at the entrance of the manifold is zero.

To derive the governing equation for the dividing flow configuration, Bajura (1971) uses the one-dimensional axial flow momentum equation, the conservation of mass along the manifold, and the Bernoulli equation in the lateral flow direction as the third equation to solve for three variables: the two velocity components (u and v) and the static pressure (p). The resulting equation of the dimensionless axial flow velocity $U(U = u/u_o)$ is written in terms of its derivatives with respect to the dimensionless coordinate $X(X = x/L)$, that is,

$$\frac{d}{dX}\left[\left(\frac{dU}{dX}\right)^2 + (\beta U)^2\right] + (\alpha U)^2 = 0 \tag{1}$$

where α and β are the two performance parameters defined as

$$\beta = \left(\frac{C_t}{H}\right)^{\frac{1}{2}} A_r \tag{2}$$

$$\alpha = \left(\frac{F}{H}\right)^{\frac{1}{2}} A_r \tag{3}$$

The parameter β measures the percentage of the turning loss, C_t, to the total head loss, H. C_t is given by

$$C_t = (2 - \gamma_d) \tag{4}$$

where γ_d is the pressure regain coefficient, which can be experimentally determined for a given manifold design. The total lateral head loss coefficient H is measured in terms of the dynamic pressure head loss of the lateral flow velocity. The coefficient H depends on the lateral flow exit port design and should include the loss due to sudden expansion or contraction and turning loss Ke and the friction loss coefficient F' ($F' = f'l/d$) of the lateral flow system given by

$$H = 1 + Ke + F' \tag{5}$$

and A_r represents the geometric area ratio of the manifold given by

$$A_r = Ap/Ac \qquad \text{(continuous flow distribution)} \tag{6a}$$

$$A_r = n(d/D)^2 \qquad \text{(discrete flow distribution)} \tag{6b}$$

where Ap and Ac are lateral peripheral area and cross-sectional areas of the manifold and n is the number of lateral outlets.

For a simple lateral flow discharge configuration, such as distributed holes, β can be expressed in terms of the discharge coefficient C_d by

$$\beta = C_d A_r \tag{7}$$

The second performance parameter α measures the ratio of the friction loss, F, to the total head loss, where F is based on the Darcy friction factor of the manifold flow, f, and is given by

$$F = fL/D \tag{8}$$

The two boundary conditions under consideration are

$$U(X=0) = 1 \quad \text{and} \quad U(X=1) = 0 \tag{9}$$

For $\alpha = 0$ (frictionless case), the dimensionless flow velocities U and V were obtained previously by Keller (1949) and Bajura (1971). For nonzero α, Eq. (1) can also be solved analytically and the solutions for U and V are

$$U = \exp(-C_1 X)\frac{\sin(C_2(1-X))}{\sin(C_2)} = \exp(-C_1 X)[\cos(C_2 X) - \cot(C_2)\sin(C_2 X)] \tag{10}$$

and

$$V = \exp(-C_1 X) \times \left[\cos(C_2 X) + \tan(C_2)\frac{1 - \frac{C_1}{C_2}\cot(C_2)}{1 + \frac{C_1}{C_2}\tan(C_2)}\sin(C_2 X)\right] \tag{11}$$

where

$$A = \left[-\frac{\alpha^2}{4} + \left(\frac{\alpha^4}{16} + \frac{\beta^6}{27}\right)^{\frac{1}{2}}\right]^{\frac{1}{3}}; \quad B = -\left[\frac{\alpha^2}{4} + \left(\frac{\alpha^4}{16} + \frac{\beta^6}{27}\right)^{\frac{1}{2}}\right]^{\frac{1}{3}}$$

$$C_1 = \frac{(A+B)}{2}; \quad C_2 = \frac{3^{\frac{1}{2}}}{2}(A-B)$$

For the combining flow configuration, one uses a new dimensionless variable U' ($U' = u/u_L$) because at $x = 0$, u_o is zero and U is infinity. The governing equation for the combining flow becomes

$$\frac{d}{dX}\left[\left(\frac{dU'}{dX}\right)^2 - (\beta U')^2\right] - (\alpha U')^2 = 0 \tag{12}$$

The boundary conditions for U' are now

$$U'(X=0) = 0 \quad \text{and} \quad U'(X=1) = 1 \tag{13}$$

Again, Eq. (13) can be solved analytically, and the solutions for U' and V' are

$$U' = \frac{\exp(C_1' X) - \exp(-C_2' X)}{\exp(C_1') - \exp(-C_2')} \tag{14}$$

and

$$V' = \frac{C_1'\exp(C_1' X) + C_2'\exp(-C_2' X)}{C_1'\exp(C_1') + C_2'\exp(-C_2')} \tag{15}$$

where

$$C_1' = \frac{2}{3^{\frac{1}{2}}}\beta\cos\left(\frac{\theta}{3}\right); \quad C_2' = \beta\left[\sin\left(\frac{\theta}{3}\right) + \frac{1}{3^{\frac{1}{2}}}\cos\left(\frac{\theta}{3}\right)\right];$$

$$\text{and } \theta = \tan^{-1}\left[\frac{\left(\frac{\beta^6}{27} - \frac{\alpha^4}{16}\right)^{\frac{1}{2}}}{\left(\frac{\alpha^2}{4}\right)}\right]$$

Note that the solutions of U' and V' are subjected to the condition of $\alpha^4/\beta^6 < 16/27$ which, fortunately, is almost always satisfied in the practical applications.

3 Numerical Results and Discussion

The numerical results of the effect of friction on the lateral flow distribution are presented in Figs. 2 and 3. The effect of the manifold design parameters, such as the area ratio A_r and L/D ratio, are included in the two performance parameters, α and β. Friction appears to have the most effect on the moderate area ratios, and $\beta = 1$ was selected for parametric evaluation of the friction effect. The results in Fig. 2 indicate that friction has a more dramatic effect on the dividing flow than on the combining flow. Figure 3 shows the flow distribution for $\beta = 2$ with and without friction. When $\beta = 2$, the flow reversal occurs in the dividing flow configuration, but the effect of friction on both dividing and combining flows is not significant.

A new parameter (λ) may be used to show the effect of friction without being coupled with the area ratio:

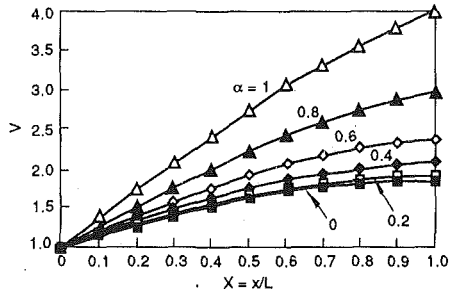

(a) Dividing flow configuration

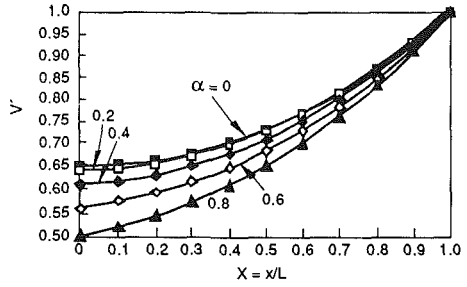

(b) Combining flow configuration

Fig. 2 Flow distribution for various values of $\alpha(\beta = 1)$

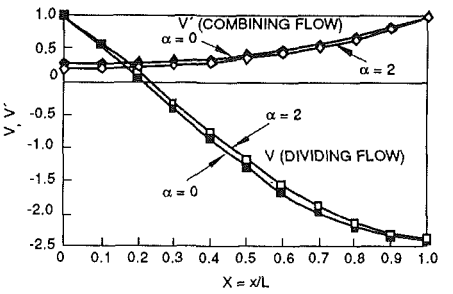

Fig. 3 Effect of friction on flow distribution for both dividing and combining flows with $\beta = 2$

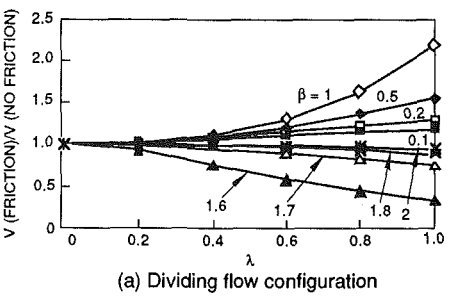

(a) Dividing flow configuration

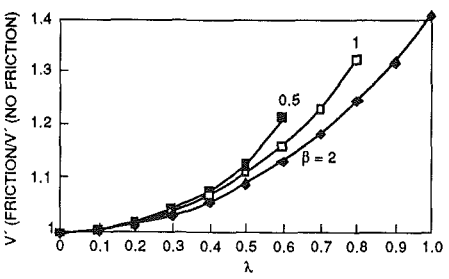

(b) Combining flow configuration

Fig. 4 Flow imbalance versus α/β with various values of β

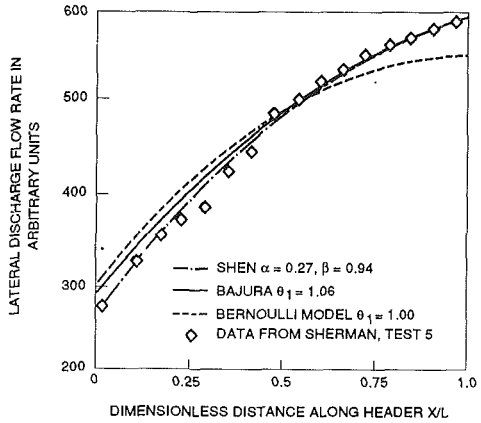

Fig. 5 Simple dividing flow manifold with large area ratio and small lateral resistance

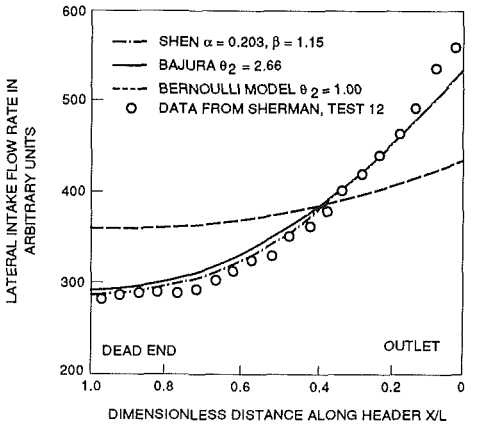

Fig. 6 Simple combining flow manifold with large area ratio and large lateral resistance

$$\lambda = \frac{\alpha}{\beta} = \left[\frac{F}{C_t}\right]^{\frac{1}{2}}$$

This new parameter represents the ratio of friction loss along the manifold to the turning loss. The ratio of flow imbalance with friction to flow imbalance without friction is plotted against λ in Fig. 4. In Fig. 4(a), friction reduces flow imbalance as indicated by Bajura (1971) but only where β is greater than $\pi/2$. Where β is less than $\pi/2$, friction increases flow imbalance. In the combining flow configuration (Fig. 4(b)), friction always accentuates flow imbalance.

A direct comparison was also made between the analyses of Bajura and Jones (1976) and Shen and the experimental results. Figures 5 and 6 were taken from Bajura and Jones (1976) with Shen's results added. For both the dividing and combining flow configurations, Shen's results give slightly better fit to the experimental data than Bajura's results. The good comparison verifies this analysis for the cases of small values of α.

In conclusion, the effect of friction on the flow manifold design can be obtained analytically and results are presented as simple algebraic equations, which are certainly valuable to the flow manifold design engineers.

References

Bajura, R. A., 1971, "A Model for Flow Distribution in Manifolds," ASME *Journal of Engineering for Power*, pp. 7–12.

Bajura, R. A., and Jones, E. H., 1976, "Flow Distribution Manifolds," ASME JOURNAL OF FLUIDS ENGINEERING, pp. 654–666.

Keller, J. D., 1949, "The Manifold Problem," ASME *Journal of Applied Mechanics*, Vol. 71, pp. 77–85.

Fluid Flow Through a Porous Medium Channel With Permeable Walls

J. M. Khodadadi[1] and J. T. Kroll[1]

A theoretical study of the fully developed fluid flow through a porous medium channel bounded by two permeable walls is presented. In the absence of inertia effects, a closed-form analytic solution to the volume-averaged momentum equation is obtained. The velocity profiles are illustrated for several combinations of the porous medium shape parameter and the blowing Reynolds number. The variations of the maximum velocity and the boundary frictional drag coefficient are also discussed.

Nomenclature

A = nondimensional pressure gradient, $W^2(dP/dx)/(\mu_f V)$
B = blowing Reynolds number, VW/ν_f
f = boundary frictional drag coefficient, $\mu_f[|(du/dy)_{y=0}| + |(du/dy)_{y=W}|]/(0.5\rho_f u^2_{\text{ave}})$
K = permeability of the porous medium
P = pressure
Re = Reynolds number in the channel, $2u_{\text{ave}}W/\nu_f$
u = velocity component in the x-direction
V = cross-flow velocity
W = channel width, Fig. 1
x, y = Cartesian coordinates, Fig. 1
γ = porous medium shape parameter, $(W^2\epsilon/K)^{0.5}$
ϵ = porosity of the porous medium
μ_f = dynamic viscosity of the fluid
ν_f = kinematic viscosity of the fluid
ρ_f = density of the fluid

Subscripts

ave = average value
max = maximum value

Introduction

An in-depth knowledge of transport processes through porous media is of great interest in diverse applications ranging from filtration technology, and transpiration cooling to design of solid-matrix heat exchangers and packed-bed chemical catalytic reactors. Most of the previous studies have utilized Darcy's law, which ignores the effects of inertial forces and the presence of solid boundaries. In this technical brief, a theoretical study of the fully-developed flow through a porous medium channel bounded by permeable parallel walls is presented (Fig. 1). The mathematical model for this flow accounts for the existence of the parallel walls, however the inertia effects are neglected.

The problem of fully-developed laminar flow through a nonporous channel with permeable walls is treated as a classic solution by White (1991). Berman (1958) analyzed the velocity profile of laminar flow in an annulus with permeable walls, whereas Wang (1971) derived an analytic solution for pulsatile flow in a channel with permeable parallel walls.

[1]Assistant Professor and Undergraduate Student, respectively, Mechanical Engineering Department, Auburn University, Auburn, AL 36849-5341. Professor Khodadadi is a Mem. ASME. J. T. Kroll is currently Graduate Research Assistant, Department of Mechanical Engineering, University of California, Irvine, CA.

Contributed by the Fluids Engineering Division of THE AMERICAN SOCIETY OF MECHANICAL ENGINEERS. Manuscript received by the Fluids Engineering Division January 14, 1991.

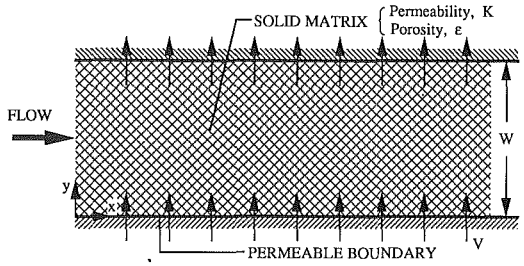

Fig. 1 Schematic of the porous medium channel bounded by two permeable parallel walls

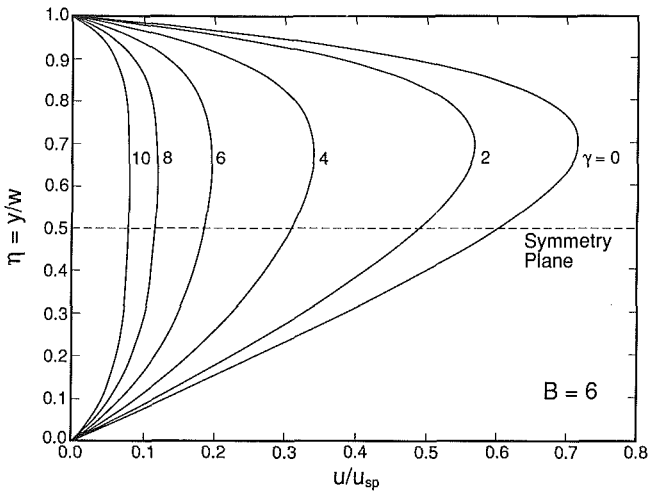

Fig. 2 Variation of the velocity profiles with γ for $B = 6$

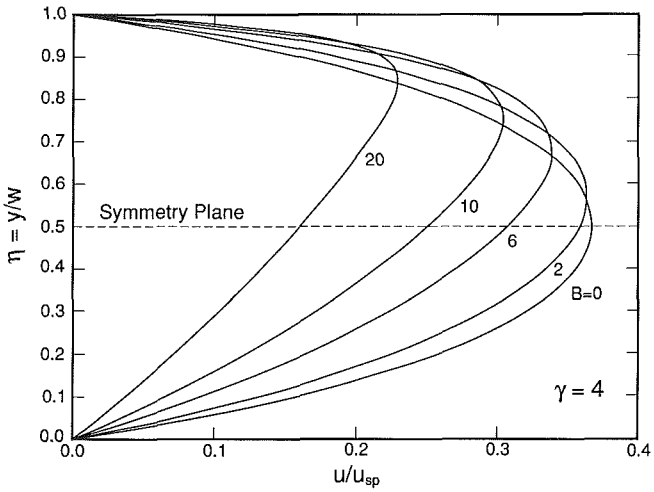

Fig. 3 Variation of the velocity profiles with B for $\gamma = 4$

Mathematical Analysis

The fully developed volume-averaged momentum equation for an incompressible fluid flowing through a porous medium with uniform porosity is

$$\frac{d^2u}{dy^2} - \left(\frac{V}{\nu_f}\right)\frac{du}{dy} - \left(\frac{\epsilon}{K}\right)u = \frac{1}{\mu_f}\frac{dP}{dx} + \left(\frac{F\epsilon^2}{\nu_f\sqrt{K}}\right)u(u^2+V^2)^{0.5} \quad (1)$$

where dP/dx is a constant. Similar to Khodadadai (1991), the last term in Eq. (1) which accounts for inertia effects is ignored here. Once the dependent variables are nondimensionalized

with respect to W and V (scales for length and velocity, respectively), Eq. (1) can be reduced to

$$\frac{d^2u^*}{d\eta^2} - B\frac{du^*}{d\eta} - \gamma^2 u^* = A \tag{2}$$

where $u^* = u/V$, $\eta = y/W$, B is the blowing Reynolds number, γ is the porous medium shape parameter, and A is the nondimensional pressure gradient. The appropriate boundary conditions for this problem are the no-slip conditions at the two walls, i.e., $u^* = 0$ at $\eta = 0$ and 1. The velocity distribution, $u^*(A,B,\gamma,\eta)$, is then given by

$$u^* = \left[\frac{A}{\gamma^2[\exp(D)-1]}\right]\left\{\exp\left[\frac{\eta(D+B)}{2}+\frac{(D-B)}{2}\right] - \exp\left[\frac{\eta(D+B)}{2}\right] - \exp\left[\frac{(D-B)(1-\eta)}{2}\right] + \exp\left[D-\frac{\eta(D-B)}{2}\right] - \exp(D) + 1\right\} \tag{3}$$

where $D = (B^2 + 4\gamma^2)^{0.5}$. As $\gamma \to 0$, Eq. (3) becomes exactly the same as the expressions given by Berman (1958) and Wang (1971) for nonporous flow passages.

The expressions for the location of the maximum velocity (η_{cr}) and the average velocity as functions of the blowing Reynolds number and the porous medium shape parameter are given by Eqs. (4) and (5), respectively:

$$\eta_{cr} = \frac{1}{D}\ln\left[\left(\frac{D-B}{D+B}\right)\left(\frac{\exp(D)-\exp[(D-B)/2]}{\exp[(D-B)/2]-1}\right)\right] \tag{4}$$

$$u^*_{ave} = \int_0^1 u^* d\eta = \left[\frac{A}{\gamma^2[\exp(D)-1]}\right]\left[\frac{D}{\gamma^2}\left\{\exp(D) - \exp\left[\frac{(D+B)}{2}\right] - \exp\left[\frac{(D-B)}{2}\right] + 1\right\} - \exp(D) + 1\right] \tag{5}$$

In order to eliminate the pressure gradient dependence, an alternate form of the velocity distribution is obtained by dividing Eq. (3) by the nondimensional velocity at the symmetry plane for flow through non-porous media bounded by two impermeable parallel plates ($u^*_{sp} = -A/8$), i.e., Poiseuille flow. The velocity profile is then only a function of two parameters, B and γ, as given by Eq. (6):

$$\frac{u}{u_{sp}} = \left[\frac{8}{\gamma^2[1-\exp(D)]}\right]\left\{\exp\left[\frac{\eta(D+B)}{2}+\frac{(D-B)}{2}\right] - \exp\left[\frac{\eta(D+B)}{2}\right] - \exp\left[\frac{(D-B)(1-\eta)}{2}\right] + \exp\left[D-\frac{\eta(D-B)}{2}\right] - \exp(D) + 1\right\} \tag{6}$$

As $\gamma \to 0$, it can be shown by applying L'Hôpital's rule that Eq. (6) becomes:

$$\frac{u}{u_{sp}} = \frac{-8}{B}\left[\frac{\exp(B\eta)-1}{\exp(B)-1} - \eta\right] \tag{7}$$

which agrees with the solution given by White (1991). The velocity profiles for this case show that when no cross-flow is present, a parabolic velocity profile is observed. As the blowing Reynolds number is increased, the mass flow rate through the channel decreases when compared to the Poiseuille flow with the same pressure gradient. The profiles also show that as the blowing Reynolds number increases, the location of the maximum velocity shifts toward the top wall.

The velocity profiles in the porous medium channel are shown in Figs. 2 and 3. In Fig. 2, the porous medium shape parameter is varied from 0 to 10, whereas the blowing Reynolds number is held constant at 6. From these profiles, one can conclude that the mass flow rate relative to the Poiseuille flow is a strong function of γ. On the other hand, the location of the maximum velocity shows little sensitivity to the value of γ. In Fig. 3, the velocity profiles as functions of the blowing Reynolds number are presented with γ held constant at 4. Once again, the relative decrease in the mass flow rate, and the trend of the maximum velocities occurring nearer to the upper wall with increasing values of the blowing Reynolds number are observed, similar to the $\gamma \to 0$ case.

The ratios of the maximum to the average velocities, i.e., u_{max}/u_{ave} or $u^*(\eta_{cr})/u^*_{ave}$, are plotted in Fig. 4 for selected blowing Reynolds numbers. The curve for the case of no cross-flow agrees with the results reported by Khodadadi (1991). As $\gamma \to 0$ with $B = 0$, u_{max}/u_{ave} approaches 1.5 as expected. For a given porous medium, as the blowing Reynolds number is increased, the average velocity decreases more markedly than the maximum velocity (e.g., see Fig. 3), and the quantity u_{max}/u_{ave} increases as a result. Furthermore, Fig. 4 suggests that the presence of a distinctive maximum is reduced as γ increases and plug-type profiles are observed in the channel.

Finally, the boundary frictional drag coefficient as a function of B and γ is given by Eq. (8):

$$f\mathrm{Re} = 2\left[\left|\left\{(D+B)\left(\exp\left[\frac{(D-B)}{2}\right]-1\right)+(D-B)\left(\exp\left[\frac{(D-B)}{2}\right]-\exp(D)\right)\right\}\right| + \left|\left\{(D+B)\exp\left[\frac{(D+B)}{2}\right]\times\left(\exp\left[\frac{(D-B)}{2}\right]-1\right)+(D-B)\exp\left[-\frac{(D-B)}{2}\right]\left(\exp\left[\frac{(D-B)}{2}\right]-\exp(D)\right)\right\}\right|\right] \Big/ \left[\frac{D}{\gamma^2}\left\{\exp(D)-\exp\left[\frac{(D+B)}{2}\right]-\exp\left[\frac{(D-B)}{2}\right]+1\right\}-\exp(D)+1\right] \tag{8}$$

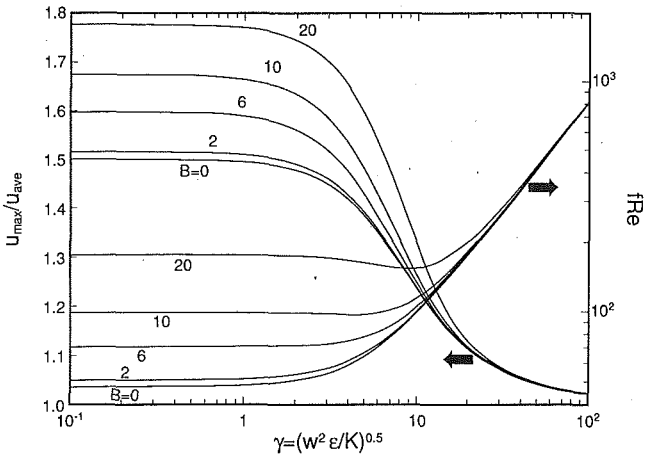

Fig. 4 Ratio of the maximum to the average velocity and the boundary frictional drag coefficient as functions of the porous medium shape parameter

The variation of the drag coefficient as a function of γ is given in Fig. 4 for selected blowing Reynolds numbers. When there is no cross-flow, fRe approaches 48, whereas for very large values of γ, it can be shown to approach 8γ. For a given porous medium, as the cross-flow intensity is increased, the drag coefficient increases as a result of steep shearing next to the top wall.

Conclusions

Based on the results of the mathematical analysis presented in this paper, an increase in either the blowing Reynolds number or the porous medium shape parameter results in a decrease in the mass flow rate relative to Poiseuille flow with the same pressure gradient. Additionally, for a given cross-flow rate, as γ increases the flow exhibits a flatter profile with a less distinctive maximum. Finally, for a given porous medium, the frictional drag increases as the blowing Reynolds number is increased.

References

Berman, A. S., 1958, "Laminar Flow in an Annulus with Porous Walls," *Journal of Applied Physics*, Vol. 29, pp. 71–75.

Khodadadi, J. M., 1991, "Oscillatory Fluid Flow Through a Porous Medium Channel Bounded by Two Impermeable Parallel Plates," ASME JOURNAL OF FLUIDS ENGINEERING, Vol. 113, pp. 509–511.

Wang, C-Y, 1971, "Pulsatile Flow in a Porous Channel," ASME *Journal of Applied Mechanics*, Vol. 38, pp. 553–555.

White, F. M., 1991, *Viscous Fluid Flow*, 2nd Edition, McGraw-Hill, NY, pp. 144–145.

Journal of Fluids Engineering

Discussion

The Oscillation of Horseshoe Vortex Systems[1]

Promode R. Bandyopadhyay.[2] Dr. Baker is to be congratulated for once again writing such an insightful article on necklace vortex. The following comments are relevant.

1. On p. 494, he has remarked that the number of vortices in the turbulent necklace vortex system of Sedney and Kitchens (1975) seem to vary erratically. However, when Sedney and Kitchens (1976) data are plotted as in Fig. 9, a systematic variation becomes evident. It represents a variation of s/D with nk/δ (δ is constant in the Fig. 9 data), where s is the upstream separation distance, k and D are obstacle height and diameter, respectively, and n is an even integer representing the total number of vortices.

Figure 9 is a kinematic result representing the angle subtended by the separating streamline with the wall at the upstream point of separation. In an analogous flow, near an airfoil trailing edge, the slope of the separation streamline which governs the length scale of the rolled-up shear layer, is a function of the Reynolds number of the incoming boundary layer at the point of separation. Since the Strouhal number is formed with this length scale, n of the obstacle flow could also depend on the Reynolds number of the incoming boundary layer as in the airfoil (Bertelrud and Liandrat 1990).

The intriguing question is: what is the mechanism that determines n? In a scenario alternative to what Dr. Baker proposes, the environment (freestream turbulence intensity, ratio of the freestream dissipation length scale to the shear layer length scale and vibration of the wall and obstacle) might be instrumental in the selection of n. This suggests that there are Reynolds number windows where the vortex system would be sensitive to excitation. In experiments, these quantities need to be monitored.

2. On p. 491, Dr. Baker has assumed that the radial velocity is proportional to the radial distance from the center of the core. Recent measurements (Bandyopadhyay et al., 1991) in a turbulent line vortex from a cylinder-wing vortex generator also show this to be valid within the mean core. The maximum radial velocity is about 1/20th of the freestream velocity and about 1/10th of the maximum azimuthal velocity.

3. In the abovementioned line vortex work, three quasi-periodic wavelengths were observed and the mean of all of them scales with the mean core diameter. It is not clear if very large wavelengths as considered by Dr. Baker are present.

Additional References

Bandyopadhyay, P. R., Stead, D. J., and Ash, R. L., 1991, "Organized Nature of Turbulent Trailing Vortex," *AIAA Journal*, Vol. 29, pp. 1627–1633.

Bertelrud, A., and Liandrat, M.-P., 1990, "Large Eddy Breakup Devices at Low and High Reynolds Numbers," Paper No. AIAA-90-1601, AIAA 21st Fluid Dyn., Plasma Dyn. and Lasers Conf., June 18–20, 1990, Seattle, WA.

Sedney, R., and Kitchens, C. W., 1976, "Measurement and Correlation of Separation Ahead of Protuberances in a Turbulent Boundary Layer." Paper No. AIAA-76-163. AIAA 14th Aerospace Sciences Meeting, Wash., D.C., Jan. 26–28, 1976.

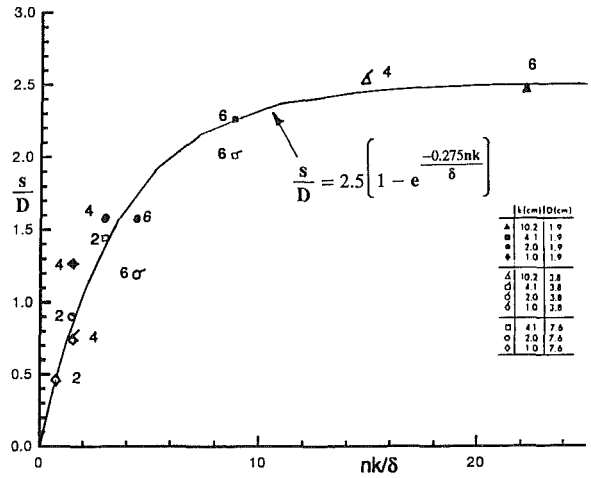

Fig. 9 Correlation between separation distance and number of vortices in Sedney and Kitchens (1976) data. Mach number = 3.5, Reynolds = 9.8 × 10^6/m, boundary layer thickness δ = 2.75 cm. The numbers indicate n.

Author's Closure

The author would like to thank Dr. Bandyopadhyay for his stimulating discussion and in reply would make the following points.

1. The approach taken to the data of Sedney and Kitchens (1976) is interesting. However, as it stands, the graph of Fig. 9 shows a combination of an independent variable (n) and a dependent variable (k/d) on the x axis, which is perhaps not ideal. An alternative approach would be to plot vortex number as a parameter in the (s/D) versus (k/d) plane to give regions of existence of different vortex number. Even this has some shortcomings since, as the writer noted, (s/D) is itself a function of other variables and is not a true independent variable.

2. The author agrees with the writer that in any future experiments care should be taken to measure freestream turbulence intensity etc., but it should be pointed out that in the work of Baker (1978) an extensive investigation showed no link between the horseshoe vortex oscillation frequencies and freestream turbulence frequencies and mechanical vibration frequencies.

3. It is gratifying to see some validation of the axial velocity assumption made by the author in his analysis. However it is not clear to the author whether the turbulent line vortex for which this has been found is precisely analogous to the plane of symmetry horseshoe vortex flow.

Clearly there is scope for future work here that will keep investigators busy for many years to come.

[1]By C. J. Baker, published in the Sept. 1991 issue of the JOURNAL OF FLUIDS ENGINEERING, Vol. 113, pp. 489–495.

[2]Code 804, NUWC Division, Newport, R.I. 02841-5047.